Design of nematic liquid crystals to control microscale dynamics

Oleg D. Lavrentovich

Advanced Materials and Liquid Crystal Institute,
Department of Physics, Materials Science Graduate Program,
Kent State University, Kent, OH 44242, USA;
ORCID 0000-0002-0128-0708

Abstract

The dynamics of small particles, both living such as swimming bacteria and inanimate, such as colloidal spheres, has fascinated scientists for centuries. If one could learn how to control and streamline their chaotic motion, that would open technological opportunities in the transformation of stored or environmental energy into systematic motion, with applications in micro-robotics, transport of matter, guided morphogenesis. This review presents an approach to command microscale dynamics by replacing an isotropic medium with a liquid crystal.

Orientational order and associated properties, such as elasticity, surface anchoring, and bulk anisotropy, enable new dynamic effects, ranging from the appearance and propagation of particle-like solitary waves to self-locomotion of an active droplet. By using photoalignment, the liquid crystal can be patterned into predesigned structures. In the presence of the electric field, these patterns enable the transport of solid and fluid particles through nonlinear electrokinetics rooted in anisotropy of conductivity and permittivity. Director patterns command the dynamics of swimming bacteria, guiding their trajectories, polarity of swimming, and distribution in space. This guidance is of a higher level of complexity than a simple following of the director by rod-like microorganisms. Namely, the director gradients mediate hydrodynamic interactions of bacteria to produce an active force and collective polar modes of swimming. The patterned director could also be engraved in a liquid crystal elastomer. When an elastomer coating is activated by heat or light, these patterns produce a deterministic surface topography. The director gradients define an activation force that shapes the elastomer in a manner similar to the active stresses triggering flows in active nematics. The patterned elastomer substrates could be used to define the orientation of cells in living tissues. The liquid-crystal guidance holds a major promise in achieving the goal of commanding microscale active flows.

INTRODUCTION

Scientific exploration of soft matter has provided the basis of truly transformative and life-changing technologies, such as liquid crystal displays (LCDs), the development of new approaches to drug delivery, sensors, nano-templated materials, etc. A unifying theme of past soft matter research and development has been the achievement of monocrystal behavior, exemplified by a uniform alignment of molecules in an LCD screen's pixels and their collective realignment by an externally applied electric field [1,2]. The new frontier of soft matter research, the one that will define the long-term development of fundamental science and technologies, is to learn how to translate nanoscale molecular organization into the mesoscale soft matter with spatially-non-uniform yet organized, functional and active structures, with tunable local and non-local responses to external cues and dynamic collective behavior coordinated in space and time. Active systems comprised of interacting units that use either internally stored energy or energy of the environment to propel themselves are of especial interest and challenge since they resemble living systems [3-6].

One of the interesting directions is to explore dynamics at the microscale, which usually corresponds to a low Reynolds number regime, i.e., to the prevalence of viscosity over inertia. The dynamics of small particles in fluids fascinated scientists for centuries, since van Leeuwenhoek observed in 1674 tiny creatures, nowadays known as “bacteria”, swimming chaotically in a droplet of water. The observations were made possible by the development of optical microscopes in the second half of the XVII century; for the historical account, see Refs. [7,8]. Much later, in the summer of 1827, Brown found that even inanimate small particles, when placed in water, engage in somewhat similar chaotic dynamics [9,10]. Since these discoveries, the dynamic behavior of small particles remained in the focus of soft matter science, promising exciting applications in energy transformation, micro-robotics, transport of matter, development of pharmaceuticals, regenerative medicine, etc., see, for example, the recent reviews [3-6,11-30] and references therein. Usually, the microscale dynamics is explored for an isotropic environment. In an isotropic medium, such as water, the dynamics can be controlled by externally applied fields, confinement, or gradients of some properties, such as a concentration of nutrients in the case of microorganisms. These approaches are often limited, for example, by a temporary character of the gradients. It is of interest to explore whether the microscale dynamics can be controlled by a liquid crystal (LC) environment instead of an isotropic one, which could provide a sense of direction associated with

the orientational order. LCs change the microscale dynamics even in the simplest case of Brownian motion by introducing anomalous diffusion regimes associated with the finite time of orientational fluctuations around particles [31]. This review focuses on designing LCs as a medium to guide microscale dynamics. The term "design" is used in a broad sense: it can be the intrinsic property of an LC such as bulk anisotropy and elasticity or surface alignment, or it can be a predesigned director pattern that enables a certain dynamic mode or controls the dynamic characteristics such as the polarity of swimming.

The review is based on the lectures presented by the author at the Spring 2019 School on The Mathematical Design of Materials at The Isaac Newton Institute, expanded by the material published since the School. The presented examples deal with particle-like solitons of the director field (Section I), liquid crystal-enabled electrokinetics (Section II), liquid crystal elastomers (Section III) and their application in the growth of living tissues (Section IV), biosynthetic systems such as living LCs, representing swimming bacteria dispersed in a lyotropic nematic, and active droplets suspended in a thermotropic nematic (Section V). Most of the themes have emerged only recently and are thus awaiting at-depth exploration.

I. ELECTRICALLY POWERED PARTICLE-LIKE SOLITONS IN NEMATICS

Most of the LC materials considered in this review are nematics. The simplest is a uniaxial nematic, formed by molecules or other entities (aggregates, anisometric cells, rod-like microswimmers, etc.) with a single direction of a preferred orientation, the so-called director $\hat{\mathbf{n}}$, which is an apolar entity, $\hat{\mathbf{n}} \equiv -\hat{\mathbf{n}}$, of a unit length, $\hat{\mathbf{n}}^2 = 1$. There also might be polar nematics described by a true vector $\hat{\mathbf{p}} \not\equiv -\hat{\mathbf{p}}$. Recent advances in synthesis and characterization of LCs formed by molecules with high dipole moments led to the discovery of a ferroelectric nematic fluid, the most symmetric ferroelectric medium [32-35]. Building units of symmetry lower than that of rods and discs could show a biaxial nematic ordering with three directors, $\hat{\mathbf{n}}$, $\hat{\mathbf{l}}$, and $\hat{\mathbf{m}} = \hat{\mathbf{n}} \times \hat{\mathbf{l}}$. Their existence in passive molecular systems is debatable [36], but there are recent reports on the biaxial nematic organization of liver tissue [37]; we will not consider biaxial nematics in what follows. Besides the director, one specifies the *degree S* of orientational ordering along the director, also called the scalar order parameter or the amplitude of the order parameter. S could depend on temperature or

density or the proximity to a core of a singular defect where $\hat{\mathbf{n}}$ is not defined. The full order parameter of a uniaxial nematic is a second rank tensor $\mathbf{Q}$ that is symmetric ($Q_{ij} = Q_{ji}$) and traceless ($Q_{ii} = 0$), with components

$$Q_{ij} = \frac{3}{2} S \left(n_i n_j - \frac{\delta_{ij}}{3} \right). \quad (1)$$

The most celebrated property of uniaxial nematics, which enabled the portable and flat-panel displays, is their reorientation in an electric field, called the Frederiks effect, caused by the anisotropy of dielectric susceptibility $\Delta\varepsilon = \varepsilon_{||} - \varepsilon_{\perp} \neq 0$; the subscripts refer to the direction with respect to $\hat{\mathbf{n}}$. An applied electric field $\mathbf{E}$ imposes a torque [2,38]

$$\mathbf{\Gamma} = \varepsilon_0 \Delta\varepsilon (\hat{\mathbf{n}} \cdot \mathbf{E})(\hat{\mathbf{n}} \times \mathbf{E}), \quad (2)$$

(ε_0 is the permittivity of vacuum) which realigns the director and changes the optical appearance of a flat nematic layer sandwiched between two glass plates with transparent electrodes and viewed between a pair of crossed polarizers, since $\hat{\mathbf{n}}$ is also the optic axis. The director realignment in the Frederiks effect is homogeneous in the plane of the cell. It is similar to the second-order phase transition with the tilt angle playing the role of the order parameter, adopting a constant value in any plane parallel to the electrodes [2,38]. The electric field could also trigger periodically modulated director patterns, as in the phenomenon called electroconvection [2,39-41], which is similar to Rayleigh-Bénard instabilities in thermal convection [42]. Theoretical description of the director's response to an electric field is difficult because of numerous mechanisms involved, such as anisotropic bulk elasticity and surface "anchoring" of the director, anisotropy of dielectric permittivity, electric conductivity and viscous drag, flexoelectric and surface electric polarization, spatial charge build-up at director gradients, injection of current carriers from electrodes, etc. Because of the above-mentioned difficulties, the theoretical models are usually reduced to one-dimensional or two-dimensional settings, often with an assumed periodicity, as, for example, in the treatment of one- and two-dimensionally periodic electrohydrodynamic instabilities [1,2,39,41,43].

An intriguing question is whether the electric field, in addition to the homogeneous and periodic distortions, could create spatially localized perturbations in a nematic, such as solitons of molecular reorientation. Since the word "soliton" is used in many different contexts, it is useful to define which types of solitons could be observed in a nematic. The most important classification

parameter is topological, as solitons could be topologically protected (non-transformable into a ground uniform state by continuous deformation of the director) or unprotected, continuously transformable into a uniform ground state [38,44]. The next two subsections describe the status of topological solitons and unprotected excitations called nematicons, followed by the discussion of recently observed topologically trivial dissipative solitons, represented by the so-called director bullets [45-48], also named directrons [48].

1.1.Topological solitons.

Early studies of spatially restricted director perturbations in uniaxial nematics, termed topological solitons or topological configurations [38,44], started about 50 years ago with the discussion of *static* linear and planar solitons produced by the magnetic or electric fields [49]. These solitons form when the external field aligns the director parallel to itself because of dielectric or diamagnetic anisotropy, but the boundary conditions and pre-existing director distortions prevent the material from simple uniform realignment. If the two equivalent states $\hat{\mathbf{n}}$ and $-\hat{\mathbf{n}}$ are trapped by the applied field, there must be a transition region in which $\hat{\mathbf{n}}$ reorients by π. This region of a director reorientation represents a static linear or planar topological soliton [38]. The planar solitons are also known as domain walls. The width of a soliton is defined by a balance of elasticity and coupling to the field. This soliton feature of a well-defined spatial extension is contrasted below and in Fig.1a-d to the behavior of director deformations that are controlled by the size of the nematic sample and thus do not belong to solitons family.

Consider a nematic cell in which the director is aligned in a planar fashion, i.e., along a certain direction in the plane of the bounding plates, Fig.1a, but experiences a reorientation by π in the bulk between the two plates. The Frank-Oseen elastic free energy density of a nematic is [38]

$$f_{FO} = \frac{1}{2}K_1(\mathrm{div}\hat{\boldsymbol{n}})^2 + \frac{1}{2}K_2(\hat{\boldsymbol{n}}\mathrm{curl}\hat{\boldsymbol{n}})^2 + \frac{1}{2}K_3(\hat{\boldsymbol{n}} \times \mathrm{curl}\hat{\boldsymbol{n}})^2, \quad (3)$$

where $K_1, K_2, \text{and } K_3$ are the elastic constants of splay, twist, and bend, respectively. Parametrizing the director as $\hat{\mathbf{n}} = [0, \cos\varphi(z), \sin\varphi(z)]$, where φ is the angle between $\hat{\mathbf{n}}$ and the y - axis and assuming for simplicity a one-constant approximation, $K_1 = K_2 = K_3 = K$, one concludes that in the equilibrium, the director angle changes linearly across the cell of thickness

d: $\varphi(z) = \pi z/d$ between two antipodal planar orientations, Fig.1a. The elastic energy per unit area of the cell is $F_{FO} = \int_{-\frac{d}{2}}^{\frac{d}{2}} f_{FO} dz = \frac{\pi^2 K}{4d}$. Obviously, if the cell thickness d increases, then the rate of the director realignment decreases, Fig.1b, and so does the elastic energy. In other words, the width of the nonuniform director in Fig. 1a,b is defined by the thickness of the cell and shows no self-confinement characteristic of solitons.

Consider the same cell, which is now acted upon by a magnetic field of induction $\mathbf{B} = (0, B, 0)$, directed along the y -axis, Fig.1c. The diamagnetic contribution to the free energy density [38] is $f_m = -\frac{1}{2}\mu_0^{-1}\Delta\chi(\hat{\mathbf{n}} \cdot \mathbf{B})^2$, where μ_0 is vacuum permeability, and $\Delta\chi = \chi_{||} - \chi_{\perp}$ is the diamagnetic anisotropy, assumed to be positive; the subscripts refer to the directions with respect to $\hat{\mathbf{n}}$. The magnetic field tends to align $\hat{\mathbf{n}}$ parallel to itself and creates a spatially-localized static soliton, Fig.1c. The Euler-Lagrange equation for an equilibrium director field reads $\frac{\partial^2 \varphi}{\partial z^2} + \frac{1}{L^2}\cos\varphi\sin\varphi = 0$, which yields a solution $\varphi(z) = 2\tan^{-1}\left(\tanh\frac{z}{2L}\right)$, where the characteristic measure $L = \frac{1}{B}\sqrt{\frac{K}{\mu_0^{-1}|\Delta\chi|}}$ of the soliton width depends on the acting magnetic field but not on the cell thickness. The soliton separates two domains of a uniform nematic, $\hat{\mathbf{n}} = (0,1,0)$, and cannot widen nor narrow, as long as $B = \text{const}$. The soliton is topologically stable in the sense that no smooth deformation could transform it into a uniform state. One such smooth operation could be a realignment of the director by π in one half of the sample; in presence of the magnetic field, this realignment would require an enormous energy that is much higher than the energy of the wall itself. However, a nematic soliton could be removed by nucleating and expanding a singular disclination loop of a strength ½, Fig.1d [50]. The strength ½ means that the director realigns by π when one circumnavigates the disclination core.

The possibility of eliminating the wall defect by a disclination line is rooted in a nonpolar nature of the director, $\hat{\mathbf{n}} \equiv -\hat{\mathbf{n}}$. It makes the nematic wall-like solitons different from Néel and Bloch walls in ferromagnets [51]. In ferromagnets, the vector character of magnetization prohibits disclinations, so that the domain walls could not be removed by a process shown in Fig,1d. Figure 1d suggests that a practical approach to produce a planar soliton is to apply an external field to a sample that already contains singular disclinations of strength 1/2. In a 3D nematic, there is only one class of topologically stable disclinations, with the director experiencing a rotation by π when

one circumnavigates the core [38,44]. In a similar way, one could create a string-like soliton by applying an electric or magnetic field to the nematic sample that already contains a point defect-hedgehog, Fig.1e. The structure of the linear soliton away from the point defect is reminiscent of the solitons described by Belavin and Polyakov [52] for an isotropic ferromagnet, the free energy density of which is similar to the one-constant approximation of Eq.(3). The magnetization vector, or, in the case of the nematic, the director, of the linear soliton far away from the point defect, can be written in cylindrical coordinates (ρ, φ, z) as $\hat{\mathbf{n}} = [sin\theta(\rho)\cos\varphi, sin\theta(\rho)\sin\varphi, cos\theta(\rho)]$, where the angle that the director makes with the z-axis changes from 0 to π when one goes from the center of the structure to its periphery: $\theta(\rho) = 2\tan^{-1}\left(\frac{\rho}{\rho_0}\right)$ [52,53]. Kleman [51] noted that the Belavin-Polyakov structure could be realized as an escaped disclination of strength 1 placed in the capillary tube with perpendicular anchoring of the director; in this case, $\theta(\rho)$ changes from 0 at the axis to $\pi/2$ at the physical limit ρ_0 of the structure, the radius of the cylindrical capillary. The topological stability of the linear soliton in Fig.1e can be established by considering the director orientations within the cross-section Σ perpendicular to the z -axis, Fig.1e. The director assumes all the possible orientations in this plane. These orientations could be presented by a sphere S^2/Z_2 of a unit radius, each point of which corresponds to the particular orientation; any two points at the end of the same diameter are identical. Since the director in the cross-section of the linear soliton covers all the points on the sphere once, the topological charge of the soliton is 1, the same as that of the hedgehog that caps the soliton [38].

The solitons in Fig.1c,d,e are stationary and do not require motion for their existence, in contrast to the traveling solitary waves [54]. Solitary director waves that exist only while moving, can be excited in a nematic channel by a pressure gradient that realigns the director and propagates the distorted region [55-58].

Fig.1. Distorted states and topological solitons in a uniaxial nematic. (a,b) Splay-bend director reorientation by π in a cell of thickness d that determines the length scale of the deformation. (c) Stationary topological soliton wall, the thickness of which is defined by the applied magnetic (or electric) field. (d). The soliton wall could be eliminated by nucleation of a disclination loop. (e) String-like soliton formed by an applied field at the point defect-hedgehog in the nematic bulk. At the surface Σ , the director adopts all possible orientations in space.

While walls and linear solitons are easy to stabilize by the external fields, Fig.1c-e, multidimensional topological solitons, such as three-dimensional (3D) particle-like nonsingular perturbations of the director field $\hat{\mathbf{n}}(\mathbf{r})$ in a nematic are deemed unstable with respect to shrinking. The reason is easy to understand by considering a hypothetical static 3D particle-like director deformation in a nematic (for an illustration, see Section 12.4 in [38] and the review [50]). A decrease in size, $L \to \lambda L$ by a factor $\lambda < 1$ entails an increase of the elastic energy density $f_{FO} \propto 1/L^2$ by a factor $1/\lambda^2$, Eq.(3), and a decrease in the topological soliton's volume by a factor of λ^3, thus the total elastic energy decreases as the soliton shrinks, $F \to \lambda F$ [38]. The instability of multidimensional solitons in nonlinear field models is generally known as the Derrick-Hobart theorem [59].

Solitons of various dimensionalities could be stabilized by an intrinsic macroscopic length scale of a medium. A good example is a cholesteric formed by chiral molecules that tend to twist with respect to each other. The Frank-Oseen energy density of a cholesteric is

$$f_{FO} = \frac{1}{2}K_1(\mathrm{div}\hat{\mathbf{n}})^2 + \frac{1}{2}K_2(\hat{\mathbf{n}}\mathrm{curl}\hat{\mathbf{n}} \pm q)^2 + \frac{1}{2}K_3(\hat{\mathbf{n}} \times \mathrm{curl}\hat{\mathbf{n}})^2 \quad ,$$

where $q = \frac{2\pi}{P}$ sets a right-angle helicoid $\hat{\mathbf{n}} = [\cos(2\pi z/P), \pm\sin(2\pi z/P), 0]$ with the pitch P. If a cholesteric cell is of a thickness $P/2$, Fig.2a, then an increase of its thickness by a factor of 2 would double the number of π – twists, Fig.2b; compare to Fig.1a,b. The intrinsic cholesteric twists introduce a characteristic length P of the deformed states. Since the chiral molecules in a cholesteric rotate freely around their long axes, their chiral interactions are weak, and as a result, P is much larger than the molecular scale of 1-10 nm, with the smallest values of P being typically above 100 nm.

The stabilizing action of the cholesteric pitch on deformed states is especially clear in cells with homeotropic (perpendicular) anchoring, Fig.2c,d. The homeotropic boundary conditions are not compatible with the twist. When the ratio P/d is on the order of 1, the balance of surface anchoring and bulk elasticity produces various structures, either in the form of particle-like "bubbles" or elongated formations, called cholesteric fingers (CFs), Fig.2c,d. Stable particle-like bubbles in cholesteric were observed by Haas and Adams [60,61], Kawachi et al. [62], Bouligand et al. [63], Smalyukh et al. [64-68], Guo et al. [69], Nych et al. [70], Posnjak et al. [71], described theoretically [53,72,73], and reviewed by Ryabchun and Bobrovsky [74] and by Smalyukh [75].

Following the pioneering examination by Cladis and Kleman [76], CFs were analyzed in details by Oswald et al. [77,78] and other groups [64,79-84]. The two most frequently met finger structures are called CF-1, proposed first by Press and Arrott [79,80], Fig.2c,d, and CF-2, proposed by Gil and Gilli [77] and Baudry et al. [80], Fig.2e,f. After the development of the three-dimensional director visualization technique [85,86], called fluorescence confocal polarizing microscopy (FCPM) [82,87,88], it became possible to establish the detailed director patterns in the vertical cross-sections of CFs, Fig.2d,f [64]. In contrast to conventional polarizing optical microscopy which produces optical contrast by integrating the spatially-varying local birefringence along the pathway of a wide beam of light, FCPM uses a polarized focused laser beam and relies on the fluorescent signal generated within a spatially restricted focus region, called voxel. The optical information from below and above the voxel does not contribute to the image. To image the director field, the sample is doped with a fluorescent anisometric dye that aligns its long axis along the director, which guarantees that the fluorescence signal depends on the angle between the polarization of the probing laser beam and the director [82,87], Fig.2c,e.

Fig.2. Cholesteric in cells of a different thickness (a,b) and topological solitons-cholesteric fingers of CF-1 (c,d) and CF2 (e,f) types. (a,b) Twist of the director with the period $P/2$ that depends on the helical twisting power of the chiral molecules; doubling the cell thickness doubles the number of π twists but does not change the length scale $P/2$. (c) FCPM texture and (d) the reconstructed director field of CF-1 in a homeotropic cell of the thickness close to P. The open circles mark the nonsingular cores of $\lambda^{-1/2}$ disclinations and the filled circles mark $\lambda^{+1/2}$ disclinations in Friedel-Kleman terminology [50,89]. (e,f) The same for CF-2; the filled circle marks λ^{+1} disclinations. In (c,e), the polarization of the probing light marked by "P" is along the y-axis. Parts (c-f) are reproduced with permission from Smalyukh et al. [64].

The stability of static topological solitons in cholesterics, such as the CFs and bubble domains, against shrinking is guaranteed by the helicoidal structure that maintains a fixed pitch. Regions of $\hat{\mathbf{n}}$ and $-\hat{\mathbf{n}}$ that differ by a π rotation are separated by half of the pitch and cannot be moved closer to each other without a dramatic increase of the elastic energy [63,72,90]. A similar mechanism of stabilization, called Dzyaloshinskii-Moriya mechanism, is known in the theory of helicoidal structures in ferromagnets [91].

Lately, the topologically nontrivial solitons of a bubble domain type in cholesterics are often called “skyrmions.” The term “skyrmion” embraces a broad range of topological solitons in various fields of physics, including Belavin-Polykov structures in ferromagnets [65,66,69,92,93], following Skyrme [94] who proposed a 3D solitons as a model of elementary particles, see the textbook by Manton and Sutcliffe [92]. The mathematical description of skyrmions is usually performed in the one-constant approximation of Eq.(3,4) mentioned above [72,73,95-102]. Lifting this assumption [53] and adding the so-called divergence terms [38] to the Frank-Oseen elastic energy density is an interesting task in the mathematical description, since liquid crystal materials offer a broad range of variability in elastic constants. One might expect new structures and symmetries in liquid crystals with strong disparities of the elastic constants.

The bubble domains and CFs are static and could exist without any applied field, as stressed already by Press and Arrott [79]. However, some of the static solitons in cholesterics could be forced to move by applying an external electric field, as demonstrated by Gil and Gilli [81] and others [66,67,80]. Gil and Gilli noted that CF-1 and CF-2 are of different symmetries [80,81]: CF-1 is invariant with respect to π rotations around the y-axis, Fig.2c,d, while CF-2 is left-right asymmetric with a mirror symmetry with respect to the midplane to the cell, Fig.2e,f. The symmetry difference manifests itself in the dynamics. Both CF-1 and CF-2 move perpendicularly to themselves when a direct current (DC) field is applied along the z-axis in Fig.2c,e [103,104]. However, an unbiased alternating current (AC) field could move only the left-right asymmetric CF-2 (the velocities are about (0.3-1) $\mu m/s$) but not CF-1 [80,103-106]. A theoretical model by Tarasov, Krekhov and Kramer [107] suggests that the motion is triggered by electric charge generation, either through anisotropy of electric conductivity (AC driving of CF-2), or through the flexoelectric effect (DC driving of CF-1). Bubble domains-skyrmions with some director asymmetry in the plane of the cell could also be moved by an electric field, with typical velocities (0.1-10) $\mu m/s$ [67,108]. Other external cues, such as temperature gradients, could also trigger drifts of CFs, as reviewed by Oswald, Dequidt, and Poy [78]. As many other examples in this review would demonstrate, the ability to move in a liquid crystal is directly related to asymmetry of the director configurations.

1.2.Nematicons.

Current studies on light-induced solitons in nematics mostly deal with optical solitons [109-114] representing propagating self-focused laser beams, called "nematicons" [109,112]. Figure 3 illustrates a principal scheme. A laser beam, which is linearly polarized along the y-axis and launched along the z -axis, enters the side of a planar nematic cell. The director is aligned parallel to the bounding plates and at some large angle $\theta_0 = 40° - 60°$ with respect to the beam's propagation direction. The electric field of the beam creates a realigning torque [113,114] similar to Eq.(2), in which $\Delta\varepsilon$ is replaced with the measure $(n_e^2 - n_o^2)$ of optical anisotropy, n_e and n_o being the extraordinary and ordinary refractive indices, respectively. For the typical case of rod-like molecules, $n_e > n_o$, the torque realigns the director towards itself, thus increasing the angle $\theta \geq \theta_0$ and the effective refractive index seen by the polarized beam, $n_{e,eff}(\theta) = \frac{n_e n_o}{\sqrt{n_e^2 \cos^2\theta + n_o^2 \sin^2\theta}}$. The spatially-varying refractive index focuses the beam [115], producing a soliton-nematicon S that propagates in the yz plane at a walk-off angle with respect to the z -axis, Fig.3a,b [113]. If the beam is linearly polarized along the x -axis, it interacts only with the ordinary refractive index and does not focus, Fig.3c [113].

Fig.3. Nematicons. (a) A light beam linearly polarized along the *y*-axis and launched along the *z*-axis, propagates through a planar nematic cell and realigns the director parallel to itself, increasing the effective refractive index and self-focusing; (b) microphotograps of a propagating nematicon; (c) beam polarized along the *x*-axis does not focus and propagates as an ordinary wave. Adapted with permission from Laudyn et al. [113] © The Optical Society.

Studies of nematicons are a part of very broad research on optical solitons in different nonlinear media [116-121], see reviews by Malomed et al. [122,123]. The "dimension" D of optical solitons is usually described using a nomenclature (M + 1)D, which means that the light beam can diffract in M dimensions as it propagates in one dimension [116,122]. Of especial interest are the so-called "light bullets" [124] or (3+1)D spatiotemporal solitons, which are self-confined in the longitudinal and both transverse directions and can be used in fast optic-logic systems [125]. Multidimensional solitons, unlike their 1D counterparts, are vulnerable to various

instabilities and are extremely hard to realize experimentally, see the discussion in Refs [121-123]. For example, there are no reports on experimental observations of stable light bullets that can survive collisions without losing energy. Since the director deformations within nematicons are topologically equivalent to the uniform state, these are topologically unprotected formations.

1.3. Dissipative solitons-directrons.

Among the broad family of solitons, there is a class of localized externally driven structures, often called dissipative solitons [126-128]. Dissipative solitons represent a portion of a pattern surrounded by a homogeneous steady state. They vanish when the driver's strength weakens below a certain threshold [126-128]. Experimentally, dissipative solitons were produced in the form of electric current filaments in a 2D planar gas-discharge system [129]. As often happens, nematics provide a fertile ground to realize entities that are difficult to form or observe in other materials. Very recently, various dissipative topologically unprotected solitons were observed in electrically driven nematics [45-48,130], Figs.4-8.

Dissipative solitons in electrically driven nematics are in the form of (3+1)D [45], Fig.4a-d, or (3+2)D [46], Fig.5, particle-like solitary waves of the director $\hat{\mathbf{n}}$, called by Li et al. [45,46] "director bullets" in analogy with the "light bullets." Although not as fast as bullets, these objects impress by their speed. A director bullet of a 40 μm length flies with a speed of 1000 $\mu m/s$, i.e., a 25 body lengths per second, Fig.4e. The speed is orders of magnitude higher than the speed of electrically powered CFs, bubbles-skyrmions, or any other objects, such as colloidal particles and microswimmers that could move through a LC.

Another descriptive term of the director bullets is a "directron", introduced later by Li et al. in Ref. [48], as it stresses the dual wave-particle character of the formation, in which the solitary wave of the director behaves like a particle in events such as collisions with other directrons, Fig.8. A mathematical model of these structures has been proposed recently by Earls and Calderer [131] in the limit of linear approximation, which is a very promising step towards a complete nonlinear description. S. Pikin pointed a possible role of field-induced injection of electric carriers in the formation of the director bullets [132]. The underlying experimental features are presented in the rest of this section.

The nematic in which the directrons were first observed by Li et al. [45,46], 4'-butyl-4-heptyl-bicyclohexyl-4-carbonitrile (CCN-47), Fig.4a, is of the (-,-) type, which means that both dielectric and conductivity anisotropies are negative, $\Delta\varepsilon = \varepsilon_{\parallel} - \varepsilon_{\perp} < 0$ and $\Delta\sigma = \sigma_{\parallel} - \sigma_{\perp} < 0$, respectively.

The directrons appear under simple experimental conditions. The cell of a sandwich type is bounded by two glass plates with transparent electrodes at the inner surfaces. Surface alignment is planar, with the director parallel to a single direction in the plane of bounding plates, $\hat{\mathbf{n}}_0 = (0,1,0)$. A sinusoidal AC electric field $\mathbf{E} = (0,0,E)$ acts across the cell. Once the electric field raises above some threshold, Fig.4d, the nematic develops spatially-confined perturbations $\hat{\mathbf{n}}(\mathbf{r})$ that coexist with a uniform director $\hat{\mathbf{n}}_0 = (0,1,0) = \text{const}$ of the surrounding, Figs.4-8. The perturbations are localized along all three spatial dimensions and do not spread while the soliton moves over macroscopic distances [45], Figs.4b,6. In the xy plane of propagation, the width and length of the solitons are thousands of times smaller than the corresponding dimensions of the cell. Along the z-axis, the stability of solitons is assisted by the surface anchoring at the bounding plates. Within a directron, the director perturbation oscillates with the frequency of the applied AC electric field, Fig.4c. The director deformations break left-right or fore-aft symmetry (or both), thus enabling directron's propagation either perpendicular to $\hat{\mathbf{n}}_0$, Fig. 4b,c, 5d-f, 6a-c, parallel to $\hat{\mathbf{n}}_0$, Figs.5a-c, 6d, or at some angle to $\hat{\mathbf{n}}_0$, when both symmetries are broken, Fig.7.

Fig.4. (a) Chemical structure of (-,-) nematic CCN-47. (b,c) Directrons B^h formed in an AC field of a high frequency: (b) optical microscopy texture with an optical compensator (red plate) inserted at 45° to the directions of polarizer (P) and analyzer (A); the inset shows the bent director field. (c) Director field within the soliton body oscillating up and down with the frequency of the applied voltage U. (d) Voltage-frequency domain of the directrons existence. (e) B^h speed vs. amplitude and frequency of the electric field. Redrawn from Li et al. [45].

1.4. Fore-aft, left-right, and mixed asymmetries of directrons.

There are different symmetry breaking scenarios that determine the propagation direction and other properties of directrons. These scenarios depend on the frequency and amplitude of the driving voltage. Directrons induced by fields of high frequency, typically f >100 Hz in CCN-47, abbreviated as the B^h directrons, show a left-right asymmetric "flying tuxedo" texture when viewed under a polarizing microscope with crossed polarizers, Fig.4b [45]. They are formed by an oscillating director deformation predominantly of a bend type, Fig.4b,c; the bend vector $\mathbf{b} = \hat{\mathbf{n}} \times \mathrm{curl}\hat{\mathbf{n}}$ shows a unique direction along the entire body of the B^h directron, see the inset in Fig.4b and Fig.6a,b [45].

The low-frequency (f <100 Hz) B^l directrons are of butterfly appearance when viewed in a polarizing microscope, Fig.5a,d, Ref. [46], and exhibit in-plane deformations of bend and splay, while the twist develops along the z-axis because of the planar anchoring at the bounding plates. In the low-frequency solitons, the vectors of bend $\mathbf{b} = \hat{\mathbf{n}} \times \mathrm{curl}\hat{\mathbf{n}}$ and splay $\mathbf{s} = \hat{\mathbf{n}}\mathrm{div}\hat{\mathbf{n}}$ change polarity as one moves along the direction of propagation, Figs.5b,c,e,f, and 6c,d. This partial "self-compensation" results in the propagation speed of B^l solitons being noticeably slower than the speed of high-frequency B^h directrons. In both cases, the velocity increases with the applied field, typically as E^2, Fig.4e, although the change in the amplitude of the field requires one to change also the frequency, as evident from the diagram in Fig.4d [45,46].

Fig.5. Low-frequency directrons B^l that propagate (a,b,c) parallel to the overall director $\hat{\mathbf{n}}_0$ and (d,e,f) perpendicularly to $\hat{\mathbf{n}}_0$. Instantaneous in-plane director tilt for B_0^l directron (c) at the time "0 ms" which corresponds to the minimum of the applied voltage and (d) at the time "25 ms" which corresponds to the maximum of a sinusoidal AC field; (e,f) similar director patterns for B_{90}^l directrons. The in-plane tilts are color-coded in accordance with the scale on the right-hand side. The tilt of the dashed lines with respect to the overall director is exaggerated by a factor of 6 for clarity. The nematic CCN-47 doped with 0.005wt% of ionic salt tetrabutylammonium bromide (TBABr). Redrawn from Li et al. [46].

The B^l director field, both instantaneous, Fig.5b,c,e,f, and averaged over the period of the driving AC electric field, Fig.6c,d, can be conveniently described by a quadrant system, Fig.6d. The director $\hat{\mathbf{n}}_0 = (0,1,0)$ separates the quadrants I and II. The deformed propagating structure of B^l can show a vertical (containing the z-axis) mirror symmetry plane, which passes either between

quadrants I and VI, Fig.6c, or between I and II, Fig.6d. There is no mirror symmetry with respect to the orthogonal vertical plane, as required for in-plane propulsion. As a result, the corresponding directron propagates along the direction that is either perpendicular, Fig.5b,c, or parallel, Fig.5ef, to the background director $\hat{\mathbf{n}}_0$. If the vertical mirror symmetry plane is absent, the soliton propagates at some angle to $\hat{\mathbf{n}}_0$, Fig.7. An important and interesting property of these B^l directrons with multiple scenarios of symmetry breaking is that a change of the electric field's amplitude and/or frequency steers them within the *xy* plane, which is perpendicular to the applied field [46], Fig.7. Since the B^l directrons are limited in space along all three directions and can move along different trajectories within the plane of the sample, they are classified as (3+2) solitons [46].

Fig.6. Time-averaged asymmetry patterns of directrons driven at high (top row) and low (bottom row) frequencies of the electric field; arrows show the flexoelectric polarization $\mathbf{P}_{fl}$ associated with (a,b,c) the bend vector $\mathbf{b} = \hat{\mathbf{n}} \times \mathrm{curl}\hat{\mathbf{n}}$ and (d) the splay vector $\mathbf{s} = \hat{\mathbf{n}}\mathrm{div}\hat{\mathbf{n}}$; (b) the polarization vector oscillates with the same frequency as the applied electric field **E**; asymmetry of the bend-splay director configuration leads to the soliton's propulsion with a velocity **v**.

Fig.7. Electric field controls symmetry, mutual transformations, and direction of propagation of low-frequency directrons. (a) B_0^1 transforms into B_{90}^1 and changes the direction of propagation after the voltage is raised at $t = 0$ s from 8 V to 11 V. (b) B_{90}^1 transform into B_0^1 when the voltage at $t = 0$ s is decreased from 11 V to 8 V. CCN-47 doped with 0.005wt% of TBABr. Redrawn from Li et al. [46].

1.5. Collisions of directrons.

The directrons show their particle-like character in collisions. High-frequency B^h directrons typically move perpendicularly to $\hat{\mathbf{n}}_0$. When two B^h directrons collide, they briefly unite and then restore their shape and propagation speed, Fig.8a,b,c [45]. Interestingly, directrons show repulsive/attractive interactions when they move in close proximity. For example, in Fig.8a,b,c, the post-collision separation of the two B^h directrons along the *x*-axis is larger than before the encounter, which demonstrates a repulsive interaction. Besides the recovery scenario illustrated in Fig.8a,b,c, collisions of two B^h solitons might lead to a number of other outcomes, such as pair annihilation or a disappearance of one soliton [45].

Fig.8. Collisions of directrons. (a,b,c) Two B^h directrons approach each other at 0 ms, collide at 88 ms and move away after a collision while restoring shapes, at 200 ms (CCN-47, $U = 55.2\ V$, $f = 800$ Hz, $T = 50\ ^\circ C$, $d = 8.0$ μm). The vertical axis shows the intensity of the transmitted light. (d,e) Two B_0^l directrons moving along $\hat{\mathbf{n}}_0$ collide and merge into a single B_{90}^l soliton that moves first at some angle and then perpendicularly to $\hat{\mathbf{n}}_0$. CCN-47 doped with 0.005wt% of TBABr; 8.5 V, 20 Hz. Redrawn from Li et al. [45] in (a,b,c) and [46] in (d,e).

The "butterfly" B^l low-frequency directrons show even richer behavior in collisions since these solitons can move along different directions [46], Fig.8d,e. For example, in addition to recovery and annihilation, two B^l solitons could change the direction of propagation by 90° after a collision or merge into one directron that would move in a direction different from the directions of the two original solitons, see Ref. [46] for more details. In particular, two B_0^l directrons moving along $\hat{\mathbf{n}}_0$ towards a collision could merge into a single B_{90}^l soliton that is redirected to move at some angle and then perpendicularly to $\hat{\mathbf{n}}_0$, Fig.8d,e.

1.6. Material parameters enabling directrons.

The critical frequency that separates the low-frequency B^l "flying tuxedos" directrons from the high-frequency B^h "butterfly" directrons can be associated with the frequency $f_c = \sqrt{\xi^2 - 1}/\tau_M$ introduced by Dubois-Violette et al. [133,134] to describe the so-called conducting and dielectric regimes of electrohydrodynamics in nematics. Here $\tau_M = \varepsilon_0 \varepsilon_\perp / \sigma_\perp$ is the Maxwell relaxation time for a planar cell, $\varepsilon_0 = 8.85 \times 10^{-12}$ F/m, and $\xi^2 = \left(1 - \frac{\sigma_\perp}{\sigma_\parallel}\frac{\varepsilon_\parallel}{\varepsilon_\perp}\right)\left(1 + \frac{\alpha_2}{\eta_c}\frac{\varepsilon_\parallel}{\Delta\varepsilon}\right)$ is the material parameter that depends on conductivities $\sigma_\parallel$ and $\sigma_\perp$, permittivities $\varepsilon_\parallel$. and $\varepsilon_\perp$, viscous coefficients α_2 and η_c. For typical material parameters [45,46] $\varepsilon_\parallel \approx 5$, $\varepsilon_\perp \approx 8$, $\sigma_\parallel, \sigma_\perp \sim (0.5-2)10^{-8}\ \Omega^{-1}\mathrm{m}^{-1}$, assuming $\alpha_2 \approx -\eta_c$, one estimates $\sqrt{\xi^2 - 1} \sim 1$ and $f_c \sim 100$ Hz. In the theory of electrohydrodynamic instabilities, the region $f < f_c$ is associated with the oscillating electric charges (conductive regime), while the region $f > f_c$ is characterized by static electric charges and oscillating director field (dielectric regime). Usually, the two mechanisms of director-electric coupling, rooted in dielectric and conductivity anisotropies, are sufficient to describe electrohydrodynamic instabilities in nematics.

In the simplest Carr-Helfrich model of a (-,+) nematic, one considers a balance of a dielectric realigning torque that stabilizes the initial planar orientation in a material with $\Delta\varepsilon < 0$, and an "anomalous" realigning torque caused by a positive conductivity anisotropy $\Delta\sigma > 0$. In the case of directrons, observed in (-,-) nematics with $\Delta\varepsilon < 0$ and $\Delta\sigma < 0$, this classic mechanism is irrelevant, as dielectric and conductivity torques could only stabilize the planar state.

An important feature of directrons that helps to understand the mechanism of their excitation is that the director oscillates with the same frequency as the AC field that drives them. Therefore, the main reason of soliton existence is the electric polarization, such as the flexoelectric polarization and the polarization caused by the space charge developing at director deformations, since both of these couple linearly to the field.

The flexoelectric polarization, introduced by Meyer [135],

$$\mathbf{P}_{\text{fl}} = e_1 \hat{\mathbf{n}} \text{div} \hat{\mathbf{n}} - e_3 \hat{\mathbf{n}} \times \text{curl} \hat{\mathbf{n}} , \tag{4}$$

where e_1 and e_3 are the flexoelectric coefficients, occurs whenever the director suffers splay and bend distortions. The original idea behind Eq.(4) is that cone-like molecules with longitudinal electric dipole would flip to accommodate splay, thus violating a local head-tail parity and producing a macroscopic electric polarization $\mathbf{P}_{\text{fl,splay}} = e_1 \hat{\mathbf{n}} \text{div} \hat{\mathbf{n}}$ along the director; in a similar fashion, banana-shaped molecules with transversal dipoles would produce a polarization $\mathbf{P}_{\text{fl,bend}} = -e_3 \hat{\mathbf{n}} \times \text{curl} \hat{\mathbf{n}}$ under bend along a direction orthogonal to the director and its curl, Fig.6. Later on, Prost and Marcerou [136] demonstrated that more symmetric ellipsoidal molecules, without permanent electric dipoles, but with quadrupolar polarization, are also capable of flexopolarization, defined by Eq.(4) with $e_1 = e_3$.

The directrons clearly show both splay and bend of the director, Figs.4-6. Flexopolarization leads to a spatial charge density $\rho_{\text{fl}} = -\text{div}\mathbf{P}_{\text{fl}}$, a corresponding Coulomb force $\rho_{\text{fl}}\mathbf{E}$ [137], and a flexoelectric torque

$$\mathbf{\Gamma}_{\text{fl}} = \mathbf{P}_{\text{fl}} \times \mathbf{E} , \tag{5}$$

which is linear in the field, in contrast to the dielectric torque $\mathbf{\Gamma} = \varepsilon_0 \Delta\varepsilon (\hat{\boldsymbol{n}} \cdot \mathbf{E})(\hat{\boldsymbol{n}} \times \mathbf{E})$ that is quadratic in the field, Eq.(3). Qualitatively, the emergence of directrons could be explained as follows, using B^h in Fig.6a,b as an example. A fluctuative arch-like director deformation $\hat{\mathbf{n}}(\mathbf{r})$

produces a polarization $\mathbf{P}_{\rm fl}$, which is enhanced and stabilized by the applied electric field **E**, Fig.6b. The oscillating AC field causes up-down oscillation of the vector $\mathbf{P}_{\rm fl}$ and of the director arch. Since the director arch is left-right asymmetric, its oscillations produce a directional flow that is coupled to the director in nematics. The asymmetric flows result in unidirectional propulsion with the velocity **v** directed perpendicularly to **E** and to the background director $\hat{\mathbf{n}}_0$, Fig.6b.

The flexoelectric force driving a B^h directron can be estimated roughly as $e^*U \sim 5 \times 10^{-10}\ N$, where $e^* \sim 10^{-11}\ C\ m^{-1}$, is an effective flexocoefficient [2] and $U = 50\ V$ is the typical voltage [45,46], Fig.4d. This estimate agrees with the expected viscous drag force, $\sim a\eta v \sim 5 \times 10^{-10}\ N$, where $a \sim 10$ μm is the effective width of the soliton, $\eta \approx 60$ mPa · s is the viscosity of CCN-47, and $v \approx 0.8 \times 10^{-3}\ m\ s^{-1}$ is the directron speed at $U = 50\ V$. The speed value corresponds to the high-frequency B^h directrons, in which the flexoelectric polarization is unidirectional, Fig.6a, and the oscillating director arch preserves the polarity of the bend vector $\mathbf{b} = \hat{\mathbf{n}} \times \mathrm{curl}\hat{\mathbf{n}}$ [45], Fig.6b. In the low-frequency B^l directrons, the situation is more complex since the flexoelectric polarizations of the two asymmetric parts of the solitons are opposite to each other, Fig.6c,d, which leads to somewhat slower propagation. The flexopolarization response is not unique for the directrons: it has been proposed as a prime mechanism of the so-called "nonstandard" stripe electroconvection in (-,-) nematics [138] and of DC-driven drift of CF-1 in cholesterics, although no quantitative conclusion could be drawn [107].

Despite relatively high velocities $v \approx 0.8 \times 10^{-3}\ m\ s^{-1}$, the directron motion corresponds to a low Reynolds number, estimated as $Re = \rho v a/\eta \sim 10^{-4}$, where $\rho = 10^3$ kg m^{-3} is the typical nematic density. The Ericksen number, i.e., the ratio of the viscous torque to the elastic torque, is relatively large, $Er = a\eta v/K \sim 50$, where $K \approx 10$ pN is the elastic constant of CCN-47, which means that the director is influenced by the flows.

Similar propulsive mechanisms of directrons are expected from any space-charge dipolar polarization at director deformations, even if the origin is different from the flexoelectric effect. Various examples of the space-charge polarization are presented in Section II on the liquid crystal-enabled eletrokinetics triggered by the anisotropy of permittivity and conductivity. Recent studies by Aya and Araoka [130] and by Shen and Dierking [47,139] show that the dissipative solitons, apparently the directrons of the B^l type, can also propagate in the nematics of the (-,+) type with

$\Delta\varepsilon < 0$ but $\Delta\sigma > 0$ [47,130] and even in the (+,+) nematics such as pentylcyanobiphenyl (5CB) and E7 mixture [139]. Aya and Araoka [130] use mixtures of the (-,-) nematic CCN-47 with a (+,+) nematic pentylcyanobiphenyl (5CB). The solitons in these studies are observed only in the mixtures that produce a (-,+) combination, typically driven by the fields of low frequencies 12-20 Hz and of amplitudes less than 10 V [130]; a change in the field amplitude redirects solitons, similarly to the case described by Li et al. [46]. The director fields of the solitons observed by Aya and Araoka [130] are similar to those of B^l solitons [46], see Fig.5 and Fig.6c,d. Apparently, the electric field creates space charges with dipolar polarization and stabilizes director deformations; the polarization and the director deformations oscillate with the field, which in combination with the director field asymmetry causes a propulsion.

Shen and Dierking [47] showed that the directrons could form not only in nematics but also in chiral nematics of the (-,+) type. The reported directrons are apparently of both B^l and B^h types since they are observed in a relatively broad range of frequencies, from 10 Hz to 800 Hz. Interestingly, the solitons in the chiral nematic show some very distinct collisions scenarios, behaving as hardbody particles that cannot pass through each other, apparently because of the mismatch in the overall twisted director [47]. The formation of dissipative solitons in cholesterics was also attributed to the flexoelectric effect, since the director distortions oscillated with the frequency of the driving field [47].

The unifying feature of directrons observed by various groups in (-,-) and (-,+) nematics is that the conductivity of the explored materials is relatively low. Li et al. [45] reported that the conductivity parameters for CCN-47 samples producing B^h solitons were $\sigma \simeq (0.5 - 0.6) \times 10^{-8}\ \Omega^{-1}\mathrm{m}^{-1}$ and $\Delta\sigma = \sigma_{||} - \sigma_{\perp} \simeq (-0.1) \times 10^{-8}\ \Omega^{-1}\mathrm{m}^{-1}$. To observe B^l directrons, CCN-47 was doped with an ionic additive, to raise the conductivity to $\sigma \simeq (1.2 - 2.5) \times 10^{-8}\ \Omega^{-1}\mathrm{m}^{-1}$, Ref. [46]. Aya and Araoka [130] observed B^l in the range $\sigma \simeq (0.8 - 4) \times 10^{-8}\ \Omega^{-1}\mathrm{m}^{-1}$. Shen and Dierking [47] measured $\Delta\sigma \simeq 1.3 \times 10^{-8}\ \Omega^{-1}\mathrm{m}^{-1}$ in the (-,+) material ZLI-2806. All these conductivities and anisotropies are much lower than those typically explored in electrohydrodynamic instabilities in LCs [41,140]. If the concentration of ions in CCN-47 is increased to $10^{21}\ \mathrm{m}^{-3}$ by doping, so that the conductivity is about $10^{-7}\ \Omega^{-1}\mathrm{m}^{-1}$, the solitons are suppressed, and the nematic undergoes a direct transition from a uniform state to periodic stripe domains. However, the experiment by Shen and Dierking on the (+,+) E7 mixture reveals that the

directrons could be excited when the conductivity is high, $10^{-7}\,\Omega^{-1}\mathrm{m}^{-1}$[139]. The potential reason is attributed to a weak azimuthal anchoring at photoaligned substrates, which allows strong flows of ions [139].

1.7. Directrons nucleation at colloids.

The nucleation of directrons can be promoted by small particles dispersed in the LC. Because of the nonvanishing surface anchoring at the surface of the particles, the director is distorted when the electric field is absent. For example, tangentially anchored spheres produce bipolar structures of quadrupolar symmetry; a twisted version of this bipolar droplet is shown later in Fig.23a). Li et al. [48] demonstrated that the colloidal spheres with tangential boundary conditions produce directrons that envelop the spheres. Without the directrons, the spheres have zero electrophoretic motility in an AC electric field. However, when a directron dresses a sphere and thus breaks the director field's symmetry, the colloid becomes mobile. The effect is called a directron-induced liquid crystal-enabled electrophoresis [48]; it can be used to move a microscopic cargo. Transport of micro-cargo by directrons was also reported by Shen and Dierking [139].

To conclude, nematics driven by an AC electric field demonstrate topologically unprotected multidimensional (3+1)D [45] and (3+2)D [46] solitons-directrons of a dissipative type that exist in a certain range of the amplitude and frequency of the AC field. Their motility is rooted in the periodic excitations of an asymmetric director field that cause directional flows. The time-resolved data on the oscillating director [45-47] suggest that the electric field couples to electric polarization of dipolar symmetry. Such polarization can be caused by the flexoelectric effect of by a space charge. The applied electric field enhances and stabilizes the spontaneous fluctuation of the director and the associated polarization. The polarization vector oscillates with the same frequency as the frequency of the AC field. When the director configuration is asymmetric, for instance, as in Fig.6b, the oscillations result in asymmetric flows and thus motility. Ionic effects play an important role since the experiments demonstrate a dramatic change in the properties of directrons at high and low frequencies and when the conductivity is changed, for example, by adding salts [45,46]. The electric field's amplitude and frequency control the director structure of directrons, their symmetry, direction of propagation, speed, mutual transformations, disappearance, and coalescence into periodic and quasiperiodic patterns. All these features await

an at-depth theoretical description, with the linear model [131] and consideration of charge injection [132] making steps forward. Without a doubt, future studies of dissipative solitons in liquid crystals would bring a deeper understanding of the variety of mechanisms responsible for their existence, which appears to be wide-spread, despite the relatively recent history of observations.

II. LIQUID CRYSTAL-ENABLED ELECTRO-KINETICS

Transport of particles or fluids by an electric field is a subject of electrokinetics. If the driving force represents a uniform electric field, one classifies two closely related sub-areas: electro-osmosis, which refers to the dynamics of fluids in contact with solids, and electrophoresis, which refers to the dynamics of dispersed particles in a fluid. Both areas are very active in terms of fundamental science and in practical developments of microfluidics [141,142], optofluidics [143], small-scale molecular synthesis [144], sensing [145], sorting [146], and biomedical devices [147,148]. Research and applications focus mainly on isotropic electrolytes such as water [149-158] or polymer solutions [159]. This Section describes first the isotropic electrolytes and then the new facets of electrokinetics that occur in a LC electrolyte, defined as an electrically neutral LC fluid that contains an equal number of positive and negative mobile ions.

2.1. Electrokinetics in isotropic electrolytes.

Any form of electrokinetics requires the separation of electric charges. The effect is well understood when the electrolyte is isotropic. In conventional linear electrokinetics, the charges are separated through dissociation of surface groups at the water-solid interface. For example, glass placed in water at pH>3 becomes negatively charged by releasing positively charged protons and forming negatively charged SiO^- groups. These negative charges immobilized at the particle attract a cloud of positive charges. An electric double layer forms, typically of a subnanometer or a nanometer thickness. If an externally applied electric field $\mathbf{E}$ is parallel to the flat glass-water interface, it moves the charges of opposite polarities into opposite directions. The two opposing Coulomb forces of an equal amplitude create a relative shift of the solid and the electrolyte. If the

solid is immobilized, the electric field will cause a flow of the electrolyte, i.e., electro-osmosis. If the solid is a particle freely suspended in the electrolyte, it will move by pushing the electrolyte backward; the ensuing effect is electrophoresis. The mechanism is easy to understand by considering a sphere. The external uniform field **E** creates a torque at the poles on the sphere where the electric double layers are parallel to the field; these torques tend to realign the local electric field of the electric double layers parallel to **E**, thus pushing the electrolyte and the particle in opposite directions. Since the electrolyte does not move at distances far away from the particle, the relative motion of the two systems of charges near the interface propels the particle with a speed [150] $u \approx \frac{\varepsilon\varepsilon_0\zeta}{\eta}E$ that is either parallel or antiparallel to **E**, depending on the polarity of immobilized charges . Here ε and η are the dielectric permittivity and viscosity of electrolyte, respectively, and ζ is the zeta potential that does not depend on **E**. The electrophoretic motion is force-free: since the system is electrically neutral, the forces on positive and negative charges are equal in amplitude and it is the spatial separation of these charges that produces propulsion.

The described conventional electrokinetics with a linear dependence $u \propto E$ could only be driven by a direct current (DC) electric field, which creates problems such as screening of the field by free ions and chemical reactions at electrodes. There is an interest in electrokinetic modes in which the velocities grow as the field's square, as in this case, one can use an AC electric field to drive steady transport and flows. In an isotropic electrolyte, these modes, called induced-charge electrokinetics (ICEK), rely on field-induced charge separation. For the field-induced charge separation to happen, the particle or the wall of a fluid cell should exhibit special properties, e.g., to be an ionic exchanger [152,153] or a metal [154-158,160].

To understand the mechanism of ICEK qualitatively, imagine a metallic sphere of a radius a in an isotropic electrolyte, acted upon by an externally applied uniform electric field, following Bazant and Squires [155,157]. Immediately after application, the electric field is perpendicular to the surface of the metallic sphere and drives ions present in the aqueous electrolyte towards the surface, forming a cloud of positive ions near one pole of the sphere and a similar cloud of negative ions at the other pole. This field-induced charged double layer grows as long as the electric field brings in the new ions, till a steady state is reached, in which the double-layer expels the field lines, creating a component of the electric field that is tangential to the metal-electrolyte interface. The field-induced zeta potential is on the order of [155,157] $\zeta \approx Ea\cos\theta$, where θ is the polar angle,

reaching maximum positive and negative values at the poles, $\theta = 0, \pi$, and being zero at the equator. The tangential field drives the induced charges from the poles towards the equatorial plane. If the sphere is glued to a substrate, the tangential field results in electro-osmosis (ICEO) with flows of a quadrupolar symmetry, Fig.9a,b. The polarity of flows does not change when the field polarity reverses since the driving force is proportional to the product of the induced charge and the field. The typical ICEO velocities thus grow with the square of the field [154,157]:

$$u_{\mathrm{ICEO}} \approx \frac{\varepsilon\varepsilon_0 a}{\eta} E^2. \tag{6}$$

ICEO is dramatically different from linear electro-osmosis in which the zeta potential, determined by the fixed surface charges, does not depend on E, so that $u \propto E$. The quadratic dependence $u_{\mathrm{ICEO}} \propto E^2$ in Eq.(6) allows one to drive steady flows with a uniform AC field, a clear advantage over DC driving of the standard linear electro-osmosis, which explains the growing interest for ICEO.

Nonlinear electro-osmosis around conductive bodies in a uniform field has been documented experimentally for mercury drops [161], solid metal spheres [162,163], metalized "volcano" posts [164], and metallic cylinders, either isolated [165,166] or in touching groups [167]. Peng et al. [163] mapped electro-osmotic flows around gold colloidal spheres, Fig.9a,b, and demonstrated that at weak and moderate fields, their speed grows with the field's square, Fig.9c. The flows in Fig.9a,b are quadrupolar and produce no net pumping of the fluid. The electrolyte flows towards the sphere along the field axis and away from it in the perpendicular plane, which makes the pattern of a contractile, or puller, type.

Fig.9. ICEO in an aqueous isotropic electrolyte around gold spheres (a-c) and glass-gold Janus particles (d-f). (a) Flows around a gold sphere of diameter 50 μm in a flat electrolytic chamber of height 60 μm, under an AC electric field $E = 10$ mV/μm, 1 kHz; flows are visualized by trajectories of fluorescent markers. (b) ICEO velocity map around the sphere. (c) Maximum inwards and outwards velocities as the functions of E^2 around the sphere. (d) Trajectories of fluorescent markers around a glass-gold Janus sphere of diameter 50 μm in a flat chamber of height 60 μm, under the AC electric field $E = 10$ mV/μm, 1 kHz. (e) ICEO velocity map around the Janus sphere exhibiting steady pumping of the electrolyte from left to right; the field is perpendicular to the axis of rotational symmetry. (f) The same, the field is parallel to the axis of rotational symmetry. Modified from Peng et al. [163].

Bazant and Squires made an important prediction that ICEK combined with broken symmetry of particles such as metal-dielectric Janus spheres should yield asymmetric flows, which could be used for ICEO pumping around immobilized solid particles and induced-charge electrophoresis (ICEO) of free particles [155,158]. Asymmetric flows around metal-glass Janus spheres were experimentally demonstrated by Peng et al. [163], Fig.9d-f. The ICEO flows near the less polarizable glass part are weaker, which breaks the quadrupolar symmetry and results in the pumping of the fluid around the sphere if the sphere is immobilized, Fig.9e,f. If the sphere is free to move, the broken symmetry will result in an electrophoretic motion. This ICEP motility was experimentally discovered for dielectric-metal Janus particles by Velev's group [156]. One can also observe the spinning of Janus doublets caused by ICEK [168].

The strong dependency of ICEO flows on the symmetry of the solid subsystem can be used in practical applications such as non-mechanical pumping of fluids [154,155] and particles [154,156,169-171] and in microfluidic chaotic stirrers [172]. Fluid mixing is a challenging problem at the micron scales, as the typical Reynolds numbers in microfluidics are very low, and the flows are of a laminar type. One of the approaches to effective mixing is to use an ICEO chamber with two different sets of electrodes that would produce two different fluid fields around a metal obstacle in the chamber. By switching between the two configurations back and forth, one can achieve chaotic advection in the chamber and thus facilitate stirring [172].

To summarize this section, we stress again that in an isotropic electrolyte, the mechanisms of electrokinetics are rooted primarily in the properties of the solid component that produces either equilibrium double layers or facilitates induction of these layers in the applied electric field. The role of the electrolyte is to supply the counter-ions to complete the build-up of the double layers. When the isotropic electrolyte is replaced with an LC electrolyte, the situation changes dramatically. It is the anisotropic properties of the LC electrolyte that allow the electric charges to be spatially separated; the nature of the solid part is of lesser importance. Next, we consider the electrolytic properties of LCs, which enable new modes of nonlinear electrokinetics.

2.2.Electro-osmotic flows around immobilized particles in nematic electrolytes.

LCs used as anisotropic electrolytes offer a distinct mode of charge separation and of electro-osmosis that is called liquid crystal-enabled electrokinetics, or LCEK [173-175]. The field-

driven space charge formation produces LCEK when two conditions are fulfilled: (i) the LC shows anisotropy of electric conductivity or dielectric permittivity, (ii) the director varies in space [175]. Since the transported particles' properties are of little importance, nematic electrolytes could propel particles such as perfect spheres with no electric charges at their surfaces; they can be solid, fluid or gas. A detailed comparison of ICEK and LCEK can be found in Ref.[176].

The essence of LCEK can be understood by considering LC-enabled electro-osmosis (LCEO) around a sphere immobilized in a nematic cell with a uniform director $\hat{\mathbf{n}}_0$=(1,0,0), following Ref. [175]. The particle sets a certain anchoring direction, either normal to itself, Fig.10a,g or tangential, Fig.10d. To match the near- and far-fields, the director acquires distortions of a quadrupolar, Fig.10a,d [177,178], or a dipolar type, Fig.10g [179]. To match the surrounding uniform director $\hat{\mathbf{n}}_0$=(1,0,0), the normally anchored sphere is accompanied either by a wedge disclination loop of strength -1/2, resembling a Saturn ring [178], Fig.10a, or by a point defect, called the hyperbolic hedgehog [179], Fig.10g. The point defect configuration of Fig.10g is energetically preferable over the Saturn ring configuration in Fig.10a, except for the case of shallow samples or strong external fields [180,181].

Fig.10. LCEOs in a nematic with a director field of quadrupolar (a-f) and dipolar (g-i) symmetry distorted by a sphere with (a-c, g-i) normal and (d-f) tangential anchoring at its surface. Filled triangles in (a) show the cross-section of a -1/2 disclination loop. Filled triangles in (b) show the cores of two surface defects-boojums at the poles. The field-induced dipole moment, shown by red block arrows, is either (a) antiparallel to the field or (d) parallel to it, depending on the director gradients. Electro-osmotic flows shown by thick arrows in (a,d) do not change polarity when the field is reversed. The corresponding (b,c) puller- and (e,f) pusher type experimental LCEO flows around glass spheres of diameter 50 μm with perpendicular and tangential anchoring, respectively. (g) An AC electric field acting on a nematic electrolyte with an immobilized glass sphere and a hyperbolic hedgehog on the right-hand side causes (h,i) LCEO flows with fore-aft asymmetry; (i) the sphere acts as a pump, moving the nematic from right to left. In all experiments, the nematic is of a zero dielectric anisotropy, $\Delta\varepsilon = 0$, and of a positive electric conductivity anisotropy $\Delta\sigma > 0$. AC field is of frequency 5 Hz and amplitude 26 mV/μm. Modified from Lazo et al. [175].

Suppose that an electric field is parallel to $\hat{\mathbf{n}}_0$=(1,0,0) and that the dielectric anisotropy is zero, $\Delta\varepsilon = 0$, so that there is no dielectric torque on the director, Fig. 10; the condition is achieved by mixing nematics with $\Delta\varepsilon > 0$ and $\Delta\varepsilon < 0$. The only action of the field is to drive the ions. Consider first the quadrupolar director, Fig.10a-f. If $\Delta\sigma > 0$, the ions prefer to move along the director lines. As a result, positive and negative charges gather in different regions of space. For

the sphere with normal boundary conditions and quadrupolar director, the director lines are converging on the left and right sides, Fig.10a. A positive field polarity, $E_x > 0$, accumulates positive charges at the left side of the sphere and negative charges on its right side. For the sphere with tangential anchoring, the director lines are diverging; the signs of the separated charges in Fig.10d are opposite to those ones in Fig.10a. Comparison of Fig.10a and Fig.10d illustrates clearly that the polarity of the space charges is determined by the sign of director gradients. Once the charges are separated in space, the electric field creates a Coulomb force of density $\propto \rho(E)E$, which yields an electro-osmotic flow of the nematic, Fig.10a,d; here $\rho(E) \propto E$ is the charge density that is proportional to the field that induces it. Reversing the field polarity alters the sign of the induced charge $\rho \propto E$ at a given location, but the product $\rho E \propto E^2$ remains polarity-insensitive. For example, if the field direction shown in Fig.10a is reversed, $E_x < 0$, then the left side of the disk would accumulate negative ions, and the right side would accumulate positive ions, but the product $\rho E \propto E^2$ would not change. Therefore, the forces and flows are independent of the field's polarity, growing as E^2. It means that the steady electro-osmotic flows in LCEK could be driven by an AC electric field. Of course, polarity reversal of charge clouds takes some time; thus, the forces and flows decay as the frequency of the AC field becomes higher than the inverse relaxation time.

The induced space charge is sensitive to the sign of director distortions $\partial\varphi/\partial y$, where φ is the angle between the unperturbed $\hat{\mathbf{n}}_0$ and the actual director, Fig.10a. The LCEO flow is of a "puller" type around the normally anchored sphere, with the inward velocities being collinear with $\mathbf{E}$, Fig.10a. The tangentially anchored sphere produces a "pusher" pattern of flow with respect to the field axis, as the velocities along this axis are directed outward, Fig.10d. The terminology of pushers and pullers is used to describe microswimmers such as flagellated bacteria, which propel themselves without an external force [3,4,11,12]. The swimmer is modeled by a force dipole, i.e., two forces of the same absolute value but of opposite polarity, associated with each swimmer. One force is propulsive, caused, for example, by a rotation of a helicoidal flagellum. The second force, equal in magnitude and opposite in direction, represents viscous drag. The forces in the case of LCEO and ICEO are electrostatic, acting on the separated charges. Since the isotropic and LC electrolytes are electrically neutral, the forces acting on positive and negative charges are equal. In ICEO, the force dipole is always of the puller type with respect to the field

direction, Fig.9b,e,f. In LCEO, it could be of both the puller, Fig.10a, and the pusher type, Fig.10d, depending on the director gradients.

Experimental validation of the considerations above for the spheres with quadrupolar director is illustrated in Figs.10b,c,e,f. The quadrupolar symmetry is natural for the tangential anchoring [182]. For the normal anchoring, the quadrupolar director field establishes the Saturn-ring configuration when the anchoring strength is weak or when the sphere is of a diameter that is close to the chamber's height [178,181,182]. The experimental LCEO flows around particles with a quadrupolar director are of a puller type when the surface anchoring is normal, Fig.10c, and of a pusher type when the anchoring is tangential, Fig.10f, as expected.

A homogeneous sphere surrounded by a quadrupolar director field does not produce any net flow, Fig.10a-f. The situation changes dramatically when the director is of a dipolar symmetry, Fig.10g. The dipolar director develops around a sphere with a normal surface anchoring placed in an otherwise uniform nematic when the sphere is noticeably smaller than the depth of the chamber and when the surface anchoring is sufficiently strong [179]. The sphere acts as a radial hedgehog of a topological charge $N = 1$, which must be compensated by a hyperbolic hedgehog of a charge N =-1 to fit into an otherwise uniform background of zero charge [179]. Note here that the charge of a point defect in a 3D nematic is poorly defined because of the identity $\hat{\mathbf{n}} \equiv -\hat{\mathbf{n}}$; the designation of signs above is customarily done by replacing the director with a vector field, which is permissible in the absence of linear defects-disclinations [183]. The core of the hyperbolic hedgehog is shown by a black circle in Fig.10g. When the electric field acts on such a sphere, glued to a substrate, it causes asymmetric vortices, Fig.10h, thus pumping the nematic electrolyte from right to left in Fig.10i. Unlike the case of ICEO, in which asymmetric flows and net pumping of the electrolyte require the particle to be asymmetric, e.g., of a Janus type, Fig.9d-f, the asymmetric LCEO in Fig.10h,i occurs around a perfectly spherical shape. The symmetry breaking required to rectify the pumping action is supplied by the dipolar nematic environment around the sphere with a hedgehog rather than by the particle's shape or inhomogeneity of the surface properties as is the case of the Janus spheres.

Suppose a colloidal sphere "dressed" in a dipolar director field is freely suspended in a nematic electrolyte, Fig.11a. In that case, it could be moved either by a DC, Fig.11b, or by an AC electric field, Fig.11c, [173-175,184], which is the LC-enabled electrophoresis (LCEP). In the DC

case, the velocity dependence on the field strength shows both linear and quadratic term, $u = \mu_1 E \pm \mu_2 E^2$, where $\mu_1 = \bar{\varepsilon}\zeta/\eta$ is the linear electrophoretic mobility, ζ is the zeta potential characterizing the charge of the particle and its spatial distribution. The nonlinear mobility μ_2 is nonzero only in the nematic phase. If the nematic is heated into the isotropic phase, the field dependence of the velocity reduces to linear, Fig.11b.

Fig.11. Liquid crystal-enabled electrophoresis (LCEP): (a) scheme of experiment with a DC in-plane field; (b) DC-triggered electrophoretic velocity of glass spheres in isotropic (circles) and nematic (triangles) phase for two orientations of the structural dipole **p** directed from the hyperbolic hedgehog towards the sphere; (c) AC field-driven electrophoresis with propulsion polarity defined by the structural dipoles. Modified from Lavrentovich et al. [173].

As clear from Fig.11b, if the DC driving is replaced by an AC driving, the linear term in $u(E)$ drops out, and the electrophoretic velocity would be directly proportional to E^2, $u = \pm\mu_2 E^2$. The sign depends on the structural polarity of the sphere-hyperbolic hedgehog pair, which can be characterized by a dipole **p** directed from the hedgehog to the sphere. If the materials of the sphere and the nematic are the same as in Fig.10g-i, the electrophoretic velocity **u** is antiparallel to **p**: the hedgehog leads the sphere. Figures 11b,c are adjusted to illustrate this case. This direction of **u** is opposite to the electro-osmotic flow around the same sphere that is immobilized, Fig.10g-i, as expected. For other materials, an opposite polarity could be observed, with the sphere leading the way [173,185]; the reason for this dependence on the properties of the material will become apparent in the next subsection.

The same sphere as shown in Fig.10i with puller flows, when free, moves parallel to $\hat{\mathbf{n}}_0$, Fig.11. This behavior of electrophoretically active sphere differs from the expectation that hydrodynamic coupling between a self-propelled spherical swimmer's flow field and anisotropic viscosities of the nematic environment would cause a puller to swim perpendicular to $\hat{\mathbf{n}}_0$, while a pusher would swim parallel to it [186]. In LCEK, the orientation of electrostatic force dipoles is along the external electric field, while their polarity also depends on the director gradients, Fig.10, and the materials parameters, while in the case of active swimmers considered in Ref. [186], the force dipole could realign in space, being rotated by the anisotropic viscous torque of the surrounding nematic.

2.3. Electrokinetic velocities vs. nematic material parameters.

To find how the LCEK velocities depend on the material parameters of the nematic, let us consider a 2D *xy* version of Fig.10a,d and estimate the density ρ of charges created as a result of conductivity anisotropy and establish how it depends on the typical scale a (the radius of an inclusion) of director distortions, the applied electric field E, and the conductivity anisotropy $\Delta\sigma$; for more details, see [175,187-191]. Assume that the dielectric anisotropy is small, $\Delta\varepsilon << \bar{\varepsilon}$, where $\bar{\varepsilon} = (\varepsilon_{||} + \varepsilon_{\perp})/2$, and that the 2D director distortions are weak, $\hat{\mathbf{n}} = (1, \varphi)$, where $\varphi = \varphi(x, y)$ is a small tilt angle between the director and the x-axis, Fig.10a. The field, applied along the x-axis, drives ionic currents $J_i = \sigma_{ij}E_j$, where $\sigma_{ij} = \sigma_{\perp}\delta_{ij} + \Delta\sigma n_i n_j$ is the conductivity tensor; i and j stand for x and y. For $\varphi << 1$, the current components are $J_x = \sigma_{||}E_x + \Delta\sigma\varphi E_y$ and $J_y = \sigma_{\perp}E_y + \Delta\sigma\varphi E_x$; the field component E_y is induced by separation of charges. Using the charge conservation law $\mathrm{div}\mathbf{J} = 0$ and Poisson's equation $\mathrm{div}\,\mathbf{D} = \rho$ (where $\mathbf{D}$ is the electric displacement), one obtains the charge density $\rho(x, y)$ caused by the anisotropy of the LC and director gradients $|\partial\varphi/\partial y| \sim 1/a$ in the presence of an electric field [175]:

$$\rho(x, y) = \left(-\frac{\Delta\sigma}{\bar{\sigma}} + \frac{\Delta\varepsilon}{\bar{\varepsilon}}\right)\varepsilon_0\bar{\varepsilon}E_x\frac{\partial\varphi}{\partial y}; \tag{7}$$

here $\bar{\sigma} = (\sigma_{||} + \sigma_{\perp})/2$ is the average conductivity. The induced charge density is thus proportional to the director gradients, the anisotropy of conductivity and permittivity, and the field itself. The amplitude of LCEO velocity around a sphere of the radius a then follows from the balance of the driving bulk force $f \propto \rho E_x$ and viscous resistance $\eta u/a^2$ [175]:

$$u_{LCEO} = \pm\beta\frac{\varepsilon_0\bar{\varepsilon}}{\eta}\left(\frac{\Delta\varepsilon}{\bar{\varepsilon}} - \frac{\Delta\sigma}{\bar{\sigma}}\right)aE_x^2. \tag{8}$$

Here the numerical coefficient β on the order of 1 is introduced to account for the approximations such as using $1/a$ as a measure of director gradients and replacing anisotropic viscosity of the LC with its average value η; the sign "+" or "–" depends on the polarity of director gradients such as $\partial\varphi/\partial y$.

Equation (8) for the LCEO velocity suggests that the efficiency and even polarity of LCEO transport can be controlled by tuning the material parameters, namely, the factor $\left(\frac{\Delta\varepsilon}{\bar{\varepsilon}} - \frac{\Delta\sigma}{\bar{\sigma}}\right)$ for a given pattern of the director gradients, which define the sign of $\partial\varphi/\partial y$. The anisotropy factor

varies broadly and could change its sign as a function of temperature or concentration in mixtures of different LCs. As a result, one can reverse the polarity of LCEK by the temperature and composition, as proven by Paladugu et al. in the experiments on LCEP of colloidal particles at varying temperatures and nematic compositions [192]. One might also expect that the polarity of LCEK could be altered by the viscous drag since the nematics show anisotropic viscosity with five independent coefficients; this fact is neglected in Eq.(8).

Experiments show that the amplitude $|u_{LCEO}^{max}|$ of LCEO velocities around glass spheres is linearly proportional to a, Fig.12a, and to E^2, Fig.12b, as expected from Eq.(8). The theoretical estimate, Eq.(8), with typical $\beta = 1$, $\Delta\sigma/\bar{\sigma} = 0.3$, $\bar{\varepsilon} = 6$, $\eta = 0.07$ kg $\cdot m^{-1} \cdot s^{-1}$, $a = 25$ μm, predicts a characteristic velocity $|u_{LCEO}^{max}| = 4.5$ μm/s when the field is $E = 26$ mV/μm, close to the experimental $|u_{LCEO}^{max}| = 3$ μm/s , Fig.12b.

Fig.12. Quantitative parameters of LCEO around a glass sphere in a uniform AC electric field of frequency 5 Hz. (a) Maximum LCEO velocity around tangentially anchored (circles) and perpendicularly anchored (crosses) spheres increases linearly with the diameter $2a$ of the sphere; velocity patterns are of quadrupolar symmetry in both cases; $E = 26$ mV/μm. (b) Maximum LCEO velocity around a tangentially anchored sphere of diameter $2a = 50$ μm grows as E^2. (c) Volume of the LC flow around a sphere with perpendicular anchoring and a dipolar structure (diameter 50 μm), shown in Fig.10i, passing along the x −axis and along the y − axis defined in Fig.10. The nematic is pumped from right to left. Modified from Lazo et al. [175].

LCEO in Fig. 10 and LCEP in Fig.11 are demonstrated with dielectric (glass) particles; there are no metal/conductive elements in the LC cell except for the two electrodes to apply the field. Since the charge separation occurs because of the medium, the strongly polarizable parts such as the metal particles in ICEK are not needed. This feature is important for potential applications. For example, LCEP can be used to transport droplets of other fluids that are not miscible with the LCs [193-195]. In the case of hydrophobic LCs, these inclusions might be water and various aqueous solutions, as demonstrated by Hernàndez-Navarro et al. [193,194] and reviewed by Ignés-Mullol and Sagués [195].

It is of interest to compare the efficiency of LCEK vs. ICEK in an isotropic electrolyte when the embedded particle is dielectric. A dielectric particle in an isotropic electrolyte can produce an ICEO velocity $u_{ICEO,diel} \sim \varepsilon\varepsilon_0\lambda_D E^2/\eta$, which is smaller than the velocity around an ideally polarizable metal particle, Eq.(6), by a factor λ_D/a [158]. For a comparable electric field,

the LCEO and ICEO velocities ratio is $\frac{|u_{LCEO}|}{|u_{ICEO,diel}|} \approx \frac{\varepsilon_{LC}\eta_{water}a}{\varepsilon_{water}\eta_{LC}\lambda_D}$, where the subscripts refer to the medium. Despite the fact that $\varepsilon_{LC}/\varepsilon_{water} \sim 0.1$ and $\eta_{water}/\eta_{LC} \sim 0.1$, it is the large ratio $a/\lambda_D \sim 10^4$ that makes the LCEO velocities higher as compared to ICEO velocities around dielectric bodies, thanks to the separation of charges over the scales $\sim a \gg \lambda_D$.

In LCEK, the electric field first induces separation of charges of density $\rho \sim E$ and then drives these charges with a force $\rho E \sim E^2$, thus the flow velocities grow with the field's square. Unlike the conventional linear electrokinetics, in which the flows are collinear with the electric field, the quadratic dependence $u \sim E^2$ decouples the directions of **E** and **u**. In particular, the velocity can be orthogonal to the field, Fig.13 [173,174]. In the LCEP experiment with a glass sphere, Fig.13, the nematic is of a small negative dielectric anisotropy, and a DC field $\mathbf{E} = (E_x, 0, 0)$ is applied in the plane of a sandwich cell perpendicularly to the overall director $\hat{\mathbf{n}}_0 = (0,1,0)$ set by planar alignment. The DC field causes two types of motion, with a velocity component $u_x(E_x)$ parallel to the field and a component $u_y(E_x)$ perpendicular to the field. The dependence $u_x(E_x)$ for small particles is practically linear, similar to the electrophoresis in isotropic electrolytes, in which the velocity is described by Smoluchowski's formula $u_x = \mu_1 E_x$. Since the velocity is directed along the applied field, one concludes that $\mu_1 > 0$ and that the dielectric particle accumulates a positive surface charge; this charge is screened by the diffuse layer of negative charges. However, $u_x(E_x)$ becomes nonlinear for larger particles and higher fields, since the linear dependence is supplemented by a cubic term, $u_x = \mu_1 E_x + \mu_3 E_x^3$, where μ_3 is a non-linear mobility [174,196], Fig. 13c. The cubic dependence, known as Stotz-Wien effect in isotropic electrolytes [197-199], is associated with the field-induced polarization of the electric double layers around the particle; in a nematic, it can also be assisted by director realignment that affects the electric double layers.

The dependence $u_y(E_x)$ in Fig.13d, is of a different quadratic character, intrinsic to the LCEP and generally LCEK. The quadratic dependence shows that LCEP does not depend on the surface charge accumulated at the surface of the particle and the permanent electric double layers. One can combine LCEP and linear electrophoresis, for example, by simultaneously applying AC and DC fields to transport colloidal particles along predesigned trajectories in space [174]. In this setting, the DC field defines the *z*-coordinate of the particle along the normal to the sandwich-type cell, while the AC field controls the in-plane trajectory [174]. Patterning of the nematic director considered later in this Section expands the possibilities of predesigned LCEK transport even further.

Fig.13. The LCEP velocity of positively charged glass spheres of diameter $2a = 5$ μm and $2a = 17$ μm in the nematic phase (25^0C) of MLC7026-000 as a function of the uniform DC electric field; in-plane geometry with $\mathbf{E} = (E_x, 0,0)$ and $\hat{\mathbf{n}}_0 = (0,1,0)$; (a,c) *x*-component of the velocity, parallel to $\mathbf{E}$ and perpendicular to $\hat{\mathbf{n}}_0$, with a linear and cubic dependence on E; (b,d) *y*-component of the velocity, parallel to $\hat{\mathbf{n}}_0$, showing a quadratic dependence on E. Redrawn from Lazo et al. [174].

LCEK can be combined not only with linear electrophoresis but also with ICEK. Sahu et al. [200] placed metal-dielectric Janus spheres in a nematic liquid crystal with $\Delta\varepsilon < 0$ and $\Delta\sigma > 0$ is and achieved an impressive level of command over trajectories by varying the amplitude and frequency (but not the direction) of the driving AC field $\mathbf{E} = (0, E_y, 0)$. The plane Σ separating the metal and dielectric hemispheres aligns parallel to the field applied between two transparent electrodes along the *y*-direction in Fig.14. The particle moves in the *xz* plane perpendicular to the field, similarly to the case described by Gangwal et al [156] for the isotropic electrolyte (this orientation yields the highest degree of polarization of the metal hemisphere). In contrast to the isotropic electrolyte, the nematic provides an additional symmetry element, a Saturn ring of a disclination loop that surrounds the Janus sphere, Figs.10a, 14. The Saturn ring is always perpendicular to the overall director $\hat{\mathbf{n}}_0 = (1,0,0)$, but the plane Σ can form any angle with $\hat{\mathbf{n}}_0$. When Σ is perpendicular to $\hat{\mathbf{n}}_0$, the sphere moves along $\hat{\mathbf{n}}_0$, with the dielectric side leading the way, Fig,14a. When Σ is parallel to $\hat{\mathbf{n}}_0$, the sphere moves perpendicularly to $\hat{\mathbf{n}}_0$, with the metal face

forward. For other orientations, the motion is at some angle to $\hat{\mathbf{n}}_0$. The controlling mechanism stems from the sensitivity of the electrostatic forces and electro-osmotic flows to both the asymmetry of the polarizability of the Janus sphere and the director structure [200]. Higher polarizability of the metal hemisphere shifts the electrostatic force dipole and electro-osmotic flows towards the metal end, Fig.14, similarly to the case of the isotropic electrolyte, Fig.9d-f. The director gradients of interest are splay at the lateral surface, a prevailing deformation in Fig.14a, and bend concentrated just outside the Saturn ring. First-principle calculations [200] show that splay couples to the gradients of the electric field along the *x*-axis and bend couples to the vertical gradients along the *y*-axis. When Σ is perpendicular to $\hat{\mathbf{n}}_0$, the symmetry of flows is broken by splay as shown in Fig.14a: the electric field causes flows of the puller type, stronger on the metal side so that the Janus spheres move with the dielectric side forward. When Σ is parallel to $\hat{\mathbf{n}}_0$, the electrostatic force dipole creates asymmetric pusher flows, Fig.14b, so that the metal hemisphere leads the way. The field dependencies of velocities along the *x*- and *z*-axis are both quadratic but of different slopes. Both velocity components also show a frequency dependence [200], similar to that observed in ICEP [154,201] and LCEP of homogeneous spheres [173],

$$u_i(\omega) = u_{0i} \frac{\omega^2 \tau_e^2}{(1+\omega^2 \tau_c^2)(1+\omega^2 \tau_e^2)}, \tag{9}$$

where $i = x, z$, $\omega = 2\pi f$ is the angular frequency of the electric field, τ_e and τ_c are the characteristic charging times of the electrodes and colloid, respectively. Usually, $\tau_e >> \tau_c$. The velocity increases as ω^2 when ω is low, but for high ω, the velocity decreases because the ions have no time to follow the rapidly oscillating field. The different amplitude and frequency dependencies of velocities along the x and z directions allow Sahu et al. [200] to control the direction of in-plane propagation of the Janus sphere in the nematic. It should be possible also to transport the particle along the orthogonal y-direction by linear electrophoresis, by adding a DC field [174].

Fig.14. Electro-osmotic flows (black curved arrows) and electrophoretic velocity (red block arrows) of a metal (yellow)-dielectric (blue) Janus sphere with perpendicular anchoring and quadrupolar Saturn ring director. Vertical green arrows show the force dipole shifted towards the metal hemisphere of higher polarizability. The force dipole is either of (a) a puller type or (b) pusher type. Redrawn from Sahu et al. [200].

2.4. Electro-osmosis in patterned nematics.

The surface properties of colloidal particles play an important role in LCEK. In particular, a homogeneous sphere with perpendicular surface anchoring is mobile only when the director field is of a dipolar symmetry. Furthermore, a sphere with a tangential surface anchoring placed in a uniform electric field shows no LCEP mobility. This dependence on surface anchoring is detrimental to potential applications. One solution for tangentially anchored particles is to make them of asymmetric shapes, such as pear-like [202,203]. Another approach is to use nematics with predesigned director patterns [187]. The director gradients needed to separate the clouds of electric charges are created by patterning the bounding plates. The electric field then drives the space charges and powers steady LCEO flows [176,184,187,192,204]. A particle placed in such a chamber would be carried by the LCEO flows, even if it has no LCEP mobility on its own.

LCEO in a patterned nematic electrolyte can be understood by considering a periodic director in Fig.15 [187], with $\hat{\mathbf{n}}_0 = (n_x, n_y, 0) = \left[\left|\cos\frac{\pi y}{L}\right|, \sin\frac{\pi y}{L}, 0\right]$, where L is the period. The pattern is created by surface photoalignment based on plasmonic metamasks [205-207]. Assume that electric conductivity of the LC is positive, while the dielectric anisotropy is zero. Once the electric field $\mathbf{E} = (E_x, 0,0)$is applied, the ions move along the x-axis, but they also shift along the y-axis, because they prefer to move parallel to the director, $\Delta\sigma > 0$, Fig.15a. The field separates the charges, forming alternate lanes of opposite polarity, Fig.15b. The charge density $\rho(y) = \varepsilon_0\bar{\varepsilon}\frac{\partial E_y}{\partial y}$ is determined by the transverse field, $E_y = -\Delta\sigma\frac{\cos\beta\sin\beta}{\sigma_{||}\cos^2\beta+\sigma_\perp\sin^2\beta}E_x$, where $\beta(y)$ is the angle between the local director $\hat{\mathbf{n}}_0$ and the x-axis [187], similarly to the case of colloids. The space charge experiences a Coulomb bulk force of density $f = \rho E$, Fig.15c, that drives electro-osmotic flows. Reversing polarity of $\mathbf{E}$ reverses polarity of ρ, but the product $f = \rho E \propto E^2$ does not change, Fig.15d. As in the case of the LCEO around colloids, the flows could be driven by an AC field, Fig.15e. Dielectric anisotropy supplements an additional source of space charge [187,191].

Fig.15. LCEO in a nematic electrolyte with a predesigned director. Ticks represent local director visualized by PolScope: (a) the electric field ***E*** drives "+" and "-" electric charges along the x-axis but because of the anisotropic conductivity, the charges shift also along the y-axis, (b) creating separated lanes of space charges; (c) the electric field moves them along the x-axis; (d) reversal of the field changes polarity of charges but does not change the

Coulomb force; (e) an AC field of frequency 5 Hz creates lanes of LCEO flows of alternating direction. Redrawn from Peng et al. [187].

The director could be predesigned with disclinations of charge $m = \pm 1/2, \pm 1, \ldots$:

$$\hat{\mathbf{n}}_0 = \left(n_x, n_y, 0\right) = [\cos(m\varphi + \varphi_0)\,,\ \sin(m\varphi + \varphi_0)\,, 0], \qquad (10)$$

where $\varphi = arctan(y/x)$ and $\varphi_0 = \text{const}$; m is a number of times the director reorients by 2π when one circumnavigates around the defect core [38]. The sign of m is positive when the director rotation is of the same polarity as the polarity of circumnavigation. For pairs of defects of charge m_1 and m_2, separated by a distance d, the argument $m\varphi$ in Eq.(10) is replaced by $m_1 \arctan[y/(x + d/2)] + m_2 \arctan[y/(x - d/2)]$ [38]. This latter form uses a superposition principle, valid when the Frank moduli for splay and bend are equal. An example is a pair $m = \pm 1/2$ in Fig.16a-c. Powered by the AC electric field, the pair works as a pump, Fig.16b. The velocity u of the LCEO flow is estimated from the balance of the Coulomb force ρE and viscous resistance $\eta u/d^2$, where d is the separation of disclinations [187]. The result is the same as Eq.(8), but the colloid's size a is replaced by d. The expected linear dependency on d is indeed confirmed by the experiment, Fig.16c [187].

Fig.16. LCEO in a patterned director field with topological defects. (a) A nematic cell with a predesigned pair of singular $m = -1/2$ and $m = +1/2$ disclinations of type A; (b) LCEO flows powered by an AC electric field; (c) maximum LCEO flow velocity vs. separation of disclinations. (d) Periodic pattern of $m = +1$ defects surrounded by $m = -1/2$ defects; (e,f) LCEO flows are of opposite polarity for two orthogonal directions of the electric field shown in the right upper corners. The filled symbols show the cores of defects. Redrawn from Peng et al. [187].

The LCEO flows can be used in mixing fluids at the microscale since they form vortices, Fig.16; in linear electrophoresis, vortices are impossible since the flows are collinear with the applied field. Figures 16d-f illustrate an important property of LCEO in patterned director: the polarity of electrolyte circulation in vortices can be reversed by redirecting the driving electric field.

LCEO in patterned nematic electrolytes can be used not only for mixing but also in the inverse problem, namely, separation of colloids that have identical bulk properties but different surface functionalization, which might be the case of beads used in biomedical applications for

antibody-antigen binding [184], Fig.17. Spheres with different surface functionalization, one that favors tangential alignment and one with perpendicular alignment, are driven by the elastic forces of the director pattern to the regions of bend and splay, respectively [208-210]. Once the electric field is applied, the LCEO flows in the bend regions move to the left and in the splay region to the right, thus separating colloids with different surface functionalization [184]. Although the scheme in Fig.17a shows a unipolar electric field in order to illustrate the space charges, it is clear that the separation will also occur in an AC field (for which the experiments shown in Fig.17b were performed) since the driving forces in LCEO do not change their direction with the field reversal, as explained above.

Fig.17. LCEO flows in a patterned director field with a periodic splay and bend separate spherical polystyrene particles (diameter 5 μm) with different surface functionalization. The splay regions attract spheres with perpendicular anchoring and a hyperbolic hedgehog and move them to the right; the bend regions attract bipolar spheres with tangential anchoring and move them to the left. Redrawn from Peng et al. [184,208].

The surface patterns discussed so far are static in nature, designed to sustain steady flows. Barcelona group led by Sagués [202,203,211] developed a dynamic control of LCEP-active colloids, employing photosensitive surface coatings that experience trans-to-cis isomerization under a UV illumination and a reversed transition under visible illumination. In the trans state, the surface yields a perpendicular anchoring, the cis state shows tangential alignment. After a UV irradiation, a portion of the sample becomes tangentially aligned; an AC field applied along the normal to the cell enhances this alignment (the dielectric anisotropy is negative) and causes LCEP of the pear-like microparticles [202,203,211]. By illuminating the sample with visible light or reducing the electric field, one realigns the director homeotropically, and the in-plane dynamics stops. An interesting aspect of the experiment is that the in-plane director forms a chiral spiral pattern with a central defect-vortex of a topological charge +1 [202,203,211]. The electrophoretically active colloids move towards the core of the defect, following the spiral trajectories and often forming chains. When the particles are close to the core, they start orbiting the core. As more particles join the central part, they form a dense cluster that rotates as a whole. This polarity of circulation follows the chirality of the underlying spiral pattern. The dynamic behavior indicates the importance of interparticle interactions that should intensify as the

concentration increases. Finally, since the illumination spot that triggers the dynamics could be moved around the nematic chamber, the entire swarms of particles could be directed from one location to another, realizing dynamic control over the colloidal swarms [202,203,211].

Theoretical modeling of LCEK and related phenomena has progressed dramatically over the last few years [175,187-191,212,213], but there are still some interesting problems awaiting their analysis. Among these is a seemingly never-completely-resolved problem of the director's dynamic response to the applied electric forcing, despite all the successes of the LC display industry. In most of the works on LCEK, the director field is assumed to be frozen and unresponsive to the electric field. This simplification neglects the coupling of the electric field to the director through dielectric anisotropy, flexoelectric, and surface polarization. The effect of charge injection from the electrodes is also not accounted for. Although experiments can be designed to suppress some of these mechanisms, e.g., by formulating nematic mixtures with $\Delta\varepsilon = 0$ [175,187], other mechanisms such as flexoelectricity or charge injection are harder to eliminate. Incorporating the director response through dielectric and flexoelectric mechanisms and accounting for ionic effects and charge injection [140,214] might be the next essential steps in expanding the description of LCEK. An interesting connection to the active matter was pointed by Conklin, Viñals, and Valls [213], who demonstrated that LCEO flows in patterned director fields with topological defects can mimic the flows of living liquid crystals [215].

Collective dynamic behavior of LCEP-driven particles is the next challenging topic to explore; the first works in this direction already show spectacular effects such as chaining and formation of rotating clusters [202,203,211]. Collective effects in a related system of Quincke rollers, representing colloidal dielectric spheres driven by an electric field and by interactions with the bounding plates, have already been explored in detail [216-219]. In particular, Quincke rollers show a unipolar circulation around spherical inclusions in an LC when their concentration increases above some threshold [216]. Designing systems with a very large number of Quincke rollers in a track-like chamber filled with isotropic solvents allowed Bartolo et al. [217-219] to show that this effect is an experimental realization of Vicsek transition in a system of collectively moving and mutually aligning objects [220] and to extract important parameters characterizing polar active matter. Collective effects of polar circulation and dynamic clustering will be discussed for so-called living liquid crystals [215,221] in Section V. The interest to further expand the LCEK research is supported by the recent experimental results such as omnidirectional propulsion of

asymmetric Janus colloidal particles [200] and by potential applications, such as mixing at microscale [208], sorting and separation [184,210] of small particles.

III. LIQUID CRYSTAL ELASTOMER SUBSTRATES

A liquid crystal elastomer (LCE) is an anisotropic rubber, as it is formed by cross-linked polymeric chains with rigid rod-like mesogenic segments in the main chain and attached as side branches; these mesogenic units are similar to the molecules forming low-molecular-weight LCs [222-225], Fig.18. Cross-linked polymeric chains are structurally anisotropic because of their coupling to the orientational order. The coupling enables the mechanical response of LCEs to external factors such as temperature and electromagnetic fields. The dynamic response of LCEs to the changing external cues shares similarities with the behavior of liquid crystals in the external electric field and with the dynamics of the so-called active nematics comprised of self-propelled orientationally ordered units. For example, as will be demonstrated later in this Section, a temperature activation of an LCE coating with director deformations of splay and bend produces stress gradients in the material [226] , Eq.(11), that are described similarly to the flexoelectric polarization [135] discussed in Section II, Eq.(4), and to the active forces described by Simha and Ramaswamy [227] for an active nematic. This similarity is the reason why we consider LCEs along with other microscale dynamic systems with an orientational order.

Fig.18. Typical materials used to fabricate patterned LCEs: azodye SD-1 used as an alignment precursor; elastomer composition with reactive monomers (RMs) and a photoinitiator Irgacure 819 is deposited onto the photoaligned azodye layer and photopolymerized. Monomers such as azobenzene derivative A3MA with UV-triggered trans-to-cis isomerization could be added to make the LCE photosensitive.

A uniformly aligned LCE strip shows the simplest example of dynamic behavior when heated: it contracts along the director and expands in the perpendicular directions since the orientational order weakens and the cross-linked polymer network becomes more isotropic [222]. Such a uniformly aligned LCE strip behaves as an artificial muscle [228]. Recent research unravels even more exciting effects when the director changes in space, $\hat{\mathbf{n}}(\mathbf{r}) \neq \text{const}$. Thin LCE films with in-plane director patterns develop 3D shape changes with non-trivial mean and Gaussian

curvatures when exposed to thermal or light activation [223,229-236], while director deformations across the film trigger wave-like shape changes and locomotion when activated by light [237].

Modes, Bhattacharya and Warner considered a thin LCE film in which the director forms a system of concentric lines [238]; the configuration is a topological point defect of strength 1. Upon heating, the LCE shrinks along $\hat{\mathbf{n}}$ by a factor $\lambda < 1$ and expands in the perpendicular directions by a factor $\lambda^{-\nu}$ where ν is the thermal Poisson ratio. For a circular director field, heating means that the perimeter contracts, $P \to P' = \lambda P$, but the radii extend, $r_0 \to r' = \lambda^{-\nu} r_0$, which could be reconciled only if the initially flat film morphs into a cone. The cone's tip carries localized positive Gaussian curvature $K = 2\pi(1 - sin\,\phi)$, where ϕ is the cone opening angle [238]. Away from the tip, the Gaussian curvature vanishes. However, defects of a topological charge different from +1 could produce Gaussian curvature everywhere around their core [239]. These theoretical considerations solve the "forward" design problem, i.e., finding the 3D shape of an activated LCE film when the director field inscribed in its 2D precursor is known. The predicted connection between the topological defects in 2D films and their 3D buckling has been confirmed experimentally, as reviewed by White and Broer [223]. A harder task is to solve an inverse design problem, i.e., to find a flat director field that would induce a desired 3D shape upon activation.

A big step forward in generalizing the theoretical insights into the design of Gaussian curvature of LCE films has been made by Aharoni, Sharon, and Kupferman [240], who considered smoothly varying director fields. Surfaces of revolution, such as spherical, pseudo-spherical, and toroidal surfaces, can be produced by patterning the 2D precursor with a smooth director field that depends only on one spatial coordinate. Another interesting feature in Ref. [240] is a recipe to remove the degeneracy of 3D "bulging". A given distorted director field could make the 3D shape to bulge either up or down upon heating. If the director is uniform across the film thickness, these two directions are equivalent. It is claimed that this degeneracy could be lifted if the director patterns at the top and the bottom surface are slightly twisted with respect to each other. Aharoni et al. [241] combined a numerical approach based on Ref. [240] with an advanced technique of elastomer preparation to demonstrate how the inverse design could produce an arbitrary desired shape, such as a face. The desired surface is first transformed into a 3D triangulated mesh that is numerically mapped into a 2D mesh with triangles that carry a certain director orientation. The director varies from one triangle to another, as needed for the faithful reconstruction of the 3D

shape. At room temperature, the elastomer film is flat. Upon heating, the varying director field causes the triangular mesh to morph into a 3D structure that approximates the targeted surface [241].

In a parallel effort, there is progress in exploiting LCE coatings in which one surface is attached to the substrate, and the other is free [242,243]. A spatially varying director field of LCE coatings causes topography changes under the influence of various cues, such as temperature [232,244-246], light [229,230,247-250], electric field [251-255], humidity [256-260], etc. Coatings with cholesteric "fingerprint" textures [242,261,262] or periodic stripe arrays [263] produce dynamic periodic elevations and grooves for applications such as dust removal. Babakhanova et al. [226,264,265] described an approach by which the change of the topography of the coating or its stretching/contraction can be deterministically pre-programmed by a surface alignment of the director field. The LCE substrate is first prepared between two plates with photoinduced patterns of molecular orientation of the alignment layer. The two patterns could be the same, to induce a quasi-2D structure [226,264], or different, to produce a 3D structure such as an array of disclinations [265]. After polymerization, one of the plates is removed. The free surface is initially flat. When activated, for example, by temperature [226,265] or light [264], the free surface changes its profile as prescribed by the director pattern. The profile is shaped by the material moving within and out-of-plane. The displacements are deterministically related to the molecular orientation field. For example, upon heating, when the scalar order parameter of the LCE decreases, a circular bend of molecular orientation causes elevations, while a radial splay causes depressions of the coating [226,265].

The relationship between the LCE coating topography and the in-plane director field is routed in the coupling of the orientational order to rubber elasticity, mediated by cross-linking of the polymer network. The coupling results in an anisotropic structure of the network characterized by the so-called step length tensor [222], $l_{ij} = l_{\perp}\delta_{ij} + \left(l_{||} - l_{\perp}\right)n_i n_j$. The step length l characterizing the polymer segments connecting cross-linking points is different when measured along $\hat{\mathbf{n}}$ ($l_{||}$) and perpendicularly to $\hat{\mathbf{n}}$ ($l_{\perp}$). For $l_{||} > l_{\perp}$, the spatial distribution of the step lengths can be represented by a prolate ellipsoid elongated along $\hat{\mathbf{n}}$, Fig.19a. If the temperature increases and the orientational order weakens, the distribution becomes more spherical, i.e., the ellipsoid shrinks along $\hat{\mathbf{n}}$ and expands in two perpendicular directions, Fig.19b. If the nematic order is

melted, the ellipsoid becomes a sphere, $l_{||}^{iso} = l_{\perp}^{iso} = \bar{l}$; note, however, that LCEs often demonstrate a paranematic ordering with a small but nonvanishing scalar order parameter S at the temperatures at which their unpolymerized precursor would be an isotropic fluid [266,267].

Fig.19. Polymer network conformation and the occurrence of the activation force. (a) Prolate ellipsoid of polymer network conformations in the uniaxial calamitic nematic phase; the long axis is along the director $\hat{\boldsymbol{n}}$; during heating, the ellipsoid shrinks along the long axis; in the isotropic phase, it becomes a sphere, as shown in part (b); the shrinking is modeled by a pair of forces $\boldsymbol{F}$. Activation force density **f** produced by contracting ellipsoids in the geometry of (c) bend and (d) splay.

The morphing of the step length ellipsoid caused by the temperature can be modeled by a force dipole, with two point forces of equal amplitude F directed from the poles of the ellipsoid towards its center upon heating, Fig.19a, or away from the center upon cooling. Whenever the director field of the LCE changes in space, so do the local axes of the ellipsoids, Fig.19c,d. The spatial gradients of the step-length tensor produce a vector quantity with the components $f_i = \mu\partial_j n_i n_j$, which can also be written in the equivalent invariant form as [226,265]

$$\mathbf{f} = -\mu(\hat{\mathbf{n}}\mathrm{div}\hat{\mathbf{n}} - \hat{\mathbf{n}} \times \mathrm{curl}\hat{\mathbf{n}}) = -\alpha\Delta S(\hat{\mathbf{n}}\mathrm{div}\hat{\mathbf{n}} - \hat{\mathbf{n}} \times \mathrm{curl}\hat{\mathbf{n}}), \qquad (11)$$

where $\mu \propto (l_{||} - l_{\perp})/\bar{l}$ is an activation parameter describing the local elastic response to the changing temperature [226]; it relates to the change in the scalar order parameter S, $\mu = \alpha\Delta S$, where $\alpha > 0$ is the elastic parameter of the LCE [265]. When the temperature of an LCE with $l_{\|} > l_{\perp}$ increases and the long axes of the polymer ellipsoids shrink, then $\Delta S < 0$ and $\mu < 0$. In the case of cooling, $\mu > 0$ since $\Delta S > 0$. Note the similarity of the activation force in Eq.(11) and the flexoelectric polarization in Eq.(4) written for quadrupolar nematics with $e_1 = e_3$. As discussed in Section V, similar equations describe an active force in active nematics.

Fig.20. LCE coating with a prepatterned director responds to heating by elevating regions of bend. (a) The flat director pattern with circular +1 defects surrounded by -1/2 disclinations; (b) Digital holographic microscopy image of the LCE free surface; (c) Surface profiles along line *OO'* in (b) at 23, 60, and 100 ˚C; (d) Heating-triggered activation forces in a circular director field move the material towards the center, causing an elevation; (e) 3D view of the free surface's topography of LCE coating at 100 ˚C with elevations at circular +1 defects; note tri-fold symmetry of small

elevations and depressions around the cores of -1/2 disclination. Part (a) courtesy of C. Peng, parts (b,c,e) courtesy of G. Babakhanova.

With μ defined as above, the vector $\mathbf{f}$ represents a spatially varying activation force density that controls the elastic response of an LCE with a non-uniform director $\hat{\mathbf{n}}(\mathbf{r}) \neq \text{const}$ to the external factors such as heating. The force field $\mathbf{f}$ is illustrated in Fig.19c and 19d for pure bend and splay, respectively. For example, in the case of bend, the point forces $\mathbf{F}$ of the two neighboring shrinking ellipsoids that are titled with respect to each other, add up to produce a net force density $\mathbf{f}$ pointed towards the curvature center of $\hat{\mathbf{n}}(\mathbf{r})$, Fig.19c. When the director field is patterned with bend and splay, the activation force defined by Eq.(11) moves the material and creates elevations, depressions, and in-plane shifts.

Figure 20 shows an example in which a heated LCE coating develops elevations at the circular $m = +1$ defects. In this director pattern, each +1 defect is surrounded by six -1/2 defects. The surface profile around the $m = -1/2$ cores shows three elevations and three depressions, as expected since there are three bend and three splay regions around each core, Fig.20b,e. Similarly, $m = +1/2$ defect cores show one elevation and one depression [226].

A unique feature of the $m = +1/2$ cores, not observed in $m = -1/2$ nor in $m = \pm 1$ defects is their shift from the bend region towards the splay region, as the temperature increases, Fig.21a,b. The shift of $m = +1/2$ defect core is fully reversible in the heating-cooling cycles. The activation force $\mathbf{f}$ in Eq.(11) helps to understand why the cores of $m = +1/2$ move towards the splay region: the angular distribution of the force around the $m = +1/2$ defect core breaks the fore-aft symmetry with a nonzero net force directed towards the splay (tail) region, Fig.21c,d. The dynamics of +1/2 defects in temperature-activated patterned LCEs is reminiscent of the dynamics of +1/2 defects in extensile and contractile active systems, discussed in experimental [268-281] and theoretical [282-292] works. In particular, activity-induced motion of +1/2 defects is described for monolayers of vibrating rods [268], living cell cultures [269-271], bacterial colonies [272,281,293], and microtubules powered by kinesin motors [274]. In all these systems, $m = +1/2$, unlike their $m = -1/2$ and ± 1 counterparts, propel either in the direction of bend or splay, depending on whether the active units are extensile or contractile. The heated LCE corresponds to a contractile case, $\mu > 0$ and $\Delta S < 0$, Eq.(11). An extensile version with $\mu < 0$ could

be manufactured by polymerizing the nematic LCE at elevated temperatures and then cooling it down.

Fig.21. In-plane shifts of +1/2 defects upon heating. (a) PolScope image of a flat LCE coating at 23 ˚C with periodic lattice of defects of strength ±1/2; red boxes A and blue boxes B enclose two types of pairs: in pair A, the director $\hat{\mathbf{n}}(\mathbf{r})$ is perpendicular to the line connecting the two cores, in pair B, $\hat{\mathbf{n}}(\mathbf{r})$ connects the cores. (b) Separation distance between $+1/2$ and $-1/2$ cores increases in pairs A and decreases in pairs B as the temperature increases. (c) Director configuration and active force $\mathbf{f}(\mathbf{r})$ calculated using Eq.(11) for pair A. (d) The same for pair B. Redrawn from Babakhanova et al. [226].

The activation force $\mathbf{f}$ yields only a qualitative prediction of how the LCE coatings with a patterned director evolve when the ambient conditions change. Analytical description of LCE coatings' profile should account for mass conservation, the dynamic coupling of the director field and rubber elasticity to the material transport, different boundary conditions at the two interfaces, anisotropic orientational elasticity of the material, surface anchoring, etc. A combined experimental and theoretical analysis has been performed recently for a nematic LCE coating in which the director is patterned with an array of singular disclinations that run in the bulk of the coating. One of the LCE surfaces is patterned with a one-dimensional periodic system of splay and bend in the shape of letters "C", resembling Néel walls, of period L, $\hat{\mathbf{n}}_0(x, y, z = d) = (\cos\frac{\pi x}{L}, \sin\frac{\pi x}{L}, 0)$, while the second surface is uniform with $\hat{\mathbf{n}}_0(x, y, z = 0) = (1,0,0)$, Fig.22a. The director frustrations imposed by different surface alignments are resolved by singular disclinations located in the splay regions [294] $x = \pm L/2, \pm 3L/2, ...$Fig.22b. As the coating is heated, the free surface develops linear microchannels-indentations above the disclination cores Fig.22c. These "valleys" are located in the regions where the in-plane director experiences splay, i.e., at $x = \pm L/2, \pm 3L/2, ...$; accordingly, the bend regions at $x = 0, \pm L, \pm 2L, ...$ show elevations.

Fig.22. LCE coating with a prepatterned system of singular disclinations. (a) Director patterns on the top and bottom surfaces. (b) Vertical cross-section of unpolymerized nematic with the core of the disclination shifted towards the patterned surface. (c) Surface profile of LCE coating of thickness $d = 5$ μm and period $L = 80$ μm at the elevated temperature. (d) Linear elasticity theory calculations of in-plane displacements $\mathbf{u}(x)$ of the heat-activated coating and the activation force $\mathbf{f}(x)$ for the corresponding director field $\hat{\mathbf{n}}(x)$. (e) Linear elasticity theory calculations of the out-of-plane displacements of the heat-activated LCE coating ($d = 6$ μm, $L = 80$ μm) for different locations of the disclination line in the LCE bulk; the top free surface of the coating is patterned as shown in part (a). Redrawn from Babakhanova et al. [265].

The experiment by Babakhanova et al. [265] shows that the microchannels can show either one valey or a double-valley shape. To describe the surface profile, one first adopts a Frank-Oseen model of disclinations in the patterned director field and then uses a linear elasticity theory to connect the complex spatially-varying director to the displacements of the LCE. The theory predicts in-plane material displacements $\mathbf{u}(x)$ which move the heated material away from the splay regions towards the bend regions, which explains the formation of the depressed microchannels, Fig.22d. Notice that the qualitative pattern of the activation force $\mathbf{f}(x)$ shown for the same director field $\hat{\mathbf{n}}(x)$, is in a good qualitative agreement with the more rigirous calculations of the in-plane displacements $\mathbf{u}(x)$ that account for the three-dimensional structure of the LCE coating and that one surface is free, and the other is clamped to the rigid substrate, Fig.22d. Moreover, the theory also predicts that the microchannels could change from the single-valley to double-valley geometry when the disclinations reside near the free surface, Fig.22e. Microchannels similar to those in Fig.22 can be used to dynamically control spatial locations of colloidal particles dispersed at their surface [264].

Coatings with a spatially varying director can also be produced from the smectic precursor [295]. Unidirectional periodic positional order of smectics makes them prone to structural instabilities triggered when the flat layers could not accommodate the boundary conditions or stresses [38]. A smectic film placed between two different surfaces, one of which aligns $\hat{\mathbf{n}}$ parallel to itself and another perpendicular to itself develops either 2D [296-300] or 1D system of structural defects [301-304] that form because of the condition of layers' equidistance. When the surface with the perpendicular alignment of $\hat{\mathbf{n}}$ is free, these 2D and 1D arrays of defects develop indentations, in the form of conical depressions [298,300,305] and rectilinear grooves [301-304], respectively. The typical depth of these indentations is on the order of 100 nm, while their width is on the order of few micrometers and depends on the thickness of the coating [300,305-307]. This phenomenon was used by Babakhanova et al. [295] to create polymerized coatings with spontaneous periodic nanogrooves and demonstrate their ability to align human dermal fibroblasts. Besides the simplicity of preparation, SmA LCE's advantage is that by controlling the surface alignment of the SmA molecules at the bottom substrate, the groves and thus the cell alignment patterns can be constructed in various geometries [306].

IV LIVING TISSUES AND THEIR ALIGNMENT BY LIQUID CRYSTAL ELASTOMERS

Biological tissues with collective cell movement [3,4,308-312] represent a fascinating example of active matter that recently became the object of intense studies in physics. Cell movement is a fundamental process involved in embryo development [313], morphogenesis [314], tissue healing and regeneration [313,315,316], formation and expansion of tumors [316-326]. The research established fruitful analogies between tissues and soft materials such as foams, emulsions, colloids, and polymers [308]. Developments of the last decade [269,281,293,327-335] demonstrate that there is another essential soft matter physics concept that could help one to understand living tissues, namely, the orientational order, a hallmark of LCs [2,38]. When biological cells are packed together in tissues and organs, they often tend to orient parallel to each other, similarly to molecules forming LCs [269,327-334]. Optical microscopy reveals a nematic type of apolar ordering, in which major axes of cells align over a macroscopic area along a common direction $\hat{\mathbf{n}}_t$. As in passive nematics out of equilibrium, the order is not perfect, exhibiting topological defects-disclinations [269,270,281,293,328,332,335,336]. These defects play a decisive role in various biologically relevant functions, as presented in a brief review by Fardin and Ladoux [337], which cites perhaps the first scientific exploration of the relationship between the tissues and disclinations by Lionel S. Penrose, who connected the fingerprint and palm skin patterns to the disclinations of strength +½ and -1/2 and argued that the number of defects was connected to the number of fingers [338]. Recent research shows even more striking examples of orientational order in various tissues and the important role of topological defects.

4.1 Orientational order and topological defects in microorganisms and tissues.

Cells in tissues interact with the environment, such as the extracellular matrix (ECM) and neighboring cells. In living tissues of human dermal fibroblasts (HDFs), murine neural progenitor (MNP) cells, C2C12 mouse myoblasts, retinal pigment epithelial (RPE1) cells, Madin-Darby canine kidney (MDCK) cells, human bronchial epithelial cells (HBECs), NIH 3T3 mouse embryo fibroblasts, etc., these interactions result in an apolar orientational order of the nematic type [37,269,270,327,332,339-341]. The director varies in space and time, producing disclinations that move within the tissue and play an important role in processes such as apoptosis, i.e., extraction

of dead cells [332] and hole formation in tissues [281]. A topological defect cannot be continuously transformed into a uniform state as such a process would require energies much higher than the elastic energy stored in the defect, thus defects appear and disappear in +/- pairs to preserve the total topological charge defined by the boundary conditions [38]. In a 2D circular domain with a fixed director at the boundary, the total charge is +1 [270,342-344], while on a spherical surface, it is +2 [38].

The two general conservation laws for surface and bulk defects in an enclosed 3D volume of a medium with a nematic or a polar type of ordering, with a certain surface alignment, write [38,183]:

$$\sum_{i=1}^{p} m_i = \chi, \tag{12}$$

valid for all surface orientations except the case when the director (or vector) is perpendicular to the enclosing surface, and

$$\sum_{j=1}^{p+q} N_j = \frac{\chi}{2}, \tag{13}$$

valid for any type of surface anchoring. Here p is the number of surface defects with 2D charges m_i, q is the number of 3D point defects (or closed disclination loops) with 3D charges N_j, and χ is the Euler characteristic of the enclosing surface, equal 2 for spheroids and 0 for tori. The relationship (12) is called the Euler-Poincaré theorem, while Eq.(13) is a consequence of the Gauss-Bonnet theorem. For passive nematics, Eqs. (12,13) describe the behavior of bulk and surface defects in spherical droplets when the surface anchoring at the surface changes [183]. The number of defects in the passive volumes at equilibrium tends to the lowest possible value, e.g., in a tangentially anchored nematic drop, Fig.23a, two surface defects, so-called boojums, with $m_1 = m_2 = +1$ and $N_1 + N_2 = +1$, would be present for any surface orientation of the director, except for the perpendicular one, while a single "bulk" point defect, such as a radial hedgehog, $N = +1$ would be present in a perpendicularly anchored droplet [183]. The number and topological charges of defects are dictated by the requirement to reduce the elastic energy.

The relationships (12,13) apply to a 3D nematic droplet, Fig.23a, and to a 2D nematic membrane with an in-plane director wrapped into a spherical shell, Fig.23b. One should be aware, however, that the energetics of topological defects in these two cases is different. In the 2D nematic shell, the +1 point defects split into four +1/2 defects, Fig.23b, since the elastic energy of each

point defect is proportional to m^2 [38]. Since the defects of the same sign repel each other elastically, these four form a tetrahedron configuration [345]. In a 3D nematic drop, however, +½ points at the surface could not be isolated defects; they represent the ends of the bulk disclinations, the elastic energy of which is proportional to the length. Thus the +1 point defects-boojums at the poles of a nematic droplet are energetically stable for tangential and tilted director anchoring [183], Fig.23a. Very often, when the twist elastic constant is smaller than the Frank moduli of splay and bend, tangentially anchored nematic spheres show a twisted parity-breaking director field, despite the absence of any chiral molecules [183,346,347], Fig.23a. Recent experiments on topological defects in shells are described in Ref. [348-352] for passive and in Ref. [274] for active nematics. In active nematics, although the topological constraints (8,9) are still valid, see, for example, the studies on spheres [274,353-355] and tori [356,357], the elastic-energy-imposed limitation on the numbers p, q of defects is lifted, since these numbers depend on activity levels.

A spectacular illustration of Eqs.(12,13) from the living world has been presented recently by Maroudas-Sacks et al. [335], who studied the regenerative morphogenesis of *Hydra*. *Hydra*'s body is formed by a double layer of epithelian cells, which produce arrays of nematically ordered supracellular actin fibers. *Hydra* is known for its remarkable regeneration capabilities: A cut-away piece of an adult animal can morph itself into a new fully functional *Hydra*, Fig.23c,d,e. The experiment explored how the nematic order of fibers and topological defects evolve when *Hydra* regenerates from a cut-away piece of tissue, in which the fibers are uniformly aligned and form no defects, Fig.23c. Regeneration starts with the piece folding into a closed hollow spheroid, Fig.23d. The closure is followed by the formation of defects with charges $m = +1/2, -1/2, +1$, Fig.23e. The early +1 defect becomes the site of head formation; it does not move within the tissue. In contrast, the comet-like $m = +1/2$ defects are mobile [268]. They move with the bend region forward, which is characteristic of extensile active nematics. These $m = +1/2$ defects play only a transient role, merging into +1 defects and annihilating with -1/2 defects. The merging of $+1/2$ into +1 defects is highly unusual from the point of view of the theory of thin shells of passive nematics, since the elastic energy of defects scale as m^2. In living systems, active forces could overcome the elastic repulsion of defects in thin films, as also evidenced by experiments on two other 2D active nematics: films of motile bacteria *Pseudomonas aeruginosa* [293] and human fibroblast tissues [271]. Furthermore, the +1 defect could be stable against splitting into a pair of two +½ defects if the *Hydra* tissue is not very thin. In nematic slabs of a finite thickness, the elastic

energy of a surface defect-boojum of an integer strength is smaller than the energy of two half-integer disclinations [358]. Yet another reason for the stabilization of a +1 defect might be a tilt of the director $\hat{\mathbf{n}}$ towards the normal $\hat{\mathbf{k}}$ to the tissue; the director projection onto the surface is a vector, which prohibits half-integer defects [183]. Note here that external circular shears could also merge two +1/2 defects into +1 one [280].

Two merging +½ singularities form a radial +1 defect that serves as a foot of the new *Hydra*. The two +1 defects establish the body axis of the system, with a clear polarity established by the order in which these defects form [335]. The topological dynamics of *Hydra* regeneration continues with the developments of tentacles, finger-line protrusions with a zero net charge, represented by a triplet of defects, one +1 at the tip and two -1/2s at the base, Fig.23e. Thus a regenerated *Hydra* adopts the following version of the Euler-Lagrange relationship (8): $+1(mouth) + (+1/2 + 1/2)(foot) + k(-1/2 + 1/2)(transient\ defects) + n(+1 - 1/2 - 1/2)(tentacles) = +2$, while in the properly developed *Hydra* $+1(mouth) + (+1)(foot) + n(+1 - 1/2 - 1/2)(tentacles) = +2$; here k is the number of annihilating pairs, and n is the number of tentacles [335].

Fig.23. Topological defects in (a) tangentially anchored nematic drop; (b) thin nematic shell. (c,d,e) Topological dynamics of *Hydra* morphogenesis: (c) cut-away piece of an adult *Hydra* with a uniform alignment of fibrils; (d) folding of the piece into a spheroid; (e) regenerated hydra with point defects of strength +1 at the mouth and foot; each tentacle shows a point defect +1 at the tip, balanced by the two -1/2 defects at the opposite sides of the base. Redrawn from Maroudas-Sacks et al. [335].

An important fact is that the elementary defects in *Hydra* and many other living tissues are of a strength $m = \pm ½$, which is direct proof that the orientational order is apolar, $\hat{\mathbf{n}}_t \equiv -\hat{\mathbf{n}}_t$ [37,269,270,328,332,334,336,340]. A recent model [359] predicts apolar order and $m = \pm ½$ defects by considering cells as deformable droplets acted upon by neighbors. Another interesting prediction [359] for tissues is that although cells are made of an internally contractile material [360], their collective behavior can be explained by considering cells as extensile, i.e., each cell exerts a pair of antiparallel forces of equal amplitude towards the environment [4].

The motion of +½ defects with their bend region (the head) leading the way is observed not only in *Hydra* but also in MDCK [332], MNP [269], and HDF tissues [271]. Monolayers of mouse embryo fibroblasts and C2C12 tissues show an opposite polarity, with the splay (tail) leading the

way, similar to the scenario in Fig.21c,d, suggesting a contractile/puller behavior [270,361]. Interestingly, Duclos et al. noticed that in the same tissue, the contractile feature of defects coexists with the extensile character of shear flows [362]. In other words, the contractile vs. extensile behavior of tissues is by no means a settled issue.

Besides contractile vs. extensile behavior, intriguing is the relationship between the nematic and polar ordering in cells engaged in collective motion. The apolar order of tissues is surprising [359] since cell motility requires polarization [363-367], i.e., front-back asymmetry. A clear example is wound healing, in which a free edge of an epithelium advances by protruding "fingers" with highly orientationally ordered cells [341,368,369]. Within the fingers, the cells follow the "leader" along a vector pointing towards the empty area. Such a process requires both alignment and polarization of cells [370]. The development of shear flows in RPE1 and C2C12 tissues confined to a rectangular stripe of a width that exceeds some threshold is another spectacular demonstration of active flows emerging in an apolar system [361,362]. Polar flows do not necessarily require polarity of individual cells and might be triggered by gradients of orientational order even in the nematic systems.

Orientationally ordered arrays of biological cells, such as melanocytes, inspired Simha and Ramaswamy [227] to propose an active stress contribution to the hydrodynamic equations describing suspensions of active particles,

$$\boldsymbol{\sigma}^{a} = -\alpha \mathbf{Q}, \tag{14}$$

where α is the activity parameter, absent in passive systems [3,4,6,227,371]; $\alpha > 0$ corresponds to extensile (pusher) particles in which the two point forces are directed outward along the elongation axis, as in Fig.10d, while $\alpha < 0$ corresponds to contractile (puller) particles in which the two forces are directed inward, as in Figs.10a,19. The active stress produces a local active force,

$$\mathbf{f} = -\nabla \cdot (\alpha \mathbf{Q}), \tag{15}$$

which could be rewritten as a sum of two terms, one associated with the gradients of the tensorial order parameter and another with the gradients of activity (caused, for example, by gradients of the concentration of active units) [30,372]:

$$\mathbf{f} = \mathbf{f}_{\mathbf{Q}} + \mathbf{f}_{\alpha} = -\alpha \nabla \cdot \mathbf{Q} - \mathbf{Q} \cdot \nabla \alpha. \tag{16}$$

If the activity and the scalar degree S of ordering do not vary in space, the active force could be recast in a form suitable for an easy geometrical interpretation, as the sum of the splay and bend terms, which enter the expression on equal footing if the system is momentum-conserving [227,373]:

$$\mathbf{f} = -\alpha[\hat{\mathbf{n}}\nabla \cdot \hat{\mathbf{n}} - \hat{\mathbf{n}} \times (\nabla \times \hat{\mathbf{n}})]. \quad (17)$$

Although both terms are insensitive to the sign of $\hat{\mathbf{n}}$, they are clearly polar. The last expression is of the same form as the activation force [226] in Eq.(11) and the flexoelectric polarization in Eq.(4) for nematics formed by molecules with no dipole moments [136]. Figures 19-22 that depict the activation force and movements in LCE can be used to illustrate how the active force in Eq.(17) causes flows in active nematics; one of course should remember that the system could be either contractile, as in Figs.19-22, or extensile, in which case the flows would be of opposite direction. The active force in Eq.(17) enhances fluctuative distortions and triggers thresholdless active flows in living LCs [215,221,374], as will be detailed in Section V. Enhancement of orientational curvatures by activity leads to intrinsic instabilities such as director undulations, nucleation of topological defects [3,4,227,273,276], and giant density fluctuations [227,268,371,375-378]. These activity-triggered instabilities are countered by elasticity [274,282,340,379,380], friction, and anchoring. In equilibrium nematics, elasticity relaxes orientational perturbations and annihilates defects of opposite charges, establishing uniform states; surface effects can favor either uniform or non-uniform states, depending on the geometry.

Friction at the interface with an underlying substrate could damp the active stresses [368,381-383] and prevent defects nucleation in tissues, as demonstrated for NIH 3T3, RPE1, C2C12 tissues [270]. In tissues shaped as disks, ±½ defects annihilate, and the stationary long-term state exhibits only two +½ defects necessitated by the circular confinement. The separation between these defects is constant, 67% of the circle diameter. The distance corresponds to the minimum of the elastic energy of a passive nematic in similar confinement, which suggests that the activity is damped by cell-substrate friction. In contrast, HBEC tissues exhibit a high number of defects with a dynamic balance of nucleation and annihilation [340].

The substrate friction is predicted [384] to modify the active force by introducing two independent activity coefficients, $\alpha_1 \neq \alpha_3$:

$$\mathbf{f} = -\alpha_1\hat{\mathbf{n}}\nabla \cdot \hat{\mathbf{n}} + \alpha_3\hat{\mathbf{n}} \times (\nabla \times \hat{\mathbf{n}}); \quad (18)$$

note the similarity with Eq.(4) written for the flexoelectric polarization of a passive nematic comprised of molecules with permanent electric dipoles. This form of the active force has not been verified experimentally.

4.2.Micropatterning of tissues.

Morphogenetic developments of tissues are mechano-elastic processes triggered by genetic changes in cells [385] and by interactions with the environment [333,341,386-388]. Boundary conditions are important since they could specify large-scale stress patterns over long distances in a way that is difficult to achieve by chemical signals [333]. Control of boundary conditions through micropatterning [311,333,341,389,390] thus has been for a long time the most effective approach to guide tissue growth. Micropatterning brought about tremendous progress in understanding how geometry impacts physiology. Micropatterning places cells in physiologically relevant situations that can be fine-tuned to affect cell behavior, an advantage over in-situ studies. It helps to understand the mechanisms of morphogenesis, such as left-right asymmetry in circular [391] and rectangular areas [361] and promises to advance regenerative medicine [333].

Micropatterning employs substrates with a well-defined cell-adhesive area. A single cell confined to an asymmetric area (such as a "teardrop" [390,392]) acquires a similarly asymmetric shape and, once released, moves with the blunt edge leading the way [392]. There is a correlation between the migration velocity and the cell-substrate adhesive area: a smaller area reduces the speeds, suggesting that the cell-substrate interaction is an important factor [311]. Petitjean et al. [393] used micropatterning with stencils to mimic the wound healing by presenting a free surface to an initially confluent epithelium monolayer. The growing tissue develops "fingers" and long-range velocity and alignment correlations.

4.3. Tissue alignment by liquid crystal elastomers.

The alignment of cells in the works cited above is guided by the edges of adherent areas since the substrates themselves set no preferred direction. There is a growing interest in developing substrates with an internal anisotropy caused by gradients of stiffness [386,388], gradients of activity [30,289,372,394], microgrooves [395-399], variable curvature [400-403], and the

orientational order [404-409]. Of particular interests are LCEs since these materials are organic, orientationally ordered, and have already demonstrated the ability to align cells parallel to the LCE director $\hat{\mathbf{n}}_s$ [224,271,407,408,410-414]. As a rule, the LCE substrates are uniformly aligned [295,412,413], but two recent publications [271,414] report that a patterned spatially varying director field $\hat{\mathbf{n}}_s(\mathbf{r})$ of LCEs can be transferred into the alignment cells pattern $\hat{\mathbf{n}}_t(\mathbf{r})$ of living tissues. The patterning of LCE [207,215,226,264,374] and transfer of these patterns onto arrays of cells [271,295] enables at-depth exploration of the interplay between the orientational order and activity in tissues. This development allows one to prescribe where the specific defects would be located. It also allows one to explore how the defects influence tissue properties such as the number density of cells, fluctuations in the number density, shape and polarity of cells, their collective dynamics, etc. An approach to pattern HDF tissues by LCE substrates [271] is described below.

The LCE substrate is supported by a smooth glass plate. The glass is covered with a photosensitive azodye such as SD-1 in Fig.18, the alignment of which is patterned by light irradiation with spatially varying linear polarization [205]. The azodye layer serves as a template for the diacrylate monomers such as the ones in Fig.18, doped with a photoinitiator. After alignment through the contact with the azodye, the monomer is UV-irradiated to photopolymerize the LCE substrate with a predesigned $\hat{\mathbf{n}}_s(\mathbf{r})$. When the substrate is covered with aqueous cell culture, the LCE and the underlying azodye layer swell, developing a non-flat profile with elongated ellipsoidal grains of an average height ~ 50 nm and the length up to ~ 30 μm, Fig.24a,b. The excessive amount of the photoinitiator facilitates the swelling [271]. The plausible reason is that the photopolymerization starts in multiple locations and makes the resulting network comprised of many loosely connected patches with voids accessible to water. The typical distance between the grains is in the range $(1-10)$ μm. These grains serve as a guiding rail for HDF cells; their dimensions are similar to the dimensions of grooves used in conventional lithography approaches for tissue alignment [395,397].

The HDF cells are deposited onto the LCE substrate from the aqueous cell culture. Once an HDF cell sets onto the substrate, it develops an elongated shape with the axis of elongation along the local $\hat{\mathbf{n}}_s(\mathbf{r})$, Fig.24d,e [271]. The order parameter S_{HDF} of HDF cells seeded on a uniaxially aligned substrate, $\hat{\mathbf{n}}_s = \mathrm{const}$, grows from 0.80 ± 0.05 to 0.96 ± 0.01 within the time interval 24-168 hours after seeding, when the number density of cells is in the range $\sigma =$

$(0.1-0.7)\sigma_c$, where $\sigma_c \approx 3\times10^8$ m^{-2} is the maximum density corresponding to confluent tissue, i.e., complete coverage of the substrate by a monolayer of cells. The high S_{HDF} at $\sigma < \sigma_c$ demonstrates that the orientational order is caused mainly by individual interactions of each cell with the LCE substrate.

Fig.24. Human dermal fibroblast (HDF) tissue grown at an LCE coating with a prepatterned disclinations $m = \pm 1/2$. (a,b) Digital holographic microscopy of the patterned LCE surface near the defect cores with elongated elevated grains; (c) PolScope texture of the patterned LCE coating. (d,e) Phase contrast microscopy of the growth of HDF cells at the LCE substrate at 72 hr and 240 hr after seeding, respectively. (f) Fluorescent microscopy textures of HDF tissues at the LCE substrate, with labeled nuclei (blue) and cytoskeleton F-actin proteins (green).(g) The director angle around defects changes with the polar angle in a nearly linear fashion. (h). Number density of cells as a function of the distance to the defect core. (i) Large number density fluctuations ΔN of the nuclei in the vicinity of defect cores. (j) Separation between half-strength defects for pairs of type A and B, identified in Fig. 21. Redrawn from Turiv et al. [271].

The LCE substrates align not only the bodies of HDF cells, but also their elongated nuclei, Fig.24f. This feature is important since orientation and shape of the nuclei impact many cell functions, such as protein expression, motility, metabolism, phenotype, and differentiation [415]. The nuclei are elongated along the same direction as the cytoskeleton, Fig.24f, and apparently, because of that show a high order parameter reaching $S_{\mathrm{nuclei}} = 0.88 \pm 0.05$ after 240 hours since seeding.

The director patterns $\hat{\mathbf{n}}_{\mathrm{s}}(\mathbf{r})$ with topological defects in Fig.24, are designed under an assumption that the elastic constants of splay and bend are equal. For an isolated defect, the angle between the director and the local in-plane axis must be a linear function of the polar azimuthal angle. The nearly linear dependency observed for the tissue director $\hat{\mathbf{n}}_{\mathrm{t}}(\mathbf{r})$, around defects, Fig.24g, suggests that either the tissue exhibits similar splay and bend moduli or that the in-plane anchoring is sufficiently strong to make $\hat{\mathbf{n}}_{\mathrm{t}}(\mathbf{r})$ very close to $\hat{\mathbf{n}}_{\mathrm{s}}(\mathbf{r})$.

In confluent tissues, the number density σ of HDF cells per unit surface area is larger near the cores of +1/2 defects as compared to the -1/2 defects, Fig.24h, which is analogous to the behavior of neural progenitor cells [269]. The ±1 defects exhibit similar disparities [271]. In 3T6 fibroblast tissues patterned by microscale topography of polydimethylsiloxane substrates, σ is about 40% higher near the cores of +1 circular defects than away from them; near -1 defects, σ is

40% lower than the far-field value [399]. Interestingly, σ varies very little in epithelial MDCK tissues of the same geometry [399].

Since in confluent monolayers the cells are in contact with each other, the strong variations of σ translate into noticeable differences of HDF cells' size and shape. As a rule, cells near the $-\frac{1}{2}$ and -1 cores are of a larger area, and of a higher aspect ratio, as compared to their counterparts near the +1/2 and +1 cores: the LCE patterns affect the phenotype of cells [271].

The HDF tissues at LCE substrates exhibit high spatial fluctuations of number density, Fig.24i [271], which is an attribute of out-of-equilibrium systems [4,268,371]. In an equilibrium system, a certain area containing N objects would show fluctuations with a standard deviation ΔN proportional to $N^{1/2}$. In contrast, active matter shows ΔN that grows somewhat faster than $N^{1/2}$ [268,339,376,416]. In the tissues shown in Fig.24f, the mean number of cells' nuclei $\langle N \rangle$ and the standard deviation ΔN are related as $\Delta N \sim \langle N \rangle^{\beta}$, with $\beta = 0.67 \pm 0.05$ around +½ defects and $\beta = 0.75 \pm 0.05$ for their -1/2 counterparts, Fig.24i. These values are close to $\beta = 0.66 \pm 0.06$ measured for a misaligned array of mouse fibroblast cells [339] and are clearly higher than the equilibrium value $\beta = 1/2$.

The LCE substrate provides a strong enough orientational anchoring to pin the $m = \pm 1/2$ defects to their predesigned locations, Fig.24j, thus overcoming the tendency of +1/2 defects to move around, as in Fig.21. However, the activity of +1/2 defects reveals itself in patterns with circular and radial +1 defects [271].

In an equilibrium 2D nematic, defects of an integer strength tend to split into pairs of semi-integer defects, since their elastic energy scales as $\propto m^2$ [38]. In the HDF tissue, both −1 and +1 defects split into two defects of a semi-integer charge separated by a distance $d \approx (200 - 500)$ μm, Fig.25. Inside the region $r < d$, $\hat{\mathbf{n}}_t$ deviates significantly from $\hat{\mathbf{n}}_s(\mathbf{r})$. As the tissue grows towards confluency, the distance d in the circular +1 configuration increases with time, Fig.25b, while in the radial $+1$ case, d decreases with time, Fig.25e. These very different scenarios are reminiscent of the defect dynamics in active nematics with extensile units, in which the comet-like $+1/2$ defects move with the bend region leading the way [4,269,332,334]. Consider a pair of $+1/2$ disclinations that splits from a parent +1 disclination at the substrate patterned as a +1 radial defect, $\hat{\mathbf{n}}_s = (n_r, n_\varphi, n_z) = (1,0,0)$ in cylindrical coordinates. In the one-constant

approximation, the elastic repulsive potential of the two $+1/2$ defects depends weakly on d: $F_E = -\frac{\pi K h}{2} ln \frac{d}{2r_c}$, where K is the average Frank elastic modulus, $h \approx 20$ μm is the thickness of the cell layer, and r_c is the size of the defect core [38]. The activity contributes an additional force f that tends to drive $+1/2$ defects either towards each other ($f < 0$) in the radial geometry or away from each other ($f > 0$) in the circular geometry [379,417], Eq.(17) and Fig. 25c,f. Since the defect splitting causes the tissue director $\hat{\mathbf{n}}_t$ to differ significantly from $\hat{\mathbf{n}}_s$ within an area of diameter d, the splitting also invokes a surface energy penalty $F_S = \beta W d^2$, where $\beta \approx 0.2$ is the numerical coefficient for the chosen geometries of radial and circular defects [271], W is the azimuthal surface anchoring coefficient [271]. The stationary value of the separation distance is then defined from the balance $f + f_{\text{elastic}} + f_{\text{surface}} = 0$ of the elastic force $f_{\text{elastic}} = -\partial F_E/\partial d = \pi K h/(2d)$, surface anchoring force $f_{\text{surface}} = -\partial F_S/\partial d = -2\beta W d$ and active force f, which yields

$$d_s = \frac{f + \sqrt{f^2 + 4\pi\beta h K W}}{4\beta W}. \quad (19)$$

According to Eq.(19), surface anchoring sets a stationary finite separation of defects that is smaller in the radial geometry, $f < 0$, and larger in the circular geometry, $f > 0$; the difference is caused by the opposite polarity of f, Fig. 25. The measured separations of defect pairs lead to the estimates $|f|/W \approx 140$ μm and $K/W \approx 180$ μm, which implies $|f| \sim K$. Considering a cell as an elastic flexible rod of Young's modulus ~10^4 N/m^2 [418,419], the bending modulus is estimated as $K \sim 5$ nN [271], which leads to $W \approx 3 \times 10^{-5}$ J/m^2, a value close to surface anchoring in many LC systems [38]. Interestingly, the estimate of the Frank constant $K \sim 5$ nN [271] of the HDF tissue of thickness $h \approx 20$ μm produces a bending modulus $Kh \sim 0.1$ μN μm, which compares well with the value $Kh \sim 0.2$ μN μm measured directly by Fouchard et al. [420] for a curling MDCK monolayer and $Kh \sim 0.5$ μN μm obtained by the analysis of MDCK monolayer buckling in a spherical confinement by Trushko et al.[419].

Fig.25. Human dermal fibroblast (HDF) monolayer at an LCE substrate patterned with -1 and +1 defects, either of (a, b, c) circular geometry or (d, e, f) radial geometry, splitting into pairs of +1/2 disclinations. The separation distance Δr (a,b) increases with time in the circular case and (d,e) decreases in the radial case, because of the active forces that are (c) centrifugal in the circular case and (f) centripetal in the radial case. Redrawn from Ref. [195].

The scenario of two +½ defects approaching each other, Fig.25e,f, has been recently observed in monolayers of *Pseudomonas aeruginosa* bacteria migrating across surfaces using hook-like pili [293]. Fast-moving hyper-piliated mutants form +1/2 defects that collide with each other forming +1 defects. Since the director makes a full turn by 2π around the core of a +1 defect, it can realign towards the normal to the surface. Such reorientation would be difficult around ½ defects since it would produce π-domain walls in the director orientation. Reorientation of the director along the axis of +1 defects, called the escape into the third dimension, is a well-known elastic energy-reducing effect in passive nematics, demonstrated by Cladis, Kleman, and Meyer [421,422]. In the active nematic of *Pseudomonas aeruginosa*, the realigned bacteria become trapped [293]. Their slower-moving wild-type counterparts, in contrast, do not create a sufficiently strong active force to bring two +1/2 defects into one +1. The colony of slow-moving bacteria thus avoids the topological trapping along the third dimension and propagates into new territory faster than the bacteria with a higher individual speed [293].

Besides their role in controlling effects such as propagation of colonies and tissues, +1/2 defects might be involved in forming multilayered structures [281]. Copenhagen et al. [281] described *Myxococcus xanthus* bacterial colonies that show a nematic orientational ordering with +1/2 and -1/2 defects. The -1/2 defects were strongly correlated with the probability of tearing a hole in a monolayer of cells, while the +1/2 defects were often associated with the appearance and growth of the second layer of cells on top of the original monolayer. To explain the effects, Copenhagen et al. [281] used the idea that the collective velocities $\mathbf{v}(\mathbf{r})$ of bacteria are triggered by active forces $\mathbf{f}$ caused by the gradients of the orientational order, Eq. (15). The active forces are balanced by a viscous friction forces $\eta_{ij}v_j$ rooted in the bacteria-substrate interactions,

$$\eta_{ij}v_j = f_i, \tag{20}$$

which are assumed to be anisotropic [269,281], since the bacteria are of a rod-like shape and should experience a smaller drag when they move parallel to their elongation axes:

$$\eta_{ij} = \eta_0(\delta_{ij} - \varepsilon Q_{ij}), \tag{21}$$

where η_0 is the isotropic friction and $\varepsilon > 0$ is the measure of the friction anisotropy. The model predicts the motion of the +1/2 defects with the bend region leading the way, as expected for extensile units. A new important feature brought about by the anisotropy of friction is that the cells in the

bend region experience a stronger friction than the cells in the splay region, since they need to move perpendicularly to themselves. This difference means that the cells inflow is stronger than the cells outflow near the cores of the +1/2 defects, Fig.26a. The accumulated cells then are forced to escape along the normal to the monolayer, forming a new layer on top of it. In the -1/2 defects, the outflows are stronger than the inflows, which explains the frequent formation of holes at these locations, Fig.26b.

Fig.26. Active extensile units around the cores of (a) +1/2 and (b) -1/2 defects with the activity-driven velocity field **v**. The velocities are stronger along the director and weaker along the directions perpendicular to the director because of the anisotropic friction with the substrate. Modified from Copenhagen et al. [281].

V. MICROSWIMMERS IN NEMATICS

The motility of microorganisms such as bacteria and spermatozoa is a triumph of evolution. Their locomotion relies on peculiar strategies to overcome viscous drag at low Reynolds number [11,12,423,424] when the inertia forces are negligible and inspires the development of biological and artificial microbots for technologies of the future such as microscale fabrication, manipulation, delivery, and controllable quorum sensing. Ideally, these microbots should be able to propel along a predesigned trajectory and perform useful work, for example, by transporting cargo.

Prior research primarily focused on isotropic environments, such as water and water-based solutions, a habitat of most living microorganisms [425-428]. In isotropic fluids, the swimming of micro-organisms is typically chaotic, making it difficult to extract useful work and design trajectories. A sense of direction could be set by gradients of nutrients. Unfortunately, gradients are transient and therefore not reliable for directing long-term transport and sustained work. Other channels of communication, such as visual or audio cues, are currently not practical when dealing with microorganisms, with rare exceptions such as photon-powered strains of motile *Escherichia Coli* bacteria [429]. Similar problems with commanding dynamics arise for artificial microparticles, such as Janus spheres and rods: their propulsion in an isotropic fluid, being ballistic at short time scales, becomes chaotic Brownian-like once the orientational diffusion erases the memory of direction [5,427,430]. At time scales shorter than the time of realignment by orientational fluctuations, the motion is directional, but at longer time scales, it becomes diffusive

with zero net displacements [431]. Such an enhanced Brownian motion is reported for active disk-like droplets of microtubules [273] and *E. coli*-containing water droplets in an isotropic oil [432]. Extraction of work from isotropic active matter could be helped by asymmetric surface interactions. For example, asymmetric ratchet gears would rotate unidirectionally when placed in a bacterial bath [425,428]. Extended directional propulsion was reported for microscopic tori chemically activated by hydrogen peroxide and interacting electrostatically with charged substrates [433].

In order to control microscale dynamics through the bulk rather than surface interactions, one could use LCs as a structured anisotropic fluid environment. Sections I and II already demonstrated that LCs enable new mechanisms of propulsion of inanimate objects such as directrons and colloids, while Sections III, IV described dynamic topographies of LCE elastomers and tissues. In this section, we consider two settings in which an LC guides microswimmers: individual bacteria swimming independently of each other in a lyotropic LC (subsection 5.1) or in a collective fashion (subsection 5.2) and droplets of bacterial dispersions placed in an immiscible thermotropic LC (subsection 5.3).

5.1. Individual bacterial swimmers in liquid crystals.

Embedding living organisms into LCs of thermotropic type is problematic since these are oil-like and hydrophobic. Not suitable are also lyotropic LCs based on surfactants since surfactants could rupture membranes of living cells. Fortunately, there is a class of materials, the so-called lyotropic chromonic liquid crystals (LCLCs) [434,435], which are not toxic to living organisms [436]. LCLCs form in aqueous dispersions of disk-like organic molecules with a flat polyaromatic core and polar periphery. Once in the water, the molecules stack on top of each other, forming elongated cylinders, thus shielding their hydrophobic cores from water and leaving the polar group at the cylinder-water interface [434,435], Fig.27a. The term “chromonic”, introduced by Lydon [434,437,438] bears connotations to chromosomes (named so since they can be stained by dye molecules that intercalate DNA; many dyes form LCLCs) and disodium cromoglycate, DSCG, one of the most studied LCLCs. DSCG forms a nematic phase at room temperatures and concentrations in the range 0.3-0.45 mol/kg [435], or 12.5-18 wt%. Upon heating, DSCG dispersion experiences a phase transition from the nematic to an isotropic state, first forming a

broad biphasic region (of width 4-9 ºC, depending on concentration) of the coexisting isotropic and nematic phases [439], then a homogeneous isotropic phase. Water solutions of orientationally ordered DNAs can also be used as a nontoxic LC environment for bacteria [440].

Fig.27. Living liquid crystal: (a) A lyotropic chromonic liquid crystal (LCLC) formed by stacks of organic disc-like molecules serves as (b) a guiding medium for (c) flagellated microswimmers *B. subtilis*; (d) at low concentration of bacteria, their trajectories are parallel to the director field; at higher concentrations, an undulation instability develops. PolScope image in part (c) modified from Zhou et al. [276]; phase contrast microscopy texture in part (d) modified from Koizumi et al. [221]. The probability of swimming from left to right and from right to left are equal to each other since the director is apolar.

When placed in the nematic phase of DSCG, elongated flagellated bacteria, such as *Escherichia coli* (*E. coli*) [441], *Proteus mirabilis* (*P. mirabilis*) [442-444], and *Bacillus subtilis* (*B. subtilis*) [276,445] all preserve their ability to swim, although to a different degree [444,445]; see a recent review by Zhao et al. [446]. All three types of bacteria are of similar geometry. For example, *B. subtilis* studied by Zhou et al. [276,445] has a rod-like head of length $L = 4 - 7\mu\text{m}$ and diameter 0.7-1 μm, to which six or more flagella are attached, each of a length 6-20 μm and a cross-sectional diameter 20 nm. A flagellum is of a stiff left-handed helicoidal shape. Hydrodynamic attractions among flagella produce a single polar rotating bundle posterior to the swimming organism [447]. The helicoidal shape of the bundle produces a thrust force [12]. A swimming bacterium is thus an extensile active unit. The thrust force f_{th} measured for various bacterial species with peritrichous flagella varies broadly, depending on the species and the work load of the rotary motor. Under a light load, such as free swimming in water, for *E. coli*, $f_{th} \approx 0.5\ pN$ [448-450], while under a heavy load, i.e. when the bacterium is stalled by obstacles, one expects $f_{th} \approx 5\ pN$ [451-453]. The thrust is balanced by a viscous drag force, so that a swimming cell represents an extensile "force dipole" of a length $l_D < L$, estimated for *E. coli* to be about 2 μm [448].

A bacterium such as *B. subtilis* and *E. coli* swimming in an isotropic or a nematic environment generates a hydrodynamic force dipole pattern [276,445,454]: the surrounding fluid is pushed away from the bacterium along the axial direction and pulled towards the bacterium along the two perpendicular directions, Fig.27b. When a bacterium swims in a birefringent LCLC, the rotating

bundle of flagella perturbs the director, Fig.27c. Since the director is also the optic axis, the perturbations of the LCLC become visible under a polarizing optical microscope as a periodic wave with a pitch 2 μm. *B. mirabilis* in the studies by Mushenheim et al. [442-444] are somewhat shorter than *B. subtilis*, with the head about 3 μm long. Typical velocities in the nematic phase of DSCG range from ~3 μm/s for *E. coli* [441], to 8 μm/s for *B. mirabilis* [444] and 8-15 μm/s for *B. subtilis* [276,445].

The director $\hat{\mathbf{n}}_0$ of an LCLC environment, either uniform [276,440,441,443,444], or spatially distorted [215,221,272,276,374,443,455], serves as an easy swimming pathway for bacteria when their concentration is below some critical value, Fig.27d. The main reason is the surface anchoring of the bacteria by a surrounding LCLC that aligns the rod-like swimmers parallel to $\hat{\mathbf{n}}_0$, although anisotropy of viscous drag should not be disregarded: motion parallel to $\hat{\mathbf{n}}_0$ usually meets a weaker viscous resistance than motion perpendicularly to $\hat{\mathbf{n}}_0$ [38]. When the bacteria stop swimming (e.g., when the supply of oxygen is reduced), their rod-like bodies are parallel to the local director $\hat{\mathbf{n}}_0$, which suggests a tangential or unidirectional planar anchoring direction, the so-called easy direction [276,440,444]. A perpendicular (homeotropic) alignment would align the rod perpendicularly to $\hat{\mathbf{n}}_0$. Alignment along $\hat{\mathbf{n}}_0$ is usually explained by the models developed by Brochard and de Gennes [456] and by Smith and Denniston [457], of a thin rod tilting in an otherwise uniform nematic. The crucial assumption is that the rod imposes an infinitely strong unidirectional surface anchoring of $\hat{\mathbf{n}}_0$ parallel to the rod's axis. In this case, a rod of a length l and a radius r, realigned by an angle φ away from $\hat{\mathbf{n}}_0$, experiences a restoring elastic torque $\tau_{el} = \varphi CKl$, where $C = 4\pi/\ln(2l/r)$ [457]. For the typical $K = 10$ pN, $l = 8$ μm, $r = 0.4$ μm, one finds $\tau_{el}/\varphi \approx 3 \times 10^{-16}\ N \cdot m$. On the other hand, the bacterium is capable of producing a realigning torque $\tau_{bact} \approx f_{th} l_D \varphi$. The product $f_{th} l_D$ is in the range $\tau_{bact}/\varphi \sim (1-10) \times 10^{-18} N \cdot m$. Therefore, $\tau_{el} / \tau_{bact} \approx 30-300$, i.e., the elastic torque, calculated by assuming an infinitely strong anchoring at the bacterium's body, appears to be prohibitively high to allow the bacterium to realign.

However, experiments by Zhou et al. [458] on swimming *B. subtilis* in a homeotropically aligned LCLC with $\hat{\mathbf{n}}_0$ perpendicular to the bounding plates show that the bacteria can realign the director by 90° and swim in the plane of the cell, thus exploring regions richer in oxygen and nutrients. The experiments were performed in cells of a thickness larger than the length of the

bacteria. In similar experiments with anomalously long *B. mirabilis,* $L = (10 - 60)$ μm, placed in the homeotropic cells of thickness 10 μm, the bacteria also swim in the direction perpendicular to $\hat{\mathbf{n}}_0$, with the velocity about 1.5 times smaller than the velocity parallel to $\hat{\mathbf{n}}_0$ in the planar cells [443], a manifestation of anisotropic viscous drag in LCs.

Swimming perpendicularly to the imposed director field suggests that the assumption of an infinite surface anchoring at the bacterium-LCLC interface leads to an overestimated stabilizing torque. To find a more realistic estimate, assume that the easy axis is parallel to the axis of a rod, but the surface energy penalty for a tilt by φ from this orientation is finite, $\frac{1}{2}W\varphi^2$ per unit area, where W is the anchoring strength coefficient, usually on the order of $W \sim 10^{-6} Jm^{-2}$ for LCLCs [459,460]. The stabilizing anchoring torque is then only $\tau_W/\varphi = 2\pi rlW \sim 2 \times 10^{-17} N \cdot m$, comparable to the bacterial torque, $\tau_W/\tau_{bact} \approx 2 - 20$. As demonstrated by Tasinkevych *et al.* [461], the stabilizing torque becomes even smaller if the alignment at the surface is tangential, i.e., degenerate in the local plane of the interface. Even if the surface in contact with an LCLC is unidirectionally treated (say, rubbed), the azimuthal anchoring energy is very weak, only about $W \sim 0.3 \times 10^{-6} Jm^{-2}$ [462]. Therefore, the dynamics of bacteria in LCLCs allows much richer dynamic scenarios than a simple following of the director, which includes the director's realignment by the bacteria, an effect especially pronounced in the collective behavior at high activities considered in the next section.

Swimming of the rod-like bacteria parallel to $\hat{\mathbf{n}}_0$ is intuitively clear because of the rod-like shape of the microorganisms. A theoretical model by Lintuvuori et al. [186] suggests that in the case of spherical swimmers, the hydrodynamic coupling between the flow field and the director realigns the swimmer so that the preferred swimming direction of a pusher is parallel to $\hat{\mathbf{n}}_0$, while the pullers move perpendicularly to $\hat{\mathbf{n}}_0$. Chi et al. [463] extended this model to swimmers of an elongated shape: When the parallel surface anchoring at the body of an elongated puller is sufficiently strong, it will swim parallel to $\hat{\mathbf{n}}_0$ [463]. Daddi-Moussa-Ider and Menzel [464] identified regimes when the hydrodynamic interactions between pushers/pullers and the surrounding nematic could produce oblique orientation, also recovering the predominant mode of swimming of pushers parallel to $\hat{\mathbf{n}}_0$, and pullers perpendicularly to $\hat{\mathbf{n}}_0$, when the viscous resistance along $\hat{\mathbf{n}}_0$ is lower than in the perpendicular directions. Interestingly, if the viscous resistance for a direction parallel to $\hat{\mathbf{n}}_0$ is higher than for other direction, the modes are reversed, and the pushers

would swim perpendicularly to $\hat{\mathbf{n}}_0$ [464]. It is suggested that such a change of scenery could be observed in nematics formed by discotic units, as opposed to calamitic nematics formed by rod-like units [464]. Note here that the theoretical models of microswimmers treat the nematic fluid mostly as a thermotropic material such as 5CB. Rheological properties of the bacteria-compatible lyotropic nematics such as DSCG explored recently [465-469] are somewhat different.

Nematic anchoring and elasticity modify the behavior of motile bacteria not only in the sense of helping them to select the direction of motion but also by promoting aggregation. *B. mirabilis* often dynamically assemble end-to-end into moving chains, either in the bulk [444] or at the nematic-isotropic interface [442]. The separation between two bacteria is rather small, about 0.3 μm. Immobilized versions of *B. mirabilis* aggregate irreversibly, but the motile chains can dissociate back into monomers [444]. The *B. mirabilis* chains in the nematic bulk are slightly tilted with respect to the far-field director [444], as expected for the equilibrium chain of elastically interacting elongated (ellipsoidal) particles with tangential surface anchoring [470].

B. subtilis in similar planar cells of DSCG interact differently from *P. mirabilis*. Instead of the end-to-end aggregation, they exhibit transient parallel alignment side-by-side with synchronization of their velocities [445]. The side-by-side attraction of swimming pushers is known for isotropic media [471]. In the nematic, the alignment and synchronization are likely enhanced by the dynamic elastic director pattern. The bacterium in motion creates director distortions that might be so strong that the nematic experiences a local transition into an isotropic state when the temperature of the sample is close to the clearing point [276]. In the general classification of colloid-induced distortions in nematics, proposed by Pergamenshchik and Uzunova [472,473], the type closest to the geometry of a swimming bacterium is the so-called chiral z-dipole. The z-component is associated with the bend and the chiral part with both twist and bend. Two parallel bodies of a characteristic width ω, with the shape of chiral z-dipoles, placed side-by-side in a nematic LCLC at a distance interact through the elastic potential $U = 12\pi K\tilde{\lambda}^2\omega^2\left(\tilde{C}^2 - \tilde{\gamma}^2\right)/d^3$, where $\tilde{\lambda}\omega\tilde{C}$ is the chiral strength and $\tilde{\lambda}\omega\tilde{\gamma}$ is the strength of the z-dipole; $\tilde{C}$ and $\tilde{\gamma}$ are shape-dependent numbers, of the order of 0.1-10, and $\tilde{\lambda}$ is the chiral pitch. For $\tilde{\lambda} = 2\ \mu\mathrm{m}$, ω =1 μm, d=2 μm, the estimate is $U = 2 \times 10^{-17}\left(\tilde{C}^2 - \tilde{\gamma}^2\right)$ J, potentially many orders of magnitude higher than the thermal energy 4×10^{-21} J and comparable to or larger than the torque of the flagellar motor ($\sim 10^{-17} - 10^{-18}$ J). The interaction can be either attractive or

repulsive, depending on the sign of $\left(\tilde{C}^2 - \tilde{\gamma}^2\right)$, thus bacteria of even a somewhat similar shape might show very different LC-mediated interactions [204].

The velocity of the bacteria in the nematic DSCG is not much smaller than the velocity in water, by a factor of about 1.5, 14 μm/s vs. 21 μm/s [445]. This relatively small difference comes as a surprise since the twist and splay viscosities of the nematic DSCG are about three orders of magnitude higher than the viscosity of water [276]. The standard model of bacterial swimming in an isotropic Newtonian fluid is based on the difference in the effective drag coefficients $\xi_{||}$ and $\xi_{\perp}$ for the parallel and perpendicular displacements of the flagellar bundle [11]. In the nematic environment, the difference in drag coefficients for the parallel and perpendicular displacements is enhanced by anisotropy of the medium. For a diffusive motion of spheres, the ratio $\xi_{||}^{LC}/\xi_{\perp}^{LC}$ can change in a broad range, from 1.1 to 2.5 [31,474]. Therefore, the anisotropy of the nematic might help the bacteria to swim [445]. Elasticity of the nematic is another potential enhancing factor. In isotropic fluids, bacterial velocity is often detrimentally affected by wobbling: the axis of the cell's body is tilted by some angle away from the flagellar axis and the direction of propagation[475]. As already discussed, the nematic environment imposes a torque that tends to align the rod-like head parallel to the overall director, thus decreasing the wobbling angle and keeping the speed high. The problem awaits its further exploration.

Dynamic distortions of the director can be used to measure the frequency of the flagella bundle rotation in an LCLC, which turns out to be in a range 6-20 Hz. The head rotates about 7 times slower and in the opposite direction. The translational velocity v of the bacteria shows a linear dependence on the frequency of flagella's rotation, and is about two times smaller than the phase velocity v_f of the flagella wave. In contrast, in the isotropic fluid, $v/v_f \approx 0.1$. The difference suggests that the fluid flow created by a bacterium in the LC does not spread much around the bacterial body, being instead localized close to the bacterial trajectory. The reconstructed flow patterns around *B. subtilis* support this conclusion [445]. Cargo transportation also confirms the concentrated character of flow. When there is a small colloidal particle in front of *B. subtilis*, the bacterium pushes this particle forward over a long distance, sometimes by hundreds of micrometers [445]. The particles start to move when the distance to the bacterium is as large as 50-80 μm. If the particle is off the bacterial trajectory by only a few micrometers, the bacterium swims over without picking it up. *B. mirabilis* also shows an ability to transport cargo

along the unidirectional path or even along a complex patterned director [476]. This ability can be enhanced when the director field is patterned to condense the bacteria into polar "jets", to be discussed later [374]. Analytical description of the flows around a bacterium swimming in a nematic is available for the case when the bacterium is considered as a force dipole (a so-called stresslet flow), the surrounding director is uniform (no anchoring at the bacterium body), and the leading contribution to the viscous resistance is by the isotropic term with the Leslie coefficient α_4 [477]. The flow velocity decays with the distance to the swimmer as $\sim\frac{1}{r^2}$, while the tilt of the dipole with respect to the director modifies the polar and azimuthal angles dependence of the flows [477].

The discussion above refers to a situation when the bacteria could swim in a bidirectional manner: since $\hat{\mathbf{n}}_0 \equiv$-$\hat{\mathbf{n}}_0$, there is no net flow on average in a uniformly aligned sample, Fig.27b. To rectify the motion, in a clever experiment by Mushenheim et al. [443], two opposite plates of the LCLC cell were treated for antagonistic surface alignment, perpendicular at one plate and planar at the other plate. This director field, resembling a rounded capital letter L, implies a polar character of the director projection $\hat{\mathbf{n}}_{xy} \neq -\hat{\mathbf{n}}_{xy}$ onto the plane of the cell. As a result, bacteria preferentially swim from the top to the bottom along the "L" – shaped director lines, thus setting a unipolar mode of swimming in the plane of the cell.

The theoretical treatment of bacterial swimming in an LC is difficult since the presence of active units needs to be accounted for in the elastic, anchoring, and hydrodynamic responses. The mentioned models of swimmers in an LC [186,458,463,464] show that the balance of hydrodynamic and anchoring torques can produce different directions of swimming. Krieger, Spagnolie, and Powers [478] considered the so-called Taylor's swimming sheet, a 1D swimmer with a small-amplitude wave of either transverse or longitudinal type, placed in a 2D hexatic LC. A hexatic LC captures the essential properties of a nematic, such as Frank elasticity, rotational viscosity, and surface anchoring. The results show that the swimming efficiency and speed depend on the Ericksen number $\mathrm{Er} = \eta v R/K$ and the de Gennes-Kleman anchoring extrapolation length K/W. For example, for transverse waves with weak anchoring, the swimming velocity decreases as Er becomes higher.

Once the concentration of microswimmers increases above some threshold so that they start to interact with each other hydrodynamically, the interaction with the surrounding LC

medium leads to new dynamic phenomena, such as a transition from apolar swimming along $\hat{\mathbf{n}}_0 \equiv -\hat{\mathbf{n}}_0$ to polar collective swimming.

5.2. Activity-triggered transition from a uniform passive nematic to undulations and topological turbulence.

In dense isotropic aqueous dispersions of bacteria, with a concentration 10^{15} - 10^{16} m^{-3} (with typical distances between the bacteria on the order of 10 μm or less), one observes spectacular collective effects of bacterial "turbulence", with vortices and jets [479-484]. Theoretical modeling of these dense dispersions [484-486] suggests that the overlapping hydrodynamic force dipoles destabilize mutual alignment with neighboring bacteria, making parallel swimming unstable. The low-Reynolds number turbulence [479-483] (also called "topological turbulence" when nucleation of topological defects is involved [487]), is a general property of active matter, triggered by active stresses generated by energy-consuming self-propelling units [227,380,484,488-492].

In a particular case of active nematics, such as dense dispersions of extensile microtubule bundles [273,493,494], epithelial tissues [340], and living LCs [276], the active stresses destabilize the underlying orientational order, competing with the elastic stresses, confinement limitations [495] such as no-slip condition [496], viscosity of an adjacent medium [497], surface anchoring [498], or external fields [493]. Below we consider a transition of a living LC from a zero-activity uniform nematic to high-activity topological turbulence, which starts with the development of undulations, Figs.27d and continues with nucleation of $\pm 1/2$ defects, Fig.28 [276]. Living LCs offer a unique possibility to control independently the activity and orientational order, which is important since the balance of the two has been at the heart of the active matter science, starting with the Vicsek model [220,312,499] and Toner-Tu theory [500].

B. subtilis is an aerobic bacterium, the motility of which is controlled by the amount of dissolved oxygen [501]. Bacteria stop swimming when there is not enough oxygen. The immobilized bacteria align with their elongated bodies parallel to $\hat{\mathbf{n}}_0$, Fig.28a. The mixture of LCLC with dormant bacteria behaves as a regular equilibrium LC, with the uniform director $\hat{\mathbf{n}}_0(\mathbf{r}) = const$, specified by the surface treatment in the planar state. Any fluctuative deformation of the director would relax to the uniform state because of the orientational elasticity. In the

experiment by Zhou et al. [276], the dormant bacteria were transformed into active swimmers by an influx of oxygen. Once the bacteria start swimming and find themselves close to each other, they interact hydrodynamically. The hydrodynamic force dipoles of the two neighboring bacteria produce a net component perpendicular to $\hat{\mathbf{n}}_0$, thus enhancing any fluctuative bend, Fig.28b,c (but not splay; splay fluctuations would be enhanced by contractile units [3,227]). The destabilizing hydrodynamic torque $\sim\beta c f_{th} l_D \varphi$, where $\beta \sim L/h$ is a dimensionless parameter that depends on the cell thickness h, is balanced by the stabilizing elastic torque $\sim K\frac{\partial^2 \varphi}{\partial x^2}$ and by the anchoring at the bounding plates, which we neglect here. The elasticity-activity balance establishes an undulation period $\xi = \sqrt{K/\beta c f_{th} l_D}$, which decreases with the increase of the activity parameter cf_{th}, Fig.28b,c. For typical $cf_{th} l_D = 10^{-3}\mathrm{N}\cdot\mathrm{m}^{-2}$, $K = 10$ pN, $\beta = 1$, one estimates $\xi = 100$ μm, close to the experimental data [276], despite the fact that the estimate neglects the stabilizing torque of the planar director anchoring at the bounding plates.

A detailed experimental exploration of the undulation instability has been recently reported by Chandrakar et al. [496] for the extensile microtubules bundles placed in channels of a well-defined cross-section. The material is shear-aligned and left to relax; active stresses produce undulations. The wavelength ξ of the undulations is approximately constant, while the amplitude grows with time, first exponentially, then linearly. The undulations occur in the plane that is normal to the channel's shortest extension. The active stress must exceed some threshold for the undulations to develop. A larger opening increases ξ. In particular, for a rectangular cross-section with height H and width W, the dependence is $\xi = 2\left[\frac{1}{\pi l_a L} - \frac{1}{L^2}\right]^{-\frac{1}{2}}$, where $L = \left[\frac{1}{W^2} - \frac{1}{H^2}\right]^{-\frac{1}{2}}$ and l_a is the active length scale dependent on the activity strength, elasticity, and viscosity of the medium.

If the active component is of a puller type, one would expect an instability of the splay type [3]. Voituriez et al. [498] considered an analog of the Frederics transition in a planar cell of an active polar film of a contractile (puller) type; surface anchoring keeps the polarization vector parallel to the plates. If the activity is low, the film preserves its uniform static polar order; as the activity (or the cell thickness) increases above some threshold, the orientation in the center of the cell becomes progressively tilted, which implies splay, and the system flows. A homeotropic cell of an extensile (pusher) type should show a similar active Frederiks transition, of the bend type.

Fig. 28. Development of nonequilibrium regimes in a living liquid crystal, following the experimental data by Zhou et al. [276]: (a) equilibrium state, dormant bacteria; (b,c) bend instability, with the period ξ decreasing as activity increases; hydrodynamic interaction of bacteria in close proximity to each other produces an active force **f** that enhances a fluctuative bend; (d) nucleation of $m = \pm 1/2$ disclination pairs of the B-type, see Fig.21d; +1/2 cores move away from -1/2 cores; (e) topological turbulence. Swimming bacteria of pusher type are shown as rods with two arrows.

As the activity increases beyond the undulation regime, the stripe pattern becomes unstable against nucleating pairs of ±½ disclinations, Fig. 28d, and transitions to chaotic dynamics of topological turbulence. As a rule, the nucleating defect pairs are of the B-type, Fig.21d, with the line that connects the cores being initially orthogonal to $\hat{\mathbf{n}}_0$. The dynamic pattern of nucleating and annihilating disclinations, Fig.28e, is globally isotropic, with the aligning action of the substrates being lost. The elastic energies of undulations and disclinations depend differently on the characteristic length scales. The elastic energy per unit area of well-developed undulations, in which the tilt angle is substantial, $\varphi \sim 1$, Fig.28d, scales as $F_{wall} \approx K/\xi r_{wall}$, where r_{wall} is the curvature radius at the wall separating "zigs" and "zags" of the periodically realigning director. In contrast, the energy per unit area of an array of $\pm 1/2$ disclinations scales as $F_{\pm 1/2} \approx K\, ln(\xi_d/r_c)\, /\xi_d^2$, where r_c is the core radius of the disclination; within the core, the scalar order parameter changes substantialy [38]. When r_{wall} approaches r_c from above, the stripes start to resemble singular walls with the a raising energy density. The elastic stress at the walls can be released by nucleating pairs of disclinations, since the ratio

$$F_{\pm 1/2}/F_{wall} = \xi r_{wall}\, ln(\xi_d/r_c)\, /\xi_d^2 \tag{22}$$

becomes smaller than 1 when r_{wall} decreases to about $\xi / ln(\xi/r_c)$. The turbulent dynamics of disclinations at small Reynolds number is a general phenomenon in active matter, observed in experiments with active gels of microtubules [273] and in numerical simulations of active nematics, see, for example, [379,502-504].

5.3. Rectification of swimming in patterned living liquid crystals.

The onset of a force component perpendicular to the director field in Fig.28b,c suggests that the LC background could be predesigned to guide microswimmers along the directions

different from $\hat{\mathbf{n}}_0$, and, most importantly, rectify the motion into polar flows [215,221,374]. Consider a vortex defect of strength +1, in which the LCLC director spirals from the center towards the periphery forming an angle $\phi_0 = 25^o$ with the radial directions, $\hat{\mathbf{n}}_0 = (n_r, n_\varphi, 0) = (\cos\varphi_0, \sin\varphi_0, 0)$, Fig.29a. At low concentrations, *B. subtilis* microswimmers follow the director, swimming towards the center of the vortex and then leaving it; there is no net flow, Fig.29b. As the number of bacteria increases, some of them follow loop trajectories that circumnavigate the core of the vortex, Fig.29c. At concentrations above $c \approx 7 \times 10^{12} m^{-3}$, which corresponds to the volume fraction $\Phi \approx 2 \times 10^{-5}$ and separation distances 50 μm, the bacteria form a complete circulating swirl, Fig.28d [445]. The circulation is unipolar, as dictated by the polarity of the underlying director vortex: Spirals with $\varphi_0 > 0$ cause a clockwise circulation, while patterns with $\varphi_0 < 0$ yield a counterclockwise circulation. The unipolar circulation occurs in all vortex patterns with $\varphi_0 \neq 0, \pi/2$. Note that the swimming trajectories make a large angle with the prescribed $\hat{\mathbf{n}}_0$, about 65° in Fig.29d [221].

Fig.29. Individual to collective swimming transition in a patterned LCLC. (a) Patterned director field with +1 spiral vortex, $\varphi_0 = 25^o$, directs the microswimmers *B. subtilis* (b) along the director at low concentrations; as the concentration increases, the bacteria (c) start to form loops around the vortex core and then (d) engage in unipolar clockwise circulation. Redrawn from Koizumi et al. [221].

Qualitatively, the collective polar circulation above the concentration threshold can be explained by hydrodynamic interactions mediated by the background director [215], as illustrated in Fig.30 for $\varphi_0 = -45^o$. Bacteria 1 and 2 in Fig.30a are separated by a large distance and do not interact with each other; these bacteria would swim parallel to the spiral director $\hat{\mathbf{n}}_0$, in and out of the vortex core. Bacteria 3 and 4 in close proximity to each other overlap their hydrodynamic force dipoles, yielding a net force **f** shown by the arrow pointing down in Fig.30a. In a similar fashion, bacteria 5 and 6 generate a net force **f** pointing upward. It is easy to see that the hydrodynamic interactions of all microswimmers should result is a circular counterclockwise active force, Fig.30b, triggering a counterclockwise bacterial swirling in Fig.30c,d. The active force can be calculated using Eq.(17) for "wet" active nematics [227,373], with a positive activity coefficient $\alpha = cf_{th}l_D > 0$ of the extensile *B. subtilis* swimmers. For the predesigned director $\hat{\mathbf{n}}_0 = \{n_r,\ n_\varphi,\ 0\} = \{1/\sqrt{2},\ -1/\sqrt{2},\ 0\}$ in Fig.30a, with the spiral angle $\varphi_0 = -45^o$, assuming $c =$

$const$, Eq. (17) yields $\mathbf{f} = \{0,\ \alpha/r,\ 0\}$ in the cylindrical coordinates, i.e., the active force is directed counterclockwise along the azimuthal direction; there is no radial component, Fig.30b [215,373]. The transition from the apolar nematic-like to polar dynamics in the expreiments with swimming bacteria [215,221,374], Figs.29-31, is caused by an increasing role of inter-swimmers interactions as compared to their interactions with the passive background.

Fig.30. (a) Patterned director field with $m = +1$ spiral vortex, $\varphi_0 = -45^o$, (b) directs the active force counterclockwise and causes (c) unidirectional counterclockwise swimming of a bacterial swarm condensed into a circular band; (d) bacterial velocity map. Redrawn from Peng et al. [215].

Coexisting and oscillating polar and apolar nematic dynamics mediated by the interaction of moving agents have been recently described for actomyosin motility assays [505,506] and solutions of filament-like particles [507-509]. It is suggested [505] that the type of ordering is a dynamic property of an active system. Theoretical modeling by Großmann, Aranson, and Peruani [509] suggests that the coexistence of polar and apolar nematic structures can be caused solely by self-propulsion of active units that interact in an apolar nematic manner.

Fig.31. Patterned director of an $m = +1$ spiral vortex with (a) $\varphi_0 = 25^o$, directs the active force (b) clockwise and towards the center, (c) causing the polar swirl of bacteria to shrink; in contrast, a vortex with (d) $\varphi_0 = 70^o$, directs (e) the active force and (f) unipolar swirls outwards. Redrawn from Koizumi et al. [221].

The above consideration of collective polar circulation can be generalized [221] to vortices of an arbitrary spiral angle, $\hat{\mathbf{n}} = \{\cos\varphi_0\,,\ \sin\varphi_0\,,\ 0\}$, in which case the active force

$$\mathbf{f} = -\alpha\{\cos 2\,\varphi_0, \sin 2\,\varphi_0, 0\}/r \tag{23}$$

shows a nonzero radial component $f_r = -\alpha\cos 2\,\varphi_0/r$ for any $\varphi_0 \neq \pm 45^o$. When splay dominates the deformation, $0 < \varphi_0 < 45^o$, the radial component points towards the center of the vortex; the condensed swarm of the bacteria in such a vortex would contract towards the center, Fig.31a-c. When $45° < \varphi_0 < 90°$, a predominantly bend deformation of the vortex expands the swarm towards the periphery since the radial component points outward, Fig.31d-f. In both cases, for positive φ_0, the azimuthal component $f_\varphi = -\alpha\sin 2\,\varphi_0/r$ is negative and directed clockwise.

The active force $\mathbf{f} = -\alpha\{\cos 2\,\varphi_0, \sin 2\,\varphi_0, 0\}/r$ characterizing the prepatterned vortices $\hat{\mathbf{n}}_0 = \{\cos\varphi_0\,,\ \sin\varphi_0\,,\ 0\}$ correctly predicts the most salient features of the experimentally observed dynamics of bacteria, such as polar circulation, contraction of swirls when $0 < \varphi_0 <$45° and their expansion when $45° < \varphi_0 < 90°$, as well as the absence of unipolar circulation in the case of pure splay, $\varphi_0 = 0$, and pure bend, $\varphi_0 =$90° [215,221], Fig.31. A more refined model that lifts the assumption $c = const$ yields similar results [221].

The concentration $c \approx 0.7 \times 10^{13} m^{-3}$ at which the individual apolar swimming transforms into collective polar swirling is much lower than the concentration $c \approx 10^{14} m^{-3}$ at which the undulation instability develops, Fig.27d. Undulations begin when the swirl attracts more bacteria so that their local concentration increases [215,221]. The undulating swirls develop protrusions and ruptures, through which some bacteria escape so that the concentration is lowered below the threshold value. The swirl then could reconstruct itself and continue a stable circulation until the next cycle of the concentration increase and decrease [221].

Sokolov et al. [510] described undulation instabilities of circular flows in a pendant droplet and a free film of a living LCs of *B. subtilis*. A small magnetically rotated particle creates circular flows that align the microswimmers along the azimuthal directions. Once the shear flow stops, the activity of bacteria develops director undulations. Unlike the situation with a uniformly aligned living LC, the circular structure forces the undulation period ξ to accommodate to the radial distance r since the number of undulation periods depends on r. The bending instability triggers strong radial flows [510]. Further development of instability produces pairs of $m = \pm 1/2$ disclinations. As in the case illustrated in Figs.28d,21d, the pairs are of type B, in which the director is along the line that connects the two cores; this line is along the radial direction, i.e., perpendicular to the circular alignment produced by the shear.

Director patterning can be used to construct not only polar circular flows of living LCs but also rectilinear flows. Figure 32a shows the pair of $m = \pm 1/2$ defects; the bacteria prefer to swim from the -1/2 defect towards the +1/2 defect, Fig.32b [215,272], in qualitative agreement with the map of the active force, Fig.32c.

The unidirectional propulsion is especially effective in C-stripe patterns with periodically alternating splay and bend $\hat{\mathbf{n}}_0(x, y, z) = \left[\cos\frac{\pi y}{L}, -\sin\frac{\pi y}{L}, 0\right]$, where L is the period [374]. The bacteria follow the director to the splay regions $y = 0, \pm L, \pm 2L, \ldots$ where they condense into polar

jets moving unidirectionally towards the positive end of the x -axis, i.e., their velocities $\mathbf{v}$ are biased towards the converging splay, $v_x > 0$, Fig.32c,d,e. In the bend regions, $y = \pm L/2, \pm 3L/2, \ldots$ the horizontal component of the bacterial velocity is zero, Fig.32e. The concentration of bacteria in jets is about 15 times higher than the average sample concentration $\langle c \rangle \approx 0.3 \times 10^{14}\ m^{-3}$. In contrast, bend regions produce no net flow and merely guide the bacteria towards the splay regions along the director lines, reversing the velocity of bacteria that accidentally swim towards the diverging splay [374]. If an individual bacterium happens to swim in the opposite direction, the diverging $\hat{\mathbf{n}}_0$ forces it to make a U-turn by swimming through the bend along $\hat{\mathbf{n}}_0$ and then joining a bacterial jet moving along the x -axis in the neighbouring splay region, Fig.32d,e.

Fig.32. Linear transport of *B. subtilis* microswimmers in patterned director fields: (a,b) bacteria swim from -1/2 defect towards the +1/2 defect; (c) splay-bend C-stripe pattern condenses bacteria into a polar jet that moves towards the converging side of splay along the *x*-axis; (d,e) array of C-stripes forms polar jets of bacteria in splay regions moving along the *x*-axis; bacteria that move against the jet are recycled by U-turns of the bend regions to swim from left to right. Experimental results by C. Peng (b) and T. Turiv (c-e). Redrawn from Peng et al. [215] and Turiv et al. [374].

The geometry of the one-dimensionally periodic splay-bend stripes resembles the hybrid aligned cell [443] that rectifies the apolar swimming of bacteria into unipolar swimming. The in-plane patterned director such as splay-bend stripes allows one to transport micro-cargo along a well-defined y -coordinate in the xy-plane of the cell, Fig.33 [374]. The splay regions that carry the bacterial jets and thus cargo could also be designed as curvilinear trajectories or combined with the hybrid alignment to push the jets closer to the substrate with a planar alignment. A similar hybrid aligned geometry with a piece of an active nematic enclosed by a boundary has been proposed by Loisy, Eggers, and Liverpool [511] as a self-propelled active droplet. The active force, Eq.(17), produces antiparallel flows in the splay and bend regions that yield a center-of-mass velocity $\overline{v} = \frac{\alpha L}{4\pi\eta}$, where L is the drop's height, η is the viscosity of the active fluid. The internal velocity profile is $v_x = -\overline{v}\cos\left(\frac{2\pi y}{L}\right)$, with y being the distance to the substrate [511], which is different from the velocities of bacteria in Fig.32e, in which $v_x = 0$ in the bend region $y = L/2$.

Splay and bend affect differently many aspects of orientationally ordered active systems. Shrinking of circulating bacterial swirls towards the core of vortices with prevalent splay, Fig.31a-c, expansion of swarms in vortices with a prevalent bend, Fig.31d-f, and condensation of microswimmers into polar jets in splay regions, Figs.32,33, show the differences when the splay and bend are imposed externally. There are also intrinsic effects. As already mentioned, a system of pushers, such as the swimming bacteria, at weak levels of activity develops bend instability [3,227,276], while pullers are expected to develop splay deformations [3]. Simulations [282,512,513] predict that a medium-level activity triggers more complex distortions, such as "kink walls" [512] in which the director field resembles rows and columns of letters "C". In these kink walls, splay (at the ends of C's) and bend (in the middle of C's) coexist and alternate with each other in a plane of the sample. It was also demonstrated [278,514] that the effective splay and bend elastic moduli are renormalized by activity.

Fig.33. Cargo transport by a rectilinear bacterial jet condensed and guided by (a) splay-bend stripe; (b,c) optical microscope images taken 48 s apart of a cargo train of six 5 μm glass spheres transported by the bacterial jet. The particles are relocated from left to right by the incoming unidirectional bacterial flow. (d) Mean squared displacement (MSD) of a single 5 μm glass sphere being transported by a bacterial jet. Redrawn from Turiv et al. [374].

As discussed above, LCs as a swimming medium enable active units to transport cargo [374,445,476], the ability hard to replicate in an isotropic medium [448]. Trivedi et al. [476] demonstrated that motile *P. mirabilis* could push non-motile fungus cells *C. albicans* along the director of the nematic LCLC based on 15wt% of a water dispersion of DSCG. This effect is important since motile microorganisms could be used to translocate non-motile cells in order to increase their survival and adaptation [515,516] or to navigate through toxic environments [517]. The study [476] suggested a pathway of measuring the mechanical strength of microswimmers by changing the size and shape of the passive load, which might be advantageous over the conventional tethering assays approach [518].

The qualitative consideration of the active force in Eq.(17) does not account for spatial variations of the bacterial concentration, activity, and scalar order parameter. In theoretical modeling, active matter is often treated as incompressible, with the active units as the only ingredient, filling the space fully. As a result, the predicted activity-triggered macroscopic flows involve the entire sample with all its material points. However, in real experimental systems, such as in Figs.29-33, there is often some space left for the passive background, which requires a more

refined theoretical modeling, already developed for the description of bacterial jets [374] and circulating swarms [221]. An intriguing example of a system with strong segregation of active and passive components [519] is a dispersion of active microtubules in a passive aqueous buffer in a volume proportion 1:1000. As shown by Wu et al. [519], when such a dilute, globally isotropic active fluid is confined into a macroscopic 3D channel, it flows in the absence of any external pressure gradients, thanks to the formation of a thin active nematic wetting layer at the bounding surface; the bulk remains isotropic. The concentration of active microtubules in this system is obviously nonuniform.

5.4. Propulsion of active droplets.

Swimming at a microscale, which implies a low Reynolds number, is challenging because viscosity overcomes inertia. Purcell described the specific modes of swimming at the microscale, among which is a rotation of a helicoidal flagellum, used by many motile bacteria such as *B. subtilis*, *E. coli*, *P. mirabilis*, and *Salmonella typhimurium* [423]. A continuous rotation allows long-range propulsion, but some bacteria often interrupt rectilinear "runs" by tumbling and selecting a new direction of swimming in order to find nutrients [449]. More symmetric bodies, such as a sphere, cannot sustain long-range directional propulsion in an isotropic environment. Spherical particles in an isotropic medium can exploit chemotaxis, i.e., propel in response to gradients of interfacial tension triggered by chemical reactions at the interface or by bulk gradients of chemicals such as surfactants. The gradients of the surface tension cause the so-called Marangoni flows inside and outside the droplet towards the higher value of the surface tension, thus moving the droplet [520-524].

The simplest arrangement in which spherical objects could swim persistently in a medium such as water without gradients of chemicals and microscopic active elements are three linearly linked spheres [525] or two spheres connected by a tube that allows transport of mass [526]. In the first case, the links expand and shrink periodically in a nonreciprocal fashion, which breaks the time-reversal symmetry as well as the translational symmetry. In the second case, the 'pushmepullyou" spheres propel by changing their volume and separation.

If the gradients of chemicals and mechanically adjustable connectors are not available, spherical or 2D circular droplets could move if their interior contains active units [511,527-537].

Activity in confined volumes could produce macroscopic flows, such as circular rotation [538-542]. Reigh et al. [543] demonstrated theoretically that a single swimmer placed in a droplet of comparable size and dispersed in another fluid is capable of propelling the droplet. Huang et al. extended the modeling to multiple enclosed microswimmers [544]. Gao and Li described theoretically an interesting 2D active droplet containing extensile units arranged in a nematically ordered structure and placed in an isotropic environment [545]. Because of the intrinsic instabilities, the director field creates bend deformations and nucleates +1/2 and -1/2 defects of B-type in Fig.21d. Since the system is extensile, the +1/2 defect moves away from the -1/2 defect (the behavior opposite to the contractile elastomer in Fig.21b,d), and the droplet follows the direction of separation. As time goes by and exceeds the time or orientational diffusion of the structure, the whole director realigns, and the droplet redirects.

It turns out that a single spherical droplet could swim if placed in an LC; the two conditions are (1) active interior flows, generated, for example, by chaotically swimming micro-organisms, (2) asymmetric director structure of the LC outside the droplet [546]. The LC environment plays a dual role: it breaks the symmetry of the system enabling the propulsion and also directs the propulsion in a manner similar to liquid crystal-enabled electrophoresis powered by the external electric field [173,175].

The active droplets in Ref. [546] represent an aqueous dispersion of motile bacteria *B. subtilis*, either in water or in a water-based nematic LCLC, Fig.34. These droplets are dispersed in an inactive hydrophobic thermotropic nematic such as 5CB and stabilized by a small amount of a surfactant (lecithin). Lecithin sets $\hat{\mathbf{n}}$ of 5CB perpendicularly to the surface of the active droplets. To match the overall uniform alignment $\hat{\mathbf{n}}_0 = \text{const}$ of 5CB in the rest of a planar cell, each droplet acquires a satellite topological defect: either a point defect-hyperbolic hedgehog [179], already discussed in the context of electro-osmosis, Figs.10g,17, and electrophoresis, Figs.11,13, or an equatorial disclination ring resembling a Saturn ring [178,181], Fig.35. These states are abbreviated HH and SR configurations, respectively. The two differ dramatically in impact on the dynamics of active droplets. The HH-structure with a polar fore-aft asymmetric director deformation enables self-propulsion of the active droplets, by rectifying chaotic flows transferred from the active interior of the droplet to the inactive nematic environment. The SR of quadrupolar symmetry produces no net displacement, but once the SR shifts from the equatorial position towards one of the poles, the droplet becomes motile since the surrounding director field becomes fore-aft asymmetric, Fig.35.

The propulsive ability of the active droplets cannot be explained by the Marangoni effect associated with gradients of the interfacial tension, as droplets with a surfactant but no active bacteria show no rectified motility.

Fig.34. Active droplet with a bacterial *B. subtilis* dispersion (a,b) propels itself in a nematic 5CB; (c) director structure with a hyperbolic hedgehog outside the droplet; (d) displacement vs time: the droplet moves along the overall director field alignment, which is the x-axis. Redrawn from Rajabi et al. [546].

Fig.35. Propulsion ability of the active droplet depends on whether the director structure outside is a hyperbolic hedgehog or a Saturn ring. The Saturn ring of quadrupolar symmetry produces no net displacement. Redrawn from Rajabi et al. [546].

Particle image velocimetry (PIV) of fluorescent tracers (for the reviews of the PIV methods, see, for example, [547,548]) reveals that inside the active droplet, bacteria induce chaotic flows, with vortices that are poorly correlated in space and time, Fig.36a. The maps of interior velocity $\boldsymbol{v}_{in}$ and color-coded vorticity $\omega = \partial v_{\text{in},y}/\partial x - \partial v_{\text{in},x}/\partial y$ show no spatial correlations above distances $L_{corr} = (30 - 40)$ μm and times ~(2-3) s, Fig. 36a. The interior flows intensify near the droplet surface, in agreement with the expectation that active particles in confined volumes accumulate at the boundaries [549,550]. The flows are predominantly tangential to the interface but show no preferred direction of circulation. This behavior is different from steady counter-rotating circulations known for quasi-2D droplets [551].

The active flows transferred through the interface cause director realignment and flow of the nematic, Fig. 36b. Similar director realignment of a thermotropic nematic in contact with a bacterial aqueous bath was observed by Kim et al. [552]. The exterior flows extend over hundreds of micrometers. Unlike the interior flows, they yield a net flow, rectified by the polar HH-structure, Fig. 36b. In the droplet's coordinate system, the nematic flows from the hedgehog towards the droplet. In the laboratory system, it means that the active droplet self-propels with the hedgehog (or the shifted SR) leading the way.

The rectification of flows outside the active droplet is rooted in the well-known flow-director coupling that causes a non-Newtonian behavior and the so-called backflow, i.e., flow induced by director reorientations [38]. The director relaxation time is relatively long, as compared

to the correlation times inside the droplet, Fig.36a: $t_N \sim \eta_N a^2/K > 10$ s for the thermotropic nematic viscosity $\eta_N = 0.1$ kg m^{-1} s^{-1}, $K = 10$ pN and the droplet radius $a > 30$ μm, which means that the activity-perturbed director is persistently out-of-equilibrium, rotating and causing nematic backflows. An important feature of the nonequilibrium director-flow coupling is that the torque equation in the Ericksen-Leslie theory is not invariant under reversals of local velocities, $\mathbf{v}(\mathbf{r}, t) \rightarrow -\mathbf{v}(\mathbf{r}, t)$. Stark and Ventzki [553] presented a particularly clear illustration: the Stokes drag on a sphere with an HH-structure depends on whether the flow is towards the sphere or the hedgehog. Another example is directional pumping in a hybrid aligned nematic cell [554]. A plate that aligns $\hat{\mathbf{n}}$ perpendicularly to itself moves periodically right (+) and left (-) with respect to an immobile plate that aligns $\hat{\mathbf{n}}$ parallel to the shifts [554]. Although the shifts are not biased, simulations by Zhang et al. [554] reveal a directional volumetric flow rate Φ of the nematic, $\Delta\Phi/\Phi_0 = (|\Phi_-| - |\Phi_+|)/\Phi_0 \neq 0$, where Φ_0 is the flow rate of a Newtonian fluid under the same shear rate. The pumping direction depends on the rotation sense of the director from the bottom to the top plate [555] and on Er [554]. Defining Er through the instantaneous tangential speed $v_a \sim (0.1 \div 10)$ μm/s of the interior velocities that are transmitted into the nematic, one finds $Er = \eta_N v_a a/K \sim 0.1 - 10$. The simulations [554] show that rectification of the flow is most effective at these values of Er, achieving $\Delta\Phi/\Phi_0 \approx \pm 0.1$. Although the geometry of the one-dimensionally distorted hybrid aligned nematic is relatively simple, the emerging backflow behavior is so complex that asymmetric flows and quantities such as $\Delta\Phi$ could be found only numerically [553-555]; an analytic description is prohibitively difficult.

Fig.36. Active flows are (a) chaotic inside the droplet and (b) directionally rectified by the polar director configuration with the hyperbolic hedgehog outside the droplet; vorticity (shown by pseudocolors) and velocity (arrows) are averaged over 5 min in (a) and 10 min in (b); maximum velocity of flow is 1 μm/s in (a) and 0.2 μm/s in (b). (c) Scheme of the director distortions across the cell which contains an inactive droplet with a hyperbolic hedgehog on the right hand side (the core is shown by a black disk); the director realigns from being parallel to the *z*-axis to being parallel to the *x*-axis as one goes from the droplet to the bounding plates. Note the left-right structural asymmetry. (d) Self-propulsion mechanism of an active droplet with a hedgehog. Bacterial activity-created flows directed to the right, $\mathbf{v}_{a+}$, and to the left, $\mathbf{v}_{a-}$, perturb the left-right asymmetric director field differently, yielding two different director configurations $\hat{\mathbf{n}}_+(\mathbf{r}, t) \neq \hat{\mathbf{n}}_-(\mathbf{r}, t)$ and two viscous resistances $\eta_+ \neq \eta_-$, which result in the rectified active force f. Redrawn from Rajabi et al. [546].

The flow rectification by polar director deformations around active droplets is similar to that in Refs. [553-555]. Consider, for example, the regions above and below a droplet, Fig.36c, where the director is hybrid-aligned. In the absence of flows, $\hat{\mathbf{n}}$ rotates by 90° from a normal to the droplet's surface to $\hat{\mathbf{n}}_0 = (1,0,0)$, as one moves away by some distance $\geq a$. The location of the hedgehog fixes the sense of rotation. If the hedgehog is on the right, Fig.36c, $\hat{\mathbf{n}}$ rotates counterclockwise (CCW) above the droplet and clockwise (CW) below it. When the bacteria cause tangential flows and vorticity at the interface, these transfer into the nematic. As follows from Fig.36a, the bacterial flows are not biased: velocity of right and left flows along the interface in Fig.36c averaged over times longer than a few seconds, are of the same amplitude, $\langle |v_{a,+}| \rangle = \langle |v_{a,-}| \rangle = \langle |v_a| \rangle$. Although unbiased, these flows trigger a polar viscous response in the nematic. For example, below the droplet, a right impulse $\propto v_{a,+}$ imposes a CW torque on the CW-rotated $\hat{\mathbf{n}}$, while a left impulse $\propto v_{a,-}$ means a CCW torque on the same CW-rotated $\hat{\mathbf{n}}$, Fig. 36c. These two different combinations of the torque polarity and director rotation produce different out-of-equilibrium director $\hat{\mathbf{n}}_+(\mathbf{r},t) \neq \hat{\mathbf{n}}_-(\mathbf{r},t)$ [554,555] and thus different viscosities $\eta_+ \neq \eta_-$, Fig. 36c, since the viscosity depends on the director configuration. Mirror symmetry of the top and bottom regions of the sample with respect to the horizontal xy plane ensures the same polarity of the rectified flows in these regions, Fig. 36c.

The difference $\eta_+ \neq \eta_-$ yields a rectified propulsion force that can be estimated roughly as $f \sim CR\langle |v_a| \rangle (\eta_+ - \eta_-)$, where C is a numerical factor that depends on the slip conditions. Since the hedgehog leads the way, $\mathbf{f}$ is directed from the sphere towards the hedgehog. As self-locomotion is force-free, $\mathbf{f}$ should be balanced by the Stokes drag that can be estimated as $f_{drag} = C\eta_N R v$, where $\eta_N \sim 0.1$ kg m^{-1} s^{-1} is the effective viscosity of the nematic, which yields an estimate for the self-propulsion speed $v \approx \langle |v_a| \rangle (\eta_+ - \eta_-)/\eta_N$. With $\langle |v_a| \rangle \sim$(1-10) μm/s and $v \sim (0.1 - 1)$ μm/s, the required viscous anisotropy is modest, $(\eta_+ - \eta_-)/\eta_N \sim 0.01 - 1$, which is well within reach for thermotropic nematics [38,554]. Similar estimates can be obtained by considering the differences in the director field near the hedgehog and at the opposite pole of the droplet, where the director is close to uniform.

Propulsion of a sphere with an SR shifted from the equatorial location is explained similarly by the acquired polar character of the director field, which sets $\eta_+ \neq \eta_-$ and rectifies directional flows around the sphere. When the SR shifts to one of the poles, Fig.35, the director structure above

and below the droplet becomes similar to the pattern in Fig.36c. The shifts of SR are caused by the flows transferred from the interior to the exterior. Numerical simulations by Gettelfinger et al. [556] predict that the nematic flow could shift the SR around the fluid droplet along the direction that coincides with the flow, provided the Eriksen number $Er = \eta_N v_a R/K$ exceeds ~10. With the typical estimates for Fig.35, η_N~0.1 kg m^{-1} s^{-1}, $K = 10$ pN, $a = 50$ μm, the instantaneous velocities of flows that could shift the SR, should exceed $|v_a|$~20 μm/s, which appears to be an achievable value.

To propel in the nematic environment, the active drop should be larger than some critical diameter, about 30 μm, apparently because the number of bacteria in small droplets is not sufficient to produce strong flows. Another factor diminishing the self-locomotion ability of small droplets might be the steeper decrease of surface anchoring energy ($\sim Wa^2$) as compared to bulk elasticity of the nematic ($\sim Ka$), which prevents the formation of a strongly polar director deformation.

The demonstrated mechanism of droplet propulsion adds to the set of principles of microscale swimming described by Purcell [423] for isotropic Newtonian fluids, in which the simplest swimmers are either three identical spheres connected by slender rods of changing length [525] or two connected spheres exchanging material between themselves [526]. In the nematic environment, thanks to orientational order and associated surface anchoring and elasticity, the simplest swimmer is a single sphere that produces a polar director distortion in its neighborhood. It acquires mobility by rectifying the chaotic internal motion in the asymmetrically ordered environment. The dependency of self-propulsion speed $v \approx \langle|v_a|\rangle(\eta_+ - \eta_-)/\eta_N$ on the difference in the viscous coefficients underscores the non-Newtonian and anisotropic nature of the propulsion mechanism. Further research should explore whether an orientationally ordered nematic interior with dynamic distortions and disclinations modeled recently [540] could contribute to the propulsion.

The concrete examples of the underlying director field controlling individual and collective behavior of rod-like microswimmers, Figs.27-33, and of LC rectifying chaotic flows into directional propulsion of an active droplet, Figs.34-36, are based on swimming *B. subtilis*, but similar effects are expected for any active entities, such as artificial microswimmers powered by chemical energy, heat or light [557-559], and bio-artificial hybrids [560]. The LC-rectified motion of microswimmers and active droplets adds to the growing list of physical effects enabled by a

replacement of an isotropic medium with an LC [204,552,561,562]. The theoretical works on swimming in a nematic [186,464,477,563] suggest that the LC environment offers a broad range of possibilities to control microscale dynamics, by means such as surface anchoring [563] and director coupling to the propulsion mechanism [186,464]. It would be of interest to explore these opportunities by varying the numerous parameters offered by the described systems.

CONCLUSION

Orientationally ordered LCs emerge as a promising medium to guide and often enable dynamics of microscopic objects, both inanimate and living. The presented examples of the dynamic behavior of electrically driven dissipative particle solitons, LC-enabled electrokinetics, activated LCEs and biological tissues guided by them, microswimmers in lyotropic and thermotropic nematics are all made possible by the orientational order of the background medium and its gradients. Most of the examples in this review deal with apolar nematics, $\hat{\mathbf{n}} = -\hat{\mathbf{n}}$. The gradients of the apolar director produce vector entities such as flexoelectric polarization in Eq. (4), a force associated with the degree of orientational order in thermally or photo-addressed LCEs, Eq.(11), or active forces in active nematics, Eqs.(17,18).

Fig.37. Pairs of $\pm 1/2$ disclinations of type A (a) and type B (b) in a nematic serve as seeds of domain walls in the ferroelecric nematic N_F. Redrawn from Lavrentovich [564].

Recent studies [33-35,565,566] demonstrate the existence of a passive ferroelectric nematic formed by rod-like molecules with strong permanent dipole moments, aligned in a polar fashion and producing a macroscopic electric polarization **P**, which adopts one of the two permissible orientations, **P** or $-\mathbf{P}$, along the director $\hat{\mathbf{n}}$, Fig.37. It is suggested that in the ground state, **P** is either uniform [35] or modulated in space [33,567]. The ferroelectric nematic N_F, expected since 1916 [568], is a new distinct member of a broad group of ferroelectrics, most of which are crystalline and thus difficult to mold into patterned polarization fields needed in applications [569]. Patterned ferroelectric nematics could lead to new effects and possibilities in controlling active matter. For example, in a phase transition from an apolar to polar nematic, the $\pm\frac{1}{2}$ disclinations should become connected by domain walls [564], Fig.37. Similar effects are

considered in the studies of early Universe, with cosmic strings seeding domain walls [570] and recently observed in superfluid anisotropic He-3 [571-573].

Among other underexplored active matter systems are active cholesterics [574-577] and active smectics [578-581]. An excellent example of how interfacing active nematics with passive smectics could be used to control the activity patterns has been presented by Guillamat et al. [493,582]. There is little doubt that further exploration of passive apolar and polar nematics, of their chiral and partially positionally ordered smectic counterparts as media to command out-of-equilibrium behavior might open doors for new technologies that harness the energy of microscale dynamics and transform it into useful work or predesigned individual and collective behavior of active units.

Acknowledgments

I dedicate this review to the memory of Maurice Kleman, a mentor and a friend. I am thankful to the former and current Ph.D. graduate students G. Babakhanova, H. Baza, V. Borshch, Y.-K. Kim, R. Koizumi, I. Lazo, B.X. Li, Yu. A. Nastishin, V.G. Nazarenko, C. Peng, I.I. Smalyukh, M. Rajabi, T. Turiv, D. Voloschenko, S. Zhou, collaborators N. L. Abbott, I.S. Aranson, D.J. Broer, M. C. Calderer, J. de Pablo, A. Doostmohammadi, M.M. Genkin, D. Golovaty, A.P.H.J. Schenning, A. Sokolov, S.V. Shiyanovskii, J. Selinger, R. Selinger, K. Thijssen, J. Viñals, N.J. Walkington, Q.-H. Wei, J.M. Yeomans, whose contributions made the presented research possible. I also thank the organizers of the Spring School on The Mathematical Design of Materials A. Zarnescu, X. Chen, M. Ravnik, and V. Slastikov for the opportunity to present at the Isaac Newton Institute for Mathematical Sciences. A part of this review was written during participation in KITP Active 20 program, supported in part by the NSF grant PHY-1748958 and NIH grant R25GM067110. The work has been supported by NSF grant DMR-1905053 and by Office of Science, U.S. Department of Energy, grant DE-SC0019105.

FIGURES AND CAPTIONS

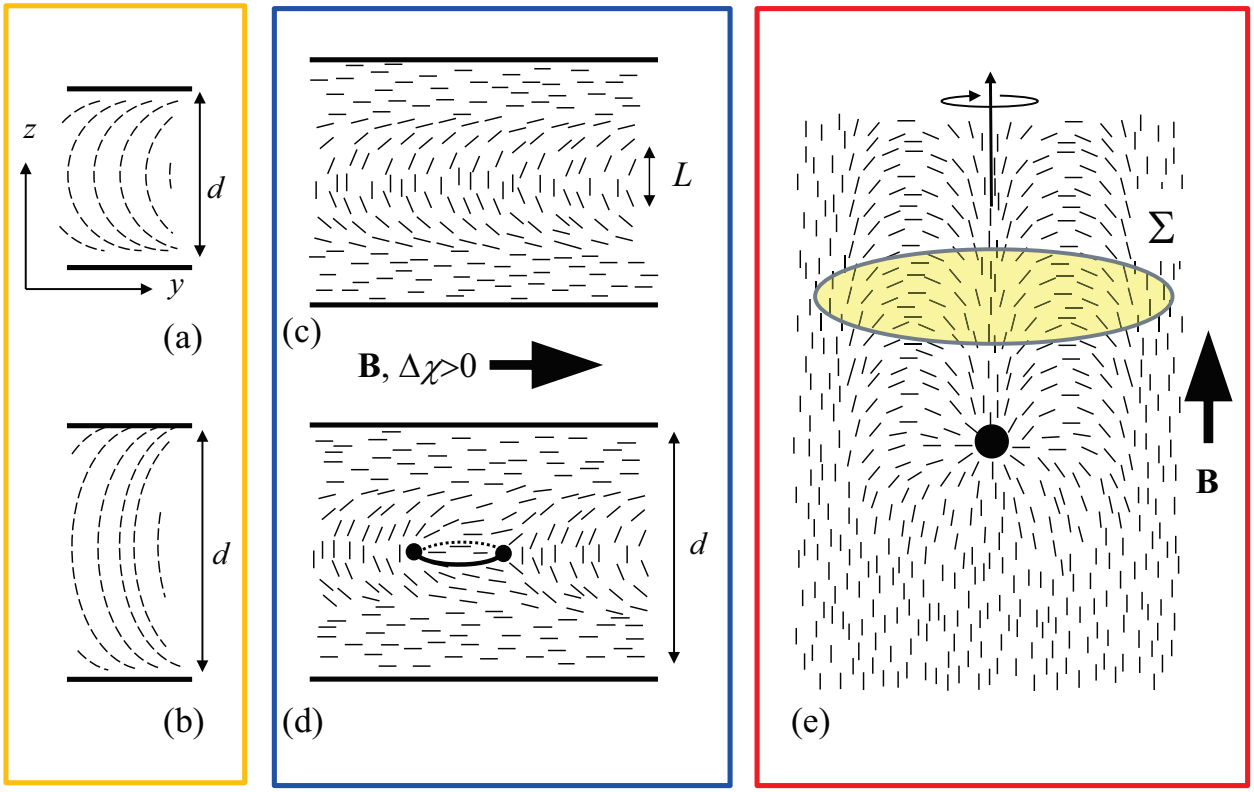

Fig. 1. Distorted states and topological solitons in a uniaxial nematic. (a,b) Splay-bend director reorientation by π in a cell of thickness d that determines the length scale of the deformation. (c) Stationary topological soliton wall, the thickness of which is defined by the applied magnetic (or electric) field. (d). The soliton wall could be eliminated by nucleation of a disclination loop. (e) String-like soliton formed by an applied field at the point defect-hedgehog in the nematic bulk. At the surface Σ , the director adopts all possible orientations in space.

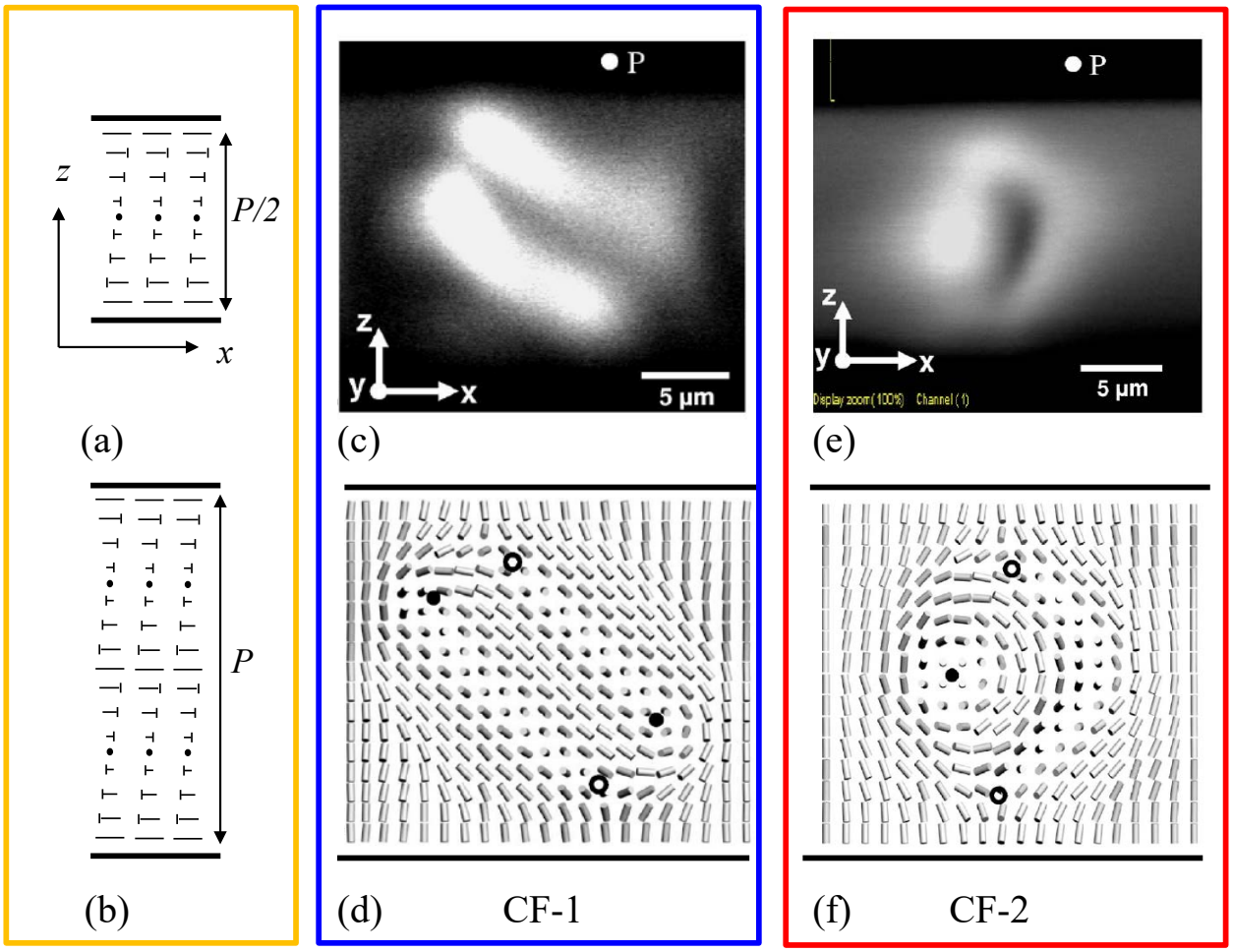

Fig.2. Cholesteric in cells of a different thickness (a,b) and topological solitons-cholesteric fingers of CF-1 (c,d) and CF2 (e,f) types. (a,b) Twist of the director with the period $P/2$ that depends on the helical twisting power of the chiral molecules; doubling the cell thickness doubles the number of π twists but does not change the length scale $P/2$. (c) FCPM texture and (d) the reconstructed director field of CF-1 in a homeotropic cell of the thickness close to P. The open circles mark the nonsingular cores of $\lambda^{-1/2}$ disclinations and the filled circles mark $\lambda^{+1/2}$ disclinations in Friedel-Kleman terminology [50,89]. (e,f) The same for CF-2; the filled circle marks λ^{+1} disclinations. In (c,e), the polarization of the probing light marked by "P" is along the y-axis. Parts (c-f) are reproduced with permission from Smalyukh et al. [64].

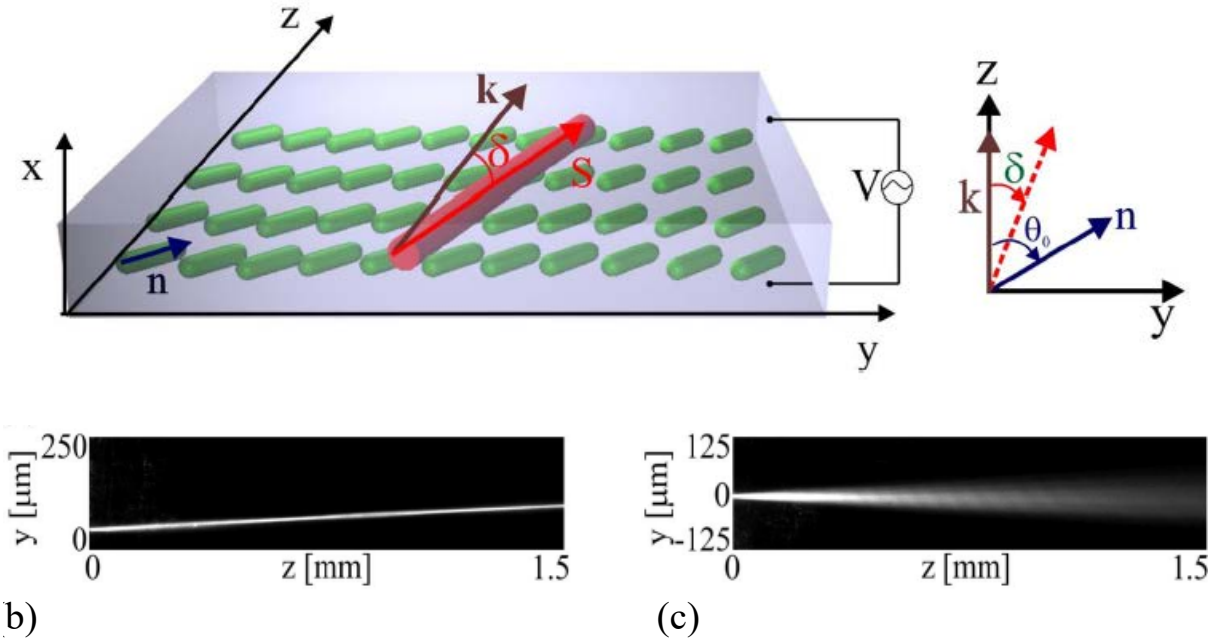

Fig.3. Nematicons. (a) A light beam linearly polarized along the *y*-axis and launched along the *z*-axis, propagates through a planar nematic cell and realigns the director parallel to itself, increasing the effective refractive index and self-focusing; (b) microphotograps of a propagating nematicon; (c) beam polarized along the *x*-axis does not focus and propagates as an ordinary wave. Adapted with permission from Laudyn et al. [113] © The Optical Society.

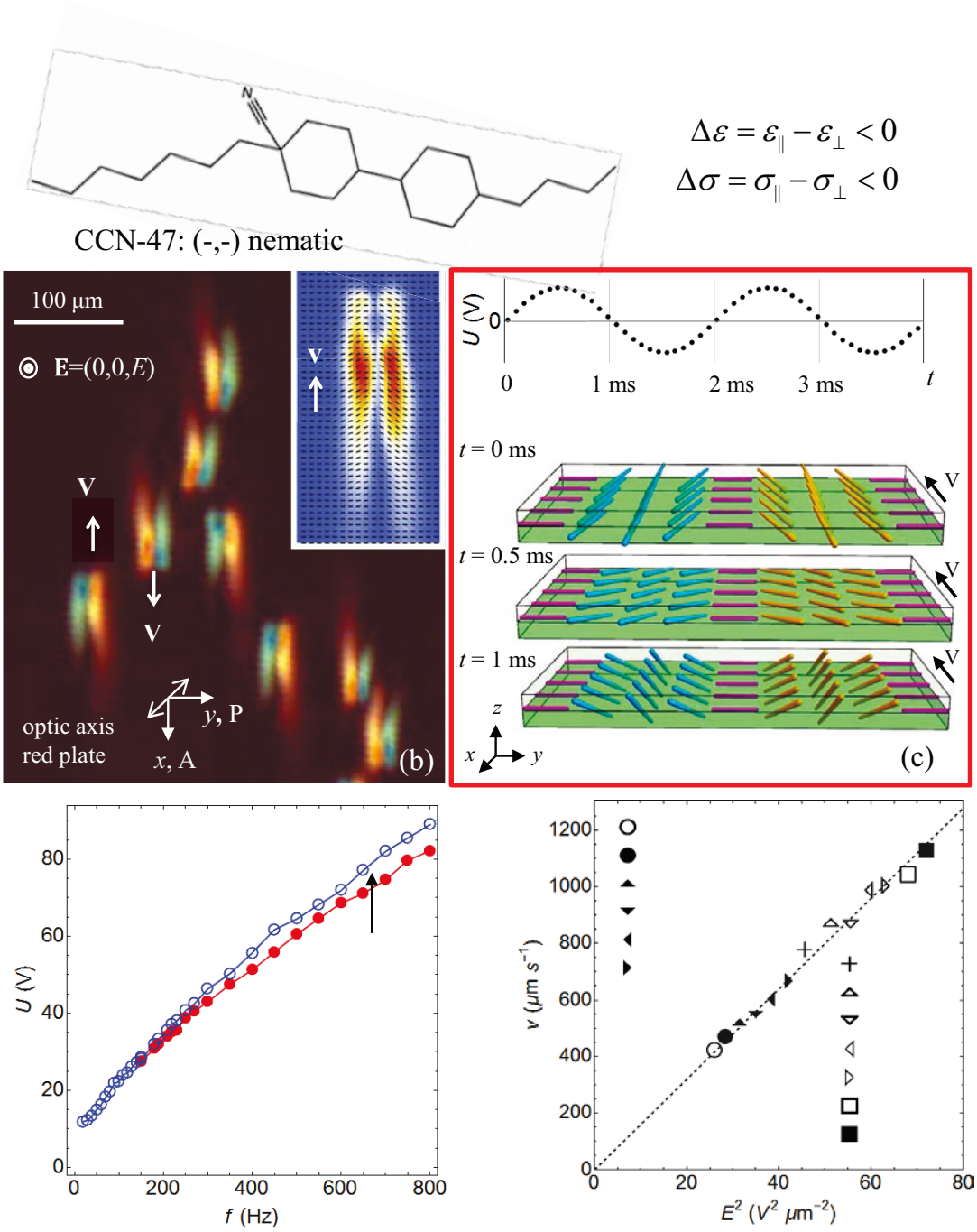

Fig.4. (a) Chemical structure of (-,-) nematic CCN-47. (b,c) Directrons B^h formed in an AC field of a high frequency: (b) optical microscopy texture with an optical compensator (red plate) inserted at 45° to the directions of polarizer (P) and analyzer (A); the inset shows the bent director field. (c) Director field within the soliton body oscillating up and down with the frequency of the applied voltage U. (d) Voltage-frequency domain of the directrons existence. (e) B^h speed vs. amplitude and frequency of the electric field. Redrawn from Li et al. [45].

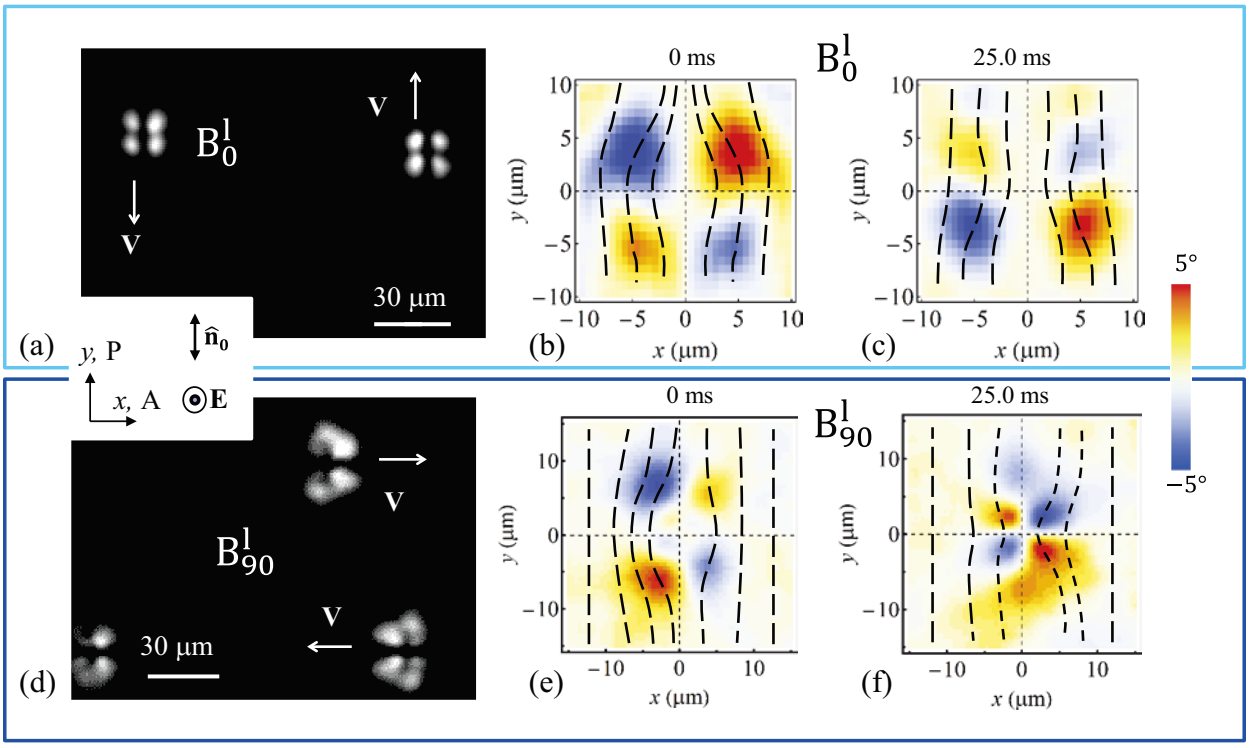

Fig.5. Low-frequency directrons B^l that propagate (a,b,c) parallel to the overall director $\hat{\mathbf{n}}_0$ and (d,e,f) perpendicularly to $\hat{\mathbf{n}}_0$. Instantaneous in-plane director tilt for B_0^l directron (c) at the time "0 ms" which corresponds to the minimum of the applied voltage and (d) at the time "25 ms" which corresponds to the maximum of a sinusoidal AC field; (e,f) similar director patterns for B_{90}^l directrons. The in-plane tilts are color-coded in accordance with the scale on the right-hand side. The tilt of the dashed lines with respect to the overall director is exaggerated by a factor of 6 for clarity. The nematic CCN-47 doped with 0.005wt% of ionic salt tetrabutylammonium bromide (TBABr). Redrawn from Li et al. [46].

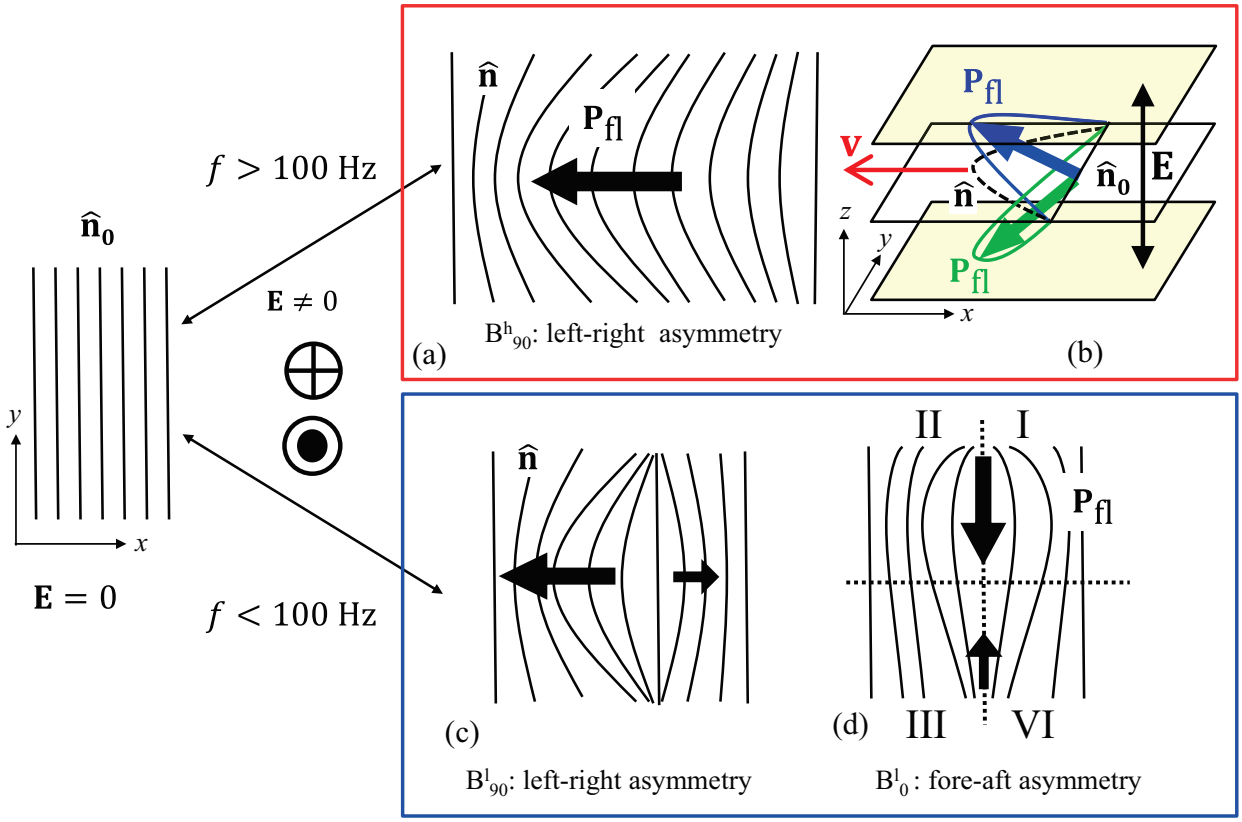

Fig.6. Time-averaged asymmetry patterns of directrons driven at high (top row) and low (bottom row) frequencies of the electric field; arrows show the flexoelectric polarization $\mathbf{P}_{fl}$ associated with (a,b,c) the bend vector $\mathbf{b} = \hat{\mathbf{n}} \times \mathrm{curl}\hat{\mathbf{n}}$ and (d) the splay vector $\mathbf{s} = \hat{\mathbf{n}}\mathrm{div}\hat{\mathbf{n}}$; (b) the polarization vector oscillates with the same frequency as the applied electric field **E**; asymmetry of the bend-splay director configuration leads to the soliton's propulsion with a velocity **v**.

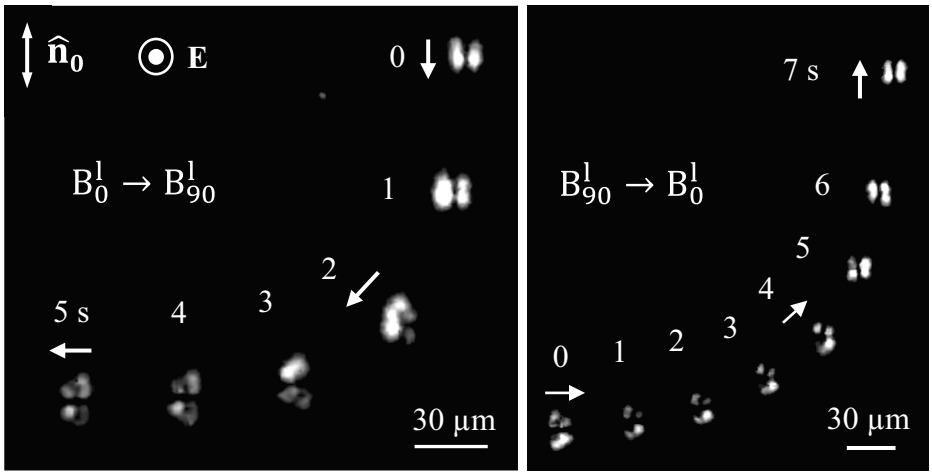

(a) (b)

Fig.7. Electric field controls symmetry, mutual transformations, and direction of propagation of low-frequency directrons. (a) B_0^l transforms into B_{90}^l and changes the direction of propagation after the voltage is raised at t =0 s from 8 V to 11 V. (b) B_{90}^l transform into B_0^l when the voltage at t =0 s is decreased from 11 V to 8 V. CCN-47 doped with 0.005wt% of TBABr. Redrawn from Li et al. [46].

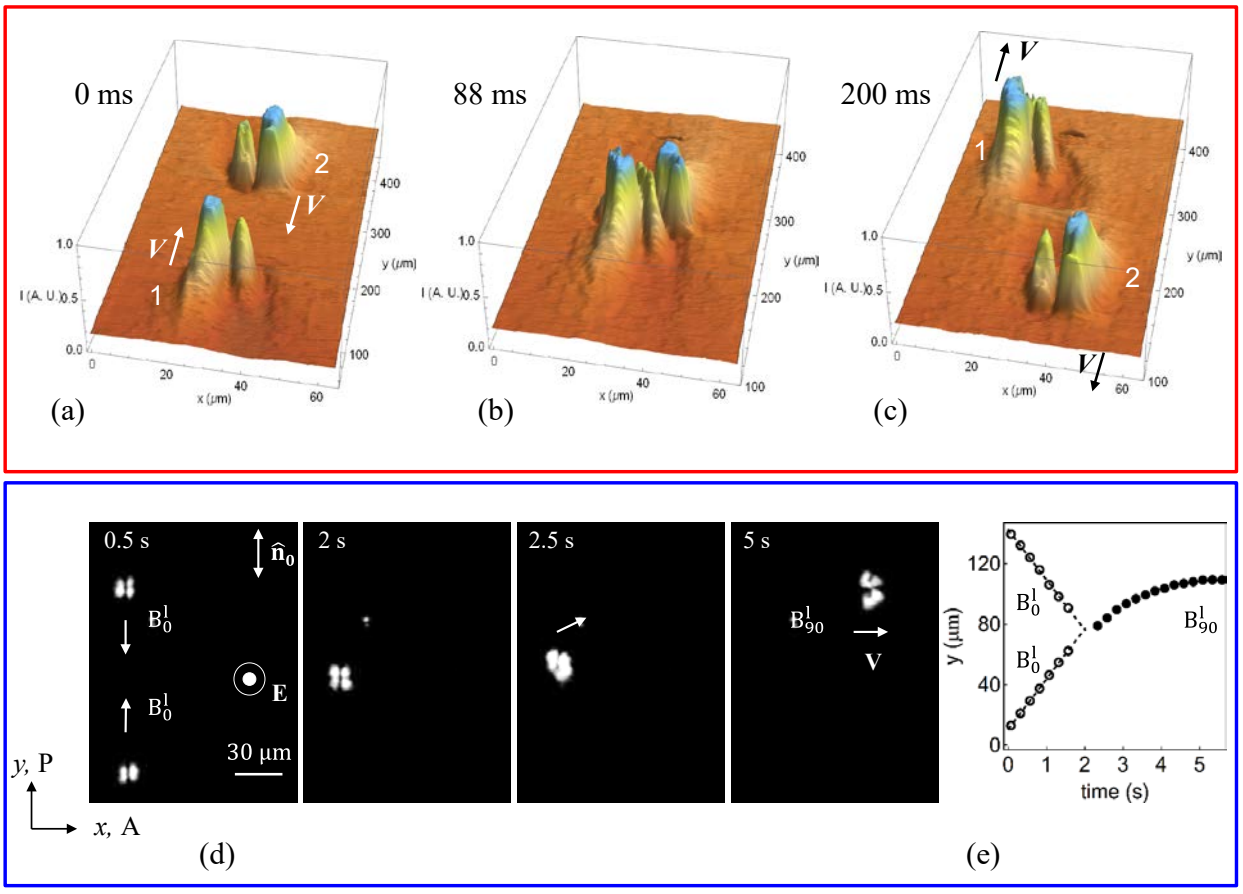

Fig.8. Collisions of directrons. (a,b,c) Two B^h directrons approach each other at 0 ms, collide at 88 ms and move away after a collision while restoring shapes, at 200 ms (CCN-47, $U = 55.2\ V$, $f = 800$ Hz, $T = 50\ °C$, $d = 8.0$ μm). The vertical axis shows the intensity of the transmitted light. (d,e) Two B_0^l directrons moving along $\hat{\mathbf{n}}_0$ collide and merge into a single B_{90}^l soliton that moves first at some angle and then perpendicularly to $\hat{\mathbf{n}}_0$. CCN-47 doped with 0.005wt% of TBABr; 8.5 V, 20 Hz. Redrawn from Ref.[45] in (a,b,c) and Ref [46] in (d,e).

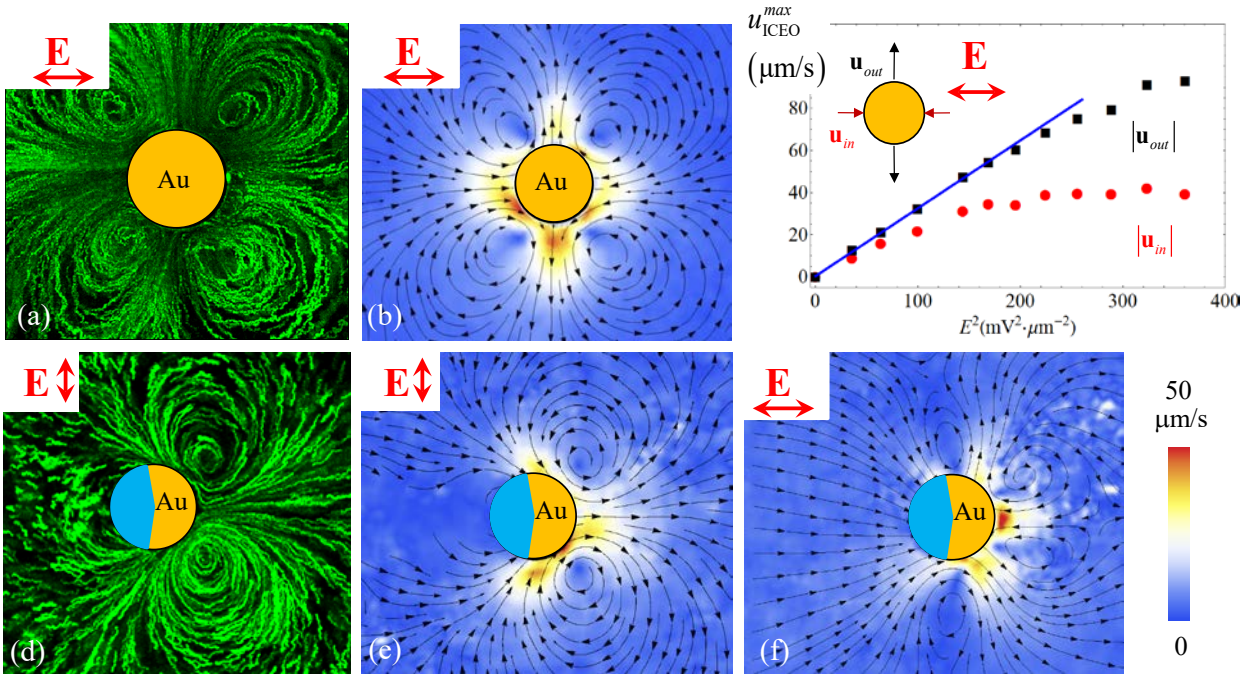

Fig.9. ICEO in an aqueous isotropic electrolyte around gold spheres (a-c) and glass-gold Janus particles (d-f). (a) Flows around a gold sphere of diameter 50 μm in a flat electrolytic chamber of height 60 μm, under an AC electric field $E = 10$ mV/μm, 1 kHz; flows are visualized by trajectories of fluorescent markers. (b) ICEO velocity map around the sphere. (c) Maximum inwards and outwards velocities as the functions of E^2 around the sphere. (d) Trajectories of fluorescent markers around a glass-gold Janus sphere of diameter 50 μm in a flat chamber of height 60 μm, under the AC electric field $E = 10$ mV/μm, 1 kHz. (e) ICEO velocity map around the Janus sphere exhibiting steady pumping of the electrolyte from left to right; the field is perpendicular to the axis of rotational symmetry. (f) The same, the field is parallel to the axis of rotational symmetry. Modified from Peng et al. [163].

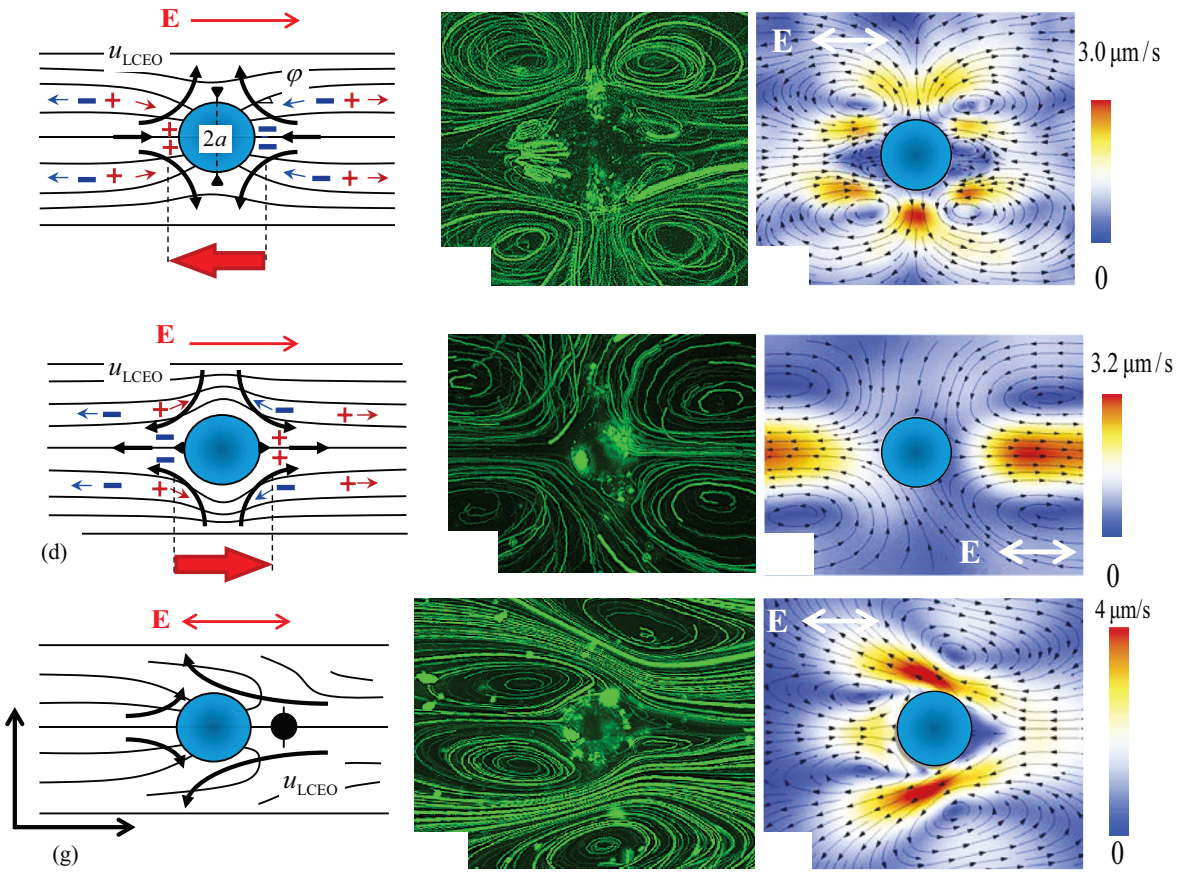

Fig.10. LCEOs in a nematic with a director field of quadrupolar (a-f) and dipolar (g-i) symmetry distorted by a sphere with (a-c, g-i) normal and (d-f) tangential anchoring at its surface. Filled triangles in (a) show the cross-section of a -1/2 disclination loop. Filled triangles in (b) show the cores of two surface defects-boojums at the poles. The field-induced dipole moment, shown by red block arrows, is either (a) antiparallel to the field or (d) parallel to it, depending on the director gradients. Electro-osmotic flows shown by thick arrows in (a,d) do not change polarity when the field is reversed. The corresponding (b,c) puller- and (e,f) pusher type experimental LCEO flows around glass spheres of diameter 50 μm with perpendicular and tangential anchoring, respectively. (g) An AC electric field acting on a nematic electrolyte with an immobilized glass sphere and a hyperbolic hedgehog on the right-hand side causes (h,i) LCEO flows with fore-aft asymmetry; (i) the sphere acts as a pump, moving the nematic from right to left. In all experiments, the nematic is of a zero dielectric anisotropy, $\Delta\varepsilon = 0$, and of a positive electric conductivity anisotropy $\Delta\sigma > 0$. AC field is of frequency 5 Hz and amplitude 26 mV/μm. Modified from Lazo et al. [175].

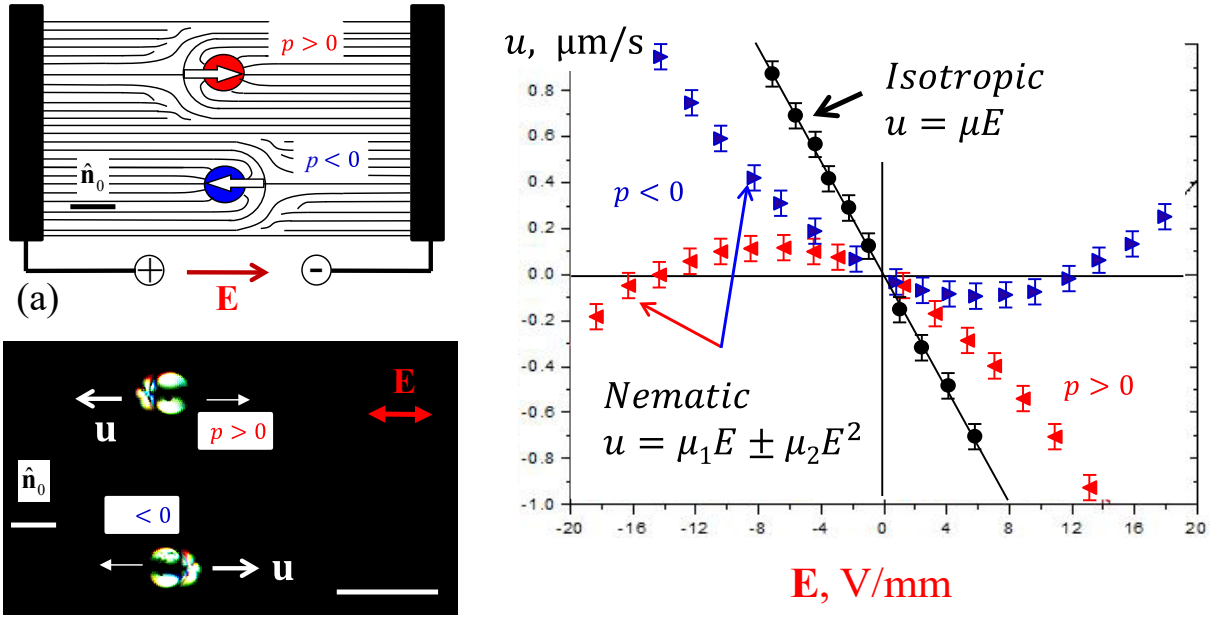

Fig.11. Liquid crystal-enabled electrophoresis (LCEP): (a) scheme of experiment with a DC in-plane field; (b) DC-triggered electrophoretic velocity of glass spheres in isotropic (circles) and nematic (triangles) phase for two orientations of the structural dipole **p** directed from the hyperbolic hedgehog towards the sphere; (c) AC field-driven electrophoresis with propulsion polarity defined by the structural dipoles. Modified from Lavrentovich et al. [173].

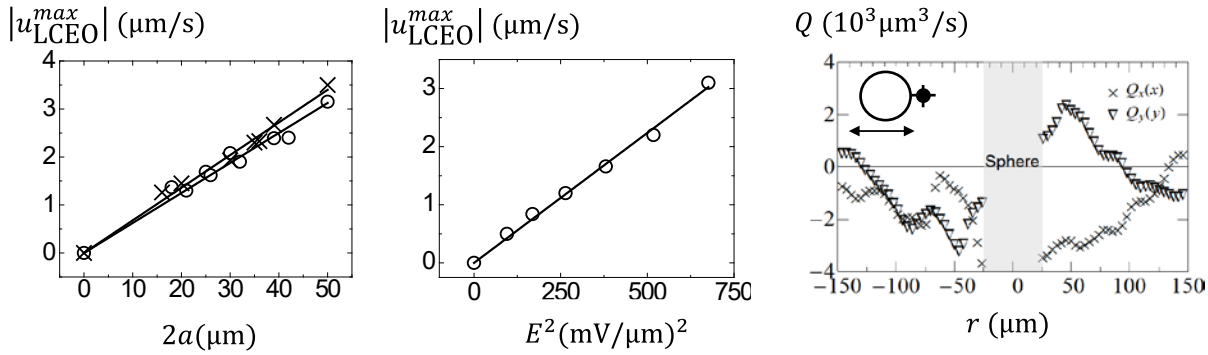

Fig.12. Quantitative parameters of LCEO around a glass sphere in a uniform AC electric field of frequency 5 Hz. (a) Maximum LCEO velocity around tangentially anchored (circles) and perpendicularly anchored (crosses) spheres increases linearly with the diameter $2a$ of the sphere; velocity patterns are of quadrupolar symmetry in both cases; $E = 26$ mV/μm. (b) Maximum LCEO velocity around a tangentially anchored sphere of diameter $2a = 50$ μm grows as E^2. (c) Volume of the LC flow around a sphere with perpendicular anchoring and a dipolar structure (diameter 50 μm), shown in Fig.10i, passing along the x −axis and along the y − axis defined in Fig.10. The nematic is pumped from right to left. Modified from Lazo et al. [175].

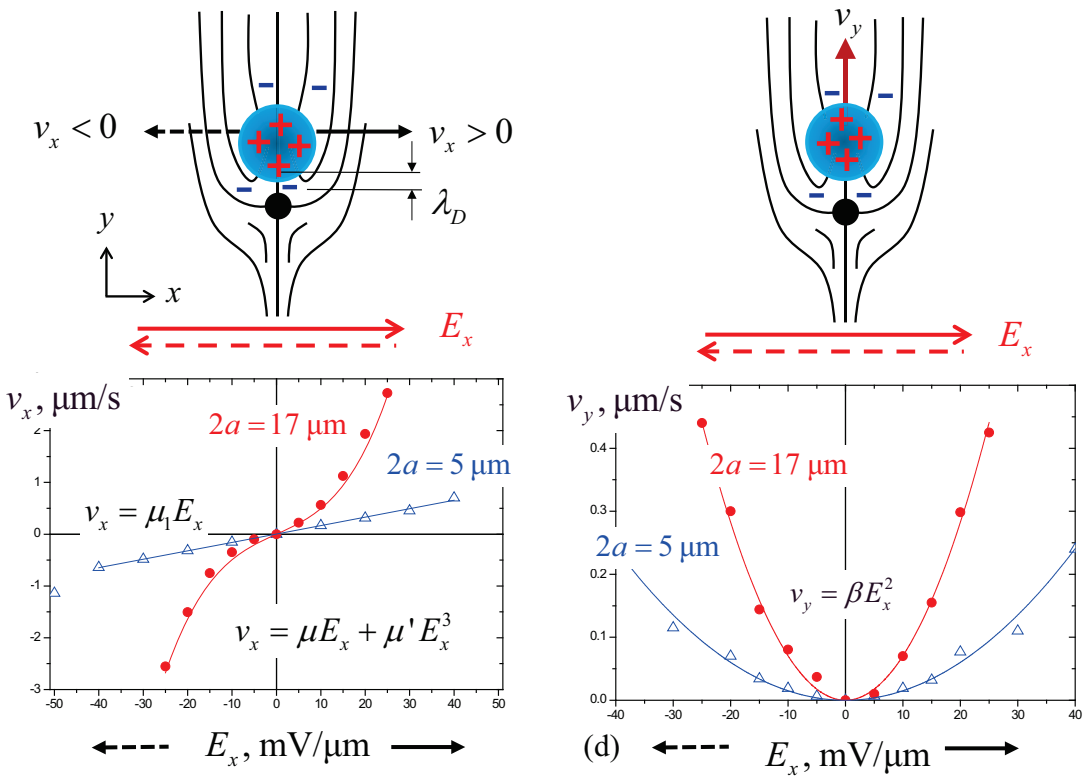

Fig.13. LCEP velocity of positively charged glass spheres of diameter $2a = 5$ μm and $2a = 17$ μm in the nematic phase (25^0C) of MLC7026-000 as a function of the uniform DC electric field; in-plane geometry with $\mathbf{E} = (E_x, 0,0)$ and $\hat{\mathbf{n}}_0 = (0,1,0)$; (a,c) x-component of the velocity, parallel to $\mathbf{E}$ and perpendicular to $\hat{\mathbf{n}}_0$, with a linear and cubic dependence on E; (b,d) y-component of the velocity, parallel to $\hat{\mathbf{n}}_0$, showing a quadratic dependence on E. Redrawn from Lazo et al. [174].

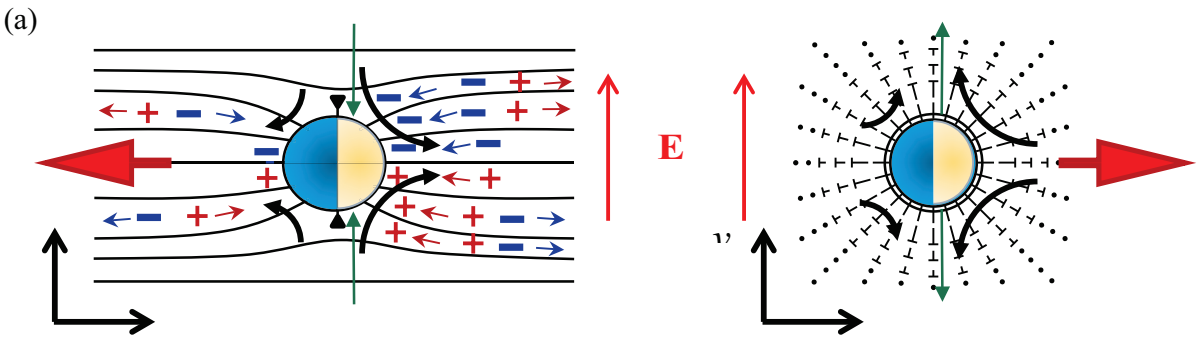

Fig.14. Electro-osmotic flows (black curved arrows) and electrophoretic velocity (red block arrows) of a metal (yellow)-dielectric (blue) Janus sphere with perpendicular anchoring and quadrupolar Saturn ring director. Vertical green arrows show the force dipole shifted towards the metal hemisphere of higher polarizability. The force dipole is either of (a) a puller type or (b) pusher type. Redrawn from Sahu et al. [200].

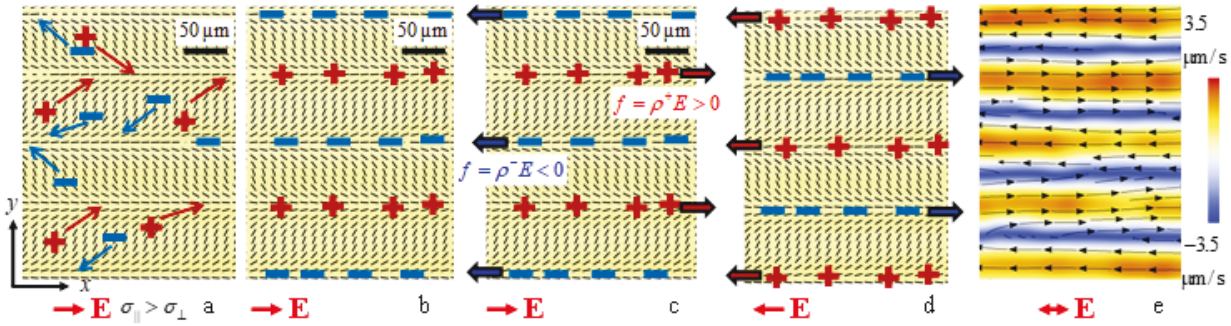

Fig.15. LCEO in a nematic electrolyte with a predesigned director. Ticks represent local director visualized by PolScope: (a) the electric field ***E*** drives "+" and "-" electric charges along the x-axis but because of the anisotropic conductivity, the charges shift also along the y-axis, (b) creating separated lanes of space charges; (c) the electric field moves them along the x -axis; (d) reversal of the field changes polarity of charges but does not change the Coulomb force; (e) an AC field of frequency 5 Hz creates lanes of LCEO flows of alternating direction. Redrawn from Peng et al. [187].

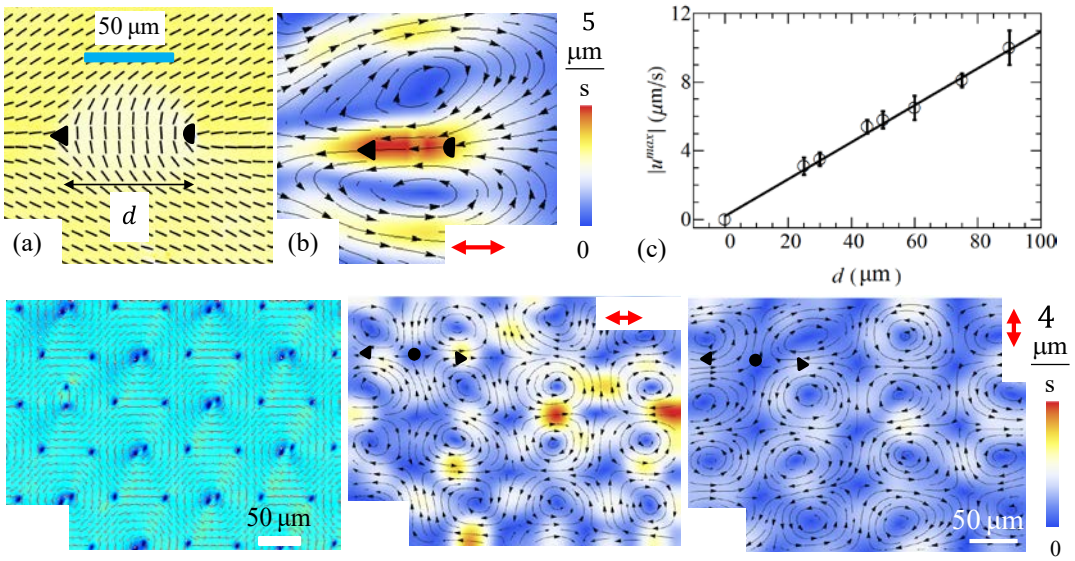

Fig.16. LCEO in a patterned director field with topological defects. (a) A nematic cell with a predesigned pair of singular $m = -1/2$ and $m = +1/2$ disclinations of type A; (b) LCEO flows powered by an AC electric field; (c) maximum LCEO flow velocity vs. separation of disclinations. (d) Periodic pattern of $m = +1$ defects surrounded by $m = -1/2$ defects; (e,f) LCEO flows are of opposite polarity for two orthogonal directions of the electric field shown in the right upper corners. The filled symbols show the cores of defects. Redrawn from Peng et al. [187].

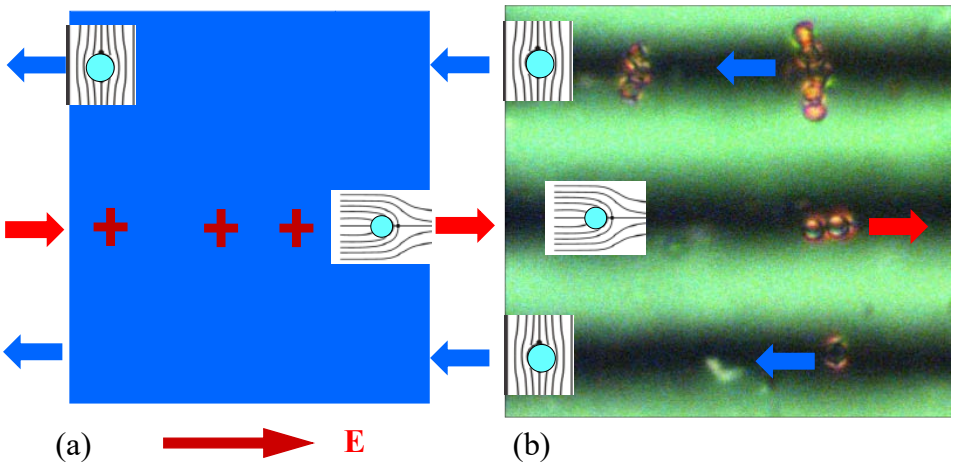

Fig.17. LCEO flows in a patterned director field with a periodic splay and bend separate spherical polystyrene particles (diameter 5 μm) with different surface functionalization. The splay regions attract spheres with perpendicular anchoring and a hyperbolic hedgehog and move them to the right; the bend regions attract bipolar spheres with tangential anchoring and move them to the left. Redrawn from Peng et al. [184,208].

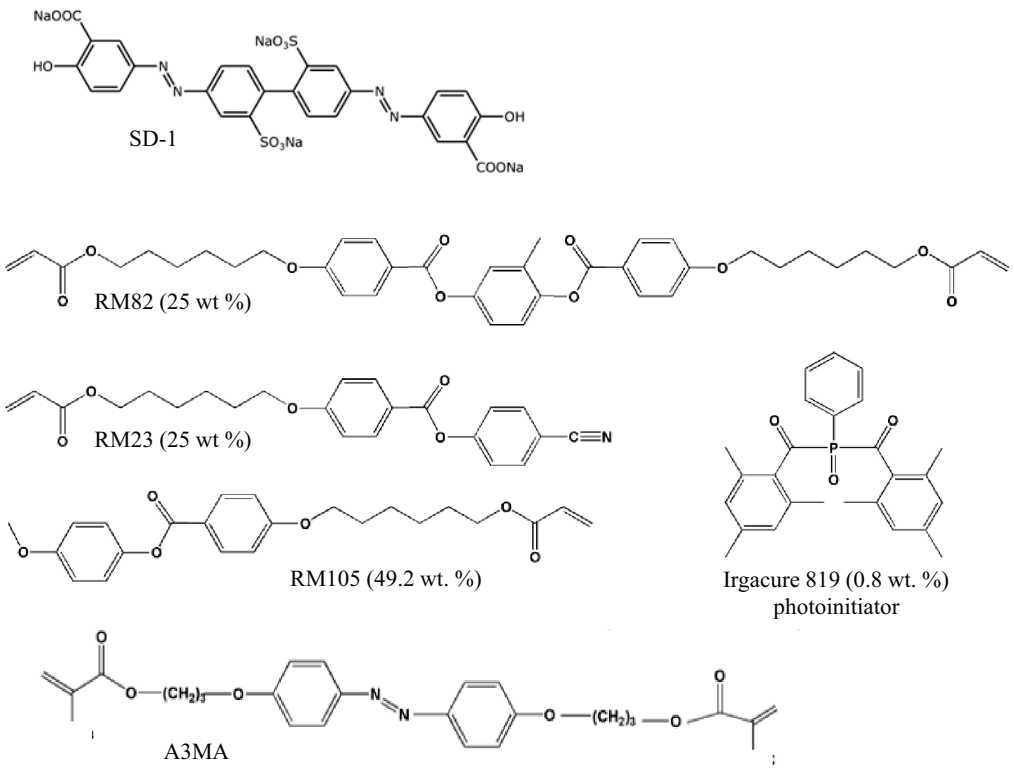

Fig.18. Typical materials used to fabricate patterned LCEs: azodye SD-1 used as an alignment precursor; elastomer composition with reactive monomers (RMs) and a photoinitiator Irgacure 819 is deposited onto the photoaligned azodye layer and photopolymerized. Monomers such as azobenzene derivative A3MA with UV-triggered trans-to-cis isomerization could be added to make the LCE photosensitive.

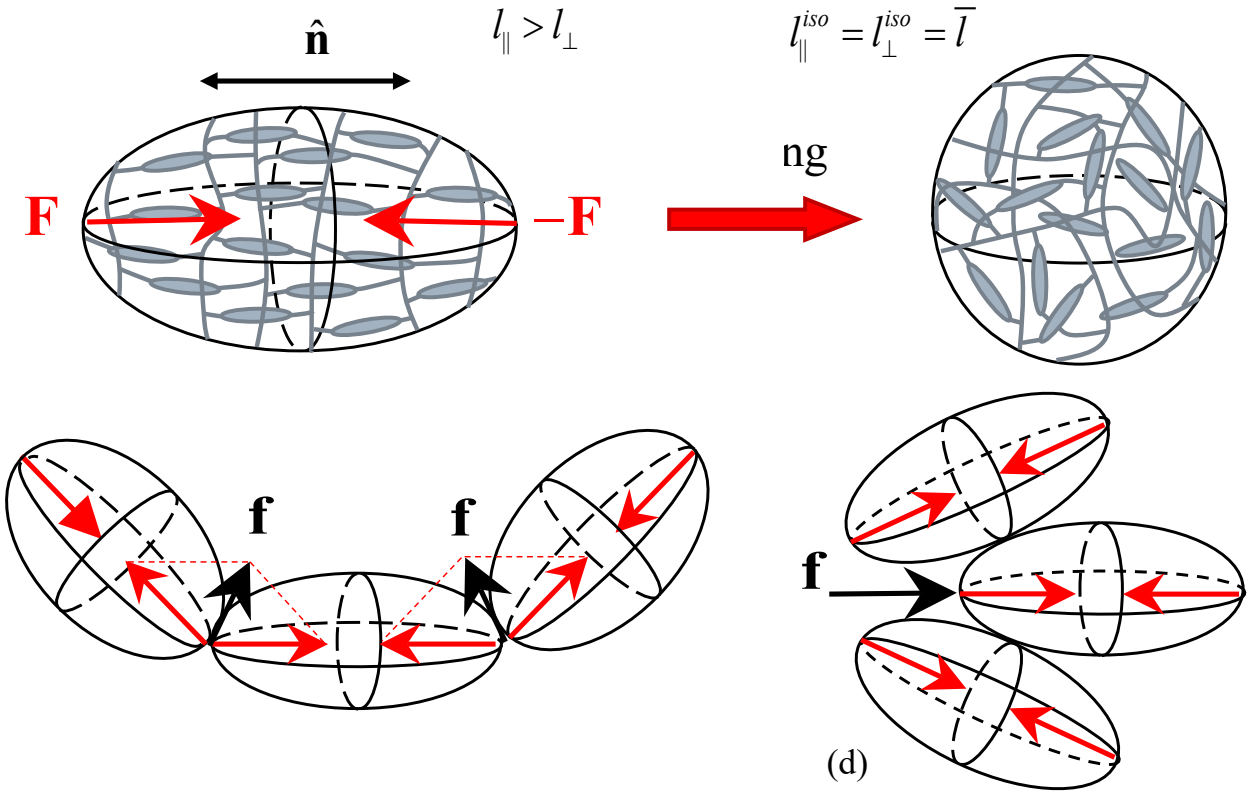

Fig.19. Polymer network conformation and the occurrence of the activation force. (a) Prolate ellipsoid of polymer network conformations in the uniaxial calamitic nematic phase; the long axis is along the director $\hat{\boldsymbol{n}}$; during heating, the ellipsoid shrinks along the long axis; in the isotropic phase, it becomes a sphere, as shown in part (b); the shrinking is modeled by a pair of forces $\boldsymbol{F}$. Activation force density **f** produced by contracting ellipsoids in the geometry of (c) bend and (d) splay.

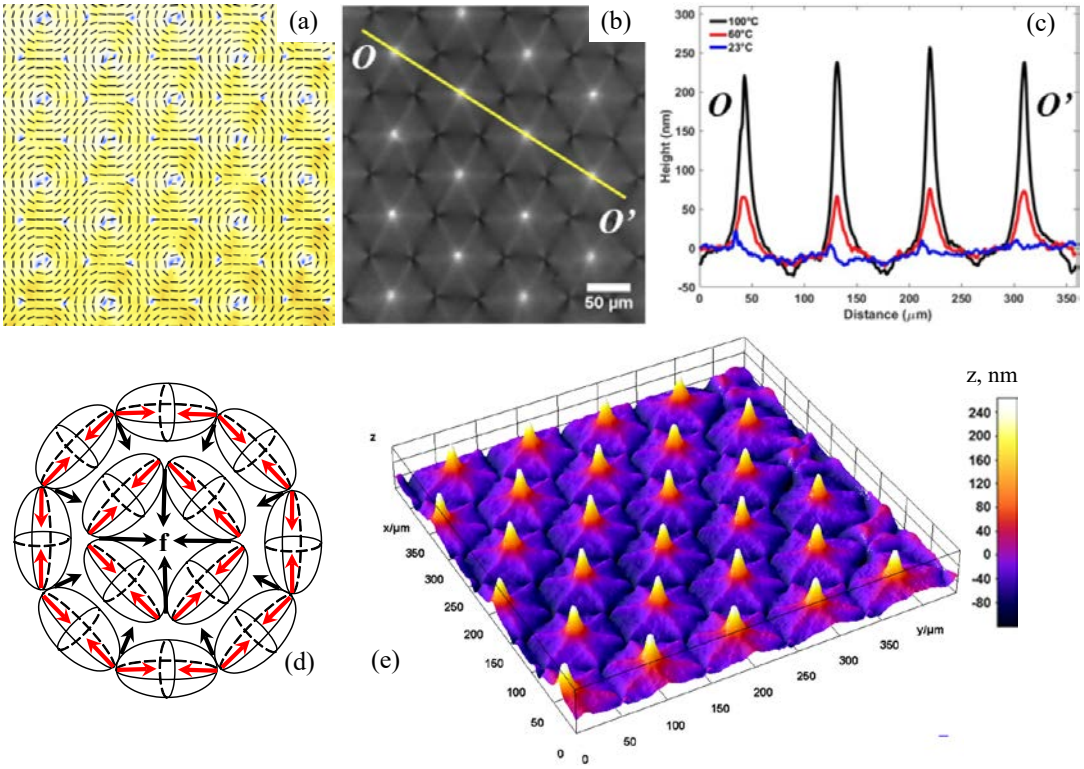

Fig.20. LCE coating with a prepatterned director responds to heating by elevating regions of bend. (a) The flat director pattern with circular +1 defects surrounded by -1/2 disclinations; (b) Digital holographic microscopy image of the LCE free surface; (c) Surface profiles along line *OO'* in (b) at 23, 60, and 100 ˚C; (d) Heating-triggered activation forces in a circular director field move the material towards the center, causing an elevation; (e) 3D view of the free surface's topography of LCE coating at 100 ˚C with elevations at circular +1 defects; note tri-fold symmetry of small elevations and depressions around the cores of -1/2 disclination. Part (a) courtesy of C. Peng, parts (b,c,e) courtesy of G. Babakhanova.

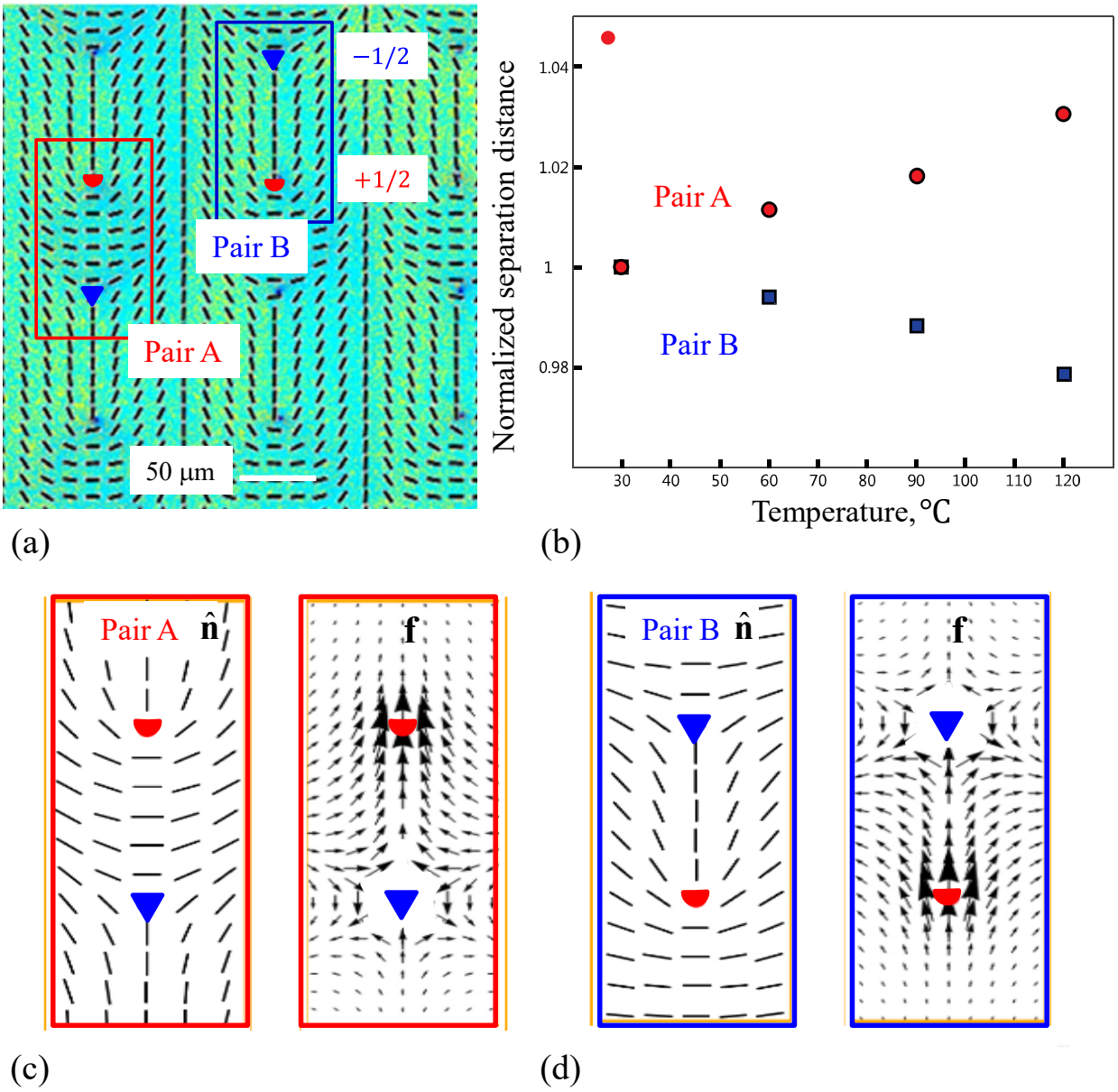

Fig.21. In-plane shifts of +1/2 defects upon heating. (a) PolScope image of a flat LCE coating at 23 ˚C with periodic lattice of defects of strength ±1/2; red boxes A and blue boxes B enclose two types of pairs: in pair A, the director $\hat{\mathbf{n}}(\mathbf{r})$ is perpendicular to the line connecting the two cores, in pair B, $\hat{\mathbf{n}}(\mathbf{r})$ connects the cores. (b) Separation distance between +1/2 and −1/2 cores increases in pairs A and decreases in pairs B as the temperature increases. (c) Director configuration and active force $\mathbf{f}(\mathbf{r})$ calculated using Eq.(11) for pair A. (d) The same for pair B. Redrawn from Babakhanova et al. [226].

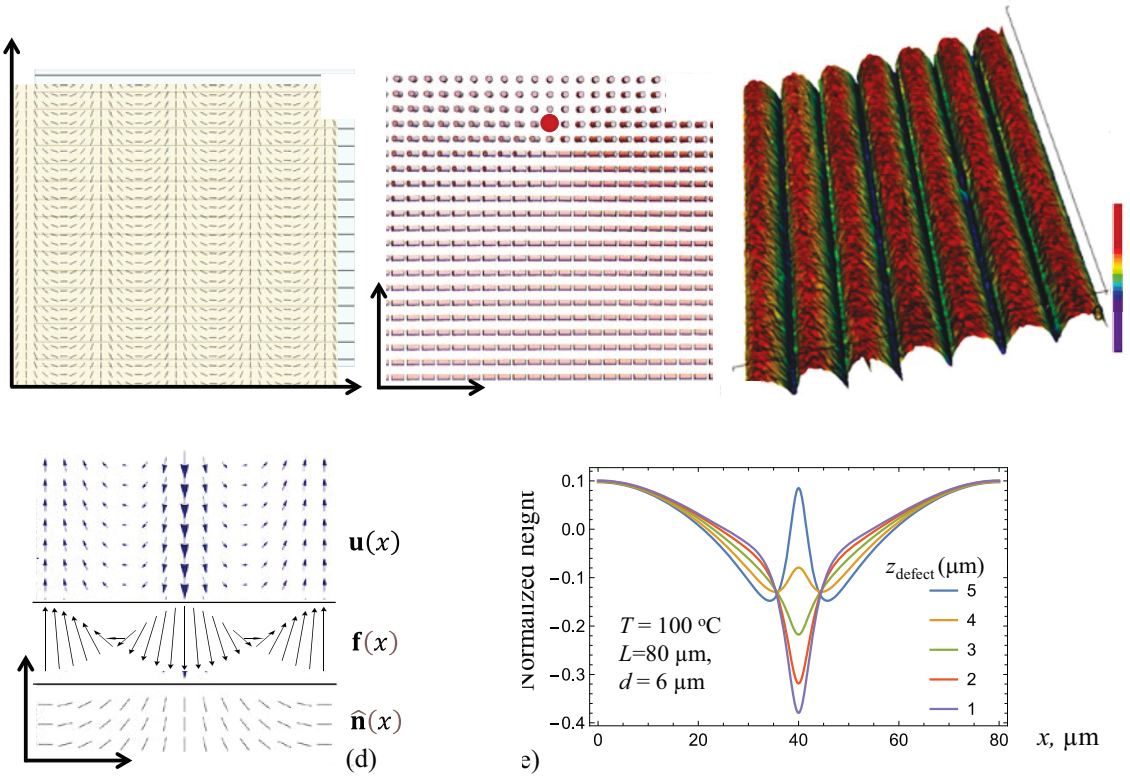

Fig.22. LCE coating with a prepatterned system of singular disclinations. (a) Director patterns on the top and bottom surfaces. (b) Vertical cross-section of unpolymerized nematic with the core of the disclination shifted towards the patterned surface. (c) Surface profile of LCE coating of thickness $d = 5$ μm and period $L = 80$ μm at the elevated temperature. (d) Linear elasticity theory calculations of in-plane displacements $\mathbf{u}(x)$ of the heat-activated coating and the activation force $\mathbf{f}(x)$ for the corresponding director field $\hat{\mathbf{n}}(x)$. (e) Linear elasticity theory calculations of the out-of-plane displacements of the heat-activated LCE coating ($d = 6$ μm, $L = 80$ μm) for different locations of the disclination line in the LCE bulk; the top free surface of the coating is patterned as shown in part (a). Redrawn from Babakhanova et al. [265].

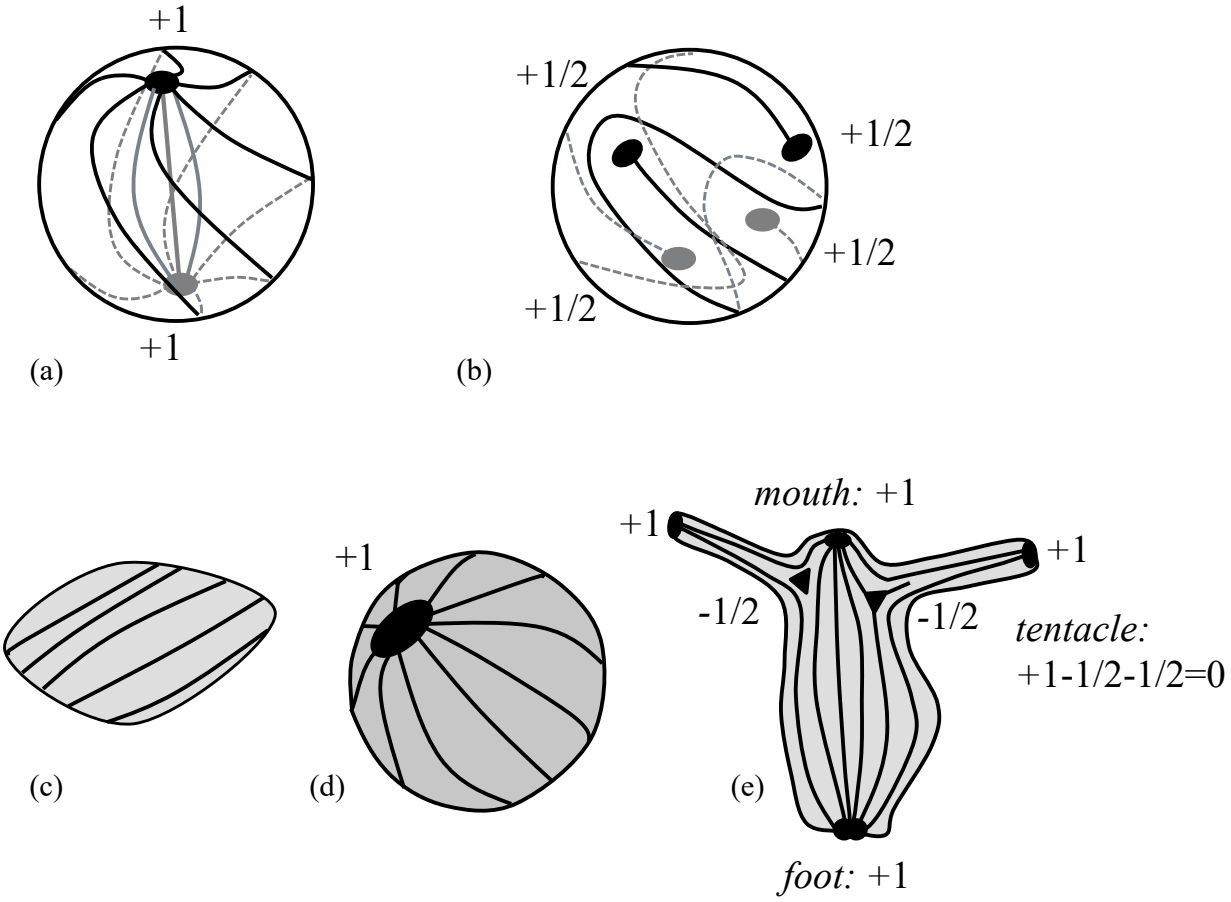

Fig.23. Topological defects in (a) tangentially anchored nematic drop; (b) thin nematic shell. (c,d,e) Topological dynamics of *Hydra* morphogenesis: (c) cut-away piece of an adult *Hydra* with a uniform alignment of fibrils; (d) folding of the piece into a spheroid; (e) regenerated hydra with point defects of strength +1 at the mouth and foot; each tentacle shows a point defect +1 at the tip, balanced by the two -1/2 defects at the opposite sides of the base. Redrawn from Maroudas-Sacks et al. [335].

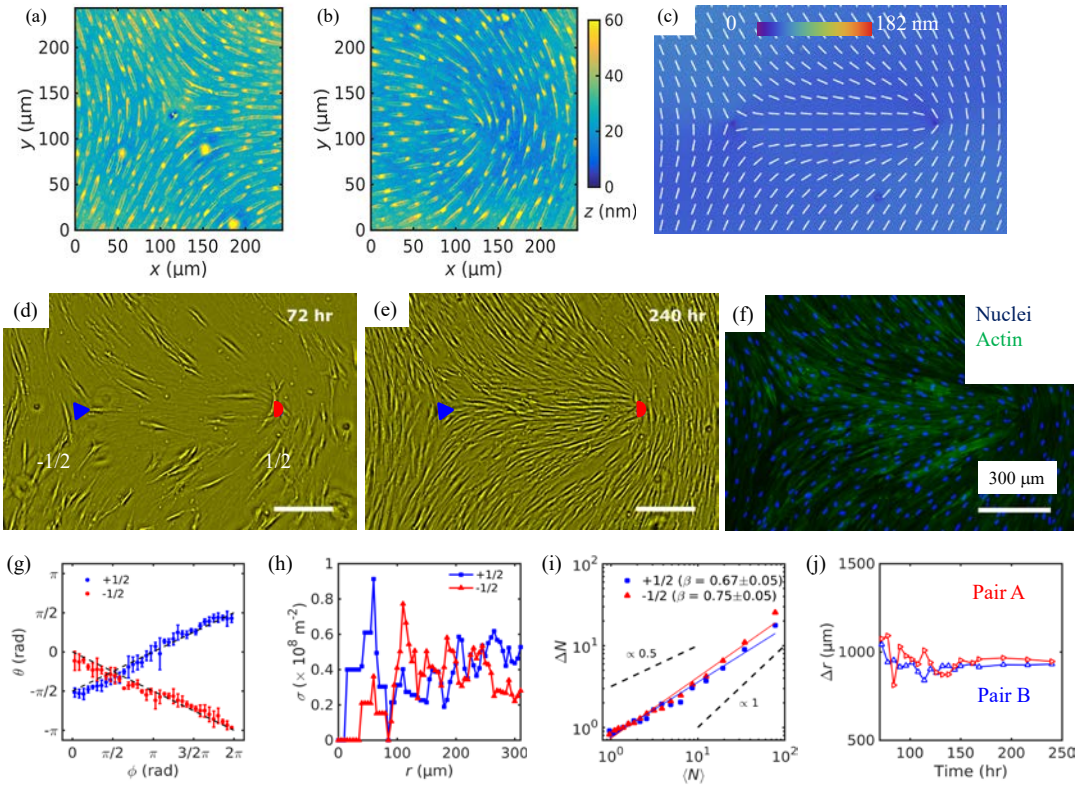

Fig.24. Human dermal fibroblast (HDF) tissue grown at an LCE coating with a prepatterned disclinations $m = \pm 1/2$. (a,b) Digital holographic microscopy of the patterned LCE surface near the defect cores with elongated elevated grains; (c) PolScope texture of the patterned LCE coating. (d,e) Phase contrast microscopy of the growth of HDF cells at the LCE substrate at 72 hr and 240 hr after seeding, respectively. (f) Fluorescent microscopy textures of HDF tissues at the LCE substrate, with labeled nuclei (blue) and cytoskeleton F-actin proteins (green).(g) The director angle around defects changes with the polar angle in a nearly linear fashion. (h). Number density of cells as a function of the distance to the defect core. (i) Large number density fluctuations ΔN of the nuclei in the vicinity of defect cores. (j) Separation between half-strength defects for pairs of type A and B, identified in Fig. 21. Redrawn from Turiv et al. [271].

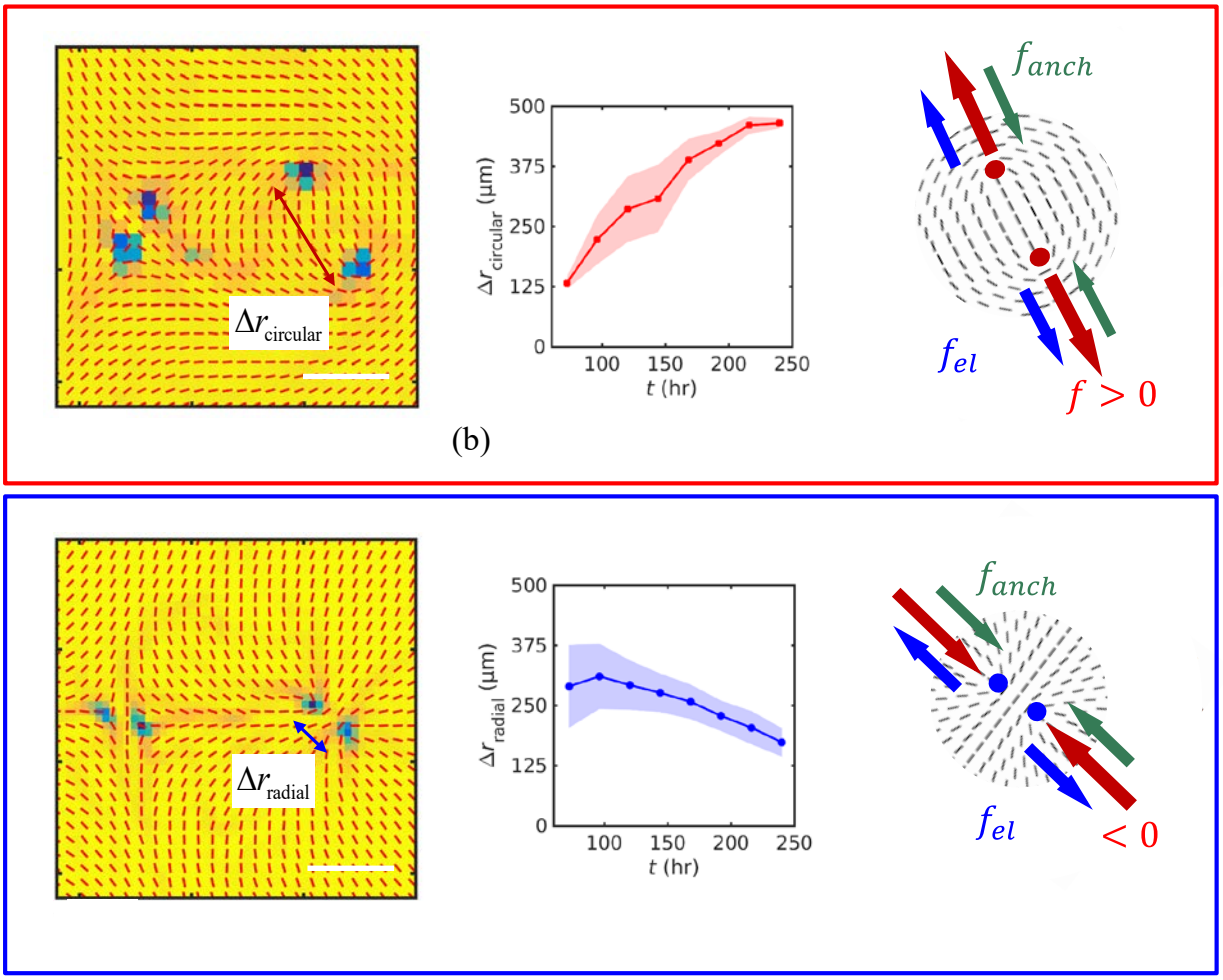

Fig.25. Human dermal fibroblast (HDF) monolayer at an LCE substrate patterned with -1 and +1 defects, either of (a, b, c) circular geometry or (d, e, f) radial geometry, splitting into pairs of +1/2 disclinations. The separation distance Δr (a,b) increases with time in the circular case and (d,e) decreases in the radial case, because of the active forces that are (c) centrifugal in the circular case and (f) centripetal in the radial case. Redrawn from Ref. [195].

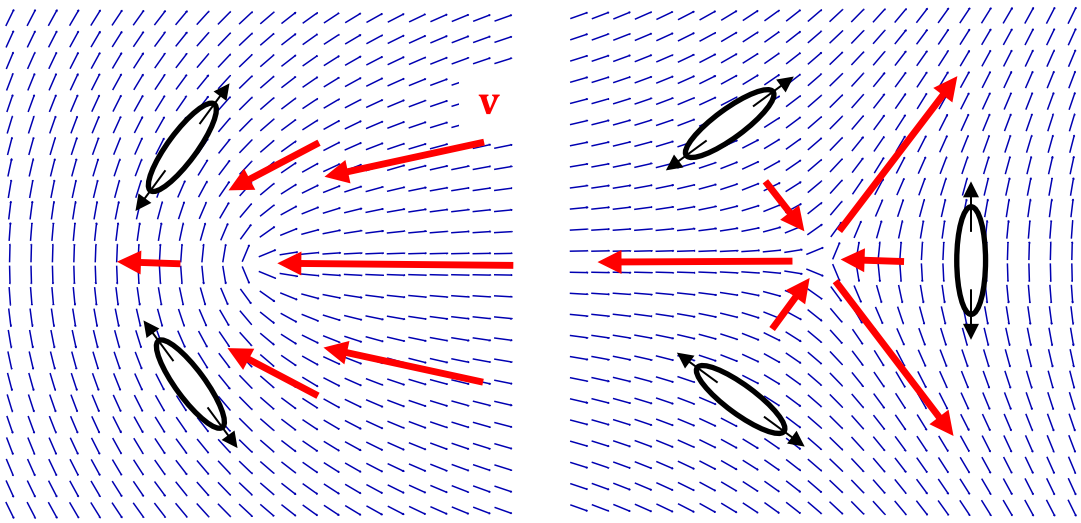

Fig.26. Active extensile units around the cores of (a) +1/2 and (b) -1/2 defects with the activity-driven velocity field **v**. The velocities are stronger along the director and weaker along the directions perpendicular to the director because of the anisotropic friction with the substrate. Modified from Copenhagen et al. [281].

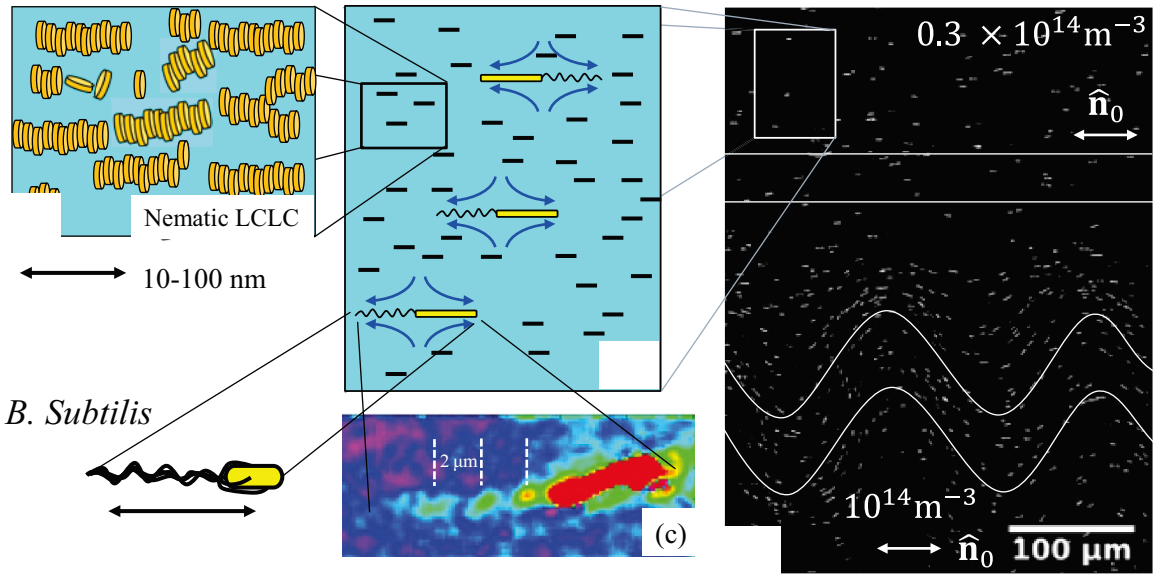

Fig.27. Living liquid crystal: (a) A lyotropic chromonic liquid crystal (LCLC) formed by stacks of organic disc-like molecules serves as (b) a guiding medium for (c) flagellated microswimmers *B. subtilis*; (d) at low concentration of bacteria, their trajectories are parallel to the director field; at higher concentrations, an undulation instability develops. PolScope image in part (c) modified from Zhou et al. [276]; phase contrast microscopy texture in part (d) modified from Koizumi et al. [221]. The probability of swimming from left to right and from right to left are equal to each other since the director is apolar.

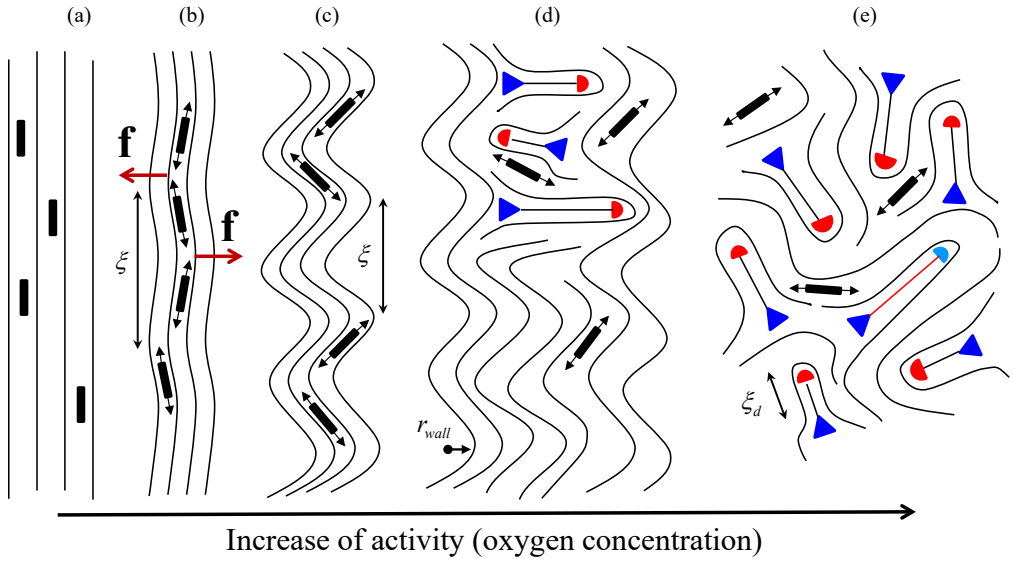

Fig. 28. Development of nonequilibrium regimes in a living liquid crystal, following the experimental data by Zhou et al. [276]: (a) equilibrium state, dormant bacteria; (b,c) bend instability, with the period ξ decreasing as activity increases; hydrodynamic interaction of bacteria in close proximity to each other produces an active force **f** that enhances a fluctuative bend; (d) nucleation of $m = \pm 1/2$ disclination pairs of the B-type, see Fig.21d; +1/2 cores move away from -1/2 cores; (e) topological turbulence. Swimming bacteria of pusher type are shown as rods with two arrows.

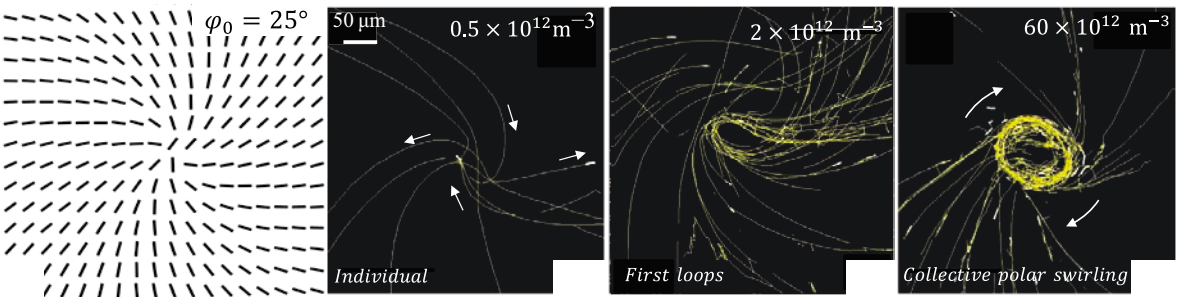

Fig.29. Individual to collective swimming transition in a patterned LCLC. (a) Patterned director field with +1 spiral vortex, $\varphi_0 = 25^o$, directs the microswimmers *B. subtilis* (b) along the director at low concentrations; as the concentration increases, the bacteria (c) start to form loops around the vortex core and then (d) engage in unipolar clockwise circulation. Redrawn from Koizumi et al. [221].

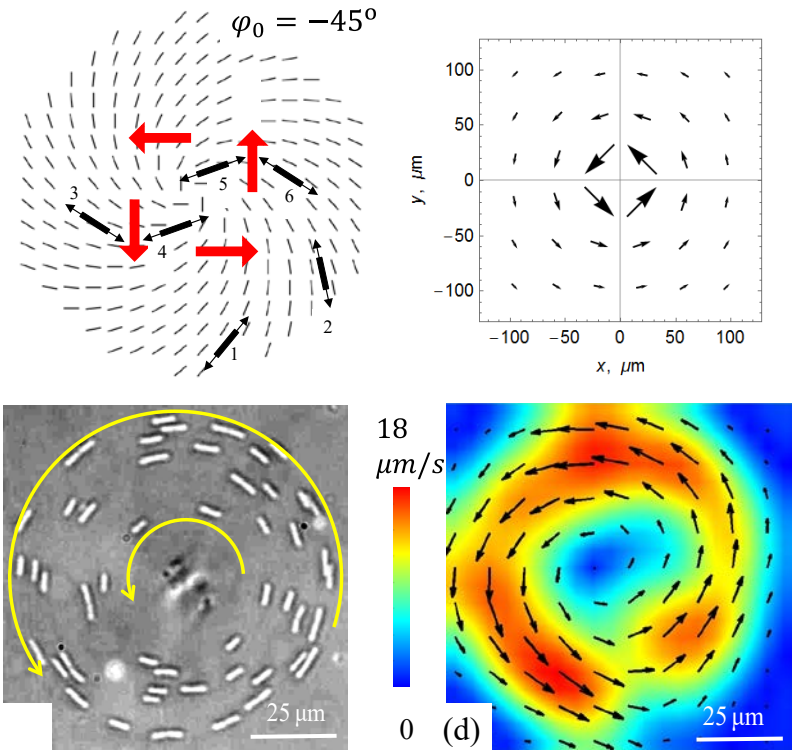

Fig.30. (a) Patterned director field with $m = +1$ spiral vortex, $\varphi_0 = -45^o$, (b) directs the active force counterclockwise and causes (c) unidirectional counterclockwise swimming of a bacterial swarm condensed into a circular band; (d) bacterial velocity map. Redrawn from Peng et al. [215].

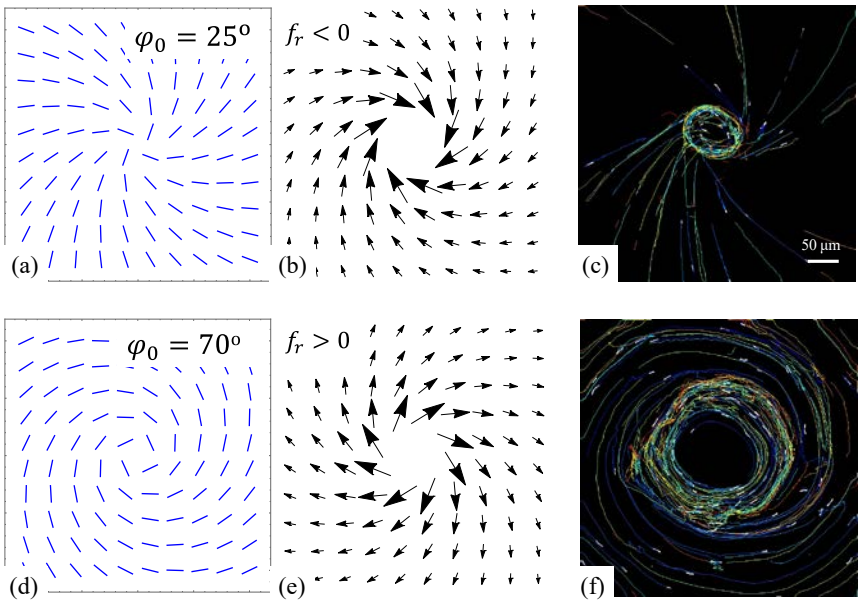

Fig.31. Patterned director of an $m = +1$ spiral vortex with (a) $\varphi_0 = 25^o$, directs the active force (b) clockwise and towards the center, (c) causing the polar swirl of bacteria to shrink; in contrast, a vortex with (d) $\varphi_0 = 70^o$, directs (e) the active force and (f) unipolar swirls outwards. Redrawn from Koizumi et al. [221].

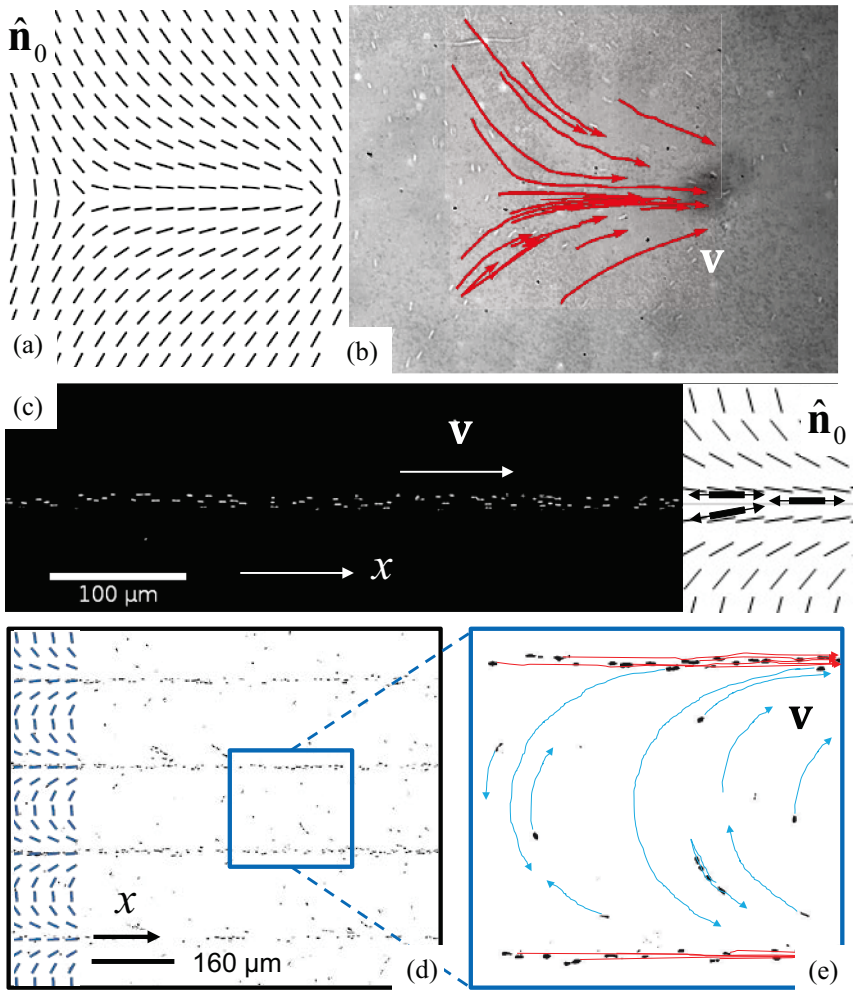

Fig.32. Linear transport of *B. subtilis* microswimmers in patterned director fields: (a,b) bacteria swim from -1/2 defect towards the +1/2 defect; (c) splay-bend C-stripe pattern condenses bacteria into a polar jet that moves towards the converging side of splay along the *x*-axis; (d,e) array of C-stripes forms polar jets of bacteria in splay regions moving along the *x*-axis; bacteria that move against the jet are recycled by U-turns of the bend regions to swim from left to right. Experimental results by C. Peng (b) and T. Turiv (c-e). Redrawn from Peng et al. [215] and Turiv et al. [374].

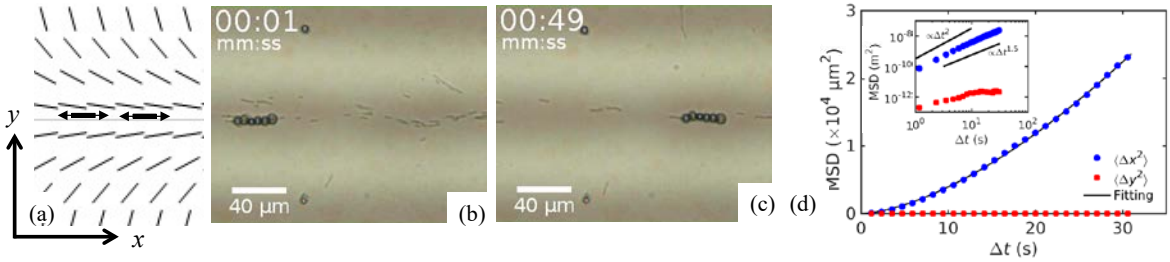

Fig.33. Cargo transport by a rectilinear bacterial jet condensed and guided by (a) splay-bend stripe; (b,c) optical microscope images taken 48 s apart of a cargo train of six 5 µm glass spheres transported by the bacterial jet. The particles are relocated from left to right by the incoming unidirectional bacterial flow. (d) Mean squared displacement (MSD) of a single 5 µm glass sphere being transported by a bacterial jet. Redrawn from Turiv et al. [374].

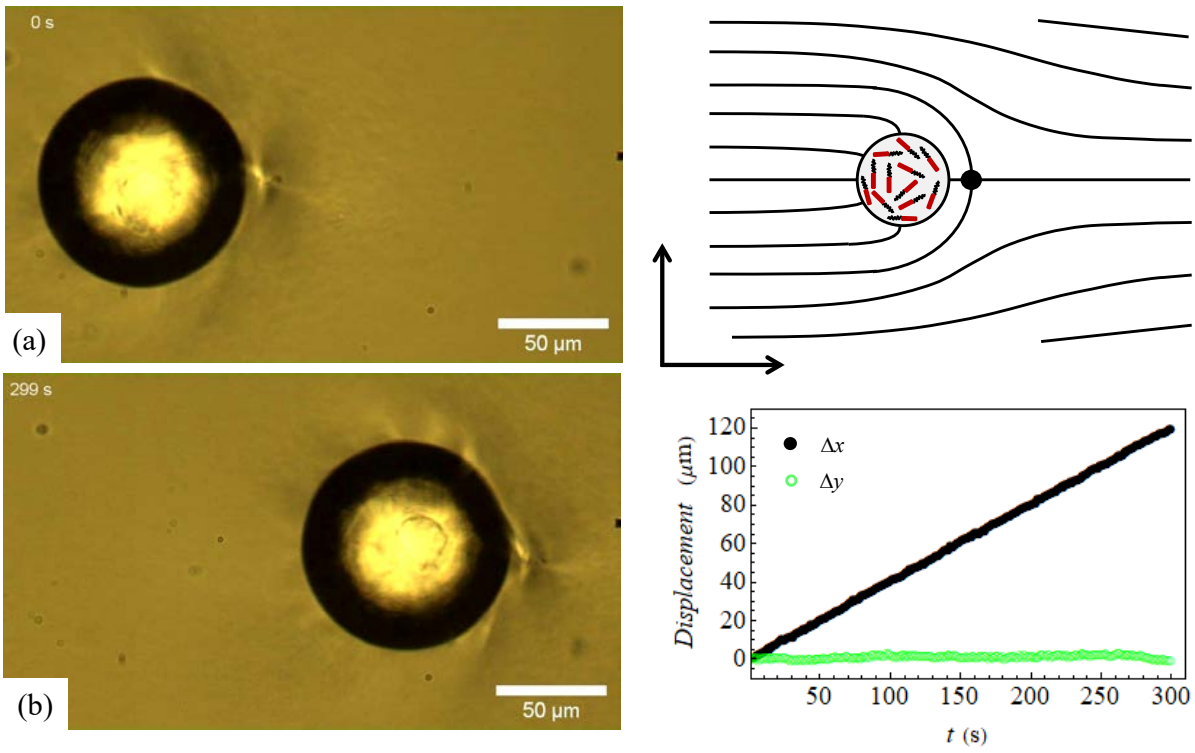

Fig.34. Active droplet with a bacterial *B. subtilis* dispersion (a,b) propels itself in a nematic 5CB; (c) director structure with a hyperbolic hedgehog outside the droplet; (d) displacement vs time: the droplet moves along the overall director field alignment, which is the x-axis. Redrawn from Rajabi et al. [546].

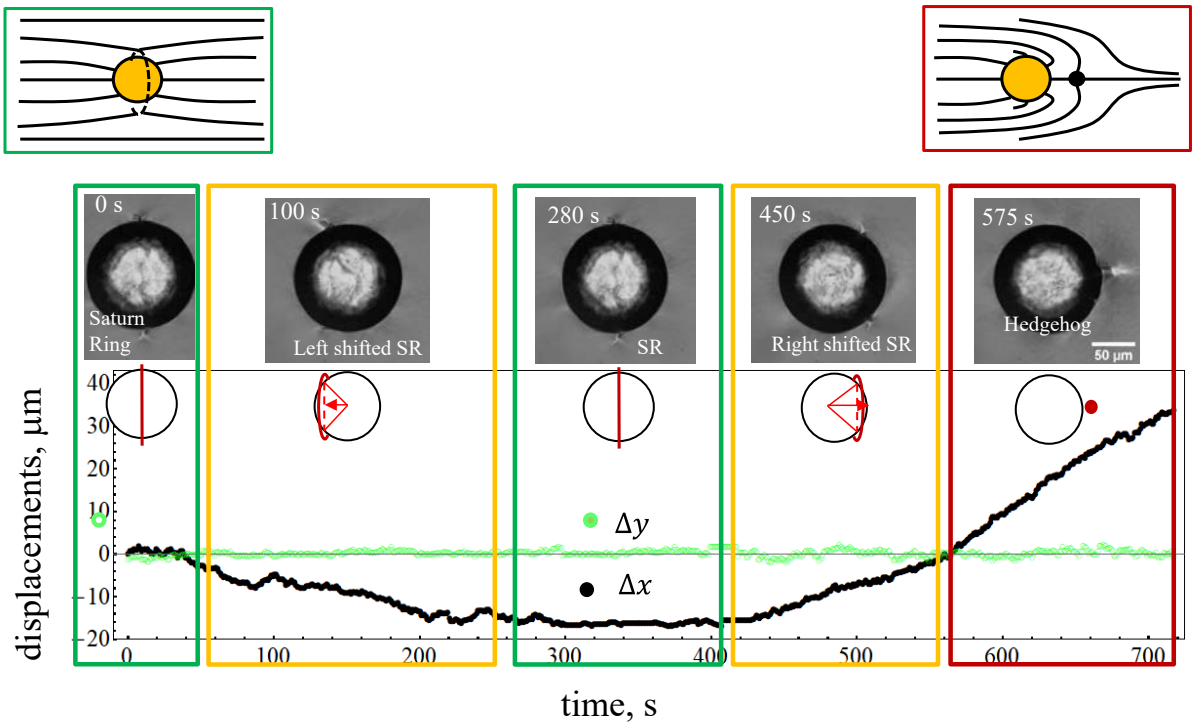

Fig.35. Propulsion ability of the active droplet depends on whether the director structure outside is a hyperbolic hedgehog or a Saturn ring. The Saturn ring of quadrupolar symmetry produces no net displacement, but once the ring shifts from the equatorial position towards one of the poles, the droplet becomes motile since the surrounding director field is no longer fore-aft symmetric. Redrawn from Rajabi et al. [546].

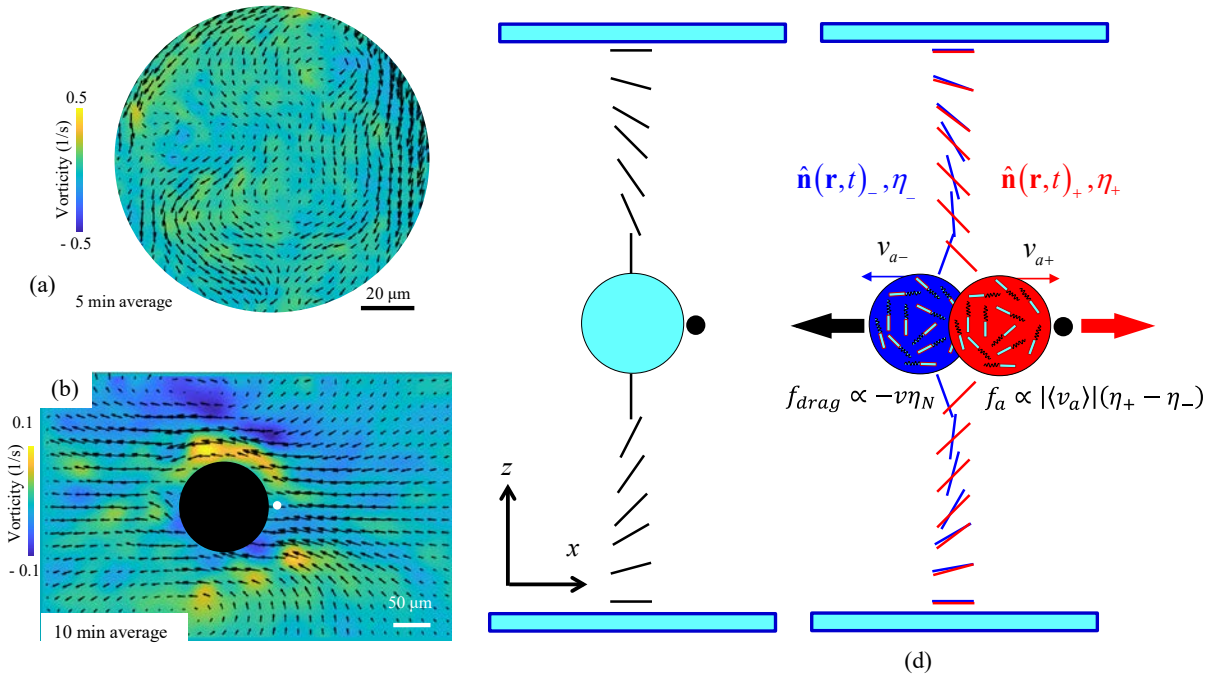

Fig.36. Active flows are (a) chaotic inside the droplet and (b) directionally rectified by the polar director configuration with the hyperbolic hedgehog outside the droplet; vorticity (shown by pseudocolors) and velocity (arrows) are averaged over 5 min in (a) and 10 min in (b); maximum velocity of flow is 1 μm/s in (a) and 0.2 μm/s in (b). (c) Scheme of the director distortions across the cell which contains an inactive droplet with a hyperbolic hedgehog on the right hand side (the core is shown by a black disk); the director realigns from being parallel to the z-axis to being parallel to the x-axis as one goes from the droplet to the bounding plates. Note the left-right structural asymmetry. (d) Self-propulsion mechanism of an active droplet with a hedgehog. Bacterial activity-created flows directed to the right, $\mathbf{v}_{a+}$, and to the left, $\mathbf{v}_{a-}$, perturb the left-right asymmetric director field differently, yielding two different director configurations $\hat{\mathbf{n}}_+(\mathbf{r},t) \neq \hat{\mathbf{n}}_-(\mathbf{r},t)$ and two viscous resistances $\eta_+ \neq \eta_-$, which result in the rectified active force f. Redrawn from Rajabi et al. [546].

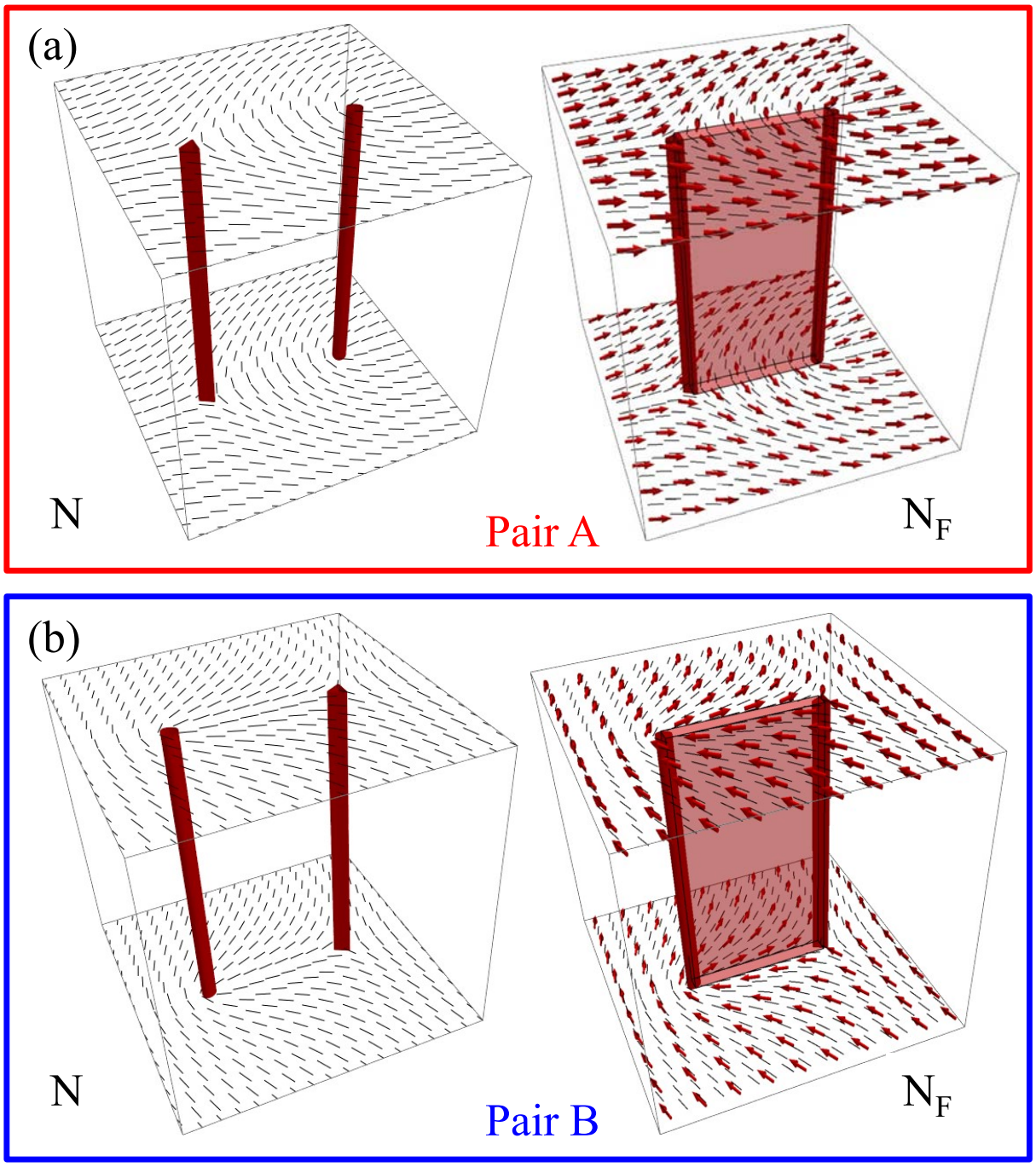

Fig.37. Pairs of $\pm 1/2$ disclinations of type A (a) and type B (b) in a nematic serve as seeds of domain walls in the ferroelectric nematic N_F. Redrawn from Lavrentovich [564].

REFERENCES

[1] D.-K. Yang and S.-T. Wu, *Fundamentals of Liquid Crystal Devices* (John Wiley & Sons, Chichester, England, 2006), pp. 394.

[2] P. G. de Gennes and J. Prost, *The Physics of Liquid Crystals* (Clarendon Press, Oxford, 1993), pp. 598.

[3] S. Ramaswamy, *The Mechanics and Statistics of Active Matter*, Annual Review of Condensed Matter Physics **1**, 323-345 (2010).

[4] M. C. Marchetti, J. F. Joanny, S. Ramaswamy, T. B. Liverpool, J. Prost, M. Rao, and R. A. Simha, *Hydrodynamics of soft active matter*, Reviews of Modern Physics **85**, 1143-1189 (2013).

[5] I. S. Aranson, *Active colloids*, Physics-Uspekhi **56**, 79-92 (2013).

[6] A. Doostmohammadi, J. Ignés-Mullol, J. M. Yeomans, and F. Sagués, *Active Nematics*, Nature Communications **9**, 3246 (2018).

[7] N. Lane, *The unseen world: reflections on Leeuwenhoek (1677) 'Concerning little animals'*, Philosophical Transactions of the Royal Society B-Biological Sciences **370**, 20140344 (2015).

[8] H. Gest, *The discovery of microorganisms by Robert Hooke and Antoni Van Leeuwenhoek, fellows of the Royal Society*, Notes and Records of the Royal Society of London **58**, 187-201 (2004).

[9] R. Brown, *A brief account of microscopical observations on the particles contained in the pollen of plants and the general existence of active molecules in organic and inorganic bodies*, Edinburgh New Philosophical Journal, 358-371 (1828).

[10] H. C. Berg, *Random Walks in Biology: New and Expanded Edition* (Princeton University Press, Princeton, NJ, 2018).

[11] E. Lauga and T. R. Powers, *The hydrodynamics of swimming microorganisms*, Reports on Progress in Physics **72**, 096601 (2009).

[12] E. Lauga, *Bacterial Hydrodynamics*, Annual Review of Fluid Mechanics **48**, 105-130 (2016).

[13] S. C. Takatori and J. F. Brady, *Forces, stresses and the (thermo?) dynamics of active matter*, Current Opinion in Colloid & Interface Science **21**, 24-33 (2016).

[14] C. J. O. Reichhardt and C. Reichhardt, *Ratchet Effects in Active Matter Systems*, Annual Review of Condensed Matter Physics, Vol 8 **8**, 51-75 (2017).

[15] D. Needleman and Z. Dogic, *Active matter at the interface between materials science and cell biology*, Nature Reviews Materials **2**, 17048 (2017).

[16] S. Ramaswamy, *Active matter*, Journal of Statistical Mechanics-Theory and Experiment (2017).

[17] B. Liebchen and H. Lowen, *Synthetic Chemotaxis and Collective Behavior in Active Matter*, Accounts of Chemical Research **51**, 2982-2990 (2018).

[18] K. Villa and M. Pumera, *Fuel-free light-driven micro/nanomachines: artificial active matter mimicking nature*, Chemical Society Reviews **48**, 4966-4978 (2019).

[19] F. J. Varnerey, E. Benet, L. Blue, A. K. Fajrial, S. L. Sridhar, J. S. Lum, G. Shakya, K. H. Song, A. N. Thomas, and M. A. Borden, *Biological active matter aggregates: Inspiration for smart colloidal materials*, Advances in Colloid and Interface Science **263**, 38-51 (2019).

[20] Y. Dou, K. Dhatt-Gauthier, and K. J. M. Bishop, *Thermodynamic costs of dynamic function in active soft matter*, Current Opinion in Solid State & Materials Science **23**, 28-40 (2019).

[21] A. Doostmohammadi and J. M. Yeomans, *Coherent motion of dense active matter*, European Physical Journal-Special Topics **227**, 2401-2411 (2019).

[22] M. Pishvar and R. L. Harne, *Foundations for Soft, Smart Matter by Active Mechanical Metamaterials*, Advanced Science **7**, 2001384 (2020).

[23] W. J. Liu, X. Chen, X. L. Lu, J. Wang, Y. A. Zhang, and Z. W. Gu, *From Passive Inorganic Oxides to Active Matters of Micro/Nanomotors*, Advanced Functional Materials **30**, 2003195 (2020).

[24] W. Wang, X. L. Lv, J. L. Moran, S. F. Duan, and Z. C. Zhou, *A practical guide to active colloids: choosing synthetic model systems for soft matter physics research*, Soft Matter **16**, 3846-3868 (2020).
[25] M. R. Shaebani, A. Wysocki, R. G. Winkler, G. Gompper, and H. Rieger, *Computational models for active matter*, Nature Reviews Physics **2**, 181-199 (2020).
[26] A. Ghosh, W. N. Xu, N. Gupta, and D. H. Gracias, *Active matter therapeutics*, Nano Today **31**, 100836 (2020).
[27] T. Speck, *Collective forces in scalar active matter*, Soft Matter **16**, 2652-2663 (2020).
[28] F. Cichos, K. Gustavsson, B. Mehlig, and G. Volpe, *Machine learning for active matter*, Nature Machine Intelligence **2**, 94-103 (2020).
[29] M. Bar, R. Grossmann, S. Heidenreich, and F. Peruani, *Self-Propelled Rods: Insights and Perspectives for Active Matter*, Annual Review of Condensed Matter Physics, Vol 11, 2020 **11**, 441-466 (2020).
[30] R. Zhang, A. Mozaffari, and J. J. de Pablo, *Autonomous materials systems from active liquid crystals*, Nature Reviews Materials, https://doi.org/10.1038/s41578-41020-00272-x (2021).
[31] T. Turiv, I. Lazo, A. Brodin, B. I. Lev, V. Reiffenrath, V. G. Nazarenko, and O. D. Lavrentovich, *Effect of Collective Molecular Reorientations on Brownian Motion of Colloids in Nematic Liquid Crystal*, Science **342**, 1351-1354 (2013).
[32] R. J. Mandle, S. J. Cowling, and J. W. Goodby, *A nematic to nematic transformation exhibited by a rod-like liquid crystal*, Physical Chemistry Chemical Physics **19**, 11429-11435 (2017).
[33] A. Mertelj, L. Cmok, N. Sebastian, R. J. Mandle, R. R. Parker, A. C. Whitwood, J. W. Goodby, and M. Copic, *Splay Nematic Phase*, Physical Review X **8**, 041025 (2018).
[34] H. Nishikawa, K. Shiroshita, H. Higuchi, Y. Okumura, Y. Haseba, S. I. Yamamoto, K. Sago, and H. Kikuchi, *A Fluid Liquid-Crystal Material with Highly Polar Order*, Advanced Materials **29**, 1702354 (2017).
[35] X. Chen, E. Korblova, D. P. Dong, X. Y. Wei, R. F. Shao, L. Radzihovsky, M. A. Glaser, J. E. Maclennan, D. Bedrov, D. M. Walba, and N. A. Clark, *First -principles experimental demonstration of ferroelectricity in a thermotropic nematic liquid crystal: Polar domains and striking electro-optics*, Proceedings of the National Academy of Sciences of the United States of America **117**, 14021-14031 (2020).
[36] A. Jákli, O. D. Lavrentovich, and J. V. Selinger, *Physics of liquid crystals of bent-shaped molecules*, Reviews of Modern Physics **90**, 045004 (2018).
[37] H. Morales-Navarrete, H. Nonaka, A. Scholich, F. Segovia-Miranda, W. de Back, K. Meyer, R. L. Bogorad, V. Koteliansky, L. Brusch, Y. Kalaidzidis, F. Julicher, B. M. Friedrich, and M. Zerial, *Liquid-crystal organization of liver tissue*, Elife **8**, e44860 (2019).
[38] M. Kleman and O. D. Lavrentovich, *Soft Matter Physics: An Introduction* (Springer, New York, 2003), Partially Ordered Systems, pp. 638.
[39] Á. Buka, N. Éber, W. Pesch, and L. Kramer, *Convective patterns in liquid crystals driven by electric field - An overview of the onset behavior*, Self-Assembly, Pattern Formation and Growth Phenomena in Nano-Systems **218**, 55-82 (2006).
[40] S. Kai and W. Zimmermann, *Pattern Dynamics in the Electrohydrodynamics of Nematic Liquid-Crystals - Defect Patterns, Transition to Turbulence and Magnetic-Field Effects*, Progress of Theoretical Physics Supplement, 458-492 (1989).
[41] N. Éber, P. Salamon, and Á. Buka, *Electrically induced patterns in nematics and how to avoid them*, Liquid Crystals Reviews **4**, 102-135 (2016).
[42] E. Guyon, J.-P. Hulin, L. Petit, and C. D. Mitescu, *Physical Hydrodynamics* (Oxford University Press, New York, 2001), pp. 506.
[43] W. Helfrich, *Conduction-Induced Alignment of Nematic Liquid Crystals - Basic Model and Stability Considerations*, Journal of Chemical Physics **51**, 4092-4105 (1969).
[44] M. V. Kurik and O. D. Lavrentovich, *Defects in Liquid-Crystals - Homotopy-Theory and Experimental Investigations*, Uspekhi Fizicheskikh Nauk **154**, 381-431 (1988).

[45] B. X. Li, V. Borshch, R. L. Xiao, S. Paladugu, T. Turiv, S. V. Shiyanovskii, and O. D. Lavrentovich, *Electrically-driven three-dimensional solitary waves as director bullets in nematic liquid crystals*, Nature Communications **9**, 2912 (2018).
[46] B. X. Li, R. L. Xiao, S. Paladugu, S. V. Shiyanovskii, and O. D. Lavrentovich, *Three-dimensional solitary waves with electrically tunable direction of propagation in nematics*, Nature Communications **10**, 3749 (2019).
[47] Y. Shen and I. Dierking, *Dynamics of electrically driven solitons in nematic and cholesteric liquid crystals*, Communications Physics **3**, 14 (2020).
[48] B. X. Li, R. L. Xiao, S. V. Shiyanovskii, and O. D. Lavrentovich, *Soliton-induced liquid crystal enabled electrophoresis*, Physical Review Research **2**, 013178 (2020).
[49] L. Lam and J. Prost, *Solitons in Liquid Crystals* (Springer-Verlag, New York, 1992), pp. 338.
[50] O. D. Lavrentovich and M. Kleman, *Cholesteric Liquid Crystals: Defects and Topology*, in *Chirality in Liquid Crystals*, edited by K. H.-S., and B. C. (Springer-Verlag, New York, 2001), pp. 115-158.
[51] M. Kleman, *Points, Lines and Walls in liquid crystals, magnetic systems and various ordered media* (John Wiley &Sons, Chichester, 1983), pp. 322.
[52] A. A. Belavin and A. M. Polyakov, *Metastable States of 2-Dimensional Isotropic Ferromagnets*, JETP Letters **22**, 245-247 (1975).
[53] A. N. Bogdanov, U. K. Rossler, and A. A. Shestakov, *Skyrmions in nematic liquid crystals*, Physical Review E **67**, 016602 (2003).
[54] T. Dauxois and M. Peyrard, *Physics of solitons* (Cambridge University Press, Cambridge, UK ; New York, 2006), pp. 422.
[55] L. Lin, C. Q. Shu, and G. Xu, *Generation and Detection of Propagating Solitons in Shearing Liquid-Crystals*, Journal of Statistical Physics **39**, 633-652 (1985).
[56] G. Z. Zhu, X. Z. Liu, and N. B. Bai, *Director Waves and Their Accompanying Flow*, Physics Letters A **117**, 229-233 (1986).
[57] J. T. Gleeson, P. Palffy-Muhoray, and W. Van Saarloos, *Propagation of Excitations Induced by Shear-Flow in Nematic Liquid-Crystals*, Physical Review A **44**, 2588-2595 (1991).
[58] S. Copar, Z. Kos, T. Emersic, and U. Tkalec, *Microfluidic control over topological states in channel-confined nematic flows*, Nature Communications **11** (2020).
[59] G. H. Derrick, *Comments on Nonlinear Wave Equations as Models for Elementary Particles*, Journal of Mathematical Physics **5**, 1252-1254 (1964).
[60] W. E. L. Haas and J. E. Adams, *New Optical Storage Mode in Liquid-Crystals*, Applied Physics Letters **25**, 535-537 (1974).
[61] W. E. L. Haas and J. E. Adams, *Electrically Variable Diffraction in Spherulitic Liquid-Crystals*, Applied Physics Letters **25**, 263-264 (1974).
[62] M. Kawachi, O. Kogure, and Y. Kato, *Bubble-Domain Texture of a Liquid-Crystal*, Japanese Journal of Applied Physics **13**, 1457-1458 (1974).
[63] Y. Bouligand, B. Derrida, V. Poenaru, Y. Pomeau, and G. Toulouse, *Distortions with Double Topological Character - Case of Cholesterics*, Journal De Physique **39**, 863-867 (1978).
[64] I. I. Smalyukh, B. I. Senyuk, P. Palffy-Muhoray, O. D. Lavrentovich, H. Huang, E. C. Gartland, V. H. Bodnar, T. Kosa, and B. Taheri, *Electric-field-induced nematic-cholesteric transition and three-dimensional director structures in homeotropic cells*, Physical Review E **72**, 061707 (2005).
[65] I. I. Smalyukh, Y. Lansac, N. A. Clark, and R. P. Trivedi, *Three-dimensional structure and multistable optical switching of triple-twisted particle-like excitations in anisotropic fluids*, Nature Materials **9**, 139-145 (2010).
[66] P. J. Ackerman, T. Boyle, and I. I. Smalyukh, *Squirming motion of baby skyrmions in nematic fluids*, Nature Communications **8**, 673 (2017).

[67] H. R. O. Sohn, P. J. Ackerman, T. J. Boyle, G. H. Sheetah, B. Fornberg, and I. I. Smalyukh, *Dynamics of topological solitons, knotted streamlines, and transport of cargo in liquid crystals*, Physical Review E **97**, 052701 (2018).
[68] J. S. B. Tai and I. I. Smalyukh, *Three-dimensional crystals of adaptive knots*, Science **365**, 1449-1453 (2019).
[69] Y. B. Guo, S. Afghah, J. Xiang, O. D. Lavrentovich, R. L. B. Selinger, and Q. H. Wei, *Cholesteric liquid crystals in rectangular microchannels: skyrmions and stripes*, Soft Matter **12**, 6312-6320 (2016).
[70] A. Nych, J.-I. Fukuda, U. Ognysta, S. Zumer, and I. Musevic, *Spontaneous formation and dynamics of half-skyrmions in a chiral liquid-crystal film*, Nature Physics **13**, 1215–1220 (2017).
[71] G. Posnjak, S. Čopar, and I. Muševič, *Points, skyrmions and torons in chiral nematic droplets*, Scientific Reports **6**, 26361 (2016).
[72] A. O. Leonov, I. E. Dragunov, U. K. Rossler, and A. N. Bogdanov, *Theory of skyrmion states in liquid crystals*, Physical Review E **90**, 042502 (2014).
[73] S. Afghah and J. V. Selinger, *Theory of helicoids and skyrmions in confined cholesteric liquid crystals*, Physical Review E **96**, 012708 (2017).
[74] A. Ryabchun and A. Bobrovsky, *Cholesteric Liquid Crystal Materials for Tunable Diffractive Optics*, Advanced Optical Materials **6**, 1800335 (2018).
[75] I. I. Smalyukh, *Review: knots and other new topological effects in liquid crystals and colloids*, Reports on Progress in Physics **83**, 106601 (2020).
[76] P. E. Cladis and M. Kleman, *Cholesteric Domain Texture*, Molecular Crystals and Liquid Crystals **16**, 1-20 (1972).
[77] P. Oswald, J. Baudry, and S. Pirkl, *Static and dynamic properties of cholesteric fingers in electric field*, Physics Reports-Review Section of Physics Letters **337**, 67-96 (2000).
[78] P. Oswald, A. Dequidt, and G. Poy, *Chapter 3: Thermomechanical effects in liquid crystals*, in *Liquid crystals: New perspectives*, edited by P. Pieranski, and M. H. Godinho (ISTE Ltd and John Wiley & Sons, Inc., London, UK, 2021), pp. 117-191.
[79] M. J. Press and A. S. Arrott, *Static Strain Waves in Cholesteric Liquid-Crystals - Response to Magnetic and Electric-Fields*, Molecular Crystals and Liquid Crystals **37**, 81-99 (1976).
[80] J. Baudry, S. Pirkl, and P. Oswald, *Looped finger transformation in frustrated cholesteric liquid crystals*, Physical Review E **59**, 5562-5571 (1999).
[81] L. Gil and J. M. Gilli, *Surprising dynamics of some cholesteric liquid crystal patterns*, Physical Review Letters **80**, 5742-5745 (1998).
[82] S. V. Shiyanovskii, I. I. Smalyukh, and O. D. Lavrentovich, *Computer simulations and fluorescence confocal polarizing microscopy of structures in cholesteric liquid crystals*, in *Defects in Liquid Crystals: Computer Simulations, Theory and Experiments.*, edited by O. D. Lavrentovich, P. Pasini, C. Zannoni, and S. Zumer (Kluwer Academic Publishers, Dordrecht, 2001), pp. 229-270.
[83] E. C. Gartland, H. Huang, O. D. Lavrentovich, P. Palffy-Muhoray, I. I. Smalyukh, T. Kosa, and B. Taheri, *Electric-Field Induced Transitions in a Cholesteric Liquid-Crystal Film with Negative Dielectric Anisotropy*, Journal of Computational and Theoretical Nanoscience **7**, 709-725 (2010).
[84] G. Durey, H. R. O. Sohn, P. J. Ackerman, E. Brasselet, I. I. Smalyukh, and T. Lopez-Leon, *Topological solitons, cholesteric fingers and singular defect lines in Janus liquid crystal shells*, Soft Matter **16**, 2669-2682 (2020).
[85] D. Voloschenko and O. D. Lavrentovich, *Optical vortices generated by dislocations in a cholesteric liquid crystal*, Optics Letters **25**, 317-319 (2000).
[86] S. V. Shiyanovskii, D. Voloschenko, T. Ishikawa, and O. D. Lavrentovich, *Director structures of cholesteric diffraction gratings*, Molecular Crystals and Liquid Crystals **358**, 225-236 (2001).

[87] I. I. Smalyukh, S. V. Shiyanovskii, and O. D. Lavrentovich, *Three-dimensional imaging of orientational order by fluorescence confocal polarizing microscopy*, Chemical Physics Letters **336**, 88-96 (2001).
[88] I. I. Smalyukh and O. D. Lavrentovich, *Three-dimensional director structures of defects in Grandjean-Cano wedges of cholesteric liquid crystals studied by fluorescence confocal polarizing microscopy*, Physical Review E **66**, 051703 (2002).
[89] J. Friedel and M. Kleman, *Application of dislocation theory to liquid crystals (National Bureau of Standards Special Publication no. 317)*, in *Fundamental aspects of dislocation theory*, edited by R. D. W. J.A. Simmons, and R. Bullough (US National Bureau of Standards, Washington, D.C., 1970), pp. 607-636.
[90] T. Akahane and T. Tako, *Molecular Alignment of Bubble Domains in Cholesteric-Nematic Mixtures*, Japanese Journal of Applied Physics **15**, 1559-1560 (1976).
[91] I. E. Dzyaloshinskii, *Theory of Helicoidal Structures in Antiferromagnets .1. Nonmetals*, Soviet Physics JETP-USSR **19**, 960-971 (1964).
[92] N. Manton and P. Sutcliffe, *Topological solitons* (Cambridge, Cambridge, U.K. ; New York, 2004), Cambridge monographs on mathematical physics, pp. 493.
[93] J.-I. Fukuda and S. Žumer, *Quasi-two-dimensional Skyrmion lattices in a chiral nematic liquid crystal*, Nature Communications **2**, 246 (2011).
[94] T. H. Skyrme, *A Non-Linear Field Theory*, Proceedings of the Royal Society of London Series a-Mathematical and Physical Sciences **260**, 127-138 (1961).
[95] A. Duzgun, J. V. Selinger, and A. Saxena, *Comparing skyrmions and merons in chiral liquid crystals and magnets*, Physical Review E **97**, 062706 (2018).
[96] H. R. O. Sohn, S. M. Vlasov, V. M. Uzdin, A. O. Leonov, and I. I. Smalyukh, *Real-space observation of skyrmion clusters with mutually orthogonal skyrmion tubes*, Physical Review B **100**, 104401 (2019).
[97] T. Machon and G. P. Alexander, *Woven Nematic Defects, Skyrmions, and the Abelian Sandpile Model*, Physical Review Letters **121**, 237801 (2018).
[98] T. Machon and G. P. Alexander, *Umbilic Lines in Orientational Order*, Physical Review X **6**, 011033 (2016).
[99] G. De Matteis, L. Martina, and V. Turco, *Skyrmion States in Chiral Liquid Crystals*, Theoretical and Mathematical Physics **196**, 1150-1163 (2018).
[100] J. Fukuda and S. Žumer, *Reflection spectra and near-field images of a liquid crystalline half-Skyrmion lattice*, Optics Express **26**, 1174-1184 (2018).
[101] A. Duzgun, A. Saxena, and J. V. Selinger, *Alignment-induced reconfigurable walls for patterning and assembly of liquid crystal skyrmions*, Physical Review Research **3**, L012005 (2021).
[102] A. Duzgun and C. Nisoli, *Skyrmion Spin Ice in Liquid Crystals*, Physical Review Letters **126** (2021).
[103] J. M. Gilli and L. Gil, *Static and Dynamic Textures Obtained under an Electric-Field in the Neighborhood of the Winding Transition of a Strongly Confined Cholesteric*, Liquid Crystals **17**, 1-15 (1994).
[104] L. Gil and S. Thiberge, *Is the electromechanical coupling the driving force for the perpendicular drift of first class cholesteric finger?*, Journal De Physique Ii **7**, 1499-1508 (1997).
[105] P. Ribiere, P. Oswald, and S. Pirkl, *Crawling and Spiraling of Cholesteric Fingers in Electric-Field*, Journal De Physique Ii **4**, 127-143 (1994).
[106] J. Baudry, S. Pirkl, and P. Oswald, *Effect of the electric conductivity on the drift velocity of the cholesteric fingers of the second type in confined geometry*, Physical Review E **60**, 2990-2993 (1999).
[107] O. S. Tarasov, A. P. Krekhov, and L. Kramer, *Dynamics of cholesteric structures in an electric field*, Physical Review E **68**, 031708 (2003).
[108] H. R. O. Sohn, C. D. D. Liu, and I. I. Smalyukh, *Schools of skyrmions with electrically tunable elastic interactions*, Nature Communications **10** (2019).
[109] M. Peccianti and G. Assanto, *Nematicons*, Physics Reports-Review Section of Physics Letters **516**, 147-208 (2012).

[110] I. B. Burgess, M. Peccianti, G. Assanto, and R. Morandotti, *Accessible Light Bullets via Synergetic Nonlinearities*, Physical Review Letters **102**, 203903 (2009).
[111] M. Peccianti, I. B. Burgess, G. Assanto, and R. Morandotti, *Space-time bullet trains via modulation instability and nonlocal solitons*, Optics Express **18**, 5934-5941 (2010).
[112] G. Assanto, *Nematicons: reorientational solitons from optics to photonics*, Liquid Crystals Reviews **6**, 170-194 (2018).
[113] U. A. Laudyn, M. Kwasny, M. A. Karpierz, and G. Assanto, *Electro-optic quenching of nematicon fluctuations*, Optics Letters **44**, 167-170 (2019).
[114] A. Madani, J. Beeckman, and K. Neyts, *Theoretical study of reorientation and torque of liquid crystal molecules under influence of external electric field and experimentally generation of spatial optical soliton beam and getting a sharp switching in chiral nematic liquid crystal*, Optik **124**, 3983-3986 (2013).
[115] N. V. Tabiryan, A. V. Sukhov, and B. Y. Zeldovich, *Orientational Optical Nonlinearity of Liquid-Crystals*, Molecular Crystals and Liquid Crystals **136**, 1-139 (1986).
[116] G. I. Stegeman and M. Segev, *Optical spatial solitons and their interactions: Universality and diversity*, Science **286**, 1518-1523 (1999).
[117] I. N. Towers, B. A. Malomed, and F. W. Wise, *Light bullets in quadratic media with normal dispersion at the second harmonic*, Physical Review Letters **90**, 123902 (2003).
[118] D. Mihalache, D. Mazilu, F. Lederer, B. A. Malomed, Y. V. Kartashov, L. C. Crasovan, and L. Torner, *Stable spatiotemporal solitons in Bessel optical lattices*, Physical Review Letters **95**, 023902 (2005).
[119] D. Mihalache, D. Mazilu, F. Lederer, B. A. Malomed, Y. V. Kartashov, L. C. Crasovan, and L. Torner, *Three-dimensional spatiotemporal optical solitons in nonlocal nonlinear media*, Physical Review E **73**, 025601 (2006).
[120] S. Minardi, F. Eilenberger, Y. V. Kartashov, A. Szameit, U. Ropke, J. Kobelke, K. Schuster, H. Bartelt, S. Nolte, L. Torner, F. Lederer, A. Tunnermann, and T. Pertsch, *Three-Dimensional Light Bullets in Arrays of Waveguides*, Physical Review Letters **105**, 263901 (2010).
[121] O. Lahav, O. Kfir, P. Sidorenko, M. Mutzafi, A. Fleischer, and O. Cohen, *Three-Dimensional Spatiotemporal Pulse-Train Solitons*, Physical Review X **7**, 041051 (2017).
[122] B. A. Malomed, D. Mihalache, F. Wise, and L. Torner, *Spatiotemporal optical solitons*, Journal of Optics B - Quantum and Semiclassical Optics **7**, R53-R72 (2005).
[123] B. Malomed, L. Torner, F. Wise, and D. Mihalache, *On multidimensional solitons and their legacy in contemporary atomic, molecular and optical physics*, Journal of Physics B - Atomic Molecular and Optical Physics **49**, 170502 (2016).
[124] Y. Silberberg, *Collapse of Optical Pulses*, Optics Letters **15**, 1282-1284 (1990).
[125] R. Mcleod, S. Blair, and K. Wagner, *Asymmetric Light Bullet Dragging Logic*, Optical Computing **139**, 657-660 (1995).
[126] H. G. Purwins, H. U. Bödeker, and S. Amiranashvili, *Dissipative solitons*, Advances in Physics **59**, 485-701 (2010).
[127] O. Descalzi, M. G. Clerc, S. Residori, and G. Assanto, *Localized States in Physics: Solitons and Patterns* (Springer, New York, 2011).
[128] E. Knobloch, *Spatial Localization in Dissipative Systems*, Annual Review of Condensed Matter Physics **6**, 325-359 (2015).
[129] H. U. Bödeker, M. C. Röttger, A. W. Liehr, T. D. Frank, R. Friedrich, and H. G. Purwins, *Noise-covered drift bifurcation of dissipative solitons in a planar gas-discharge system*, Physical Review E **67**, 056220 (2003).
[130] S. Aya and F. Araoka, *Kinetics of motile solitons in nematic liquid crystals*, Nature Communications **11**, 3248 (2020).
[131] A. Earls and M. C. Calderer, *Three-dimensional solitons in nematic liquid crystals, Part I: Linear analysis*, arXiv:1910.05959v1 (2019).

[132] S. A. Pikin, *On the Structural Instability of a Nematic in an Alternating Electric Field and Its Connection with Convection and the Flexoelectric Effect*, Journal of Surface Investigation: X-ray, Synchrotron and Neutron Techniques **13**, 1078-1082 (2019).
[133] P. G. de Gennes and J. Prost, *The Physics of Liquid Crystals* (Clarendon Press, 1995).
[134] E. Dubois-Violette, P. G. de Gennes, and O. Parodi, *Hydrodynamic instabilities of nematic liquid crystals under A. C. electric fields*, J. Phys. France **32**, 305-317 (1971).
[135] R. B. Meyer, *Piezoelectric Effects in Liquid Crystals*, Physical Review Letters **22**, 918-920 (1969).
[136] J. Prost and J. P. Marcerou, *On the microscopic interpretation of flexoelectricity*, Journal De Physique **38**, 315-324 (1977).
[137] A. Krekhov, W. Pesch, N. Éber, T. Toth-Katona, and Á. Buka, *Nonstandard electroconvection and flexoelectricity in nematic liquid crystals*, Physical Review E **77**, 021705 (2008).
[138] A. Krekhov, W. Pesch, and Á. Buka, *Flexoelectricity and pattern formation in nematic liquid crystals*, Physical Review E **83**, 051706 (2011).
[139] Y. Shen and I. Dierking, *Dynamic dissipative solitons in nematics with positive anisotropies*, Soft Matter **16**, 5325-5333 (2020).
[140] Y. Garbovskiy, *Conventional and unconventional ionic phenomena in tunable soft materials made of liquid crystals and nanoparticles*, Nano Express **2**, 012004 (2021).
[141] G. M. Whitesides, *The origins and the future of microfluidics*, Nature **442**, 368-373 (2006).
[142] H. A. Stone, A. D. Stroock, and A. Ajdari, *Engineering flows in small devices: Microfluidics toward a lab-on-a-chip*, Annual Review of Fluid Mechanics **36**, 381-411 (2004).
[143] D. Psaltis, S. R. Quake, and C. H. Yang, *Developing optofluidic technology through the fusion of microfluidics and optics*, Nature **442**, 381-386 (2006).
[144] A. J. deMello, *Control and detection of chemical reactions in microfluidic systems*, Nature **442**, 394-402 (2006).
[145] J. M. Karlinsey, *Sample introduction techniques for microchip electrophoresis: A review*, Analytica Chimica Acta **725**, 1-13 (2012).
[146] P. Sajeesh and A. K. Sen, *Particle separation and sorting in microfluidic devices: a review*, Microfluidics and Nanofluidics **17**, 1-52 (2014).
[147] J. El-Ali, P. K. Sorger, and K. F. Jensen, *Cells on chips*, Nature **442**, 403-411 (2006).
[148] H. Craighead, *Future lab-on-a-chip technologies for interrogating individual molecules*, Nature **442**, 387-393 (2006).
[149] H. Morgan and N. G. Green, *AC Electrokinetics: colloids and nanoparticles* (Research Studies Press Ltd., Baldock, 2003), Vol. 2, Microtechnology and Microsystems series, pp. 324.
[150] W. B. Russel, D. A. Saville, and W. R. Schowalter, *Colloidal Dispersions* (Cambridge University Press, Cambridge, 1989), pp. 526.
[151] A. Ramos, *Electrokinetics and Electrohydrodynamics in Microsystems* (Springer, Wien, 2011), Vol. 530, CISM Courses and Lectures, pp. 298.
[152] S. S. Dukhin, N. A. Mishchuk, A. A. Tarovskii, and A. A. Baran, *Electrophoresis of the 2nd Kind*, Colloid Journal of the Ussr **49**, 544-545 (1987).
[153] S. S. Dukhin, N. A. Mishchuk, and P. V. Takhistov, *Electroosmosis of the 2nd Kind and Unrestricted Current Increase in the Mixed Monolayer of an Ion-Exchanger*, Colloid Journal of the Ussr **51**, 540-542 (1989).
[154] T. M. Squires and M. Z. Bazant, *Induced-charge electro-osmosis*, Journal of Fluid Mechanics **509**, 217-252 (2004).
[155] T. M. Squires and M. Z. Bazant, *Breaking symmetries in induced-charge electro-osmosis and electrophoresis*, Journal of Fluid Mechanics **560**, 65-101 (2006).
[156] S. Gangwal, O. J. Cayre, M. Z. Bazant, and O. D. Velev, *Induced-charge electrophoresis of metallodielectric particles*, Physical Review Letters **100**, 058302 (2008).

[157] M. Z. Bazant and T. M. Squires, *Induced-charge electrokinetic phenomena*, Current Opinion in Colloid & Interface Science **15**, 203-213 (2010).
[158] M. Z. Bazant and T. M. Squires, *Induced-charge electrokinetic phenomena: Theory and microfluidic applications*, Physical Review Letters **92**, 066101 (2004).
[159] C. L. Zhao and C. Yang, *Electrokinetics of non-Newtonian fluids: A review*, Advances in Colloid and Interface Science **201**, 94-108 (2013).
[160] A. Ramos, H. Morgan, N. G. Green, and A. Castellanos, *AC electric-field-induced fluid flow in microelectrodes*, Journal of Colloid and Interface Science **217**, 420-422 (1999).
[161] V. A. Murtsovkin and G. I. Mantrov, *Steady Flows in the Neighborhood of a Drop of Mercury with the Application of a Variable External Electric-Field*, Colloid Journal of the Ussr **53**, 240-244 (1991).
[162] N. I. Gamayunov, G. I. Mantrov, and V. A. Murtsovkin, *Study of Flows Induced in the Vicinity of Conducting Particles by an External Electric-Field*, Colloid Journal of the Ussr **54**, 20-23 (1992).
[163] C. H. Peng, I. Lazo, S. V. Shiyanovskii, and O. D. Lavrentovich, *Induced-charge electro-osmosis around metal and Janus spheres in water: Patterns of flow and breaking symmetries*, Physical Review E **90**, 051002 (2014).
[164] C. K. Harnett, J. Templeton, K. A. Dunphy-Guzman, Y. M. Senousy, and M. P. Kanouff, *Model based design of a microfluidic mixer driven by induced charge electroosmosis*, Lab on a Chip **8**, 565-572 (2008).
[165] J. A. Levitan, S. Devasenathipathy, V. Studer, Y. X. Ben, T. Thorsen, T. M. Squires, and M. Z. Bazant, *Experimental observation of induced-charge electro-osmosis around a metal wire in a microchannel*, Colloids and Surfaces a-Physicochemical and Engineering Aspects **267**, 122-132 (2005).
[166] C. Canpolat, S. Z. Qian, and A. Beskok, *Micro-PIV measurements of induced-charge electro-osmosis around a metal rod*, Microfluidics and Nanofluidics **14**, 153-162 (2013).
[167] C. Canpolat, M. K. Zhang, W. Rosen, S. Z. Qian, and A. Beskok, *Induced-Charge Electroosmosis Around Touching Metal Rods*, Journal of Fluids Engineering-Transactions of the Asme **135**, 021103 (2013).
[168] A. Boymelgreen, G. Yossifon, S. Park, and T. Miloh, *Spinning Janus doublets driven in uniform ac electric fields*, Physical Review E **89**, 011003 (2014).
[169] E. Yariv, *Induced-charge electrophoresis of nonspherical particles*, Physics of Fluids **17**, 051702 (2005).
[170] H. Zhao and H. H. Bau, *On the effect of induced electro-osmosis on a cylindrical particle next to a surface*, Langmuir **23**, 4053-4063 (2007).
[171] D. Saintillan, E. Darve, and E. S. G. Shaqfeh, *Hydrodynamic interactions in the induced-charge electrophoresis of colloidal rod dispersions*, Journal of Fluid Mechanics **563**, 223-259 (2006).
[172] H. Zhao and H. H. Bau, *Microfluidic chaotic stirrer utilizing induced-charge electro-osmosis*, Physical Review E **75**, 066217 (2007).
[173] O. D. Lavrentovich, I. Lazo, and O. P. Pishnyak, *Nonlinear electrophoresis of dielectric and metal spheres in a nematic liquid crystal*, Nature **467**, 947-950 (2010).
[174] I. Lazo and O. D. Lavrentovich, *Liquid-crystal-enabled electrophoresis of spheres in a nematic medium with negative dielectric anisotropy*, Philosophical Transactions of the Royal Society a-Mathematical Physical and Engineering Sciences **371**, 20120255 (2013).
[175] I. Lazo, C. H. Peng, J. Xiang, S. V. Shiyanovskii, and O. D. Lavrentovich, *Liquid crystal-enabled electro-osmosis through spatial charge separation in distorted regions as a novel mechanism of electrokinetics*, Nature Communications **5**, 5033 (2014).
[176] O. D. Lavrentovich, *Liquid crystal-enabled electrophoresis and electro-osmosis*, in *Liquid Crystals with Nano and Microparticles*, edited by J. P. F. Lagerwall, and G. Scalia (World Scientific, New Jersey 2017), pp. 415-457.
[177] S. Ramaswamy, R. Nityananda, V. A. Raghunathan, and J. Prost, *Power-law forces between particles in a nematic*, Molecular Crystals and Liquid Crystals Science and Technology Section a-Molecular Crystals and Liquid Crystals **288**, 175-180 (1996).

[178] O. V. Kuksenok, R. W. Ruhwandl, S. V. Shiyanovskii, and E. M. Terentjev, *Director structure around a colloid particle suspended in a nematic liquid crystal*, Physical Review E **54**, 5198-5203 (1996).
[179] P. Poulin, H. Stark, T. C. Lubensky, and D. A. Weitz, *Novel colloidal interactions in anisotropic fluids*, Science **275**, 1770-1773 (1997).
[180] H. Stark, *Saturn-ring defects around microspheres suspended in nematic liquid crystals: An analogy between confined geometries and magnetic fields*, Physical Review E **66**, 032701 (2002).
[181] Y. D. Gu and N. L. Abbott, *Observation of Saturn-ring defects around solid microspheres in nematic liquid crystals*, Physical Review Letters **85**, 4719-4722 (2000).
[182] H. Stark, *Physics of colloidal dispersions in nematic liquid crystals*, Physics Reports-Review Section of Physics Letters **351**, 387-474 (2001).
[183] G. E. Volovik and O. D. Lavrentovich, *Topological Dynamics of Defects: Boojums in Nematic Drops*, Sov. Phys. JETP **58**, 1159-1166 (1983).
[184] C. Peng, T. Turiv, Y. Guo, Q.-H. Wei, and O. D. Lavrentovich, *Sorting and separation of microparticles by surface properties using liquid crystal-enabled electro-osmosis*, Liquid Crystals **45**, 1936-1943 (2018).
[185] C. Peng and O. D. Lavrentovich, *Chapter 2: Control of micro-particles with liquid crystals*, in *Liquid crystals: New perspectives*, edited by P. Pieranski, and M. H. Godinho (ISTE Ltd and John Wiley & Sons, Inc., London, UK, 2021), pp. 81-116.
[186] J. S. Lintuvuori, A. Würger, and K. Stratford, *Hydrodynamics Defines the Stable Swimming Direction of Spherical Squirmers in a Nematic Liquid Crystal*, Physical Review Letters **119**, 068001 (2017).
[187] C. H. Peng, Y. B. Guo, C. Conklin, J. Viñals, S. V. Shiyanovskii, Q. H. Wei, and O. D. Lavrentovich, *Liquid crystals with patterned molecular orientation as an electrolytic active medium*, Physical Review E **92**, 052502 (2015).
[188] M. C. Calderer, D. Golovaty, O. Lavrentovich, and N. J. Walkington, *Modeling of nematic electrolytes and nonlinear electroosmosis*, SIAM J. Appl. Math. **76**, 2260-2285 (2016).
[189] O. M. Tovkach, M. C. Calderer, D. Golovaty, O. Lavrentovich, and N. J. Walkington, *Electro-osmosis in nematic liquid crystals*, Physical Review E **94**, 012702 (2016).
[190] O. M. Tovkach, C. Conklin, M. C. Calderer, D. Golovaty, O. D. Lavrentovich, J. Viñals, and N. J. Walkington, *Q-tensor model for electrokinetics in nematic liquid crystals*, Physical Review Fluids **2**, 053302 (2017).
[191] C. Conklin, O. M. Tovkach, J. Viñals, M. C. Calderer, D. Golovaty, O. D. Lavrentovich, and N. J. Walkington, *Electrokinetic effects in nematic suspensions: Single-particle electro-osmosis and interparticle interactions*, Physical Review E **98**, 022703 (2018).
[192] S. Paladugu, C. Conklin, J. Viñals, and O. D. Lavrentovich, *Nonlinear Electrophoresis of Colloids Controlled by Anisotropic Conductivity and Permittivity of Liquid-Crystalline Electrolyte*, Physical Review Applied **7**, 034033 (2017).
[193] S. Hernàndez-Navarro, P. Tierno, J. Ignés-Mullol, and F. Sagués, *AC electrophoresis of microdroplets in anisotropic liquids: transport, assembling and reaction*, Soft Matter **9**, 7999-8004 (2013).
[194] S. Hernàndez-Navarro, P. Tierno, J. Ignés-Mullol, and F. Sagués, *Liquid-crystal enabled electrophoresis: Scenarios for driving and reconfigurable assembling of colloids*, European Physical Journal-Special Topics **224**, 1263-1273 (2015).
[195] J. Ignés-Mullol and F. Sagués, *Active, self-motile, and driven emulsions*, Current Opinion in Colloid & Interface Science **49**, 16-26 (2020).
[196] A. V. Ryzhkova, F. V. Podgornov, and W. Haase, *Nonlinear electrophoretic motion of dielectric microparticles in nematic liquid crystals*, Applied Physics Letters **96**, 151901 (2010).
[197] T. S. Simonova and S. S. Dukhin, *Nonlinear Polarization of Diffusion Part of Thin Double-Layer of a Spherical-Particle*, Colloid Journal of the Ussr **38**, 65-70 (1976).

[198] A. S. Dukhin and S. S. Dukhin, *Aperiodic capillary electrophoresis method using an alternating current electric field for separation of macromolecules*, Electrophoresis **26**, 2149-2153 (2005).
[199] S. Stotz, *field dependence of the electrophoretic mobility of particles suspended in low-conductivity liquids*, J. Colloid Interface Sci. **65**, 118-130 (1978).
[200] D. K. Sahu, S. Kole, S. Ramaswamy, and S. Dhara, *Omnidirectional transport and navigation of Janus particles through a nematic liquid crystal film*, Physical Review Research **2**, 032009(R) (2020).
[201] I. N. Simonov and V. N. Shilov, *Theory of Low-Frequency Dielectric-Dispersion of a Suspension of Ideally Polarizable Spherical-Particles*, Colloid Journal of the Ussr **39**, 775-780 (1977).
[202] S. Hernàndez-Navarro, P. Tierno, J. A. Farrera, J. Ignés-Mullol, and F. Sagués, *Reconfigurable Swarms of Nematic Colloids Controlled by Photoactivated Surface Patterns*, Angewandte Chemie-International Edition **53**, 10696-10700 (2014).
[203] A. V. Straube, J. M. Pages, A. Ortiz-Ambriz, P. Tierno, J. Ignés-Mullol, and F. Sagués, *Assembly and transport of nematic colloidal swarms above photo-patterned defects and surfaces*, New Journal of Physics **20**, 075006 (2018).
[204] O. D. Lavrentovich, *Active colloids in liquid crystals*, Current Opinion in Colloid & Interface Science **21**, 97-109 (2016).
[205] Y. Guo, M. Jiang, C. Peng, K. Sun, O. Yaroshchuk, O. Lavrentovich, and Q. H. Wei, *High-Resolution and High-Throughput Plasmonic Photopatterning of Complex Molecular Orientations in Liquid Crystals*, Advanced Materials **28**, 2353-2358 (2016).
[206] Y. B. Guo, M. Jiang, C. H. Peng, K. Sun, O. Yaroshchuk, O. D. Lavrentovich, and Q. H. Wei, *Designs of Plasmonic Metamasks for Photopatterning Molecular Orientations in Liquid Crystals*, Crystals **7**, 8 (2017).
[207] C. H. Peng, Y. B. Guo, T. Turiv, M. Jiang, Q. H. Wei, and O. D. Lavrentovich, *Patterning of Lyotropic Chromonic Liquid Crystals by Photoalignment with Photonic Metamasks*, Advanced Materials **29**, 1606112 (2017).
[208] C. Peng, T. Turiv, Y. Guo, S. V. Shiyanovskii, and O. D. Lavrentovich, *Control of colloidal placement by modulated molecular orientation in nematic cells*, Science Advances **2**, e1600932 (2016).
[209] C. Peng, T. Turiv, R. Zhang, Y. Guo, S. V. Shiyanovskii, Q.-H. Wei, J. de Pablo, and O. D. Lavrentovich, *Controlling placement of nonspherical (boomerang) colloids in nematic cells with photopatterned director*, Journal of Physics: Condens. Matter **29**, 014005 (2017).
[210] C. H. Peng and O. D. Lavrentovich, *Liquid Crystals-Enabled AC Electrokinetics*, Micromachines **10**, 45 (2019).
[211] S. Hernàndez-Navarro, P. Tierno, J. Ignés-Mullol, and F. Sagués, *Nematic Colloidal Swarms Assembled and Transported on Photosensitive Surfaces*, IEEE Transactions on Nanobioscience **14**, 267-271 (2015).
[212] C. Conklin and J. Viñals, *Electrokinetic flows in liquid crystal thin films with fixed anchoring*, Soft Matter **13**, 725-739 (2017).
[213] C. Conklin, J. Viñals, and O. T. Valls, *A connection between living liquid crystals and electrokinetic phenomena in nematic fluids*, Soft Matter **14**, 4641-4648 (2018).
[214] P. P. Korniychuk, A. M. Gabovich, K. Singer, A. I. Voitenko, and Y. A. Reznikov, *Transient and steady electric currents through a liquid crystal cell*, Liquid Crystals **37**, 1171-1181 (2010).
[215] C. Peng, T. Turiv, Y. Guo, Q.-H. Wei, and O. D. Lavrentovich, *Command of active matter by topological defects and patterns*, Science **354**, 882-885 (2016).
[216] A. Jákli, B. Senyuk, G. X. Liao, and O. D. Lavrentovich, *Colloidal micromotor in smectic A liquid crystal driven by DC electric field*, Soft Matter **4**, 2471-2474 (2008).
[217] A. Bricard, J. B. Caussin, N. Desreumaux, O. Dauchot, and D. Bartolo, *Emergence of macroscopic directed motion in populations of motile colloids*, Nature **503**, 95-98 (2013).

[218] A. Bricard, J. B. Caussin, D. Das, C. Savoie, V. Chikkadi, K. Shitara, O. Chepizhko, F. Peruani, D. Saintillan, and D. Bartolo, *Emergent vortices in populations of colloidal rollers*, Nature Communications **6**, 7470 (2015).
[219] D. Geyer, A. Morin, and D. Bartolo, *Sounds and hydrodynamics of polar active fluids*, Nature Materials **17**, 789-793 (2018).
[220] T. Vicsek, A. Czirok, E. Benjacob, I. Cohen, and O. Shochet, *Novel Type of Phase-Transition in a System of Self-Driven Particles*, Physical Review Letters **75**, 1226-1229 (1995).
[221] R. Koizumi, T. Turiv, M. M. Genkin, R. J. Lastowski, H. Yu, I. Chaganava, Q.-H. Wei, I. S. Aranson, and O. D. Lavrentovich, *Control of bacterial swirls by spiral nematic vortices: Transition from individual to collective motion and contraction, expansion, and stable circulation of bacterial swirls*, Physical Review Research **2**, 033060 (2020).
[222] M. Warner and E. M. Terentjev, *Liquid Crystal Elastomers* (Clarendon Press, Oxford, 2007), pp. 408.
[223] T. J. White and D. J. Broer, *Programmable and adaptive mechanics with liquid crystal polymer networks and elastomers*, Nature Materials **14**, 1087-1098 (2015).
[224] C. P. Ambulo, S. Tasmim, S. F. Wang, M. K. Abdelrahman, P. E. Zimmern, and T. H. Ware, *Processing advances in liquid crystal elastomers provide a path to biomedical applications*, Journal of Applied Physics **128**, 140901 (2020).
[225] S. W. Ula, N. A. Traugutt, R. H. Volpe, R. R. Patel, K. Yu, and C. M. Yakacki, *Liquid crystal elastomers: an introduction and review of emerging technologies*, Liquid Crystals Reviews **6**, 78-107 (2018).
[226] G. Babakhanova, T. Turiv, Y. B. Guo, M. Hendrikx, Q. H. Wei, A. Schenning, D. J. Broer, and O. D. Lavrentovich, *Liquid crystal elastomer coatings with programmed response of surface profile*, Nature Communications **9**, 456 (2018).
[227] R. A. Simha and S. Ramaswamy, *Hydrodynamic fluctuations and instabilities in ordered suspensions of self-propelled particles*, Physical Review Letters **89**, 058101 (2002).
[228] D. L. Thomsen, P. Keller, J. Naciri, R. Pink, H. Jeon, D. Shenoy, and B. R. Ratna, *Liquid crystal elastomers with mechanical properties of a muscle*, Macromolecules **34**, 5868-5875 (2001).
[229] M. Warner, C. D. Modes, and D. Corbett, *Curvature in nematic elastica responding to light and heat*, Proceedings of the Royal Society a-Mathematical Physical and Engineering Sciences **466**, 2975-2989 (2010).
[230] M. E. McConney, A. Martinez, V. P. Tondiglia, K. M. Lee, D. Langley, I. I. Smalyukh, and T. J. White, *Topography from Topology: Photoinduced Surface Features Generated in Liquid Crystal Polymer Networks*, Advanced Materials **25**, 5880-5885 (2013).
[231] L. T. de Haan, A. P. H. J. Schenning, and D. J. Broer, *Programmed morphing of liquid crystal networks*, Polymer **55**, 5885-5896 (2014).
[232] T. H. Ware, M. E. McConney, J. J. Wie, V. P. Tondiglia, and T. J. White, *Voxelated liquid crystal elastomers*, Science **347**, 982-984 (2015).
[233] Y. Xia, G. Cedillo-Servin, R. D. Kamien, and S. Yang, *Guided Folding of Nematic Liquid Crystal Elastomer Sheets into 3D via Patterned 1D Microchannels*, Advanced Materials **28**, 9637-9643 (2016).
[234] C. Mostajeran, M. Warner, T. H. Ware, and T. J. White, *Encoding Gaussian curvature in glassy and elastomeric liquid crystal solids*, Proceedings of the Royal Society a-Mathematical Physical and Engineering Sciences **472**, 20160112 (2016).
[235] C. P. Ambulo, J. J. Burroughs, J. M. Boothby, H. Kim, M. R. Shankar, and T. H. Ware, *Four-dimensional Printing of Liquid Crystal Elastomers*, Acs Applied Materials & Interfaces **9**, 37332-37339 (2017).
[236] N. P. Godman, B. A. Kowalski, A. D. Auguste, H. Koerner, and T. J. White, *Synthesis of Elastomeric Liquid Crystalline Polymer Networks via Chain Transfer*, Acs Macro Letters **6**, 1290-1295 (2017).

[237] A. H. Gelebart, D. J. Mulder, M. Varga, A. Konya, G. Vantomme, E. W. Meijer, R. L. B. Selinger, and D. J. Broer, *Making waves in a photoactive polymer film*, Nature **546**, 632-635 (2017).
[238] C. D. Modes, K. Bhattacharya, and M. Warner, *Disclination-mediated thermo-optical response in nematic glass sheets*, Physical Review E **81**, 060701 (2010).
[239] C. D. Modes and M. Warner, *Blueprinting nematic glass: Systematically constructing and combining active points of curvature for emergent morphology*, Physical Review E **84**, 021711 (2011).
[240] H. Aharoni, E. Sharon, and R. Kupferman, *Geometry of Thin Nematic Elastomer Sheets*, Physical Review Letters **113**, 257801 (2014).
[241] H. Aharoni, Y. Xia, X. Y. Zhang, R. D. Kamien, and S. Yang, *Universal inverse design of surfaces with thin nematic elastomer sheets*, Proceedings of the National Academy of Sciences of the United States of America **115**, 7206-7211 (2018).
[242] D. Q. Liu and D. J. Broer, *Liquid crystal polymer networks: switchable surface topographies*, Liquid Crystals Reviews **1**, 20-28 (2013).
[243] J. E. Stumpel, D. J. Broer, and A. P. H. J. Schenning, *Stimuli-responsive photonic polymer coatings*, Chemical Communications **50**, 15839-15848 (2014).
[244] G. Babakhanova, T. Turiv, Y. Guo, M. Hendrikx, Q. H. Wei, A. Schenning, D. J. Broer, and O. D. Lavrentovich, *Liquid crystal elastomer coatings with programmed response of surface profile*, Nat Commun **9**, 456 (2018).
[245] H. Kim, J. Gibson, J. M. Maeng, M. O. Saed, K. Pimentel, R. T. Rihani, J. J. Pancrazio, S. V. Georgakopoulos, and T. H. Ware, *Responsive, 3D Electronics Enabled by Liquid Crystal Elastomer Substrates*, Acs Applied Materials & Interfaces **11**, 19506-19513 (2019).
[246] G. Babakhanova, A. P. H. J. Schenning, D. J. Broer, and O. D. Lavrentovich, *Surface structures of hybrid aligned liquid crystal network coatings containing reverse tilt domains*, Emerging Liquid Crystal Technologies XIV **10941**, 109410I (2019).
[247] G. Babakhanova, H. Yu, I. Chaganava, Q. H. Wei, P. Shiller, and O. D. Lavrentovich, *Controlled Placement of Microparticles at the Water-Liquid Crystal Elastomer Interface*, Acs Applied Materials & Interfaces **11**, 15007-15013 (2019).
[248] A. H. Gelebart, D. Jan Mulder, M. Varga, A. Konya, G. Vantomme, E. W. Meijer, R. L. B. Selinger, and D. J. Broer, *Making waves in a photoactive polymer film*, Nature **546**, 632-636 (2017).
[249] S. Serak, N. Tabiryan, R. Vergara, T. J. White, R. A. Vaia, and T. J. Bunning, *Liquid crystalline polymer cantilever oscillators fueled by light*, Soft Matter **6**, 779-783 (2010).
[250] D. Q. Liu, L. Liu, P. R. Onck, and D. J. Broer, *Reverse switching of surface roughness in a self-organized polydomain liquid crystal coating*, Proceedings of the National Academy of Sciences of the United States of America **112**, 3880-3885 (2015).
[251] W. Feng, D. J. Broer, and D. Q. Liu, *Oscillating Chiral-Nematic Fingerprints Wipe Away Dust*, Advanced Materials **30**, 1704970 (2018).
[252] E. M. Akinoglu, L. T. de Haan, S. R. Li, Z. K. Xian, L. L. Shui, J. W. Gao, G. F. Zhou, and M. Giersig, *Nanoid Canyons On-Demand: Electrically Switchable Surface Topography in Liquid Crystal Networks*, Acs Applied Materials & Interfaces **10**, 37743-37748 (2018).
[253] F. L. L. Visschers, H. Gojzewski, G. J. Vancso, D. J. Broer, and D. Q. Liu, *Oscillating Surfaces Fueled by a Continuous AC Electric Field*, Advanced Materials Interfaces **6**, 1901292 (2019).
[254] H. M. van der Kooij, S. A. Semerdzhiev, J. Buijs, D. J. Broer, D. Q. Liu, and J. Sprakel, *Morphing of liquid crystal surfaces by emergent collectivity*, Nature Communications **10**, 3501 (2019).
[255] G. L. A. Kusters, I. P. Verheul, N. B. Tito, P. van der Schoot, and C. Storm, *Dynamical Landau-de Gennes theory for electrically-responsive liquid crystal networks*, Physical Review E **102**, 042703 (2020).
[256] M. Dai, O. T. Picot, J. M. N. Verjans, L. T. de Haan, A. P. H. J. Schenning, T. Peijs, and C. W. M. Bastiaansen, *Humidity-Responsive Bilayer Actuators Based on a Liquid-Crystalline Polymer Network*, Acs Applied Materials & Interfaces **5**, 4945-4950 (2013).

[257] L. T. de Haan, J. M. N. Verjans, D. J. Broer, C. W. M. Bastiaansen, and A. P. H. J. Schenning, *Humidity-Responsive Liquid Crystalline Polymer Actuators with an Asymmetry in the Molecular Trigger That Bend, Fold, and Curl*, Journal of the American Chemical Society **136**, 10585-10588 (2014).
[258] R. C. P. Verpaalen, A. E. J. Souren, M. G. Debije, T. A. P. Engels, C. W. M. Bastiaansen, and A. P. H. J. Schenning, *Unravelling humidity-gated, temperature responsive bilayer actuators*, Soft Matter **16**, 2753-2759 (2020).
[259] O. M. Wani, R. Verpaalen, H. Zeng, A. Priimagi, and A. Schenning, *An Artificial Nocturnal Flower via Humidity-Gated Photoactuation in Liquid Crystal Networks*, Advanced Materials **31**, e1805985 (2019).
[260] T. Turiv, J. Krieger, G. Babakhanova, H. Yu, S. V. Shiyanovskii, Q.-H. Wei, M.-H. Kim, and O. D. Lavrentovich, *Topology control of human fibroblast cells monolayer by liquid crystal elastomer*, Science Advances **6**, eaaz6485 (2020).
[261] D. Q. Liu, C. W. M. Bastiaansen, J. M. J. den Toonder, and D. J. Broer, *Photo-Switchable Surface Topologies in Chiral Nematic Coatings*, Angewandte Chemie-International Edition **51**, 892-896 (2012).
[262] W. Feng, D. J. Broer, and D. Q. Liu, *Oscillating Chiral-Nematic Fingerprints Wipe Away Dust*, Adv. Mater. **30**, 1704970 (2018).
[263] J. E. Stumpel, B. Ziolkowski, L. Florea, D. Diamond, D. J. Broer, and A. P. H. J. Schenning, *Photoswitchable Ratchet Surface Topographies Based on Self-Protonating Spiropyran-NIPAAM Hydrogels*, Acs Applied Materials & Interfaces **6**, 7268-7274 (2014).
[264] G. Babakhanova, H. Yu, I. Chaganava, Q. Wei, -H., P. Shiller, and O. D. Lavrentovich, *Controlled Placement of Microparticles at the Water–Liquid Crystal Elastomer Interface*, Acs Applied Materials & Interfaces **11**, 15007-15013 (2019).
[265] G. Babakhanova, Y. M. Golestani, H. Baza, S. Afghah, H. Yu, M. Varga, Q.-H. Wei, P. Shiller, J. V. Selinger, R. L. B. Selinger, and O. D. Lavrentovich, *Dynamically morphing microchannels in liquid crystal elastomer coatings containing disclinations*, Journal of Applied Physics **128**, 184702 (2020).
[266] A. Lebar, Z. Kutnjak, S. Žumer, H. Finkelmann, A. Sanchez-Ferrer, and B. Zalar, *Evidence of supercritical behavior in liquid single crystal elastomers*, Physical Review Letters **94**, 197801 (2005).
[267] A. Lebar, G. Cordoyiannis, Z. Kutnjak, and B. Zalar, *The Isotropic-to-Nematic Conversion in Liquid Crystalline Elastomers*, Liquid Crystal Elastomers: Materials and Applications **250**, 147-185 (2012).
[268] V. Narayan, S. Ramaswamy, and N. Menon, *Long-lived giant number fluctuations in a swarming granular nematic*, Science **317**, 105-108 (2007).
[269] K. Kawaguchi, R. Kageyama, and M. Sano, *Topological defects control collective dynamics in neural progenitor cell cultures*, Nature **545**, 327-331 (2017).
[270] G. Duclos, C. Erlenkamper, J. F. Joanny, and P. Silberzan, *Topological defects in confined populations of spindle-shaped cells*, Nature Physics **13**, 58-62 (2017).
[271] T. Turiv, J. Krieger, G. Babakhanova, H. Yu, S. V. Shiyanovskii, Q. Wei, -H., M.-H. Kim, and O. D. Lavrentovich, *Topology control of human fibroblast cells monolayer by liquid crystal elastomer*, Science Advances **6**, eaaz6485 (2020).
[272] M. M. Genkin, A. Sokolov, O. D. Lavrentovich, and I. S. Aranson, *Topological Defects in a Living Nematic Ensnare Swimming Bacteria*, Physical Review X **7**, 011029 (2017).
[273] T. Sanchez, D. T. N. Chen, S. J. DeCamp, M. Heymann, and Z. Dogic, *Spontaneous motion in hierarchically assembled active matter*, Nature **491**, 431-434 (2012).
[274] F. C. Keber, E. Loiseau, T. Sanchez, S. J. DeCamp, L. Giomi, M. J. Bowick, M. C. Marchetti, Z. Dogic, and A. R. Bausch, *Topology and dynamics of active nematic vesicles*, Science **345**, 1135-1139 (2014).
[275] S. J. DeCamp, G. S. Redner, A. Baskaran, M. F. Hagan, and Z. Dogic, *Orientational order of motile defects in active nematics*, Nature Materials **14**, 1110-1115 (2015).
[276] S. Zhou, A. Sokolov, O. D. Lavrentovich, and I. S. Aranson, *Living liquid crystals*, Proceedings of the National Academy of Sciences of the United States of America **111**, 1265-1270 (2014).

[277] R. Zhang, N. Kumar, J. L. Ross, M. L. Gardel, and J. J. de Pablo, *Interplay of structure, elasticity, and dynamics in actin-based nematic materials*, Proceedings of the National Academy of Sciences of the United States of America **115**, E124-E133 (2018).
[278] N. Kumar, R. Zhang, J. J. de Pablo, and M. L. Gardel, *Tunable structure and dynamics of active liquid crystals*, Science Advances **4**, eaat7779 (2018).
[279] A. J. Tan, E. Roberts, S. A. Smith, U. A. Olvera, J. Arteaga, S. Fortini, K. A. Mitchell, and L. S. Hirst, *Topological chaos in active nematics*, Nature Physics **15**, 1033-1039 (2019).
[280] D. P. Rivas, T. N. Shendruk, R. R. Henry, D. H. Reich, and R. L. Leheny, *Driven topological transitions in active nematic films*, Soft Matter **16**, 9331-9338 (2020).
[281] K. Copenhagen, R. Alert, N. S. Wingreen, and J. W. Shaevitz, *Topological defects promote layer formation in Myxococcus xanthus colonies*, Nature Physics **17**, 211-215 (2021).
[282] L. Giomi, M. J. Bowick, P. Mishra, R. Sknepnek, and M. C. Marchetti, *Defect dynamics in active nematics*, Philosophical Transactions of the Royal Society a-Mathematical Physical and Engineering Sciences **372**, 20130365 (2014).
[283] L. M. Pismen, *Dynamics of defects in an active nematic layer*, Physical Review E **88**, 050502 (2013).
[284] A. J. Vromans and L. Giomi, *Orientational properties of nematic disclinations*, Soft Matter **12**, 6490-6495 (2016).
[285] X. Z. Tang and J. V. Selinger, *Orientation of topological defects in 2D nematic liquid crystals*, Soft Matter **13**, 5481-5490 (2017).
[286] D. Cortese, J. Eggers, and T. B. Liverpool, *Pair creation, motion, and annihilation of topological defects in two-dimensional nematic liquid crystals*, Physical Review E **97**, 022704 (2018).
[287] S. Shankar, S. Ramaswamy, M. C. Marchetti, and M. J. Bowick, *Defect Unbinding in Active Nematics*, Physical Review Letters **121**, 108002 (2018).
[288] X. Z. Tang and J. V. Selinger, *Theory of defect motion in 2D passive and active nematic liquid crystals*, Soft Matter **15**, 587-601 (2019).
[289] S. Shankar and M. C. Marchetti, *Hydrodynamics of Active Defects: From Order to Chaos to Defect Ordering*, Physical Review X **9**, 041047 (2019).
[290] A. Patelli, I. Djafer-Cherif, I. S. Aranson, E. Bertin, and H. Chate, *Understanding Dense Active Nematics from Microscopic Models*, Physical Review Letters **123**, 258001 (2019).
[291] M. M. Norton, P. Grover, M. F. Hagan, and S. Fraden, *Optimal Control of Active Nematics*, Physical Review Letters **125**, 178005 (2020).
[292] Z. Y. Li, D. Q. Zhang, S. Z. Lin, and B. Li, *Pattern Formation and Defect Ordering in Active Chiral Nematics*, Physical Review Letters **125**, 098002 (2020).
[293] O. J. Meacock, A. Doostmohammadi, K. R. Foster, J. M. Yeomans, and W. M. Durham, *Bacteria solve the problem of crowding by moving slowly*, Nature Physics **17**, 205-210 (2021).
[294] M. F. Wang, Y. N. Li, and H. Yokoyama, *Artificial web of disclination lines in nematic liquid crystals*, Nature Communications **8**, 388 (2017).
[295] G. Babakhanova, J. Krieger, B. X. Li, T. Turiv, M.-H. Kim, and O. D. Lavrentovich, *Cell alignment by smectic liquid crystal elastomer coatings withnanogrooves*, Journal of Biomedical Materials Research Part A **108**, 1223–1230 (2020).
[296] J. B. Fournier, I. Dozov, and G. Durand, *Surface Frustration and Texture Instability in Smectic-a Liquid-Crystals*, Physical Review A **41**, 2252-2255 (1990).
[297] O. D. Lavrentovich, M. Kleman, and V. M. Pergamenshchik, *Nucleation of Focal Conic Domains in Smectic A Liquid-Crystals*, Journal De Physique Ii **4**, 377-404 (1994).
[298] D. K. Yoon, M. C. Choi, Y. H. Kim, M. W. Kim, O. D. Lavrentovich, and H.-T. Jung, *Internal structure visualization and lithographic use of periodic toroidal holes in liquid crystals*, Nature Materials **6**, 866-870 (2007).

[299] M. C. Choi, T. Pfohl, Z. Wen, Y. Li, M. W. Kim, J. N. Israelachvili, and C. R. Safinya, *Ordered patterns of liquid crystal toroidal defects by microchannel confinement*, Proc Natl Acad Sci U S A **101**, 17340-17344 (2004).
[300] V. Designolle, S. Herminghaus, T. Pfohl, and C. Bahr, *AFM study of defect-induced depressions of the smectic-A/air interface*, Langmuir **22**, 363-368 (2006).
[301] J. P. Michel, E. Lacaze, M. Alba, M. De Boissieu, M. Gailhanou, and M. Goldmann, *Optical gratings formed in thin smectic films frustrated on a single crystalline substrate*, Phys Rev E Stat Nonlin Soft Matter Phys **70**, 011709 (2004).
[302] B. Zappone, E. Lacaze, H. Ayeb, M. Goldmann, N. Boudet, P. Barois, and M. Albae, *Self-ordered arrays of linear defects and virtual singularities in thin smectic-A films (vol 7, pg 1161, 2011)*, Soft Matter **7**, 11550-11550 (2011).
[303] D. Coursault, J. Grand, B. Zappone, H. Ayeb, G. Levi, N. Felidj, and E. Lacaze, *Linear Self-Assembly of Nanoparticles Within Liquid Crystal Defect Arrays*, Advanced Materials **24**, 1461-1465 (2012).
[304] C. Blanc, D. Coursault, and E. Lacaze, *Ordering nano- and microparticles assemblies with liquid crystals*, Liquid Crystals Reviews **1**, 83-109 (2013).
[305] Y. H. Kim, D. K. Yoon, M. C. Choi, H. S. Jeon, M. W. Kim, O. D. Lavrentovich, and H.-T. Jung, *Confined Self-Assembly of Toric Focal Conic Domains (The Effects of Confined Geometry on the Feature Size of Toric Focal Conic Domains)*, Langmuir **25**, 1685-1691 (2009).
[306] B. Zappone and E. Lacaze, *Surface-frustrated periodic textures of smectic-A liquid crystals on crystalline surfaces*, Physical Review E **78**, 061704 (2008).
[307] W. Guo and C. Bahr, *Influence of anchoring strength on focal conic domains in smectic films*, Physical Review E **79**, 011707 (2009).
[308] D. Gonzalez-Rodriguez, K. Guevorkian, S. Douezan, and F. Brochard-Wyart, *Soft Matter Models of Developing Tissues and Tumors*, Science **338**, 910-917 (2012).
[309] J. Prost, F. Julicher, and J. F. Joanny, *Active gel physics*, Nature Physics **11**, 111-117 (2015).
[310] V. Hakim and P. Silberzan, *Collective cell migration: a physics perspective*, Reports on Progress in Physics **80**, 076601 (2017).
[311] D. Mohammed, G. Charras, E. Vercruysse, M. Versaevel, J. Lantoine, L. Alaimo, C. Bruyere, M. Luciano, K. Glinel, G. Delhaye, O. Theodoly, and S. Gabriele, *Substrate area confinement is a key determinant of cell velocity in collective migration*, Nature Physics **15**, 858-866 (2019).
[312] E. Mehes and T. Vicsek, *Collective motion of cells: from experiments to models*, Integrative Biology **6**, 831-854 (2014).
[313] O. Ilina and P. Friedl, *Mechanisms of collective cell migration at a glance*, Journal of Cell Science **122**, 3203-3208 (2009).
[314] R. Keller, *Shaping the vertebrate body plan by polarized embryonic cell movements*, Science **298**, 1950-1954 (2002).
[315] R. Farooqui and G. Fenteany, *Multiple rows of cells behind an epithelial wound edge extend cryptic lamellipodia to collectively drive cell-sheet movement*, Journal of Cell Science **118**, 51-63 (2005).
[316] P. Friedl and D. Gilmour, *Collective cell migration in morphogenesis, regeneration and cancer*, Nature Reviews Molecular Cell Biology **10**, 445-457 (2009).
[317] M. Chuai, D. Hughes, and C. J. Weijer, *Collective Epithelial and Mesenchymal Cell Migration During Gastrulation*, Current Genomics **13**, 267-277 (2012).
[318] M. Cetera, G. R. R. S. Juan, P. W. Oakes, L. Lewellyn, M. J. Fairchild, G. Tanentzapf, M. L. Gardel, and S. Horne-Badovinac, *Epithelial rotation promotes the global alignment of contractile actin bundles during Drosophila egg chamber elongation*, Nature Communications **5**, 5511 (2014).
[319] A. S. Ghabrial and M. A. Krasnow, *Social interactions among epithelial cells during tracheal branching morphogenesis*, Nature **441**, 746-749 (2006).

[320] G. Peyret, R. Mueller, J. d'Alessandro, S. Begnaud, P. Marcq, R. M. Mege, J. M. Yeomans, A. Doostmohammadi, and B. Ladoux, *Sustained Oscillations of Epithelial Cell Sheets*, Biophysical Journal **117**, 464-478 (2019).
[321] A. J. Ridley, M. A. Schwartz, K. Burridge, R. A. Firtel, M. H. Ginsberg, G. Borisy, J. T. Parsons, and A. R. Horwitz, *Cell migration: Integrating signals from front to back*, Science **302**, 1704-1709 (2003).
[322] R. Mayor and S. Etienne-Manneville, *The front and rear of collective cell migration*, Nature Reviews Molecular Cell Biology **17**, 97-109 (2016).
[323] P. Friedl and S. Alexander, *Cancer Invasion and the Microenvironment: Plasticity and Reciprocity*, Cell **147**, 992-1009 (2011).
[324] I. Y. Wong, S. Javaid, E. A. Wong, S. Perk, D. A. Haber, M. Toner, and D. Irimia, *Collective and individual migration following the epithelial-mesenchymal transition*, Nature Materials **13**, 1063-1071 (2014).
[325] S. R. K. Vedula, M. C. Leong, T. L. Lai, P. Hersen, A. J. Kabla, C. T. Lim, and B. Ladoux, *Emerging modes of collective cell migration induced by geometrical constraints*, Proceedings of the National Academy of Sciences of the United States of America **109**, 12974-12979 (2012).
[326] H. D. T. Nia, L. L. Munn, and R. K. Jain, *Physical traits of cancer*, Science **370**, eaaz0868 (2020).
[327] R. Kemkemer, V. Teichgraber, S. Schrank-Kaufmann, D. Kaufmann, and H. Gruler, *Nematic order-disorder state transition in a liquid crystal analogue formed by oriented and migrating amoeboid cells*, European Physical Journal E **3**, 101-110 (2000).
[328] R. Kemkemer, D. Kling, D. Kaufmann, and H. Gruler, *Elastic properties of nematoid arrangements formed by amoeboid cells*, European Physical Journal E **1**, 215-225 (2000).
[329] M. Duvert, Y. Bouligand, and C. Salat, *The Liquid-Crystalline Nature of the Cytoskeleton in Epidermal-Cells of the Chaetognath Sagitta*, Tissue & Cell **16**, 469-481 (1984).
[330] Y. Bouligand, *Liquid crystals and biological morphogenesis: Ancient and new questions*, Comptes Rendus Chimie **11**, 281-296 (2008).
[331] Y. Bouligand, *Liquid Crystals and Morphogenesis*, in *Morphogenesis: Origin of Patterns and Shapes*, edited by P. Bourgine, and A. Lesne (Springer-Verlag, Berlin, 2011), pp. 49-86.
[332] T. B. Saw, A. Doostmohammadi, V. Nier, L. Kocgozlu, S. Thampi, Y. Toyama, P. Marcq, C. T. Lim, J. M. Yeomans, and B. Ladoux, *Topological defects in epithelia govern cell death and extrusion*, Nature **544**, 212-216 (2017).
[333] M. Théry, *Micropatterning as a tool to decipher cell morphogenesis and functions*, Journal of Cell Science **123**, 4201-4213 (2010).
[334] T. B. Saw, W. Xi, B. Ladoux, and C. T. Lim, *Biological Tissues as Active Nematic Liquid Crystals*, Advanced Materials **30**, 1802579 (2018).
[335] Y. Maroudas-Sacks, L. Garion, L. Shani-Zerbib, A. Livshits, E. Draun, and K. Keren, *Topological defects in the nematic order of actin fibres as organization centres of Hydra morphogenesis*, Nature Physics **17**, 251-259 (2021).
[336] N. D. Bade, R. D. Kamien, R. K. Assoian, and K. J. Stebe, *Edges impose planar alignment in nematic monolayers by directing cell elongation and enhancing migration*, Soft Matter **14**, 6867-6874 (2018).
[337] B. Ladoux and M.-A. Fardin, *Living proof of effective defects*, Nature Physics **17**, 172-173 (2021).
[338] L. S. Penrose, *Dermatoglyphic Topology*, Nature **205**, 544-& (1965).
[339] G. Duclos, S. Garcia, H. G. Yevick, and P. Silberzan, *Perfect nematic order in confined monolayers of spindle-shaped cells*, Soft Matter **10**, 2346-2353 (2014).
[340] C. Blanch-Mercader, V. Yashunsky, S. Garcia, G. Duclos, L. Giomi, and P. Silberzan, *Turbulent Dynamics of Epithelial Cell Cultures*, Physical Review Letters **120**, 208101 (2018).
[341] B. Ladoux and R. M. Mege, *Mechanobiology of collective cell behaviours*, Nature Reviews Molecular Cell Biology **18**, 743-757 (2017).

[342] M. Deforet, V. Hakim, H. G. Yevick, G. Duclos, and P. Silberzan, *Emergence of collective modes and tri-dimensional structures from epithelial confinement*, Nature Communications **5**, 3747 (2014).
[343] K. Doxzen, S. R. K. Vedula, M. C. Leong, H. Hirata, N. S. Gov, A. J. Kabla, B. Ladoux, and C. T. Lim, *Guidance of collective cell migration by substrate geometry*, Integrative Biology **5**, 1026-1035 (2013).
[344] P. Guillamat, C. Blanch-Mercader, K. Kruse, and A. Roux, *Integer topological defects organize stresses driving tissue morphogenesis*, https://www.biorxiv.org/content/10.1101/2020.06.02.129262v1 (2020).
[345] D. R. Nelson, *Toward a tetravalent chemistry of colloids*, Nano Letters **2**, 1125-1129 (2002).
[346] R. D. Williams, *2 Transitions in Tangentially Anchored Nematic Droplets*, Journal of Physics A-Mathematical and General **19**, 3211-3222 (1986).
[347] O. D. Lavrentovich and V. V. Sergan, *Parity-Breaking Phase-Transition in Tangentially Anchored Nematic Drops*, Nuovo Cimento Della Societa Italiana Di Fisica D-Condensed Matter Atomic Molecular and Chemical Physics Fluids Plasmas Biophysics **12**, 1219-1222 (1990).
[348] V. Koning, T. Lopez-Leon, A. Darmon, A. Fernandez-Nieves, and V. Vitelli, *Spherical nematic shells with a threefold valence*, Physical Review E **94**, 012703 (2016).
[349] M. Urbanski, C. G. Reyes, J. Noh, A. Sharma, Y. Geng, V. S. R. Jampani, and J. P. F. Lagerwall, *Liquid crystals in micron-scale droplets, shells and fibers*, Journal of Physics-Condensed Matter **29**, 133003 (2017).
[350] J. Noh, Y. W. Wang, H. L. Liang, V. S. R. Jampani, A. Majumdar, and J. P. F. Lagerwall, *Dynamic tuning of the director field in liquid crystal shells using block copolymers*, Physical Review Research **2**, 033160 (2020).
[351] A. Sharma, V. S. R. Jampani, and J. P. F. Lagerwall, *Realignment of Liquid Crystal Shells Driven by Temperature-Dependent Surfactant Solubility*, Langmuir **35**, 11132-11140 (2019).
[352] G. Durey, Y. Ishii, and T. Lopez-Leon, *Temperature-Driven Anchoring Transitions at Liquid Crystal/Water Interfaces*, Langmuir **36**, 9368-9376 (2020).
[353] D. Khoromskaia and G. P. Alexander, *Vortex formation and dynamics of defects in active nematic shells*, New Journal of Physics **19**, 103043 (2017).
[354] Y. H. Zhang, M. Deserno, and Z. C. Tu, *Dynamics of active nematic defects on the surface of a sphere*, Physical Review E **102**, 012607 (2020).
[355] A. T. Brown, *A theoretical phase diagram for an active nematic on a spherical surface*, Soft Matter **16**, 4682-4691 (2020).
[356] P. W. Ellis, D. J. G. Pearce, Y. W. Chang, G. Goldsztein, L. Giomi, and A. Fernandez-Nieves, *Curvature-induced defect unbinding and dynamics in active nematic toroids*, Nature Physics **14**, 85-90 (2018).
[357] D. J. G. Pearce, P. W. Ellis, A. Fernandez-Nieves, and L. Giomi, *Geometrical Control of Active Turbulence in Curved Topographies*, Physical Review Letters **122**, 168002 (2019).
[358] C. Chiccoli, I. Feruli, O. D. Lavrentovich, P. Pasini, S. V. Shiyanovskii, and C. Zannoni, *Topological defects in schlieren textures of biaxial and uniaxial nematics*, Phys Rev E Stat Nonlin Soft Matter Phys **66**, 030701 (2002).
[359] R. Mueller, J. M. Yeomans, and A. Doostmohammadi, *Emergence of Active Nematic Behavior in Monolayers of Isotropic Cells*, Physical Review Letters **122**, 048004 (2019).
[360] W. Pomp, K. Schakenraad, H. E. Balcioglu, H. van Hoorn, E. H. J. Danen, R. M. H. Merks, T. Schmidt, and L. Giomi, *Cytoskeletal Anisotropy Controls Geometry and Forces of Adherent Cells*, Physical Review Letters **121**, 178101 (2018).
[361] G. Duclos, C. Blanch-Mercader, V. Yashunsky, G. Salbreux, J. F. Joanny, J. Prost, and P. Silberzan, *Spontaneous shear flow in confined cellular nematics*, Nature Physics **14**, 728-733 (2018).

[362] G. Duclos, C. Blanch-Mercader, V. Yashunsky, G. Salbreux, J. F. Joanny, J. Prost, and P. Silberzan, *Author Correction: Spontaneous shear flow in confined cellular nematics (vol 14, pg 728, 2018)*, Nature Physics **15**, 868-868 (2019).
[363] M. Leoni and P. Sens, *Polarization of cells and soft objects driven by mechanical interactions: Consequences for migration and chemotaxis*, Physical Review E **91**, 022720 (2015).
[364] S. Jain, V. M. L. Cachoux, G. H. N. S. Narayana, S. de Beco, J. D'Alessandro, V. Cellerin, T. C. Chen, M. L. Heuze, P. Marcq, R. M. Mege, A. J. Kabla, C. T. Lim, and B. Ladoux, *The role of single-cell mechanical behaviour and polarity in driving collective cell migration*, Nature Physics **16**, 802-809 (2020).
[365] A. Erzberger, A. Jacobo, A. Dasgupta, and A. J. Hudspeth, *Mechanochemical symmetry breaking during morphogenesis of lateral-line sensory organs*, Nature Physics **16**, 949-957 (2020).
[366] E. Loiseau, S. Gsell, A. Nommick, C. Jomard, D. Gras, P. Chanez, U. D'Ortona, L. Kodjabachian, J. Favier, and A. Viallat, *Active mucus-cilia hydrodynamic coupling drives self-organization of human bronchial epithelium*, Nature Physics **16**, 1158-1164 (2020).
[367] U. Schnell and T. J. Carroll, *Planar cell polarity of the kidney*, Experimental Cell Research **343**, 258-266 (2016).
[368] X. Trepat, M. R. Wasserman, T. E. Angelini, E. Millet, D. A. Weitz, J. P. Butler, and J. J. Fredberg, *Physical forces during collective cell migration*, Nature Physics **5**, 426-430 (2009).
[369] M. Reffay, L. Petitjean, S. Coscoy, E. Grasland-Mongrain, F. Amblard, A. Buguin, and P. Silberzan, *Orientation and Polarity in Collectively Migrating Cell Structures: Statics and Dynamics*, Biophysical Journal **100**, 2566-2575 (2011).
[370] M. T. Butler and J. B. Wallingford, *Planar cell polarity in development and disease*, Nature Reviews Molecular Cell Biology **18**, 375-388 (2017).
[371] S. Ramaswamy, R. A. Simha, and J. Toner, *Active nematics on a substrate: Giant number fluctuations and long-time tails*, Europhysics Letters **62**, 196-202 (2003).
[372] R. Zhang, S. A. Redford, P. V. Ruijgrok, N. Kumar, A. Mozaffari, S. Zemsky, A. R. Dinner, V. Vitelli, Z. Bryant, M. L. Gardel, and J. J. de Pablo, *Spatiotemporal control of liquid crystal structure and dynamics through activity patterning*, Nature Materials, 10.1038/s41563-41020-00901-41564 (2021).
[373] R. Green, J. Toner, and V. Vitelli, *Geometry of thresholdless active flow in nematic microfluidics*, Physical Review Fluids **2**, 104201 (2017).
[374] T. Turiv, R. Koizumi, K. Thijssen, M. M. Genkin, H. Yu, C. Peng, Q.-H. Wei, J. M. Yeomans, I. A. Aranson, A. Doostmohammadi, and O. D. Lavrentovich, *Polar jets of swimming bacteria condensed by a patterned liquid crystal*, Nature Physics **16**, 481–487 (2020).
[375] J. Toner and Y. H. Tu, *Flocks, herds, and schools: A quantitative theory of flocking*, Physical Review E **58**, 4828-4858 (1998).
[376] H. Chaté, F. Ginelli, and R. Montagne, *Simple model for active nematics: Quasi-long-range order and giant fluctuations*, Physical Review Letters **96**, 180602 (2006).
[377] H. P. Zhang, A. Be'er, E. L. Florin, and H. L. Swinney, *Collective motion and density fluctuations in bacterial colonies*, Proceedings of the National Academy of Sciences of the United States of America **107**, 13626-13630 (2010).
[378] V. Schaller and A. R. Bausch, *Topological defects and density fluctuations in collectively moving systems*, Proceedings of the National Academy of Sciences of the United States of America **110**, 4488-4493 (2013).
[379] L. Giomi, M. J. Bowick, X. Ma, and M. C. Marchetti, *Defect Annihilation and Proliferation in Active Nematics*, Physical Review Letters **110**, 228101 (2013).
[380] L. Giomi, *Geometry and Topology of Turbulence in Active Nematics*, Physical Review X **5**, 031003 (2015).
[381] T. E. Angelini, E. Hannezo, X. Trepat, J. J. Fredberg, and D. A. Weitz, *Cell Migration Driven by Cooperative Substrate Deformation Patterns*, Physical Review Letters **104**, 168104 (2010).

[382] T. E. Angelini, E. Hannezo, X. Trepat, M. Marquez, J. J. Fredberg, and D. A. Weitz, *Glass-like dynamics of collective cell migration*, Proceedings of the National Academy of Sciences of the United States of America **108**, 4714-4719 (2011).
[383] D. T. Tambe, C. C. Hardin, T. E. Angelini, K. Rajendran, C. Y. Park, X. Serra-Picamal, E. H. H. Zhou, M. H. Zaman, J. P. Butler, D. A. Weitz, J. J. Fredberg, and X. Trepat, *Collective cell guidance by cooperative intercellular forces*, Nature Materials **10**, 469-475 (2011).
[384] A. Maitra, P. Srivastava, M. C. Marchetti, J. S. Lintuvuori, S. Ramaswamy, and M. Lenz, *A nonequilibrium force can stabilize 2D active nematics*, Proceedings of the National Academy of Sciences of the United States of America **115**, 6934-6939 (2018).
[385] F. Julicher and S. Eaton, *Emergence of tissue shape changes from collective cell behaviours*, Seminars in Cell & Developmental Biology **67**, 103-112 (2017).
[386] C. M. Lo, H. B. Wang, M. Dembo, and Y. L. Wang, *Cell movement is guided by the rigidity of the substrate*, Biophysical Journal **79**, 144-152 (2000).
[387] P. A. Janmey and R. T. Miller, *Mechanisms of mechanical signaling in development and disease*, Journal of Cell Science **124**, 9-18 (2011).
[388] U. S. Schwarz and S. A. Safran, *Physics of adherent cells*, Reviews of Modern Physics **85**, 1327-1381 (2013).
[389] B. Szabo, Z. Kornyei, J. Zach, D. Selmeczi, G. Csucs, A. Czirok, and T. Vicsek, *Auto-reverse nuclear migration in bipolar mammalian cells on micropatterned surfaces*, Cell Motility and the Cytoskeleton **59**, 38-49 (2004).
[390] M. Gupta, B. L. Doss, L. Kocgozlu, M. Pan, R. M. Mege, A. Callan-Jones, R. Voituriez, and B. Ladoux, *Cell shape and substrate stiffness drive actin-based cell polarity*, Physical Review E **99**, 012412 (2019).
[391] L. Q. Wan, K. Ronaldson, M. Park, G. Taylor, Y. Zhang, J. M. Gimble, and G. Vunjak-Novakovic, *Micropatterned mammalian cells exhibit phenotype-specific left-right asymmetry*, Proceedings of the National Academy of Sciences of the United States of America **108**, 12295-12300 (2011).
[392] X. Y. Jiang, D. A. Bruzewicz, A. P. Wong, M. Piel, and G. M. Whitesides, *Directing cell migration with asymmetric micropatterns*, Proceedings of the National Academy of Sciences of the United States of America **102**, 975-978 (2005).
[393] L. Petitjean, M. Reffay, E. Grasland-Mongrain, M. Poujade, B. Ladoux, A. Buguin, and P. Silberzan, *Velocity Fields in a Collectively Migrating Epithelium*, Biophysical Journal **98**, 1790-1800 (2010).
[394] X. Z. Tang and J. V. Selinger, *Alignment of a topological defect by an activity gradient*, Physical Review E **103**, 022703 (2021).
[395] D. H. Kim, K. Han, K. Gupta, K. W. Kwon, K. Y. Suh, and A. Levchenko, *Mechanosensitivity of fibroblast cell shape and movement to anisotropic substratum topography gradients*, Biomaterials **30**, 5433-5444 (2009).
[396] C. Rianna, L. Rossano, R. H. Kollarigowda, F. Formiggini, S. Cavalli, M. Ventre, and P. A. Netti, *Spatio-Temporal Control of Dynamic Topographic Patterns on Azopolymers for Cell Culture Applications*, Advanced Functional Materials **26**, 7572-7580 (2016).
[397] J. M. Molitoris, S. Paliwal, R. B. Sekar, R. Blake, J. Park, N. A. Trayanova, L. Tung, and A. Levchenko, *Precisely parameterized experimental and computational models of tissue organization*, Integrative Biology (United Kingdom) **8**, 230-242 (2016).
[398] K. D. Endresen, B. Kim, and F. Serra, *Topological defects of integer charge in cell monolayers*, Arxiv, 1912.03271v03271 (2019).
[399] K. D. Endresen, M. Kim, M. Pittman, Y. Chen, and F. Serra, *Topological defects of integer charge in cell monolayers*, Soft Matter, https://doi.org/10.1039/D1031SM00100K (2021).
[400] S. J. P. Callens, R. J. C. Uyttendaele, L. E. Fratila-Apachitei, and A. A. Zadpoor, *Substrate curvature as a cue to guide spatiotemporal cell and tissue organization*, Biomaterials **232**, 119739 (2020).

[401] D. Baptista, L. Teixeira, C. van Blitterswijk, S. Giselbrecht, and R. Truckenmuller, *Overlooked? Underestimated? Effects of Substrate Curvature on Cell Behavior*, Trends in Biotechnology **37**, 838-854 (2019).
[402] N. D. Bade, T. N. Xu, R. D. Kamien, R. K. Assoian, and K. J. Stebe, *Gaussian Curvature Directs Stress Fiber Orientation and Cell Migration*, Biophysical Journal **114**, 1467-1476 (2018).
[403] D. M. Sussman, *Interplay of curvature and rigidity in shape-based models of confluent tissue*, Physical Review Research **2**, 023417 (2020).
[404] A. Agarwal, E. Huang, S. Palecek, and N. L. Abbott, *Optically Responsive and Mechanically Tunable Colloid-In-Liquid Crystal Gels that Support Growth of Fibroblasts*, Advanced Materials **20**, 4804-4809 (2008).
[405] D. Martella and C. Parmeggiani, *Advances in Cell Scaffolds for Tissue Engineering: The Value of Liquid Crystalline Elastomers*, Chemistry-a European Journal **24**, 12206-12220 (2018).
[406] D. Martella, P. Paoli, J. M. Pioner, L. Sacconi, R. Coppini, L. Santini, M. Lulli, E. Cerbai, D. S. Wiersma, C. Poggesi, C. Ferrantini, and C. Parmeggiani, *Liquid Crystalline Networks toward Regenerative Medicine and Tissue Repair*, Small **13**, 1702677 (2017).
[407] M. E. Prevot, H. Andro, S. L. M. Alexander, S. Ustunel, C. Zhu, Z. Nikolov, S. T. Rafferty, M. T. Brannum, B. Kinsel, L. T. J. Korley, E. J. Freeman, J. A. McDonough, R. J. Clements, and E. Hegmann, *Liquid crystal elastomer foams with elastic properties specifically engineered as biodegradable brain tissue scaffolds*, Soft Matter **14**, 354-360 (2018).
[408] A. Agrawal, H. Y. Chen, H. Kim, B. H. Zhu, O. Adetiba, A. Miranda, A. C. Chipara, P. M. Ajayan, J. G. Jacot, and R. Verduzco, *Electromechanically Responsive Liquid Crystal Elastomer Nanocomposites for Active Cell Culture*, Acs Macro Letters **5**, 1386-1390 (2016).
[409] Y. X. Gao, T. Mori, S. Manning, Y. Zhao, A. D. Nielsen, A. Neshat, A. Sharma, C. J. Mahnen, H. R. Everson, S. Crotty, R. J. Clements, C. Malcuit, and E. Hegmann, *Biocompatible 3D Liquid Crystal Elastomer Cell Scaffolds and Foams with Primary and Secondary Porous Architecture*, Acs Macro Letters **5**, 14-19 (2016).
[410] A. M. Lowe and N. L. Abbott, *Liquid crystalline materials for biological applications*, Chemistry of Materials **24**, 746-758 (2012).
[411] A. Agrawal, O. Adetiba, H. Kim, H. Chen, J. G. Jacot, and R. Verduzco, *Stimuli-responsive liquid crystal elastomers for dynamic cell culture*, Journal of Materials Research **30**, 453-462 (2015).
[412] G. Kocer, J. Ter Schiphorst, M. Hendrikx, H. G. Kassa, P. Leclere, A. Schenning, and P. Jonkheijm, *Light-Responsive Hierarchically Structured Liquid Crystal Polymer Networks for Harnessing Cell Adhesion and Migration*, Advanced Materials **29**, 1606407 (2017).
[413] D. Martella, L. Pattelli, C. Matassini, F. Ridi, M. Bonini, P. Paoli, P. Baglioni, D. S. Wiersma, and C. Parmeggiani, *Liquid Crystal-Induced Myoblast Alignment*, Advanced Healthcare Materials **8**, 1801489 (2019).
[414] J. H. Jiang, N. P. Dhakal, Y. B. Guo, C. Andre, L. Thompson, O. Skalli, and C. H. Peng, *Controlled Dynamics of Neural Tumor Cells by Templated Liquid Crystalline Polymer Networks*, Advanced Healthcare Materials **9**, 2000487 (2020).
[415] B. M. Skinner and E. E. P. Johnson, *Nuclear morphologies: their diversity and functional relevance*, Chromosoma **126**, 195-212 (2017).
[416] D. Nishiguchi, K. H. Nagai, H. Chaté, and M. Sano, *Long-range nematic order and anomalous fluctuations in suspensions of swimming filamentous bacteria*, Physical Review E **95**, 020601 (2017).
[417] S. Shankar, S. Ramaswamy, M. C. Marchetti, and M. J. Bowick, *Defect Unbinding in Active Nematics*, Physical Review Letters **121**, 108002 (2018).
[418] A. R. Harris, L. Peter, J. Bellis, B. Baum, A. J. Kabla, and G. T. Charras, *Characterizing the mechanics of cultured cell monolayers*, Proceedings of the National Academy of Sciences of the United States of America **109**, 16449-16454 (2012).

[419] A. Trushko, I. Di Meglio, A. Merzouki, C. Blanch-Mercader, S. Abuhattum, J. Guck, K. Alessandri, P. Nassoy, K. Kruse, B. Chopard, and A. Roux, *Buckling of an Epithelium Growing under Spherical Confinement*, Developmental Cell **54**, 655-668 (2020).
[420] J. Fouchard, T. P. J. Wyatt, A. Proag, A. Lisica, N. Khalilgharibi, P. Recho, M. Suzanne, A. Kabla, and G. Charras, *Curling of epithelial monolayers reveals coupling between active bending and tissue tension*, Proceedings of the National Academy of Sciences of the United States of America **117**, 9377-9383 (2020).
[421] P. E. Cladis and M. Kleman, *Non-Singular Disclinations of Strength S = + 1 in Nematics*, Journal De Physique **33**, 591-598 (1972).
[422] R. B. Meyer, *Existence of Even Indexed Disclinations in Nematic Liquid-Crystals*, Philosophical Magazine **27**, 405-424 (1973).
[423] E. M. Purcell, *Life at Low Reynolds-Number*, American Journal of Physics **45**, 3-11 (1977).
[424] E. Lauga, *Life around the scallop theorem*, Soft Matter **7**, 3060-3065 (2011).
[425] R. Di Leonardo, L. Angelani, D. Dell'Arciprete, G. Ruocco, V. Iebba, S. Schippa, M. P. Conte, F. Mecarini, F. De Angelis, and E. Di Fabrizio, *Bacterial ratchet motors*, Proceedings of the National Academy of Sciences of the United States of America **107**, 9541-9545 (2010).
[426] S. Thutupalli, R. Seemann, and S. Herminghaus, *Swarming behavior of simple model squirmers*, New Journal of Physics **13**, 073021 (2011).
[427] C. Bechinger, R. Di Leonardo, H. Lowen, C. Reichhardt, G. Volpe, and G. Volpe, *Active Particles in Complex and Crowded Environments*, Reviews of Modern Physics **88**, 045006 (2016).
[428] A. Sokolov, M. M. Apodaca, B. A. Grzybowski, and I. S. Aranson, *Swimming bacteria power microscopic gears*, Proceedings of the National Academy of Sciences of the United States of America **107**, 969-974 (2010).
[429] J. Arlt, V. A. Martinez, A. Dawson, T. Pilizota, and W. C. K. Poon, *Painting with light-powered bacteria*, Nature Communications **9**, 768 (2018).
[430] J. Moran and J. Posner, *Microscopic self-propelled particles could one day be used to clean up wastewater or deliver drugs in the body*, Physics Today **72**, 45-50 (2019).
[431] J. R. Howse, R. A. L. Jones, A. J. Ryan, T. Gough, R. Vafabakhsh, and R. Golestanian, *Self-motile colloidal particles: From directed propulsion to random walk*, Physical Review Letters **99**, 048102 (2007).
[432] G. Ramos, M. L. Cordero, and R. Soto, *Bacteria driving droplets*, Soft Matter **16**, 1359-1365 (2020).
[433] R. D. Baker, T. Montenegro-Johnson, A. D. Sediako, M. J. Thomson, A. Sen, E. Lauga, and I. S. Aranson, *Shape-programmed 3D printed swimming microtori for the transport of passive and active agents*, Nature Communications **10**, 4932 (2019).
[434] J. Lydon, *Chromonic liquid crystalline phases*, Liquid Crystals **38**, 1663-1681 (2011).
[435] H. S. Park and O. D. Lavrentovich, *Lyotropic Chromonic Liquid Crystals: Emerging Applications* in *Liquid Crystals Beyond Displays: Chemistry, Physics, and Applications*, edited by Q. Li (John Wiley & Sons, Hoboken, New Jersey, 2012), pp. 449-484.
[436] C. J. Woolverton, E. Gustely, L. Li, and O. D. Lavrentovich, *Liquid crystal effects on bacterial viability*, Liquid Crystals **32**, 417-423 (2005).
[437] J. Lydon, *Chromonic mesophases*, Current Opinion in Colloid & Interface Science **8**, 480-490 (2004).
[438] J. Lydon, *Chromonic review*, Journal of Materials Chemistry **20**, 10071-10099 (2010).
[439] K. Y.-K., S. S.V., and L. O.D., *Morphogenesis of defects and tactoids during isotropic–nematic phase transition in self-assembled lyotropic chromonic liquid crystals*, Journal of Physics: Condensed Matter **25**, 404202 (2013).
[440] I. I. Smalyukh, J. Butler, J. D. Shrout, M. R. Parsek, and G. C. L. Wong, *Elasticity-mediated nematiclike bacterial organization in model extracellular DNA matrix*, Physical Review E **78**, 030701 (2008).
[441] A. Kumar, T. Galstian, S. K. Pattanayek, and S. Rainville, *The Motility of Bacteria in an Anisotropic Liquid Environment*, Molecular Crystals and Liquid Crystals **574**, 33-39 (2013).

[442] P. C. Mushenheim, R. R. Trivedi, D. B. Weibel, and N. L. Abbott, *Using Liquid Crystals to Reveal How Mechanical Anisotropy Changes Interfacial Behaviors of Motile Bacteria*, Biophysical Journal **107**, 255-265 (2014).
[443] P. C. Mushenheim, R. R. Trivedi, S. S. Roy, M. S. Arnold, D. B. Weibel, and N. L. Abbott, *Effects of confinement, surface-induced orientation and strain on dynamic behavior of bacteria in thin liquid crystalline films*, Soft Matter **11**, 6821-6831 (2015).
[444] P. C. Mushenheim, R. R. Trivedi, H. H. Tuson, D. B. Weibel, and N. L. Abbott, *Dynamic self-assembly of motile bacteria in liquid crystals*, Soft Matter **10**, 79-86 (2014).
[445] A. Sokolov, S. Zhou, O. D. Lavrentovich, and I. S. Aranson, *Individual behavior and pairwise interactions between microswimmers in anisotropic liquid*, Physical Review E **91**, 013009 (2015).
[446] J. G. Zhao, U. Gulan, T. Horie, N. Ohmura, J. Han, C. Yang, J. Kong, S. Wang, and B. Xu, *Advances in Biological Liquid Crystals*, Small **15**, 1900019 (2019).
[447] L. H. Cisneros, J. O. Kessler, R. Ortiz, R. Cortez, and M. A. Bees, *Unexpected Bipolar Flagellar Arrangements and Long-Range Flows Driven by Bacteria near Solid Boundaries*, Physical Review Letters **101**, 168102 (2008).
[448] K. Drescher, J. Dunkel, L. H. Cisneros, S. Ganguly, and R. E. Goldstein, *Fluid dynamics and noise in bacterial cell-cell and cell-surface scattering*, Proceedings of the National Academy of Sciences of the United States of America **108**, 10940-10945 (2011).
[449] N. C. Darnton, L. Turner, S. Rojevsky, and H. C. Berg, *On torque and tumbling in swimming Escherichia coli*, Journal of Bacteriology **189**, 1756-1764 (2007).
[450] S. Chattopadhyay, R. Moldovan, C. Yeung, and X. L. Wu, *Swimming efficiency of bacterium Escherichia coli*, Proceedings of the National Academy of Sciences of the United States of America **103**, 13712-13717 (2006).
[451] K. A. Fahrner, W. S. Ryu, and H. C. Berg, *Biomechanics: Bacterial flagellar switching under load*, Nature **423**, 938 (2003).
[452] S. W. Reid, M. C. Leake, J. H. Chandler, C. J. Lo, J. P. Armitage, and R. M. Berry, *The maximum number of torque-generating units in the flagellar motor of Escherichia coli is at least 11*, Proceedings of the National Academy of Sciences of the United States of America **103**, 8066-8071 (2006).
[453] R. M. Berry and H. C. Berg, *Absence of a barrier to backwards rotation of the bacterial flagellar motor demonstrated with optical tweezers*, Proceedings of the National Academy of Sciences of the United States of America **94**, 14433-14437 (1997).
[454] J. L. Hu, M. C. Yang, G. Gompper, and R. G. Winkler, *Modelling the mechanics and hydrodynamics of swimming E. coli*, Soft Matter **11**, 7867-7876 (2015).
[455] M. M. Genkin, A. Sokolov, and I. S. Aranson, *Spontaneous topological charging of tactoids in a living nematic*, New Journal of Physics **20**, 043027 (2018).
[456] F. Brochard and P. G. de Gennes, *Theory of Magnetic Suspensions in Liquid Crystals*, Journal De Physique **31**, 691-708 (1970).
[457] C. J. Smith and C. Denniston, *Elastic response of a nematic liquid crystal to an immersed nanowire*, Journal of Applied Physics **101**, 014305 (2007).
[458] S. Zhou, O. Tovkach, D. Golovaty, A. Sokolov, I. S. Aranson, and O. D. Lavrentovich, *Dynamic states of swimming bacteria in a nematic liquid crystal cell with homeotropic alignment*, New Journal of Physics **19**, 055006 (2017).
[459] V. G. Nazarenko, O. P. Boiko, H. S. Park, O. M. Brodyn, M. M. Omelchenko, L. Tortora, Y. A. Nastishin, and O. D. Lavrentovich, *Surface Alignment and Anchoring Transitions in Nematic Lyotropic Chromonic Liquid Crystal*, Physical Review Letters **105**, 017801 (2010).
[460] S. V. Shiyanovskii, O. D. Lavrentovich, T. Schneider, T. Ishikawa, I. I. Smalyukh, C. J. Woolverton, G. D. Niehaus, and K. J. Doane, *Lyotropic chromonic liquid crystals for biological sensing applications*, Molecular Crystals and Liquid Crystals **434**, 587-598 (2005).

[461] M. Tasinkevych, F. Mondiot, O. Mondain-Monval, and J. C. Loudet, *Dispersions of ellipsoidal particles in a nematic liquid crystal*, Soft Matter **10**, 2047-2058 (2014).
[462] C. K. McGinn, L. I. Laderman, N. Zimmermann, H. S. Kitzerow, and P. J. Collings, *Planar anchoring strength and pitch measurements in achiral and chiral chromonic liquid crystals using 90-degree twist cells*, Physical Review E **88**, 062513 (2013).
[463] H. Chi, M. Potomkin, L. Zhang, L. Berlyand, and I. S. Aranson, *Surface anchoring controls orientation of a microswimmer in nematic liquid crystal*, Communications Physics **3**, 162 (2020).
[464] A. Daddi-Moussa-Ider and A. M. Menzel, *Dynamics of a simple model microswimmer in an anisotropic fluid: Implications for alignment behavior and active transport in a nematic liquid crystal*, Physical Review Fluids **3**, 094102 (2018).
[465] T. L. Crowley, C. Bottrill, D. Mateer, W. J. Harrison, and G. J. T. Tiddy, *Lyotropic chromonic liquid crystals: neutron scattering studies of shear-induced orientation and reorientation*, Colloids and Surfaces a-Physicochemical and Engineering Aspects **129**, 95-115 (1997).
[466] A. F. Kostko, B. H. Cipriano, O. A. Pinchuk, L. Ziserman, M. A. Anisimov, D. Danino, and S. R. Raghavan, *Salt effects on the phase behavior, structure, and rheology of chromonic liquid crystals*, Journal of Physical Chemistry B **109**, 19126-19133 (2005).
[467] S. Zhou, K. Neupane, Y. A. Nastishin, A. R. Baldwin, S. V. Shiyanovskii, O. D. Lavrentovich, and S. Sprunt, *Elasticity, viscosity, and orientational fluctuations of a lyotropic chromonic nematic liquid crystal disodium cromoglycate*, Soft Matter **10**, 6571-6581 (2014).
[468] Y. J. Cha, M. J. Gim, H. Ahn, T. J. Shin, J. Jeong, and D. K. Yoon, *Orthogonal Liquid Crystal Alignment Layer: Templating Speed-Dependent Orientation of Chromonic Liquid Crystals*, Acs Applied Materials & Interfaces **9**, 18355-18361 (2017).
[469] H. Baza, T. Turiv, B.-X. Li, R. Li, B. M. Yavit, M. Fukuto, and O. D. Lavrentovich, *Shear-induced polydomain structures of nematic lyotropic chromonic liquid crystal disodium cromoglycate*, Soft Matter **16**, 8565-8576 (2020).
[470] F. Mondiot, S. P. Chandran, O. Mondain-Monval, and J. C. Loudet, *Shape-Induced Dispersion of Colloids in Anisotropic Fluids*, Physical Review Letters **103**, 238303 (2009).
[471] I. O. Gotze and G. Gompper, *Mesoscale simulations of hydrodynamic squirmer interactions*, Physical Review E **82**, 041921 (2010).
[472] V. M. Pergamenshchik and V. A. Uzunova, *Dipolar colloids in nematostatics: Tensorial structure, symmetry, different types, and their interaction*, Physical Review E **83**, 021701 (2011).
[473] V. A. Uzunova and V. M. Pergamenshchik, *Chiral dipole induced by azimuthal anchoring on the surface of a planar elastic quadrupole*, Physical Review E **84**, 031702 (2011).
[474] B. Senyuk, D. Glugla, and I. I. Smalyukh, *Rotational and translational diffusion of anisotropic gold nanoparticles in liquid crystals controlled by varying surface anchoring*, Physical Review E **88**, 062507 (2013).
[475] A. E. Patteson, A. Gopinath, M. Goulian, and P. E. Arratia, *Running and tumbling with E-coli in polymeric solutions*, Scientific Reports **5**, 15761 (2015).
[476] R. R. Trivedi, R. Maeda, N. L. Abbott, S. E. Spagnolie, and D. B. Weibel, *Bacterial transport of colloids in liquid crystalline environments*, Soft Matter **11**, 8404-8408 (2015).
[477] Z. Kos and M. Ravnik, *Elementary Flow Field Profiles of Micro-Swimmers in Weakly Anisotropic Nematic Fluids: Stokeslet, Stresslet, Rotlet and Source Flows*, Fluids **3**, 15 (2018).
[478] M. S. Krieger, S. E. Spagnolie, and T. R. Powers, *Locomotion and transport in a hexatic liquid crystal*, Physical Review E **90**, 052503 (2014).
[479] C. Dombrowski, L. Cisneros, S. Chatkaew, R. E. Goldstein, and J. O. Kessler, *Self-concentration and large-scale coherence in bacterial dynamics*, Physical Review Letters **93**, 098103 (2004).

[480] N. H. Mendelson, A. Bourque, K. Wilkening, K. R. Anderson, and J. C. Watkins, *Organized cell swimming motions in Bacillus subtilis colonies: Patterns of short-lived whirls and jets*, Journal of Bacteriology **181**, 600-609 (1999).
[481] A. Sokolov, I. S. Aranson, J. O. Kessler, and R. E. Goldstein, *Concentration dependence of the collective dynamics of swimming bacteria*, Physical Review Letters **98**, 158102 (2007).
[482] L. H. Cisneros, J. O. Kessler, S. Ganguly, and R. E. Goldstein, *Dynamics of swimming bacteria: Transition to directional order at high concentration*, Physical Review E **83**, 061907 (2011).
[483] H. H. Wensink, J. Dunkel, S. Heidenreich, K. Drescher, R. E. Goldstein, H. Lowen, and J. M. Yeomans, *Meso-scale turbulence in living fluids*, Proceedings of the National Academy of Sciences of the United States of America **109**, 14308-14313 (2012).
[484] J. Dunkel, S. Heidenreich, K. Drescher, H. H. Wensink, M. Bar, and R. E. Goldstein, *Fluid Dynamics of Bacterial Turbulence*, Physical Review Letters **110**, 228102 (2013).
[485] T. Ishikawa, G. Sekiya, Y. Imai, and T. Yamaguchi, *Hydrodynamic interactions between two swimming bacteria*, Biophysical Journal **93**, 2217-2225 (2007).
[486] C. W. Wolgemuth, *Collective swimming and the dynamics of bacterial turbulence*, Biophysical Journal **95**, 1564-1574 (2008).
[487] T. H. Tan, J. H. Liu, P. W. Miller, M. Tekant, J. Dunkel, and N. Fakhri, *Topological turbulence in the membrane of a living cell*, Nature Physics **16**, 657-662 (2020).
[488] S. Ramaswamy and M. Rao, *Active-filament hydrodynamics: instabilities, boundary conditions and rheology*, New Journal of Physics **9**, 423 (2007).
[489] T. B. Liverpool and M. C. Marchetti, *Instabilities of isotropic solutions of active polar filaments*, Physical Review Letters **90**, 138102 (2003).
[490] D. Marenduzzo, E. Orlandini, M. E. Cates, and J. M. Yeomans, *Steady-state hydrodynamic instabilities of active liquid crystals: Hybrid lattice Boltzmann simulations*, Physical Review E **76**, 031921 (2007).
[491] D. Saintillan and M. J. Shelley, *Instabilities, pattern formation, and mixing in active suspensions*, Physics of Fluids **20**, 123304 (2008).
[492] R. Alert, J. F. Joanny, and J. Casademunt, *Universal scaling of active nematic turbulence*, Nature Physics **16**, 682-688 (2020).
[493] P. Guillamat, J. Ignés-Mullol, and F. Sagués, *Control of active liquid crystals with a magnetic field*, Proceedings of the National Academy of Sciences of the United States of America **113**, 5498-5502 (2016).
[494] P. Guillamat, J. Ignés-Mullol, and F. Sagués, *Taming active turbulence with patterned soft interfaces*, Nature Communications **8**, 564 (2017).
[495] J. Hardouin, R. Hughes, A. Doostmohammadi, J. Laurent, T. Lopez-Leon, J. M. Yeomans, J. Ignés-Mullol, and F. Sagués, *Reconfigurable flows and defect landscape of confined active nematics*, Communications Physics **2**, 121 (2019).
[496] P. Chandrakar, M. Varghese, A. A. Aghvami, A. Baskaran, Z. Dogic, and G. Duclos, *Confinement Controls the Bend Instability of Three-Dimensional Active Liquid Crystals*, Physical Review Letters **125**, 257801.
[497] B. Martinez-Prat, J. Ignés-Mullol, J. Casademunt, and F. Sagués, *Selection mechanism at the onset of active turbulence*, Nature Physics **15**, 362-366 (2019).
[498] R. Voituriez, J. F. Joanny, and J. Prost, *Spontaneous flow transition in active polar gels*, Europhysics Letters **70**, 404-410 (2005).
[499] T. Vicsek and A. Zafeiris, *Collective motion*, Physics Reports-Review Section of Physics Letters **517**, 71-140 (2012).
[500] J. Toner and Y. H. Tu, *Long-Range Order in a 2-Dimensional Dynamical XY Model - How Birds Fly Together*, Physical Review Letters **75**, 4326-4329 (1995).

[501] A. Sokolov and I. S. Aranson, *Physical Properties of Collective Motion in Suspensions of Bacteria*, Physical Review Letters **109**, 248109 (2012).
[502] S. P. Thampi, R. Golestanian, and J. M. Yeomans, *Velocity Correlations in an Active Nematic*, Physical Review Letters **111**, 118101 (2013).
[503] S. P. Thampi, R. Golestanian, and J. M. Yeomans, *Active nematic materials with substrate friction*, Physical Review E **90**, 062307 (2014).
[504] T. Gao, R. Blackwell, M. A. Glaser, M. D. Betterton, and M. J. Shelley, *Multiscale Polar Theory of Microtubule and Motor-Protein Assemblies*, Physical Review Letters **114**, 048101 (2015).
[505] L. Huber, R. Suzuki, T. Kruger, E. Frey, and A. R. Bausch, *Emergence of coexisting ordered states in active matter systems*, Science **361**, 255-258 (2018).
[506] J. Denk and E. Frey, *Pattern-induced local symmetry breaking in active-matter systems*, Proceedings of the National Academy of Sciences of the United States of America **117**, 31623-31630 (2020).
[507] A. Ahmadi, T. B. Liverpool, and M. C. Marchetti, *Nematic and polar order in active filament solutions*, Physical Review E **72**, 060901 (2005).
[508] A. Ahmadi, M. C. Marchetti, and T. B. Liverpool, *Hydrodynamics of isotropic and liquid crystalline active polymer solutions*, Physical Review E **74**, 061913 (2006).
[509] R. Grossmann, I. S. Aranson, and F. Peruani, *A particle-field approach bridges phase separation and collective motion in active matter*, Nature Communications **11**, 5365 (2020).
[510] A. Sokolov, A. Mozaffari, R. Zhang, J. J. de Pablo, and A. Snezhko, *Emergence of Radial Tree of Bend Stripes in Active Nematics*, Physical Review X **9**, 031014 (2019).
[511] A. Loisy, J. Eggers, and T. B. Liverpool, *Tractionless Self-Propulsion of Active Drops*, Physical Review Letters **123**, 248006 (2019).
[512] P. Srivastava, P. Mishra, and M. C. Marchetti, *Negative stiffness and modulated states in active nematics*, Soft Matter **12**, 8214-8225 (2016).
[513] E. Putzig, G. S. Redner, A. Baskaran, and A. Baskaran, *Instabilities, defects, and defect ordering in an overdamped active nematic*, Soft Matter **12**, 3854-3859 (2016).
[514] A. Joshi, E. Putzig, A. Baskaran, and M. F. Hagan, *The interplay between activity and filament flexibility determines the emergent properties of active nematics*, Soft Matter **15**, 94-101 (2019).
[515] C. J. Ingham, O. Kalisman, A. Finkelshtein, and E. Ben-Jacob, *Mutually facilitated dispersal between the nonmotile fungus Aspergillus fumigatus and the swarming bacterium Paenibacillus vortex*, Proceedings of the National Academy of Sciences of the United States of America **108**, 19731-19736 (2011).
[516] A. Shklarsh, A. Finkelshtein, G. Ariel, O. Kalisman, C. Ingham, and E. Ben-Jacob, *Collective navigation of cargo-carrying swarms*, Interface Focus **2**, 786-798 (2012).
[517] A. Finkelshtein, D. Roth, E. Ben Jacob, and C. J. Inghamd, *Bacterial Swarms Recruit Cargo Bacteria To Pave the Way in Toxic Environments*, Mbio **6**, e00074-00015 (2015).
[518] P. P. Lele, B. G. Hosu, and H. C. Berg, *Dynamics of mechanosensing in the bacterial flagellar motor*, Proceedings of the National Academy of Sciences of the United States of America **110**, 11839-11844 (2013).
[519] K. T. Wu, J. B. Hishamunda, D. T. N. Chen, S. J. DeCamp, Y. W. Chang, A. Fernandez-Nieves, S. Fraden, and Z. Dogic, *Transition from turbulent to coherent flows in confined three-dimensional active fluids*, Science **355**, eaal1979 (2017).
[520] C. C. Maass, C. Krüger, S. Herminghaus, and C. Bahr, *Swimming Droplets*, Annual Review of Condensed Matter Physics **7**, 171-193 (2016).
[521] M. Schmitt and H. Stark, *Swimming active droplet: A theoretical analysis*, Epl **101**, 44008 (2013).

[522] C. Y. Jin, C. Kruger, and C. C. Maass, *Chemotaxis and autochemotaxis of self-propelling droplet swimmers*, Proceedings of the National Academy of Sciences of the United States of America **114**, 5089-5094 (2017).
[523] C. Y. Jin, J. Vachier, S. Bandyopadhyay, T. Macharashvili, and C. C. Maass, *Fine balance of chemotactic and hydrodynamic torques: When microswimmers orbit a pillar just once*, Physical Review E **100**, 040601 (2019).
[524] C. H. Meredith, P. G. Moerman, J. Groenewold, Y. J. Chiu, W. K. Kegel, A. van Blaaderen, and L. D. Zarzar, *Predator-prey interactions between droplets driven by non-reciprocal oil exchange*, Nature Chemistry **12**, 1136-1142 (2020).
[525] A. Najafi and R. Golestanian, *Simple swimmer at low Reynolds number: Three linked spheres*, Physical Review E **69**, 062901 (2004).
[526] J. E. Avron, O. Kenneth, and D. H. Oaknin, *Pushmepullyou: an efficient micro-swimmer*, New Journal of Physics **7**, 234 (2005).
[527] K. Kruse, J. F. Joanny, F. Julicher, and J. Prost, *Contractility and retrograde flow in lamellipodium motion*, Physical Biology **3**, 130-137 (2006).
[528] K. Keren, Z. Pincus, G. M. Allen, E. L. Barnhart, G. Marriott, A. Mogilner, and J. A. Theriot, *Mechanism of shape determination in motile cells*, Nature **453**, 475-480 (2008).
[529] F. Ziebert, S. Swaminathan, and I. S. Aranson, *Model for self-polarization and motility of keratocyte fragments*, Journal of the Royal Society Interface **9**, 1084-1092 (2012).
[530] E. Tjhung, D. Marenduzzo, and M. E. Cates, *Spontaneous symmetry breaking in active droplets provides a generic route to motility*, Proceedings of the National Academy of Sciences of the United States of America **109**, 12381-12386 (2012).
[531] D. Khoromskaia and G. P. Alexander, *Motility of active fluid drops on surfaces*, Physical Review E **92**, 062311 (2015).
[532] E. Tjhung, A. Tiribocchi, D. Marenduzzo, and M. E. Cates, *A minimal physical model captures the shapes of crawling cells*, Nature Communications **6**, 5420 (2015).
[533] L. Giomi and A. DeSimone, *Spontaneous Division and Motility in Active Nematic Droplets*, Physical Review Letters **112**, 147802 (2014).
[534] A. C. Callan-Jones and R. Voituriez, *Active gel model of amoeboid cell motility*, New Journal of Physics **15**, 025022 (2013).
[535] P. Recho, T. Putelat, and L. Truskinovsky, *Contraction-Driven Cell Motility*, Physical Review Letters **111**, 108102 (2013).
[536] C. A. Whitfield and R. J. Hawkins, *Instabilities, motion and deformation of active fluid droplets*, New Journal of Physics **18**, 123016 (2016).
[537] N. Yoshinaga, *Self-propulsion of an active polar drop*, Journal of Chemical Physics **150**, 184904 (2019).
[538] E. Lushi, H. Wioland, and R. E. Goldstein, *Fluid flows created by swimming bacteria drive self-organization in confined suspensions*, Proceedings of the National Academy of Sciences of the United States of America **111**, 9733-9738 (2014).
[539] A. C. H. Tsang and E. Kanso, *Circularly confined microswimmers exhibit multiple global patterns*, Physical Review E **91**, 043008 (2015).
[540] S. Čopar, J. Aplinc, Ž. Kos, S. Žumer, and M. Ravnik, *Topology of Three-Dimensional Active Nematic Turbulence Confined to Droplets*, Physical Review X **9**, 031051 (2019).
[541] J. M. Hardouin, J. Laurent, T. Lopez-Leon, J. Ignés-Mullol, and F. Sagués, *Active microfluidic transport in two-dimensional handlebodies*, Soft Matter **16**, 9230-9241 (2020).
[542] T. Gao, M. D. Betterton, A. S. Jhang, and M. J. Shelley, *Analytical structure, dynamics, and coarse graining of a kinetic model of an active fluid*, Physical Review Fluids **2**, 093302 (2017).

[543] S. Y. Reigh, L. L. Zhu, F. Gallaire, and E. Lauga, *Swimming with a cage: low-Reynolds-number locomotion inside a droplet*, Soft Matter **13**, 3161-3173 (2017).
[544] Z. H. Huang, T. Omori, and T. Ishikawa, *Active droplet driven by a collective motion of enclosed microswimmers*, Physical Review E **102**, 022603 (2020).
[545] T. Gao and Z. R. Li, *Self-Driven Droplet Powered By Active Nematics*, Physical Review Letters **119**, 108002 (2017).
[546] M. Rajabi, B. Hend, T. Turiv, and O. D. Lavrentovich, *Directional self-locomotion of active droplets enabled by nematic environment*, Nature Physics **17**, 260-266 (2021).
[547] R. J. Adrian, *Particle-Imaging Techniques for Experimental Fluid-Mechanics*, Annual Review of Fluid Mechanics **23**, 261-304 (1991).
[548] I. Grant, *Particle image velocimetry: A review*, Proceedings of the Institution of Mechanical Engineers Part C-Journal of Mechanical Engineering Science **211**, 55-76 (1997).
[549] I. D. Vladescu, E. J. Marsden, J. Schwarz-Linek, V. A. Martinez, J. Arlt, A. N. Morozov, D. Marenduzzo, M. E. Cates, and W. C. K. Poon, *Filling an Emulsion Drop with Motile Bacteria*, Physical Review Letters **113**, 268101 (2014).
[550] Y. Fily, A. Baskaran, and M. F. Hagan, *Dynamics of self-propelled particles under strong confinement*, Soft Matter **10**, 5609-5617 (2014).
[551] H. Wioland, F. G. Woodhouse, J. Dunkel, J. O. Kessler, and R. E. Goldstein, *Confinement Stabilizes a Bacterial Suspension into a Spiral Vortex*, Physical Review Letters **110**, 268102 (2013).
[552] Y. K. Kim, J. Noh, K. Nayani, and N. L. Abbott, *Soft matter from liquid crystals*, Soft Matter **15**, 6913-6929 (2019).
[553] H. Stark and D. Ventzki, *Non-linear Stokes drag of spherical particles in a nematic solvent*, Europhysics Letters **57**, 60-66 (2002).
[554] R. Zhang, T. Roberts, I. S. Aranson, and J. J. de Pablo, *Lattice Boltzmann simulation of asymmetric flow in nematic liquid crystals with finite anchoring*, Journal of Chemical Physics **144**, 084905 (2016).
[555] D. Marenduzzo, E. Orlandini, and J. M. Yeomans, *Interplay between shear flow and elastic deformations in liquid crystals*, Journal of Chemical Physics **121**, 582-591 (2004).
[556] B. T. Gettelfinger, J. A. Moreno-Razo, G. M. Koenig, J. P. Hernandez-Ortiz, N. L. Abbott, and J. J. de Pablo, *Flow induced deformation of defects around nanoparticles and nanodroplets suspended in liquid crystals*, Soft Matter **6**, 896-901 (2010).
[557] J. Elgeti, R. G. Winkler, and G. Gompper, *Physics of microswimmers-single particle motion and collective behavior: a review*, Reports on Progress in Physics **78**, 056601 (2015).
[558] M. M. Stanton, C. Trichet-Paredes, and S. Sanchez, *Applications of three-dimensional (3D) printing for microswimmers and bio-hybrid robotics*, Lab on a Chip **15**, 1634-1637 (2015).
[559] A. C. H. Tsang, E. Demir, Y. Ding, and O. S. Palk, *Roads to Smart Artificial Microswimmers*, Advanced Intelligent Systems **2**, 1900137 (2020).
[560] L. Ricotti, B. Trimmer, A. W. Feinberg, R. Raman, K. K. Parker, R. Bashir, M. Sitti, S. Martel, P. Dario, and A. Menciassi, *Biohybrid actuators for robotics: A review of devices actuated by living cells*, Science Robotics **2**, eaaq0495 (2017).
[561] O. D. Lavrentovich, *Transport of particles in liquid crystals*, Soft Matter **10**, 1264-1283 (2014).
[562] A. Sokolov, A. Mozaffari, R. Zhang, J. J. de Pablo, and A. Snezhko, *Emergence of radial tree of bend stripes in active nematics*, Physical Review X **9**, 031014 (2019).
[563] J. Shi and T. R. Powers, *Swimming in an anisotropic fluid: How speed depends on alignment angle*, Physical Review Fluids **2**, 123102 (2017).
[564] O. D. Lavrentovich, *Ferroelectric nematic liquid crystal, a century in waiting*, Proceedings of the National Academy of Sciences of the United States of America **117**, 14629-14631 (2020).
[565] R. J. Mandle and A. Mertelj, *Orientational order in the splay nematic ground state*, Physical Chemistry Chemical Physics **21**, 18769-18772 (2019).

[566] N. Sebastian, L. Cmok, R. J. Mandle, M. R. de la Fuente, I. D. Olenik, M. Copic, and A. Mertelj, *Ferroelectric-Ferroelastic Phase Transition in a Nematic Liquid Crystal*, Physical Review Letters **124**, 037801 (2020).
[567] M. P. Rosseto and J. V. Selinger, *Theory of the splay nematic phase: Single versus double splay*, Physical Review E **101**, 052707 (2020).
[568] M. Born, *Über anisotrope Flüssigkeiten. Versuch einer Theorie der flüssigen Kristalle und des elektrischen Kerr-Effects in Flüssigkeiten/On anisotropic fluids. The test of a theory of fluid crystals and of electrical Kerr effects in fluids*, Sitzungsberichte Der Koniglich Preussischen Akademie Der Wissenschaften, 614-650 (1916).
[569] L. W. Martin and A. M. Rappe, *Thin-film ferroelectric materials and their applications*, Nature Reviews Materials **2**, 16087 (2017).
[570] M. B. Hindmarsh and T. W. B. Kibble, *Cosmic Strings*, Reports on Progress in Physics **58**, 477-562 (1995).
[571] J. T. Makinen, V. V. Dmitriev, J. Nissinen, J. Rysti, G. E. Volovik, A. N. Yudin, K. Zhang, and V. B. Eltsov, *Half-quantum vortices and walls bounded by strings in the polar-distorted phases of topological superfluid He-3*, Nature Communications **10**, 237 (2019).
[572] G. E. Volovik and K. Zhang, *String monopoles, vortex skyrmions, and nexus objects in the polar distorted B phase of 3 He*, Physical Review Research **2**, 023263 (2020).
[573] K. Zhang, *One-dimensional nexus objects, network of Kibble-Lazarides-Shafi string walls, and their spin dynamic response in polar-distorted B-phase of 3He*, Physical Review Research **2**, 043356 (2020).
[574] C. A. Whitfield, T. C. Adhyapak, A. Tiribocchi, G. P. Alexander, D. Marenduzzo, and S. Ramaswamy, *Hydrodynamic instabilities in active cholesteric liquid crystals*, European Physical Journal E **40**, 50 (2017).
[575] S. J. Kole, G. P. Alexander, S. Ramaswamy, and A. Maitra, *Active cholesterics: odder than odd elasticity*, arXiv:2012.14321 (2020).
[576] L. N. Carenza, G. Gonnella, D. Marenduzzo, and G. Negro, *Rotation and propulsion in 3D active chiral droplets*, Proceedings of the National Academy of Sciences of the United States of America **116**, 22065-22070 (2019).
[577] L. N. Carenza, G. Gonnella, D. Marenduzzo, and G. Negro, *Chaotic and periodical dynamics of active chiral droplets*, Physica a-Statistical Mechanics and Its Applications **559**, 125025 (2020).
[578] T. C. Adhyapak, S. Ramaswamy, and J. Toner, *Live Soap: Stability, Order, and Fluctuations in Apolar Active Smectics*, Physical Review Letters **110**, 118102 (2013).
[579] P. Romanczuk, H. Chaté, L. M. Chen, S. Ngo, and J. Toner, *Emergent smectic order in simple active particle models*, New Journal of Physics **18**, 063015 (2016).
[580] N. Kumar, R. K. Gupta, H. Soni, S. Ramaswamy, and A. K. Sood, *Trapping and sorting active particles: Motility-induced condensation and smectic defects*, Physical Review E **99**, 032605 (2019).
[581] C. Ferreiro-Cordova, J. Toner, H. Lowen, and H. H. Wensink, *Long-time anomalous swimmer diffusion in smectic liquid crystals*, Physical Review E **97**, 062606 (2018).
[582] K. Thijssen, L. Metselaar, J. M. Yeomans, and A. Doostmohammadi, *Active nematics with anisotropic friction: the decisive role of the flow aligning parameter*, Soft Matter **16**, 2065-2074 (2020).